REACTIONS OF IRON AND NICKEL ALLOY DROPLETS WITH GASES

A thesis
presented for the degree of
Doctor of Philosophy
of the
University of London
and for the Diploma of the Imperial College

by

MANUEL ENRIQUE GUZMAN MANZO

John Percy Research Group
Department of Metallurgy and Materials Science
Imperial College of Science and Technology
London SW7 2BP

March 1984

Dedicated to my beloved wife, Victoria

ABSTRACT

Some reactions between levitated drops of iron and nickel alloys with flowing gases were studied.

The oxidation of molten Fe-18Cr-2C alloy specimens with pure oxygen and oxygen-argon gas mixtures was studied. Free-falling drops at an initial temperature of 1650°C were reacted with the oxidizing gas for times ranging from 24 to 267 msec. The reaction was observed by high-speed cinematography. Rapid quenching of the reacted drops allowed a good separation between the metal and oxide phases. The experimental evidence was that an oxide of chromium and iron formed immediately without decarburization when the drop was brought into contact with the oxidizing gas. A mechanism of reaction was suggested.

The equilibria between molten iron and CO/CO_2 gas mixtures were studied at high carbon concentrations. The effect of carbon on the activity coefficient of oxygen was measured by fixing the oxygen activity and varying the carbon activity by changing the total pressure of the system. Total pressures up to 80 atm were used. Thin films formed on the levitated drops slowed down the reactions or blocked them almost completely, despite the high purity materials used in this work (impurities in the 10 ppm range). The kinetics of the reactions were compared with the results predicted for carburization and decarburization of molten iron free of oxide films.

The oxidation of molten Ni-20S alloy specimens with air and pure oxygen at temperatures as low as 1050°C was studied. High pressure levitation melting allowed the low temperatures required to be achieved. The reaction occurred either with SO_2 evolution or formation of an oxide layer. A simple kinetic model was proposed for predicting the conditions which determined the nature of the reaction. The growth of the oxide layer was also studied.

Table of Contents

Page

Chapter Five: STUDY OF THE OXIDATION OF NICKEL-SULFUR DROPS WITH OXYGEN-BEARING GASES AT LOW TEMPERATURES 191

APPENDICES

Page

Appendix

LIST OF FIGURES

Figure

LIST OF PLATES

Plate

LIST OF TABLES

Table

Chapter One

GENERAL INTRODUCTION

The study of the reactions taking place in metal-gas, metal-slag and metal-gas-slag systems has the greatest importance in metal production by pyrometallurgical processes. Most studies of the thermodynamic equilibria and kinetics of these reactions have been done by using crucibles to contain the molten metal. This technique has some limitations mainly related to secondary reactions between the crucible and the melt.

The levitation melting technique overcomes these problems as the melt is suspended without physical contact with a container. However, the levitation melting process has its own limitations as it will be detailed later in Chapter Two.

The aims of this work were to study some reactions between molten metal and gas relevant to steelmaking and nickel production, by using the levitation melting technique. The purpose was to obtain fundamental information about kinetics and equilibrium to contribute to a better understanding of the mechanisms of these reactions occurring in industrial processes.

The thesis was divided into self-contained chapters, each of them describing a particular subject.

The experimental technique and details of the equipment and materials used throughout this work are given in Chapter Two. However, when a technique is more specific it is described in the corresponding chapter.

Chapter Three deals with the study of the first stages of the oxidation of a commercial Fe-18Cr-2C alloy, supplied by British Steel Corporation, by using the free-fall technique. The experimental procedure attempted to simulate the conditions existing at the tip of the tuyeres when an oxygen-argon mixture is injected into the molten metal in the AOD stainless steelmaking process. The purpose of this study was to answer questions about oxide formation, oxide composition and whether CO evolution occurs at very short times of reaction between the melt and the oxidizing gas. The reaction was followed by high speed cinematography and the reacted metal was quenched in a spinning quencher allowing phase separation for later analysis.

The most important and fundamental reaction in steelmaking is the carbon-oxygen reaction, which has received a great deal of attention for decades. However, there is still controversy about the effect of carbon on the oxygen activity coefficient in molten iron. The purpose of the present work was to measure the interaction parameter of carbon on oxygen. To carry out this work a new high pressure levitation apparatus (HPLA) was used. As reported in Chapter Four the study was wider than the original scope as the kinetics of carburization and decarburization had to be studied to determine the time at which equilibrium was reached. In this respect the purity of the starting materials was shown to be critical as far as the kinetics of the reaction is concerned. Existing theoretical models were applied to interpret the kinetic data of carburization and decarburization and also for the calculation of the oxygen concentration at the surface during the initial stage of carburization.

The last part of the research programme was concerned about the reaction of a molten nickel-sulfur alloy, with a nominal composition of 20 wt% sulfur, with air and oxygen. The alloy was supplied by Clydach Refinery (INCO Europe Limited). Chapter Five deals with this topic. It was required to study the oxidation of the molten alloy at a temperature as low as 1000°C. The use of the high pressures available in the HPLA allowed the convective heat transfer coefficient to be sufficiently large to control the temperature at the low values required. The results obtained during the first stage of oxidation allowed the prediction of the conditions for solid oxide layer formation or autogenous oxidation. A theoretical model was developed for this stage of the reaction and this could be extrapolated to higher temperatures. The process of formation of the oxide layer was recorded on film by using a cine camera. The growth of the solid oxide layer covering the melt was also studied.

Chapter Two

EXPERIMENTAL

2.1 Introduction

The experimental techniques used in this work are described in this chapter. The aim is to provide a general background necessary to assess the experimental data. The experiments of the studies described in Chapters Four and Five were carried out in the same equipment and following basically the same procedure.

2.2 The Levitation Melting Technique

The levitation melting technique is now a well established technique for fundamental work in metallurgy and physicochemical studies.

An electrical conductor placed in a high frequency non-uniform electromagnetic field levitates as a result of a lifting force. Eddy currents are induced in it and the heat produced by Joule dissipation melts the specimen.

The magnetic field is usually produced by two coaxial coils wound in opposite directions with several turns in each coil. These coils are connected to a high frequency generator which supplies the current. Generators of 5-60 kW and 10-500kHz have been used.[1,2] At these high frequencies the penetration of the electromagnetic field in the metal of high conductivity is confined to a thin surface layer.[3]

The levitation melting technique has been developing since the 'fifties and pioneering work was done by Okress et al[1] searching for a method of melting the more reactive high melting point metals such as Ti, Zr, V, Ta and Mo without the problems of crucible contamination. In their work the fundamental equations of the levitation melting theory were established. It was also evident the intrinsic low electrical heating efficiency of the induction coils used to levitate relatively small mass of sample.

Peifer[4] reviewed the development of this technique and its potential use in basic research. The application to large scale operations was considered remote mainly because of the small masses which it was possible to levitate and the instabilities of the melt. The possibility of industrial application of levitation melting was considered and discussed by Rostron.[5] In recent years large quantities of high purity alloys have been prepared by the levitation process.[2] It is claimed that the precision of their composition and their homogeneity make these alloys excellent analytical standards. The potential use in the industry has been possible because of the progress achieved in the design of high frequency generators so the small mass, in the past about 20g for the denser metals, has sometimes multiplied by a factor of ten.[2]

The potential for application of the levitation melting technique to perform physicochemical experiments was early recognised by Jenkins et al.[6] They investigated the factors for the design of levitation coils appropriate for this kind of study and suitable designs were found. The design of levitation coils is highly empirical. The performance of a number of coils has been studied with respect to their lifting and heating characteristics.[7]

Although the conditions to levitate and melt metals and alloys were established in the 'sixties, little was known about the internal flow of the liquid. It was always assumed, based on direct observation, that the droplet was a well stirred system. Knowledge of the fluid flow field is of great importance from a practical and fundamental point of view. The mixing of the melt constituents would give a homogeneous product, one advantage quoted for the levitation melting process. On the other hand this information was needed for the interpretation of measured kinetics data. Recent studies have shown that even though there are high velocities of circulation the system is not very well mixed.[3,8]

Sneyd and Moffat[3] arrived at the conclusion that the interior flow is likely to be turbulent, the fluid motion may consist of two or four eddies symmetrically located in the droplet depending on the relative sizes of the coil and the melt.

El-Kaddah and Szekely[8] calculated the electromagnetic force field of the specimen, the fluid flow field generated by the electromagnetic forces and the temperature field resulting from the balance between heat generation and heat dissipation due to convection and radiation. Their results showed that, while the fluid flow field is highly turbulent in the central zone of the drop, laminarization occurs near the free surface. This laminarized zone occupies a major volume of the specimen. They also noted the existence of two recirculating loops at each side of the droplet. The calculated linear velocities were very high, of the order of 0.3m/sec. The calculated temperature field was not uniform and a temperature difference of up to about 10°C was found.

The advantages and disadvantages of the levitation melting technique are summarized in the following paragraphs.

Advantages of levitation melting:

a) The specimen is not contaminated by a container or crucible during heating and melting.

b) The specimen can be protected by inert gas or vacuum during heating and melting.

c) Homogeneity of the melt due to electromagnetic stirring.

d) The starting specimen can be in various forms. For example sintered powders may be levitated and then melted. Separate metal and alloying constituents can be levitated together, e.g. Ti and TiO_2 to make Ti-O alloys. Slag phases can be encapsulated in the starting specimen and levitated together in equilibrium studies.

e) Rapid heating and melting.

f) Rapid attainment of equilibrium in gas-liquid metal systems.

g) Alloys can be made 'in situ' and alloying additions can be made while the metal droplet is levitated.

Disadvantages of levitation melting:

a) Temperature control and measurement are difficult. This is the main disadvantage of this technique.

b) High vaporization rate of volatile elements.

c) Steep temperature gradients between the melt and surrounding gas which cause thermal diffusion in the gas phase and enhanced vaporization of the melt.

d) Small mass of the specimen which it is possible to maintain in the molten state.

The reactions involving liquid metal and gases in metallurgical processes can occur in different ways.[9] The melt can form droplets falling freely in the reacting gas, the gas may be dispersed as bubbles in the melt and, the liquid and the gas may be both continuous phases reacting across the interface.

In free-fall experiments the sample is usually melted in an inert atmosphere by using a levitation melting apparatus and then released by switching off the power of the HF generator. The reaction column is separated from the upper section containing the inert gas by a plastic membrane which is burnt by the falling drop providing a step in the reactive gas concentration. Apparatuses used in previous works only differ in the method of quenching the reacted droplet. Quenching has been carried out in cleaned water,[10,11] in silicone oil,[11] between copper plates brought together as the specimen fell between them[12] and on the inner surface of a spinning copper tube.[13]

The kinetics of reactions involving free-falling droplets and gases depends on the degree of internal circulation at the moment when the droplet was formed[9] and no direct comparison with results involving levitated droplets can be made.[10]

Levitation melting at high pressure had not been used extensively. Previous work had only been done in this laboratory[12,14] to study nucleation of carbon monoxide in molten iron and the carbon-oxygen reaction. In this apparatus, designed by El-Kaddah and Robertson,[15] the specimen was levitated within a recrystallized alumina tube which could withstand internal pressures of 100 atmospheres with a safety factor of eight. Although the apparatus was used satisfactorily the alumina tube had the disadvantage of poor thermal shock resistance and failure could occur when the droplet hit the walls. A new high pressure apparatus in which the insulating tube containing the levitated specimen was not under stress was designed by El-Kaddah. A stainless steel pressure vessel contained the levitation coil and the silica tube. An additional problem emerged as the electromagnetic field induced currents in the pressure vessel heating it to unacceptably high temperatures. The system could not operate for more than a few minutes before the pressure vessel got too hot. Modification of the design of this apparatus to make it operational was undertaken in the present work.

2.3 The levitation coils

The design of levitation coils appropriate for metallurgical and physicochemical studies has been discussed elsewhere.[6] Two designs were selected as they have proved to give satisfactory operation concerning stability of the melt and steady temperature within the ranges of interest in the current investigation.[6,12,14]

The designs of these coils are shown in Figure 2.1.

The levitation coils were made of 0.1 inch O.D. silver tubing of 0.01 inch wall thickness. Also one coil of design (1) was made of $^1/8$ inch O.D. copper tubing of 0.018 inch wall thickness to operate during the preliminary tests of the high pressure levitation apparatus but later changed to silver coil to reduce the impedance of the coil and improve the cooling by water.

The levitation coil of design (1) consisted of two coaxial coils with two top turns wound in one sense and five bottom turns wound in the opposite direction and connected in series. The distance between the two sets of turns was 2mm. The two lower turns were co-planar and the next three formed a cone of semi-apex angle of 30° with the inner lower turn.

The system of design (2) consisted of four lower turns, two pairs of co-planar turns, with a similar number of reverse turns above at 10mm separation.

The design (1) allows good stability of small and large charges, it is considered a 'general purpose coil'. The design (2) gives

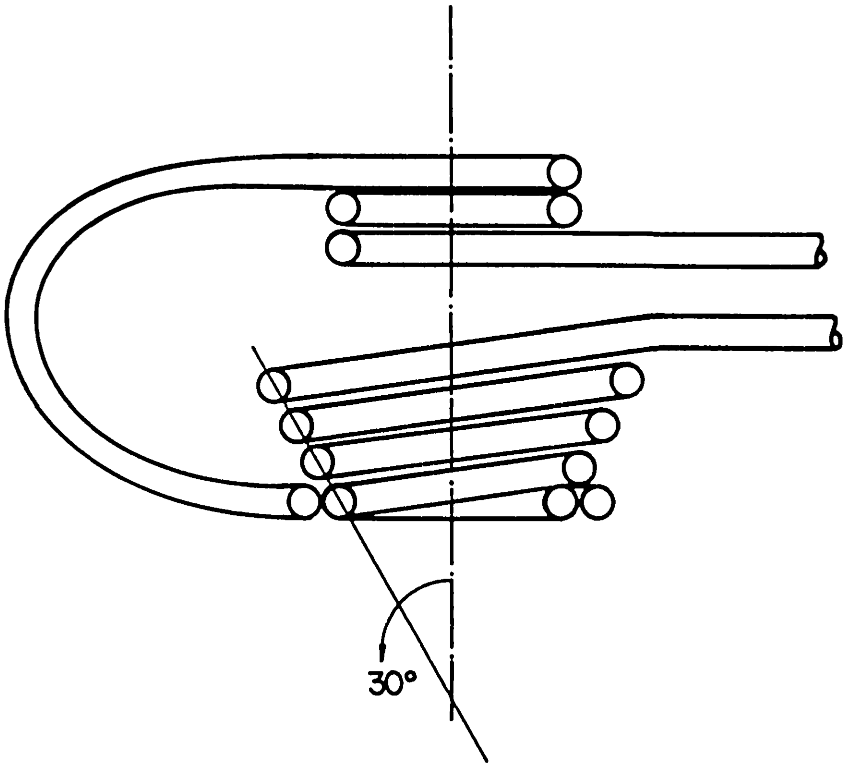

Design (1)

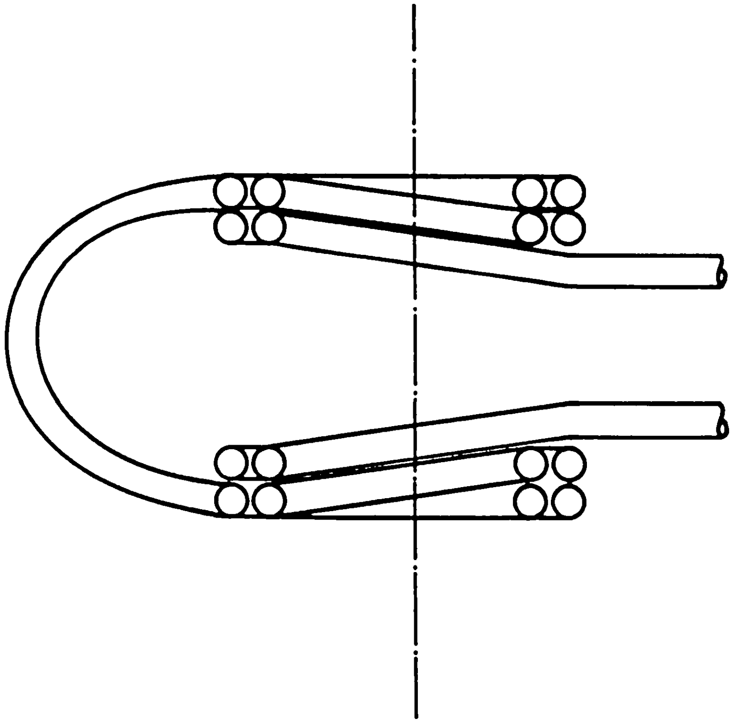

Design (2)

FIGURE 2.1. Levitation coils used in the present work.

high stability of small charges but higher temperatures of the melt are obtained.

For a particular coil design the temperature of the melt depends on the power input, convection loss and radiation loss. In this investigation the mass of the sample was kept at about 1g but in general increasing the mass of the melt usually results in an increase of its temperature. The radiation loss can be altered by changing the radiation properties of the surroundings, for example by using spherical reflectors.[6] The heat loss by convection to the surrounding gas depends upon its heat capacity, viscosity, thermal conductivity and flow rate. The temperature can be then adjusted either by changing the surrounding gas or by altering the flow rate for a particular gas.

2.4 The high frequency generator

The power necessary to levitate the specimen was drawn from a high frequency generator, 'J J Induction Generator', of 10kW and 450kHz. The HF generator had facilities for working in manual or automatic mode. Manual operation was used throughout this work and good control was achieved. The melt temperature was always maintained in the range ±5°C. A detailed description of the principles of operation of this apparatus has been given elsewhere.[14]

As was mentioned before the levitation melting process is highly inefficient in terms of available energy transferred to the specimen. In fact only a very small fraction of the power is useful and most of the energy is taken away by the water circulating through the coils.[12] The cooling water was delivered by a back-up pump at about 120 psi.

2.5 The free-fall apparatus

2.5.1 Apparatus

The experimental set-up is shown schematically in Figure 2.2. The levitation system consisted of a coil of design (1) (see section 2.3). The silica tube, around which the coils were wound, was 17.5mm O.D. and 180mm length. Two square bolted stainless steel plates maintained the silica tube in place. The upper one had a window where a 45° glass prism was located to allow temperature measurement by using a two-colour pyrometer (see section 2.7).

The cylindrical chamber, built in aluminium, had a window for looking at the push rod movement and could be removed for putting the specimen onto the push rod. The push rod was fitted to the chamber by 'O' rings. A lateral connection in the chamber allowed the flushing out by inert gas.

The glass tube was the reaction chamber. It was attached through a flange and 'O' rings to the chamber described above. It had a 'cling-wrap' membrane on both ends and a lateral connection for oxygen feeding. The lower membrane had a little hole so a continuous flow of gas could be obtained. Various glass tube lengths were used, allowing corresponding times of reaction.

The quenching device, or spinning quencher, consisted of 25.4mm O.D. copper tubing of 10cm length. It was driven by a D.C. motor controlled by an electronic speed controller. The speed was in the range 2000 to 6000 rpm.

2.5.2 Operation

The silica tube and chamber were flushed out for 10 min by using helium flowing downwards. The specimen in a small silica cup was raised to the levitation position using the push rod which

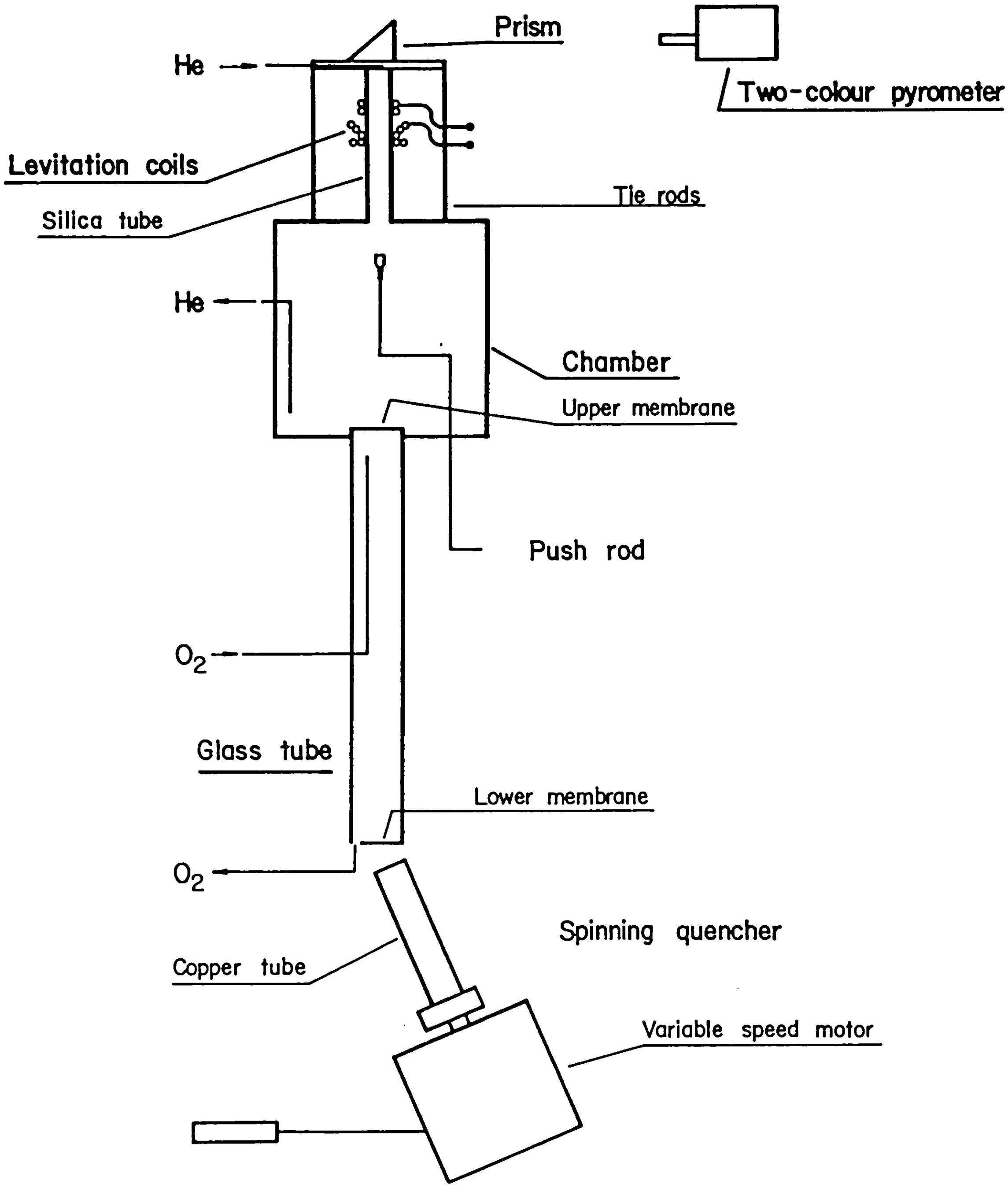

FIGURE 2.2. Free-fall apparatus.

was then lowered and swung away from the central axis of the apparatus. The droplet temperature was adjusted to the required value. The oxygen flow rate was turned on so that the gas reached the upper membrane. The speed of the spinning quencher was adjusted and the droplet allowed to fall.

The helium pressure was always slightly greater than the oxygen pressure to prevent any oxidation before the droplet entered to the glass tube.

2.5.3 Displacement versus time of the free-falling drop

The following equation has been found[12] to describe the displacement of the free-falling drop after passing through the upper membrane positioned 30cm below the levitation position:

$$s = 258t + 490.5t^2$$

where s is the displacement from the membrane in cm and t the time in sec.

Four glass tubes were available of lengths 6, 38, 70 and 104cm, therefore the corresponding times of reaction were 22, 120, 197 and 267 msec.

2.6 The high pressure levitation apparatus

The design of the high pressure levitation apparatus (HPLA) was originally made by El-Kaddah to accomplish the following requirements:

a) The silica tube containing the levitated specimen must not be subjected to stress.

b) Working pressure of up to 100 atmospheres.

c) The apparatus must have facilities to introduce the specimen within the levitation coil, any additional alloying elements, and for quenching the droplet under pressure.

d) The apparatus must have windows to allow direct observation and filming of the droplet while the reaction is taking place.

The apparatus was similar to the other one previously designed by El-Kaddah and Robertson[15] with respect to the turn table and pneumatic system to raise the specimen or the mould for quenching after reaction. The key was the design of the pressure vessel to contain the levitation coil and to achieve equal gas pressures on both sides of the silica tube. The pressure vessel was built in stainless steel and the objectives were achieved except by the excessive induction heating of the vessel that prevented its use.

The following additional requirements were stated in the modification of the HPLA design:

a) The system must operate for long periods of time without too much heating of the pressure vessel.

b) The apparatus must have facilities to reduce the pressure in a very short time to allow nucleation studies.

In order to achieve these objectives a cooling system was designed along with a new gas train.

As the design of the HPLA has not been reported previously a description is given in the following paragraphs together with the modifications carried out in this work and the results of preliminary tests to check its operation.

Photographs of the HPLA set-up and a detail of the pressure chamber are shown in Plates 2.1 and 2.2 respectively.

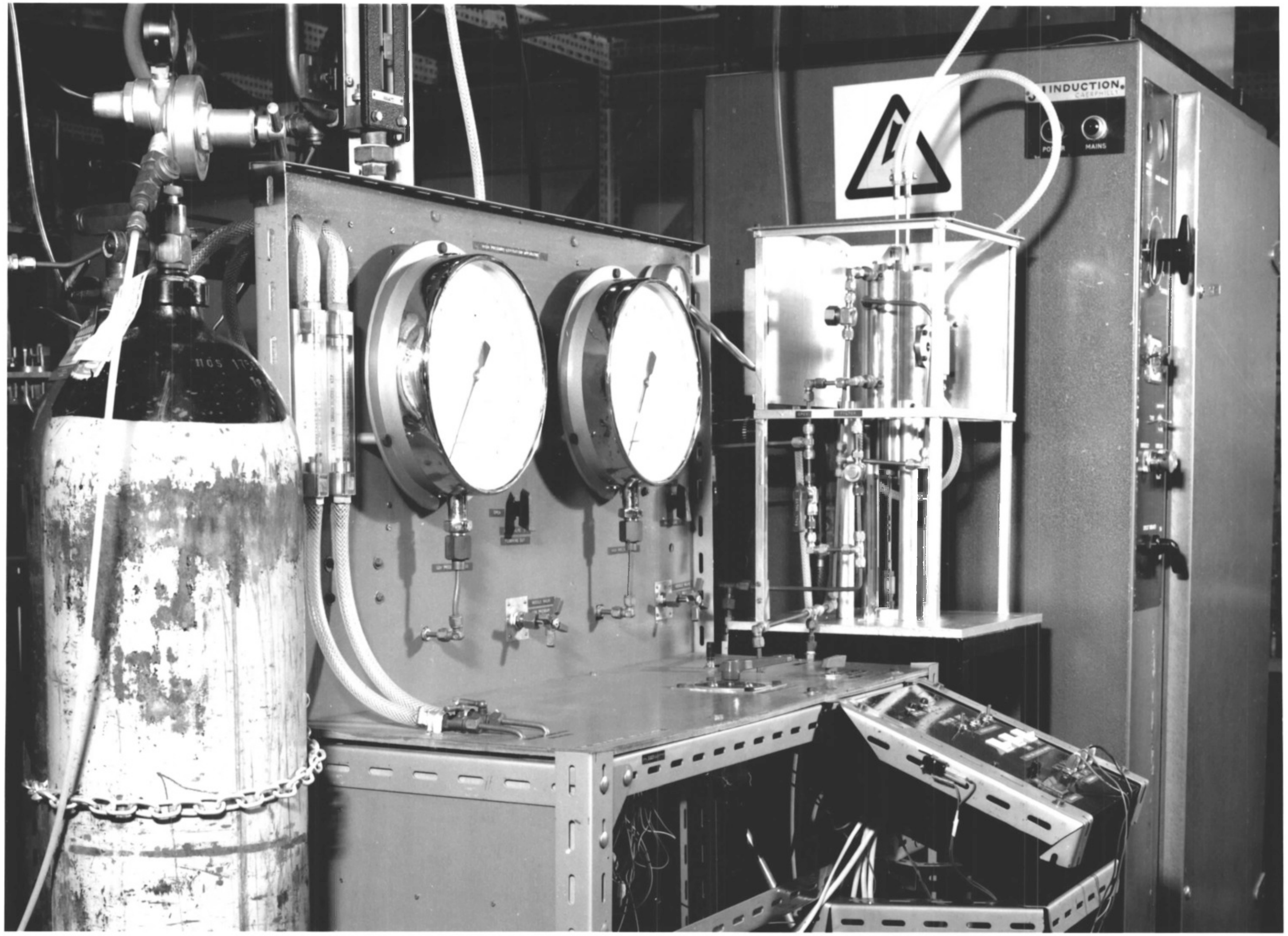

PLATE No. 2.1 - HIGH PRESSURE LEVITATION APPARATUS

2.6.1 The pressure chamber

The pressure chamber consisted of a stainless steel cylindrical vessel of 76.4mm I.D., 114.8mm O.D. and 190mm height. A cross section of the front view of the pressure chamber is shown in Figure A1.1 of Appendix 1. The design of this pressure vessel had a safety factor of 14.

The pressure chamber had a bolted lid which had a flange for locating a glass window to allow specimen observation from the top through a 45° glass prism and another flange for the upper end of the silica tube, both flanges were sealed by 'O' rings. A cross section and the top view of the lid are shown in Figure A1.2.

A glass window was placed in the middle of the pressure chamber inside a flange sealed with an 'O' ring. This window allowed lateral observation of the levitated specimen.

An orifice in one side of the vessel allowed the connection of the levitation coil with the high frequency generator. The leads of the coil passed through a block of recrystallized alumina placed inside a bolted flange. The position of this orifice is shown on the right hand side of the Figure A1.1. The flange was originally made of stainless steel and it was found to be the hottest place of the pressure vessel. Therefore it was replaced by a brass flange, which has a higher electrical conductivity, cooled by circulating water. The brass flange is shown in Figure A1.3.

The turn-table was inside a flange bolted to the lower part of the pressure chamber. It had four positions to contain a 45° small glass prism to allow observation of the levitated specimen from the bottom, a silica cup with the specimen, a silica cup with another element or compound and a copper quenching mould. It was rotated by a lever fixed to a shaft on its axis. A thrust ball-bearing located

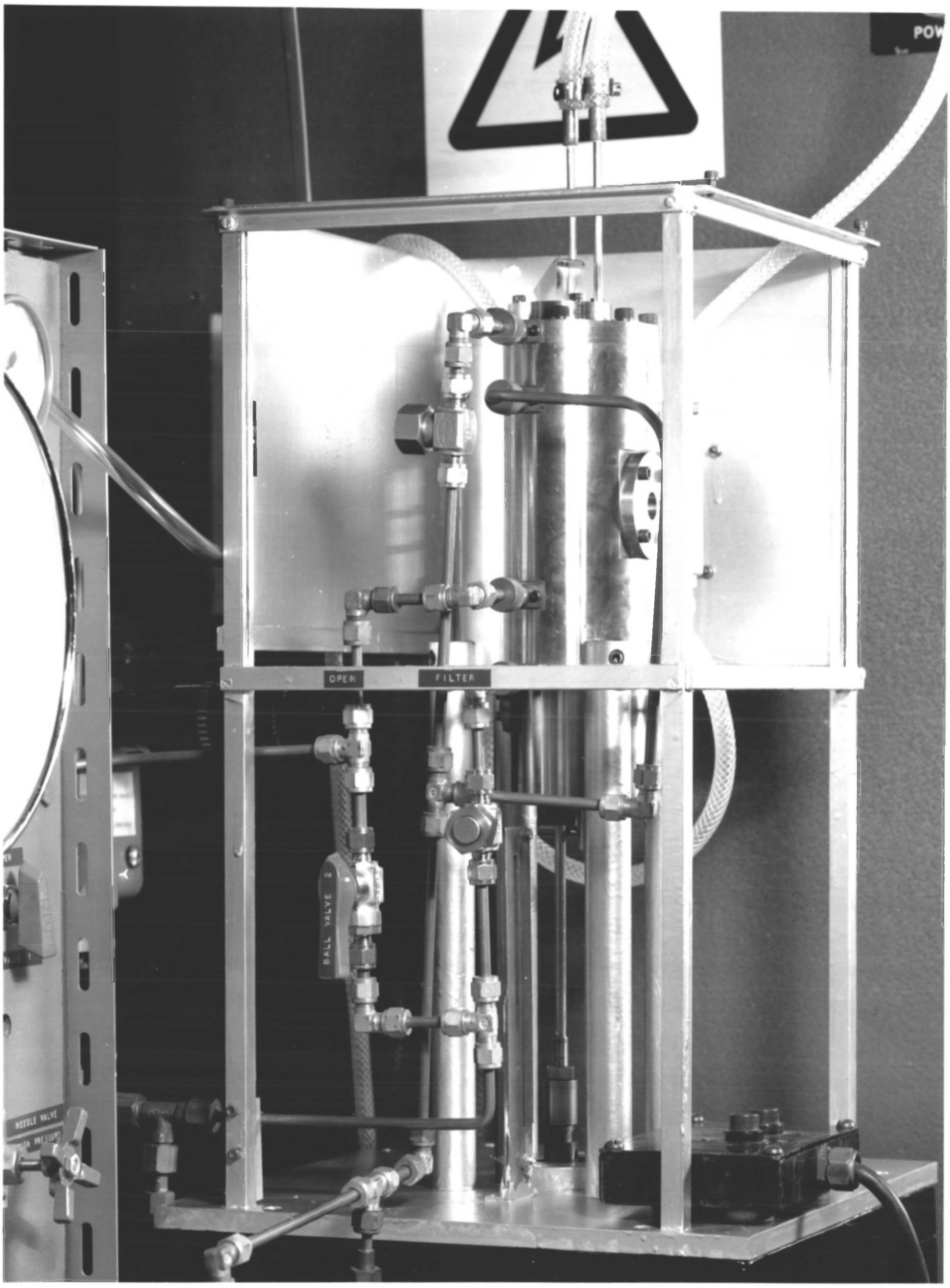

PLATE No. 2.2

PRESSURE CHAMBER

under the turn-table allowed smooth rotation under pressure.

A push rod made of brass allowed the silica cups or the copper mould to be raised up to the levitation position. The push rod had a 'Perspex' tip to minimize the heating of its end. It was operated by a pneumatic cylinder, MARTONAIR S/920/5, connected to a five port valve, MARTONAIR M 1702U/6123.

2.6.2 The cooling system

The cooling system was designed to prevent induction heating of the pressure chamber. A schematic drawing of the cooling system is given in Figure A1.4 whereas Figure A1.5 shows a drawing of the corresponding A-A, B-B and top views.

The cooling system consisted of a cylindrical sheet of copper, 72mm O.D. and 138.2mm height, with $^1/4$ inch copper tubing brazed to its inner surface which could withstand 100 atmospheres with a safety factor of 3. The cylinder was split vertically to prevent a continuous circumferential path for the circulation of induced currents. The holes in its wall allowed observation through the lateral window of the pressure chamber and space for the coil leads.

The copper tubing ends in 4.5mm O.D. brass tubings which had brass fittings for hose connections so water could be circulated inside it. The flow rate of water was controlled by a valve and a rotameter.

The cooling system was placed within the pressure chamber and the ends of the copper tubing passed through the lid. The system is shown schematically in Figure 2.3.

2.6.3 The gas train

The gas train of the HPLA was designed for a working pressure of 2000 psi. Half hard copper tubing of $^1/4$ inch O.D. and $^1/4$ inch Gyrolok fittings were used.

The gas train together with the cooling system of the HPLA is shown in Figure 2.3. A description of the whole system is given in the following paragraph.

Description of the gas train and cooling system:

1 Reactant and inert gas cylinders.
2 Check valve, Hoke 6133 G4S.
3 Precision high pressure controller, Hoke 5563 F4A.
4 Solenoid valve, Hoke Tomco A and B normally closed.
5 High pressure gauge, 0-100 bar, Standard Test Gauge-Budenberg.
6 Low pressure gauge, 0-40 bar, Standard Test Gauge-Budenberg.
7 Differential pressure switch, Delta 1/223/SS/25.
8 Bar Stock Needle Valve, Hoke 2215 G4Y.
9 Bar Stock Needle Valve, Hoke 2215 G4Y.
10 Ball valve, Hoke 7155 G4Y.
11 Pressure gauge, small 'Contex' Budenberg, 0-10 bar.
12 Helium cylinder.
13 Pressure transducer, Transducer (CEL Ltd). Range: 2000 psi, Type: 0/S/3000.
14 Pressure transducer, Bell and Howell, Range: 0-100 bar, Type: 4-366-0001.
15 Ball valve, Hoke 7115 G4Y.
16 Ball valve, Hoke 7115 G4Y.
17 Solenoid valve, Hoke Tomco A and B, normally closed.
18 Filter, Hoke 632 G4Y.
19 Filter, Hoke 632 G4Y.
20 Pressure chamber.
21 Silica tube, 15.7mm O.D., 188mm length.
22 Ball valve, Hoke 7115 G4Y.

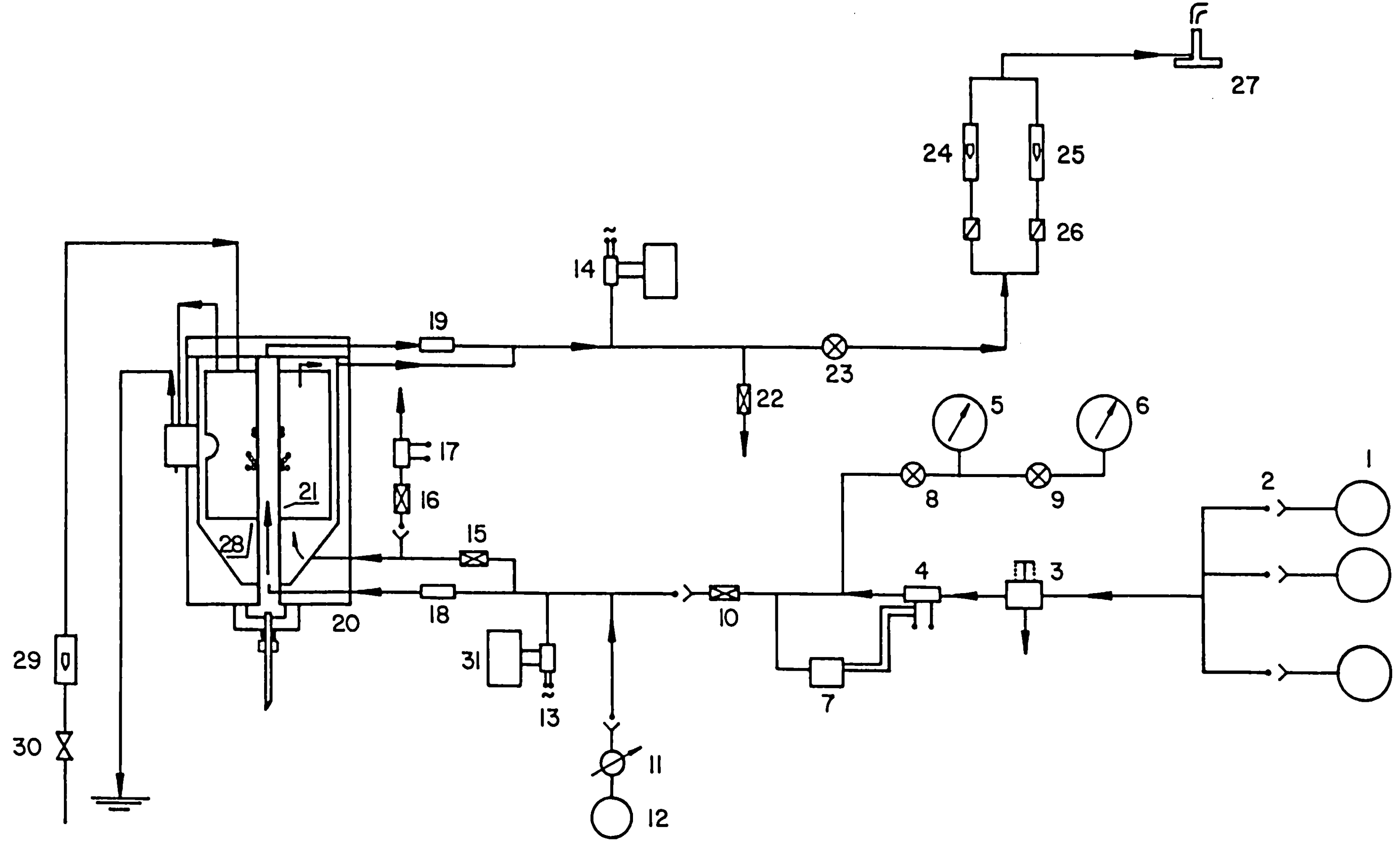

FIGURE 2.3. Gas train and cooling system of the HPLA.

23 Needle valve, Hoke Milli-mite forged needle valve 1315 G415.

24 He Rotameter, GAPMETER B6, Range: 0.5-9 lt/min NTP.

25 CO Rotameter, GAPMETER A6, Range: 2-25 lt/min NTP.

26 On-off valves.

27 Gas burner.

28 Cylindrical copper sheet.

29 Water rotameter, Rotameter Manufacturing Co Ltd, R779366.

30 Water valve, Hatersley B.S. 154/B, $^1/4$ inch.

31 Recorder.

2.6.4 Preliminary tests

1 Heating and cooling of the pressure chamber

The increase in temperature of the central part of the pressure chamber and of the original stainless steel flange containing the alumina block while the power of the HF generator was on is shown in Figure 2.4. The decrease in temperature as a function of time after switching off the power is also given in this figure. In this test (Run P-2) the cooling system was used. The levitation coil had the design (1) made of copper tubing and the anode current during operation was 1.8A.

The heating and cooling of the stainless steel flange when the HPLA was operating without the cooling system is shown in Figure 2.5. The conditions were the same as above (Run P-6). This test showed that the HPLA cannot operate without the cooling system.

In Runs P-7 and P-8 the cooling system and the brass flange containing the alumina block were used. The levitation coil had the design (1) of silver tubing and the anode current was 1.6A. After 30 min of operation the temperature of the brass flange reached

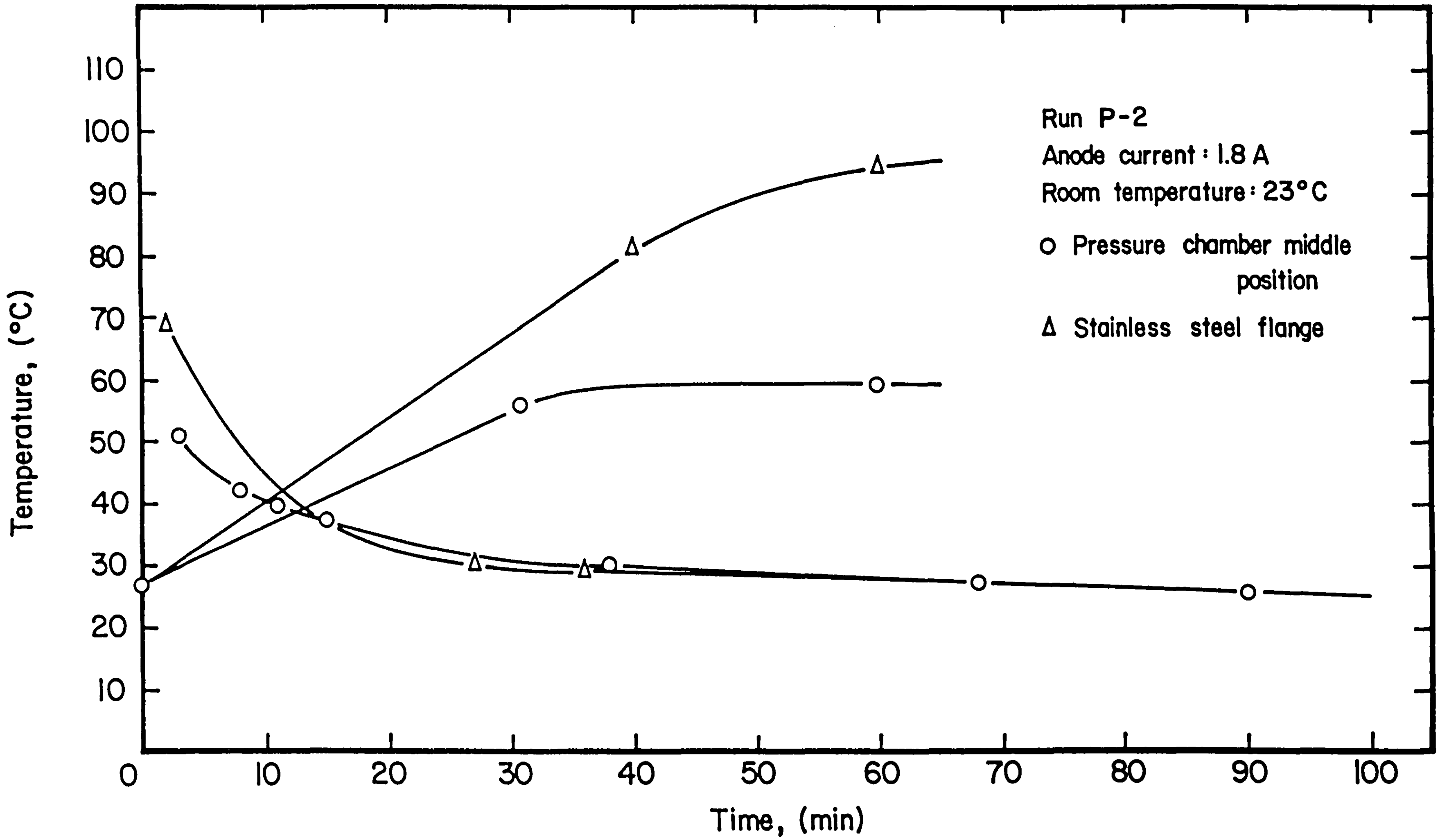

FIGURE 2.4. Heating and cooling of the pressure chamber.

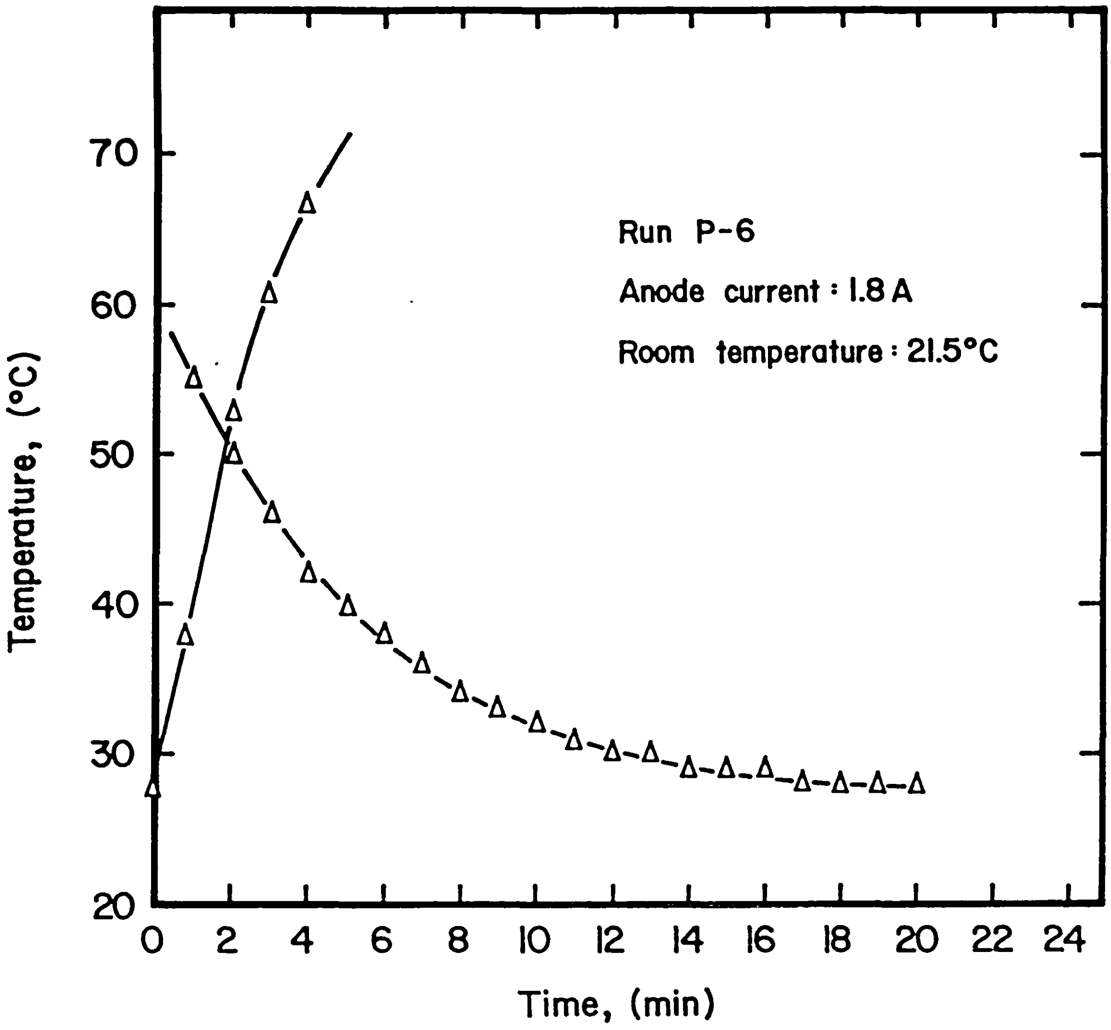

FIGURE 2.5. Heating and cooling of the stainless steel flange. HPLA without the cooling system.

a steady value of 30°C. The room temperature was 23°C.

In Run P-10 the modified system operated for 120 min at 1.7A anode current without appreciable heating of the pressure vessel and brass flange. The steady temperature of the flange was about 30°C.

2 Heating of the water of the cooling system

The water leaving the cooling system attained a steady temperature after 20 min (Run P-7). At an initial temperature of 16.5°C and a flow rate of 365.9 cc/min the final temperature of the water was 21.2°C.

3 Heating of the cooling water of the levitation coil

The flow rate of the cooling water was 1923 cc/min and the initial temperature was 16.5°C. The steady temperature of the water after leaving the coil was 46.5°C and 49.8°C when silver levitation coils of design (1) and (2) respectively were used. The levitation coils operated at 1.8A anode current.

4 Levitation melting at high pressure

The operation of the HPLA was checked by levitating 1g specimens of Fe-18Cr-2C commercial alloy and spec-pure iron.

Typical curves of temperature of the droplet as a function of anode current are given in Figures 2.6 and 2.7 when silver levitation coils of design (1) and (2) respectively are used.

The dependence of the temperature of the droplet on the total pressure of the system is illustrated in Figure 2.8.

Further work in the HPLA has shown that the system can operate for indefinite periods of time with only slight heating of the pressure chamber, about 6°C above the room temperature.

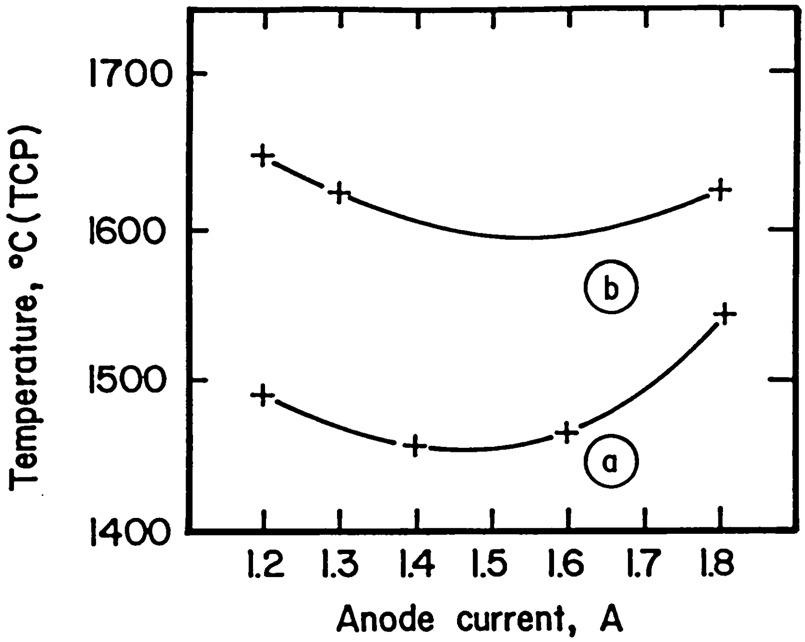

FIGURE 2.6. Droplet temperature as a function of the anode current. Levitation coil of design 1. Total pressure and flow rate: (a) 40 barg, 20 slm. (b) 20 barg, 1 slm. Gas: N_2. Material: Fe-18Cr-2C.

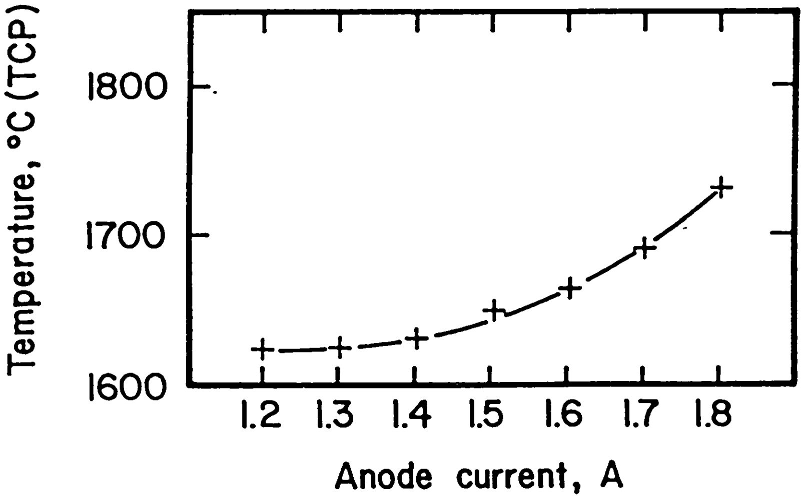

FIGURE 2.7. Droplet temperature as a function of the anode current. Levitation coil of design 2. Total pressure: 30 barg. Flow rate: 2 slm. Gas: N_2. Material: Fe-18Cr-2C.

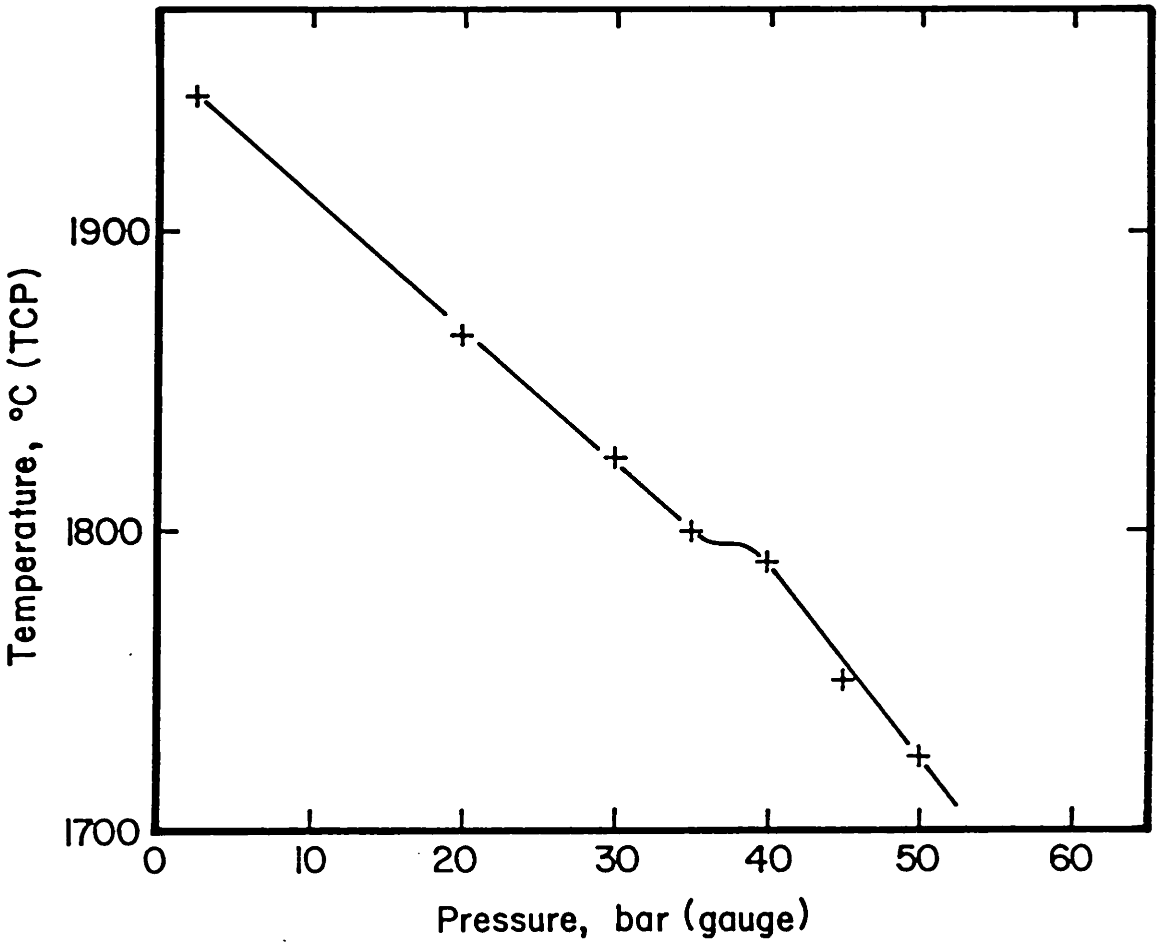

FIGURE 2.8. Droplet temperature as a function of the total pressure. Anode current: 1.6 A. Flow rate: 2 slm. Gas: Ar. Material: spec-pure iron.

The HPLA has all the facilities to be used for equilibrium, kinetics and nucleation studies.

2.6.5 Operation of the high pressure levitation apparatus

The general procedure to operate the HPLA is as follows (see Figure 2.3):

1 Set the high frequency generator output power to manual operation.

2 Adjust the pressure range in the differential pressure switch (7).

3 Activate solenoid valve (4), normally closed, and open valve (15).

4 Open valve (8) to measure the pressure with the high pressure gauge (5).

5 Flush out the air from the system by using the pressure controller (3) with appropriate inert gas at low pressure.

6 Open valve (9) to use the low pressure gauge.

7 Adjust the flow rate of the gas by using the needle valve (23) and the rotameter (24).

8 Pass water through the cooling system (29) and (30).

9 Levitate the specimen by switching on the power of the generator and raising the specimen into the coil.

10 Shut valve (9).

11 Pressurize the system by the pressure controller (3).

12 Adjust the flow rate of gas through the needle valve (23).

13 Introduce the reactant gas.

14 Shut ball valve (15).

15 Change to the proper rotameter (25).

16 Burn the combustible gases leaving the system.

17 Read the temperature through the lower window by using the two-colour pyrometer.

18 At the conclusion of the run quench the drop under pressure by raising the copper mould and switching off the power of the generator.

19 Change the reactant gas to helium.

20 Depressurize the system by bleeding the gas through the pressure controller (3) and by opening valves (16), (17) and (22).

2.7 Temperature measurement

In levitation melting the temperature of the droplet is measured by optical pyrometers. Attempts to measure the temperature by using thermocouples have not been successful.[16] The best and extensively used device is the Two-Colour Pyrometer (TCP). A 'Milletron' transistorized Thermo-O-Scope TCP was used in this work.

The temperature measurement is based in the principle of ratio pyrometry. In this method the ratio of the red radiation, in a band around 0.65 microns, and green radiation, in a band around 0.55 microns, is measured. This ratio is a function of the temperature and independent of geometry, transmitance and emittance if the body is black or grey. The system maintains a constant red photomultiplier anode current, so the anode signal from the green tube is a measurement of the relative amount of green signal compared to the red.

The TCP allows continuous temperature measurement and the output can be read directly in °C (°TCP) and printed by a recorder. A 75mm lens and a +4 close-up lens were used to provide good observation of the levitated specimen. Temperatures in two ranges can be measured, between 1100-1600°C and between 1500-2000°C. However, the high temperature range can be expanded by using an extension filter. The TCP has a very rapid time of response to changes in temperature, about 20 msec.[16]

As the TCP measures temperature by measuring colour care must be taken in checking for spectral transmission any intercepting material between the specimen and the TCP. Also, strong light coming from adjacent sources or reflected from heated objects may cause errors in the temperature measurement.

The TCP has been calibrated by the manufacturers under black body conditions. Liquid iron does not behave as a grey body, on the other hand the radiation from the specimen passes through the glass disc and the prism before reaching the measuring system so correction must be done for a possible difference in transmittance of green and red radiations. Calibration was carried out to take into account these effects. The melting point of spec-pure iron (1535°C) was measured with the TCP and the difference between the actual and measured temperatures was taken as a constant correction in the whole temperature range.

The measured melting point of spec-pure iron was 25°C higher in three different calibrations where the whole droplet surface was in the field of view. When the aperture of the lens was maximum, fully open, the reading was 50°C higher than the actual melting point due to the effect of reflected radiation coming from the walls of the silica tube. In this work the temperature was always measured by adjusting the aperture so that only the whole surface of the droplet was in the field of view.

In the free-fall experiments the temperature of the levitated specimen was measured from the top. In the experiments carried out in the HPLA the temperature was measured from the bottom through the prism located in the turn table. Measuring from the top was in general not possible due to haze when the specimen was levitated in a dense gas at high pressure.

2.8 Cine film and photographic techniques

A 'Fastax' cine camera running at about 800 pictures per second was used to observe the behaviour of the molten Fe-18Cr-2C alloy falling in an atmosphere of pure oxygen. Black and white Ilford FP4, 16mm, 100 ASA cine film was used. The lens was set at f8. Sometimes a 1kW lamp was used to illuminate the glass tube.

A 'Bolex' cine camera of 64 pictures per second nominal maximum speed was used to follow the oxidation of molten Ni-S alloy in air. The camera was used at maximum speed, which was found to be 72 pictures per second after calibration. A 75mm and a +4 close-up lens were used. The cine film used was Ilford Mark V, 16mm, black and white, 400 ASA. The lens was set at f11 and the variable shutter half closed.

A 'Leica' photographic camera was used to take still pictures during the reaction of molten iron with CO/CO_2 gas mixtures. A 90mm lens and an extension were used. The lens was set at f11 or f8 and the exposure time was $^1/1000$ sec. Black and white Ilford FP4 135, 125 ASA film was used.

2.9 Specimen preparation

Specimens were cut from the original alloy or metal by using a jig-saw or a slitting wheel depending on the hardness of the material. The mass of the specimen was adjusted at 1 ± 0.1g or 1 ± 0.01g by filing or grinding. The specimens were cleaned with tissue paper and then carefully washed with acetone before levitation melting.

The iron-carbon alloy was made in a specially built furnace heated by induction. The iron carbonyl powder and the electrographite carbon were mixed in proportion near to the eutectic composition and melted in a crucible made from an electrographite carbon block. The melt was agitated with a thin bar of spec-pure graphite while oxygen was injected. Cyclic melting and solidification allowed us to obtain a graphitic alloy which could be cut with a jig-saw.

Spec-pure iron-carbon alloy was prepared by equilibrating spec-pure iron with the CO-0.995 vol. pct. CO_2 gas mixture at 80 atm and 1550°C.

The specimens of iron-carbon alloy containing slag were prepared by introducing the slag in a drilled hole which was closed with a lid of iron-carbon alloy. The lid had a small orifice to prevent a large increase in pressure of the gas inside the hole as the specimen heated up.

The nickel-sulfur alloy specimens were obtained by melting the as-supplied powder alloy in small spec-pure graphite crucibles under an atmosphere of helium. The levitation coil of the free-fall apparatus was used with this purpose. The small crucibles containing about one gram of alloy were raised to the coil position by using a thin silica tube as push rod. Melting of the alloy occurred almost immediately and the crucible was lowered. The final specimens were almost spherical. The sulfur lost during melting of the alloy was determined to be an average of 0.38 wt % (by mass balance).

2.10 Materials used in this work

The composition of the materials used in the present work is given in Tables 2.1 and 2.2.

Table 2.1 gives the chemical analysis of solid materials as reported by the suppliers. With the exception of Fe-18Cr-2C and Ni-S alloys the materials were of high purity quality with impurities in the order of ppm.

The Fe-18Cr-2C commercial alloy was supplied by British Steel Corporation (sample 4016). The more important impurities from the point of view of oxidation are silicon and manganese as they can form more stable oxides than iron and chromium.

The Ni-S alloy was supplied by Clydach Refinery (INCO Europe Ltd, Wales). This alloy has been obtained from a Guatemalan nickel ore. The main impurities were iron and cobalt. The level of these impurities was checked obtaining 0.39 (±0.01) wt % Fe and 0.56 (±0.01) wt % Co, thus confirming the reported analysis.

The spec-pure iron was obtained from Johnson Matthey Chemicals Ltd, the iron carbonyl powder (MR Grade) from Koch-Light Ltd and the electrographite carbon block (EY9A Grade) from The Morgan Crucible Company Ltd. The total ash content of the electrographite carbon was less than 0.05 wt %.

Carbon, oxygen and sulfur analyses of the three batches of iron-carbon alloy (see section 2.9) were done by Wiggin Alloys Ltd (INCO, Hereford). The carbon contents of batches 1, 2 and 3 were 4.6, 5.7 and 4.3 wt % respectively. The oxygen contents were 50, 40 and 30 ppm respectively. The sulfur content was 60 ppm.

Silicon, chromium and aluminium were not detected in spectrographic analysis of the iron-carbon alloys; the limits of detection were 10, 5 and 10 ppm respectively. Analysis of titanium by the same technique showed a content between 5 and 10 ppm.

Gases used in this work were supplied by BOC Special Gases. Their composition is given in Table 2.2. Special gas mixtures, such as CO/CO_2 and H_2/Ar, were of Certified Standard grade, all the other gases were of high purity grade.

Table 2.1: Chemical analysis of solid materials used in this work

MATERIAL	CHEMICAL ANALYSIS, wt %										
	C	Si	Mn	P	S	Cr	Mo	Ni	Cu	Sn	Fe	Co
Fe-18Cr-2C	1.98	0.25	0.56	0.035	0.030	18.7	0.17	0.12	0.070	0.010	Balance	-
Ni-S	-	-	-	-	20.75	-	-	77.8	0.12	-	0.40	0.60

MATERIAL	CHEMICAL ANALYSIS, ppm											
	C	Si	Mn,Ag	P,S	B,Pb	Ca,Mg	Ni,Mo	Cr	Fe	Al	O,N	Cu	Ti,Co,V
Spec-pure iron 1	-	3	2	-	-	Ca 1	-	1	Balance	-	O 60	-	-
Spec-pure iron 2	-	2	<1	-	-	Ca 1 Mg 2	Ni 1	1	Balance	1	O 100	2	Co 3
Spec-pure iron 3	-	2	<1	-	-	Ca 1 Mg 2	Ni 1	1	Balance	1	O 170	2	Co 3
Iron carbonyl powder	<1000	-	-	-	-	-	-	-	Balance	-	O<3000 N<1000	-	-
Electrographite carbon	Balance	<5	<5	-	B200 Pb<10	Ca10 Mg<5	Ni10 Mo<5	10	-	<5	-	<5	Ti10 V 5

Table 2.2: Chemical analysis of gases used in this work

GAS	CHEMICAL ANALYSIS			
	CO vol %	CO_2 vol %	H_2 ppm	Hydrocarbons ppm
CO - 1% CO_2	Balance	1.05	<10	<100
CO - 2% CO_2	Balance	2.05	<10	<100
CO - 4% CO_2	Balance	3.95	240	19
CO - 1% CO_2	Balance	0.995	980	105
CO - 2% CO_2	Balance	2.00	660	35

GAS	CHEMICAL ANALYSIS				
	O_2 ppm	N_2 ppm	H_2 vol. %	H_2O ppm	Ar vol. %
Ar	<4	<15	<.0001	-	Balance
H_2 - Ar	<5	-	24.4	<2	Balance

Chapter Three

INITIAL STAGES OF THE OXIDATION OF MOLTEN IRON-CHROMIUM-CARBON ALLOY WITH OXYGEN AND OXYGEN-ARGON GAS MIXTURES

3.1 Introduction

In this chapter is described the work carried out on the oxidation of a commercial Fe-18Cr-2C alloy with oxygen-bearing gas mixtures for very short times of reaction. Free-falling droplets of the alloy at an initial temperature of 1650°C reacted with the oxidizing gas for times in the range 24 to 267 msec.

Observation of the droplets for the shortest time of reaction using high-speed cinematography, chemical analysis of quenched specimens reacted for different times and analysis of the solid layer of reaction product allowed us to postulate a mechanism of reaction which may be applied to the first stages of reaction in the AOD stainless steelmaking process.

3.2 Previous works

In many investigations the oxidation of molten binary iron-carbon alloys has been taken as a 'base-line case' to compare with the behaviour of the alloy containing a third element which can form more stable oxides than iron.[16,17]

Robertson[16] studied the oxidation of iron-carbon melts with pure oxygen using the levitation melting technique. It was found that the reaction of an Fe-4C alloy with pure oxygen was affected by low concentrations of readily oxidized elements like siliconand aluminium. When a contaminated Fe-4C alloy was reacted with pure oxygen a liquid oxide film was observed to form immediately on the surface of the drop and boiling of carbon monoxide occurred after a short time of reaction. The clean Fe-4C alloy specimens reacted in pure oxygen for a relatively long time without boiling. When boiling started in the clean specimens an oxide phase was not always observed.

Robertson[16] indicated that during the reaction of a clean Fe-C melt with oxidizing gas the following behaviour may be observed:

a) The rate of diffusion of carbon to the metal-gas interface is faster than the rate of oxygen diffusion through the gas boundary layer close to the drop. In this case the reaction occurs at the metal/gas interface and there is no ebullition of CO.

b) The rate of oxygen supply to the interface is greater than the rate of carbon diffusion. In this case oxygen dissolves in the liquid metal and may react there with carbon to form carbon monoxide. Subsurface reaction produces boiling, causing the ejection of small particles and fuming.

A shift in the mechanism of reaction may occur during decarburization from high to low carbon content so a non-boiling melt may become boiling at a certain critical carbon level.

The behaviour of levitated Fe-4C-2Si drops reacting with pure oxygen was observed by Robertson[16] to be erratic when the surface of the specimen was not previously cleaned with hydrogen. The clean specimens reacted very vigorously with oxygen and an oxide layer of high emissivity was formed almost immediately covering the droplet in less than 4 msec.

There are a small number of investigations on the reactions of iron-carbon alloys with oxidizing gases using the free fall technique. Moreover these studies were broadly consistent with those using levitated drops. Robertson[16] proposed that the behaviour of the drop must be the same in both cases as the turbulence in the drop due to chemical reaction is much more important than that produced by eddy currents. Therefore the turbulence would persist in the free falling droplet while it is reacting with oxidant gas. See and Warner[11] agreed in that the nature of the reaction is the same in levitated and falling drops but recognized that the kind of stirring could be different in both cases. The absence of induction stirring was considered by Baker[19] to suggest that subsurface reaction could occur between oxygen and carbon in free falling iron-carbon drops containing high concentration of carbon. It was also considered that the gas boundary layer around the drop would be continuously disturbed during the fall. Baker and Ward[18] found that nucleation of carbon monoxide started at much higher carbon concentration than in levitation experiments and suggested that mixed transport control would start at higher carbon levels in free fall because there is not induction stirring. Any circulation within the drop was considered to be slight. The same argument was used by Roddis[10] to explain the absorption of oxygen in free falling drops at 1600°C containing less than 4 wt % carbon.

Baker and Ward[18] found that free falling iron-carbon drops containing 4.5 wt % carbon reacted with pure oxygen producing carbon monoxide due to surface reaction. Drops containing 1.86 wt % carbon boiled when they were reacted with pure oxygen. Boiling was filmed when the droplet had fallen 24cm through pure oxygen.

In the work of Roddis[10] the existence of the two modes of reaction between dissolved carbon and oxygen was proved in free falling drops depending on temperature and carbon content of the iron-carbon melt. At 1600°C and 4 wt % carbon the reaction produced CO at the drop surface. At 2.86 wt % carbon and 1600°C the mechanism of reaction was found to be subsurface CO formation.

The studies on the effect of a dissolved element in iron-carbon melts on the nature of the oxidation in free fall experiments have been mainly restricted to silicon. The behaviour of Fe-C-Si alloys during free fall through pure oxygen was studied by Baker[19] and See and Warner.[11] Drops of Fe-4C-1Si at 1600°C were covered by an oxide layer of high emissivity at very short time, about 4 msec, followed by almost immediate carbon monoxide bursting through the surface.

The mechanism of oxidation of Fe-Cr-C melts in oxygen has not been completely determined. However, the reaction has been studied because of its importance in the production of chromium steels. Most previous studies were concerned about the thermodynamics of the system and they were carried out by holding the melt in crucibles. Hilty[20] found a linear relationship between carbon and chromium contents in the melt after equilibrium was reached during injection of oxygen at the slag-metal interface. The oxide phase involved in the equilibrium was considered CrO but its composition was not determined experimentally.

Later, Dennis and Richardson[21] reviewed the previous work in their study on the equilibrium between Fe-Cr-C melts and CO/CO_2 mixtures. They showed that the oxidation of carbon out of iron-chromium melts is controlled by the following equilibrium:

$$Cr_2O_3(s) + \underline{C} = 2\underline{Cr} + 3CO(g) \qquad (3.1)$$

The oxide phase was identified as Cr_2O_3 and it was suggested that this was the stable phase in the work of Hilty.[20] They determined the relationship between carbon and chromium contents in liquid iron in equilibrium with Cr_2O_3 at different temperatures.

The equilibrium given by equation 3.1 was studied by Nakamura[22] over a wider temperature range, 1600 to 1900°C, by equilibrating the melt with carbon monoxide. The melt, containing 10-20 wt % chromium, was held in a crucible lined with Cr_2O_3. Chromium was found to increase the solubility of carbon and oxygen, the interaction coefficients e_O^{Cr} and e_C^{Cr} were -0.047 and -0.023 respectively at 1600°C.

The introduction of the AOD process in the late 'sixties to produce stainless steel renewed the interest in the study of the decarburization of Fe-Cr-C melts. In this process extremely low carbon content is achieved while the loss of chromium is negligible. Decarburization from 1.5-2.0 wt % carbon to 0.01-0.05 wt % is achieved by injecting O_2/Ar mixtures through submerged tuyeres.[23,24]

In the summary of Choulet et al[25] of the argon-oxygen process for refining stainless steels the most stable oxide phase in the reaction controlling the process was considered to be Cr_3O_4. The reaction would be as follows:

$$Cr_3O_4(s) + 4\underline{C} = 4CO(g) + 3\underline{Cr} \qquad (3.2)$$

However, the possibility of the oxide being $FeO.Cr_2O_3$ instead of Cr_3O_4 was also recognized. Kuwano et al[26] postulated Cr_3O_4 as the oxide phase during their study on decarburization of Fe-Cr-C melts by oxygen top blowing under reduced pressures. They observed a liquid oxide film and CO nucleation near the oxide, the formation of the oxide occurred despite the high carbon content in the bath. At carbon contents lower than 0.1 wt % the liquid oxide film changed into solid slag which covered the surface completely. The oxide phases were not analyzed in this work.

In the work of Fruehan[27] O_2/Ar mixtures were injected into a shallow melt of Fe-Cr-C, containing about 18% Cr and 0.5 wt % C, with the objective of determining the sequence and mechanisms for the oxidation of carbon and chromium. It was observed that chromium was oxidized much faster than carbon and under conditions for which it should not under equilibrium conditions. The ratio k_{Cr}/k_C was found to be independent of the gas composition and about 28. From these results it was suggested that in the AOD process the main reactions at the tuyere zone would be the oxidation of chromium and iron with some oxidation of carbon:

$$2\underline{Cr} + \frac{3}{2} O_2(g) = Cr_2O_3(s) \qquad (3.3)$$

$$Fe(l) + \tfrac{1}{2}O_2(g) = FeO(l) \qquad (3.4)$$

$$\underline{C} + \tfrac{1}{2}O_2(g) = CO(g) \qquad (3.5)$$

The liquid iron oxide should be quickly reduced by chromium in the melt and as the argon bubbles containing oxides rise in the bath Cr_2O_3 should be reduced by carbon according to equation 3.1. This mechanism of reaction is now accepted even though the oxide phases involved have not been identified.

As the rate of refining in the AOD converter would be controlled by the reaction 3.1 the reduction kinetics of dense chromic oxide by carbon dissolved in iron has been studied by several investigators.[28,29,30]

Studies on the behaviour of Fe-Cr-C melts reacting in pure oxygen or oxygen-bearing gases by using the levitation melting and the free fall techniques have only been carried out in this laboratory by Rao[12] and Harris.[13]

In the work of Rao[12] on the study of the reaction of levitated drops of a commercial Fe-18Cr-2C alloy with oxygen-bearing gases two modes of behaviour were found depending on the oxygen content in the gas mixture. In the first mode surface reaction occurred between carbon and oxygen, a halo due to burning of CO in the gas boundary layer was observed. In the other mode of reaction oxides were formed almost immediately on the surface and there was little CO burning. This latter behaviour occurred with oxygen-argon mixtures containing more than about 67% of oxygen. Short times of reaction were achieved by injecting a pulse of reaction gas into the levitation chamber. During the reaction of Fe-18Cr-2C drops at 1700°C in pure oxygen a liquid oxide phase covered the surface of the drop after 10 msec, a solid oxide phase was observed after 25 msec and boiling occurred after 225 msec of reaction. The compositions of the oxide phases observed were not determined.

The oxidation of free falling Fe-18Cr-2C drops with oxygen for 170 msec produced very thin films of reaction product. When Fe-2C alloy was reacted in the same way either with pure oxygen or oxygen-argon mixtures no film was observed in the quenched specimen.[12] Harris[13] found that in the oxidation of Fe-18Cr-0.1C alloy falling freely in pure oxygen for 231 msec the oxides Cr_2O_3 and Fe_3O_4 were formed.

The work of Rao[12] demonstrated that oxide formation occurred at very short times so that the levitation melting technique was not appropriate because the change of gas concentration in the levitation chamber was relatively slow. The free fall technique was found to provide the sharp change in gas concentration required but further work was necessary to look at the mechanism of reaction and to identify the products of reaction.

3.3 Experimental

3.3.1 General procedure

The free-fall apparatus described in section 2.5 was used in this work.

One gram of the commercial Fe-18Cr-2C alloy was levitated in helium. The temperature of the droplet was kept at 1650°C (TCP) by fixing the anode current at 1.4A and the flow rate of inert gas at 2.27 slm. The reaction column was flushed out for 10 min with oxygen at a flow rate of 0.34 slm. The same flow rate of oxygen was used during the reaction. The four tubes available were used to obtain different times of reaction, between 24 msec and 267 msec. The speed of the spinning quencher was adjusted to 2400 rpm and the inclination with respect to the horizontal was in general 75 degrees. In runs 1-10 to 1-15 argon was injected inside the copper tube to obtain an inert atmosphere during quenching. The times of reaction of runs with pure oxygen are given in Table 3.1.

Table 3.1: Reaction times during oxidation of molten Fe-18Cr-2C alloy at 1650°C (TCP)

Run Number	OCAT 1	1 - i (i=1,20)	3	3-1	5	5-1	6	6 - i (i=1,5)
Time of reaction, msec	24	24	120	120	197	197	267	267
Gas	Pure oxygen							

Oxidation of the molten alloy with O_2/Ar gas mixture was carried out under the same procedure as above but the time of reaction was fixed at 24 msec. The oxygen-argon ratios used in the experiments were as follows:

Run Number	OA 1	2	3	4
O_2/Ar ratio	3/1	1/1	1/3	0

3.3.2 The spinning copper quencher

The main characteristics of this apparatus were given in Section 2.5. Before doing the oxidation experiments the operation of the spinning copper quencher was studied. In this work iron specimens (98.6 wt % Fe), instead of the Fe-18Cr-2C alloy, were used. One gram specimens were levitated and melted in helium. The temperature was fixed at 1650°C (TCP) and the drop was allowed to fall freely 69cm to impinge on the inner surface of the rotating copper tube. The melt solidified on the copper and formed a thin helical ribbon.

When the quencher formed small angles with respect to the horizontal too many whiskers were produced, there were difficulties in hitting inside the copper tube and splashing out was inevitable. In the case of angles near to 90° most of the material was quenched on the bottom. The results given in Table 3.2 were obtained under conditions where no splashing occurred and good types of ribbon were produced. In this table θ (deg) is the angle of the quencher with respect to the horizontal, N (rpm) is the angular speed of the quencher, the recovery was defined as the ratio of the mass quenched to the initial mass of the specimen, and e (mm) is the thickness of the ribbon.

Table 3.2: Recovery and thickness of the ribbon during quenching of iron samples in the spinning quencher

Run No.	θ Deg	N rpm	Recovery %	e mm	$\bar{e}$ mm
1	60	3000	99	0.08-0.10	0.09
2	60	2400	99	0.14-0.15	0.15
3	75	3000	100	0.08-0.09	0.09
4	75	2400	97	0.13-0.12	0.13
5	75	2400	99	0.09-0.11	0.10

Figure 3.1 is a schematic drawing of the initial part of the ribbons produced in runs 1 and 3 showing the effect of increasing the angle of the quencher from 60° to 75°. The angular speed in both cases was 3000 rpm.

Plate 3.1 shows photographs of ribbons of iron and of commercial Fe-18Cr-2C alloy. The latter were obtained by quenching droplets oxidized in pure oxygen. The iron ribbons were produced at 3000 and 2400 rpm when the angle of the quencher was 75°. The iron-chromium-carbon ribbons were formed at 2400 rpm and 75°.

The features of the ribbon formation are shown schematically in Figures 3.2 and 3.3. The droplet impingement on the inner surface of the copper tube is shown in Figure 3.2, the liquid wetted the substrate and moved down under the effect of the centrifugal, gravitational and surface tension forces. Figure 3.3 shows the solidification of the liquid on the substrate. As the movement continued down the tube the mass of the liquid decreased. The width of the ribbon (W) increased and so the liquid film became thinner. At a certain time the liquid front was split in many small droplets which solidified on the substrate forming whiskers. Presumably the interface between the thin liquid film and the substrate becomes unstable. This phenomenon must depend on a number of variables. In practice the production of whiskers was more pronounced at lower θ and higher N.

The solidification time of liquid iron at 1650°C on a copper substrate to obtain a ribbon of 0.1mm thickness was estimated as 4 msec. The calculation is shown in Appendix 2. The corresponding rate of cooling was of the order of 10^5 K/s. Cooling rates of this order are within the range of rapid solidification processes.[31]

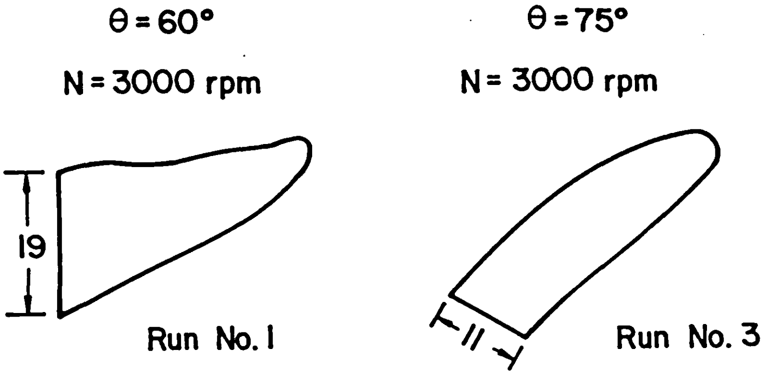

FIGURE 3.1. Initial part of the ribbon at different inclination angles of the spinning quencher.

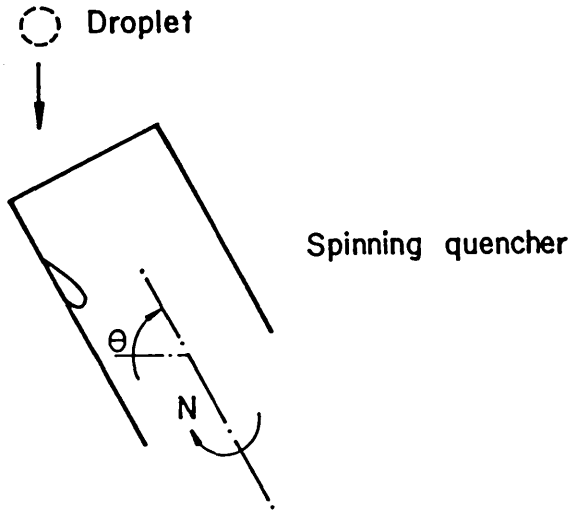

FIGURE 3.2. Droplet impingement and wetting.

PLATE No. 3.1

RIBBONS OBTAINED IN THE SPINNING COPPER QUENCHER

IRON. Run No. 3
θ = 75°, N = 2400 rpm

IRON. Run No. 4
θ = 75°, N = 3000 rpm

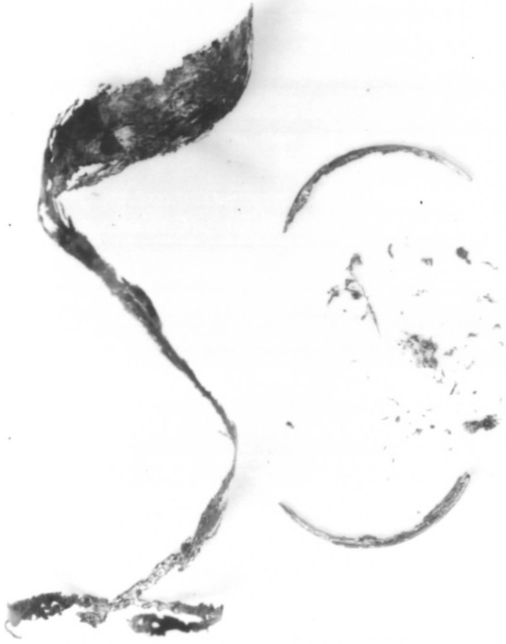

Fe-18Cr-2C. Run OCAT 1-1
θ = 75°, N = 2400 rpm

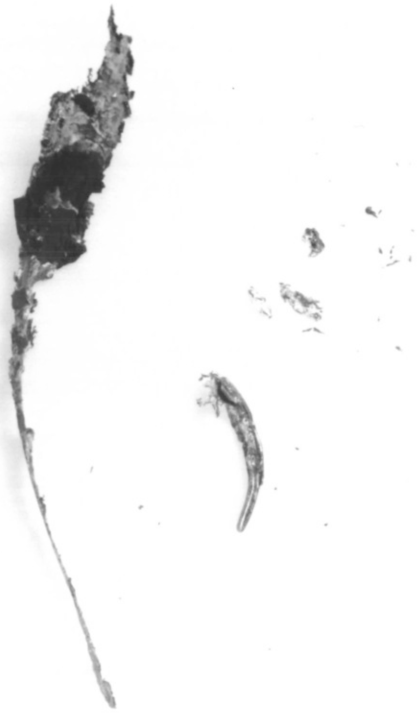

Fe-18Cr-2C. Run OCAT 3
θ = 75°, N = 2400 rpm

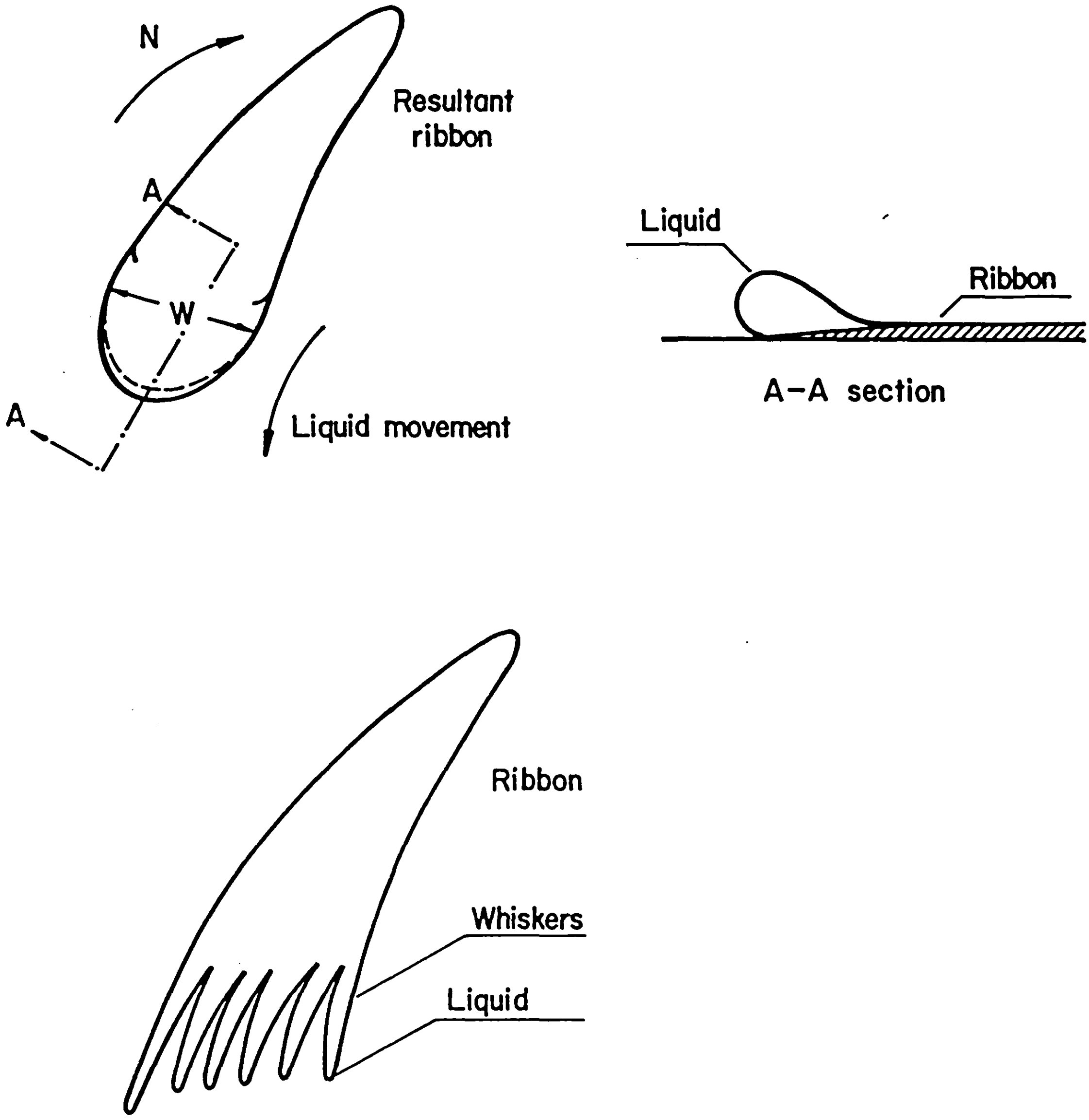

FIGURE 3.3. Liquid movement on the copper substrate.

3.3.3 Analysis of the specimens

Chemical analyses of oxygen by the vacuum fusion method were carried out at Wiggins Alloy Ltd (Hereford). Analyses of the layer of reaction product were carried out by EPMA, X-ray diffraction and LIMA (laser induced ion mass analysis). The latter analyses were carried out at AWRE (Aldermaston).

LIMA is a relatively new analytical technique[32] that employs a laser and a time-of-flight mass spectrometer. A short pulse of laser radiation is focussed to a micron-sized spot on the sample contained within an ultra-high vacuum chamber. This intense pulse evaporates and ionizes a small volume of sample. These ions are mass analyzed producing a complete mass spectrum from a single laser pulse in less than 100 μs. Sampling areas of a few microns diameter and a sampling depth around a micron are possible on metals, insulators and semiconductors. Depth profiles ranging from less than a micron to tens of microns can be obtained. LIMA can detect the presence of elements in high concentration or trace elements. The maximum sensitivity is 1 ppm or better on most elements. This range of sensitivity is achieved by varying the laser power.

Attempts at extracting the oxides formed during reaction were carried out by dissolving the metal in a bromine-methanol solution.[33] These experiments were not very successful.

3.4 Results

The high speed cine film allowed us to observe the droplet after passing the upper membrane of the 6cm reaction column. The average time taken by the droplet to travel this length was 24 msec. This compared favourably with the 22 msec obtained from Rao's results (section 2.5). The film also showed that the lower membrane burned at the time of contact with the drop. The membrane was then completely burned in oxygen from the column. The droplet took 3 msec in hitting the inner surface of the spinning quencher. Plate 3.2 shows the droplet in different positions within the 6cm length reaction column during oxidation with pure oxygen in run OCAT 1-18.

During the reaction for 24 msec a flame front was not observed nor particle ejection from within the liquid. No noticeable change in the brightness of the drop was observed. Analysis of the cine film by using a microdensitometer did not show a difference in brightness at the top and bottom positions of the reaction column.

The reaction did not seem to be vigorous at times longer than 24 msec as there was no indication of particle ejection on the wall of the glass tube even after 267 msec of reaction. This behaviour is different to the one found by Rao[12] who observed boiling of levitated Fe-18Cr-2C drop after 225 msec of reaction in pure oxygen.

With the purpose of comparison with the present results the sequence of events observed by Rao[12] in levitated drops of Fe-18Cr-2C alloy reacting with pure oxygen are shown in Plate 3.3. A brief explanation of the different stages of the reaction is given in the opposite page to this plate.

In the present work a layer of reaction product was obtained at every time of reaction in pure oxygen and oxygen-argon mixtures. The layer was observed after quenching on the surface of the ribbon (Plate 3.1). When pure argon was flowing into the reaction column no layer of reaction product was obtained (run OA4). The appearance of the layer was the same regardless of the time of reaction and it did not change when argon was injected into the quencher.

DESCRIPTION OF PLATE NO. 3.2

PICTURE NO.	TIME (msec)	
1	0.0	The droplet enters into the reaction column
2	5.0	
3	7.5	Reaction in pure oxygen
4	18.8	
5	27.5	The droplet leaves the reaction column
6	28.8	
7	31.3	The droplet enters into the copper quencher
8	32.3	
9	35.0	The lower membrane burning in oxygen

PLATE No. 3.2

OXIDATION OF COMMERCIAL Fe-18Cr-2C ALLOY
IN PURE OXYGEN DURING FREE-FALL. RUN OCAT 1-18

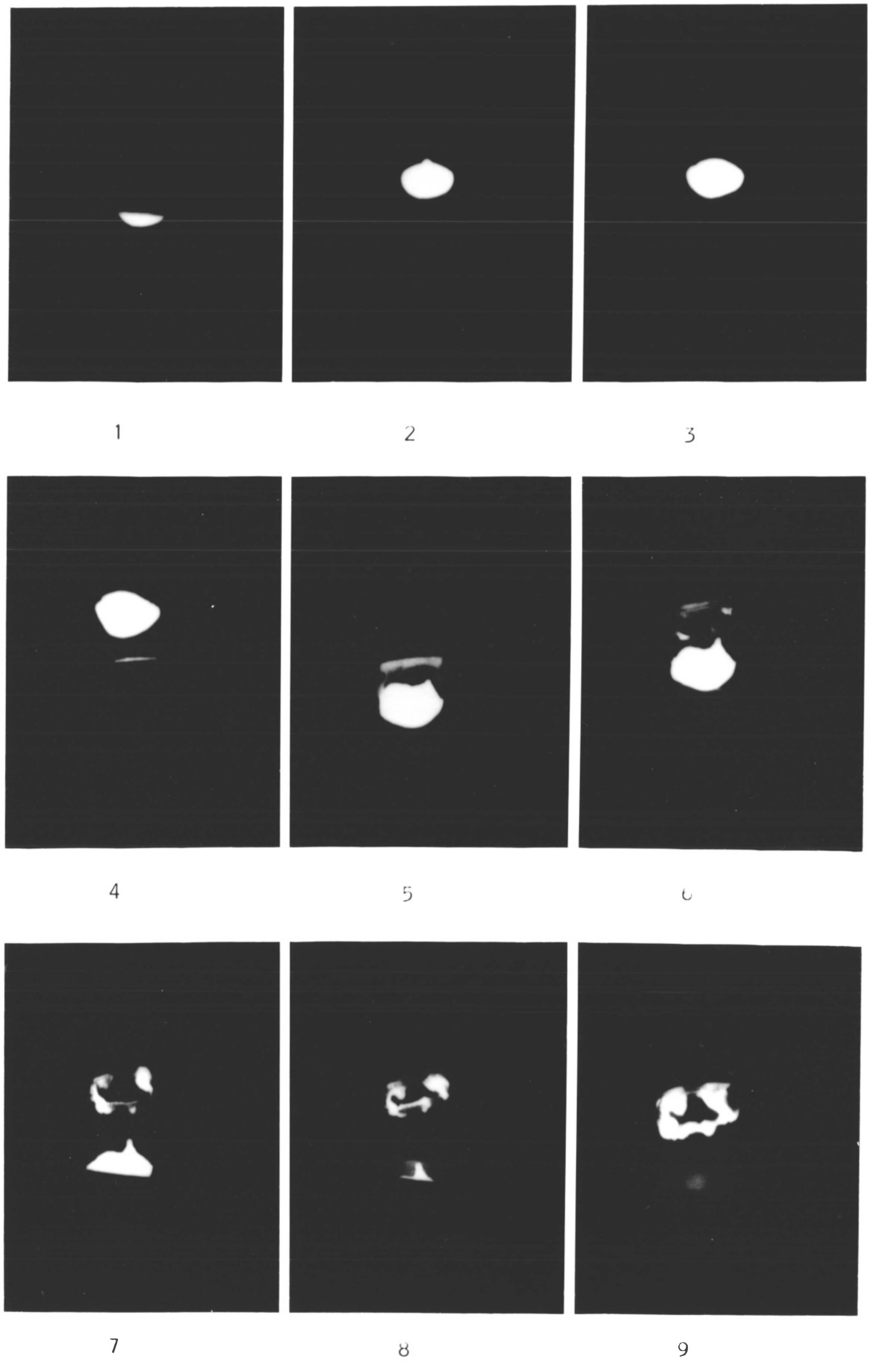

1 2 3

4 5 6

7 8 9

PLATE NO. 3.3

HIGH SPEED CINE FILM PRINTS OF THE INITIAL STAGES OF OXIDE FORMATION

Alloy used = Fe-18% Cr-2%C
Reaction gas = oxygen
Temperature = 1700°C
Approximate speed of filming = 1650 pps

<u>Note</u>: In plate 4 the sequence of frames is from left to right, except in the No 1 set, where it is from right to left. Taking No 1 set as zero time the times for the others are calculated and presented below in msec.

PICTURE NO.	TIME msec	
1	0	The first signs of oxide formation can be observed.
2	26	The appearance of small dark islands on the oxide film. Two such islands can be observed while coalescing.
3	33.3	The islands grow in size and angular shapes appear.
4	176.7	Very large dark angular islands on the levitated drop.
5	224.5	First signs of boil due to the reaction of carbon with oxide giving CO.
6	604.3	Very violent boil can be observed.
7	650	In the gas phase the ejected particles reacting with oxygen while on the levitated drop oxide is being reduced by carbon.

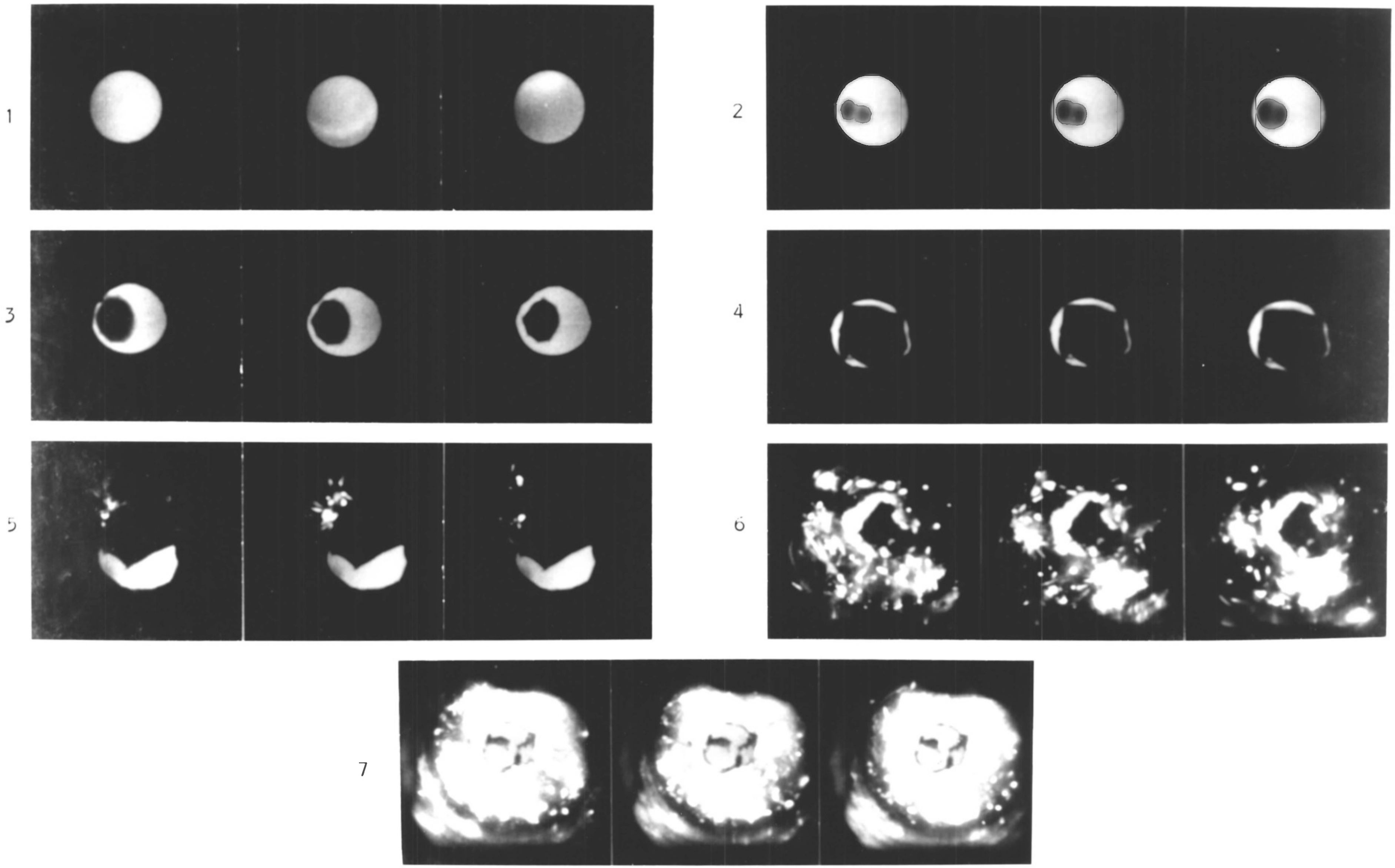

PLATE No. 3.3 - INITIAL STAGES OF THE OXIDATION OF A LEVITATED Fe-18Cr-2C ALLOY DROPLET IN PURE OXYGEN (After Rao[12])

3.4.1 Analysis of the ribbons

The average thickness of the ribbons was 0.17mm. Some ribbons were cut into small pieces to carry out oxygen analyses which were performed by the vacuum fusion technique (see section 4.2.4). Table 3.3 shows the results of oxygen analysis of the original alloy and samples of the ribbons obtained in runs OCAT 1-10 and 5-1 at 24 msec and 197 msec of reaction in pure oxygen respectively. In Figure 3.4 are shown the average oxygen concentrations as a function of time of reaction.

Table 3.3: Oxygen concentration of Fe-18Cr-2C alloy at different times of reaction with pure oxygen at 1650°C (TCP)

Run number	Sample number	Time msec	Oxygen wt %
Original alloy		0	
	1		0.012
	2		0.011
OCAT 1-10		24	
	1		0.057
	2		0.091
	3		0.070
	4		0.045
	5		0.058
	6		0.054
	7		0.041
	8		0.061
OCAT 5-1		197	
	1		0.236
	2		0.189
	3		0.193
	4		0.234

3.4.2 Analysis of the layer of reaction product

The layer of reaction product was strongly adhered to the inner surface of the ribbon. It formed black patches on the surface

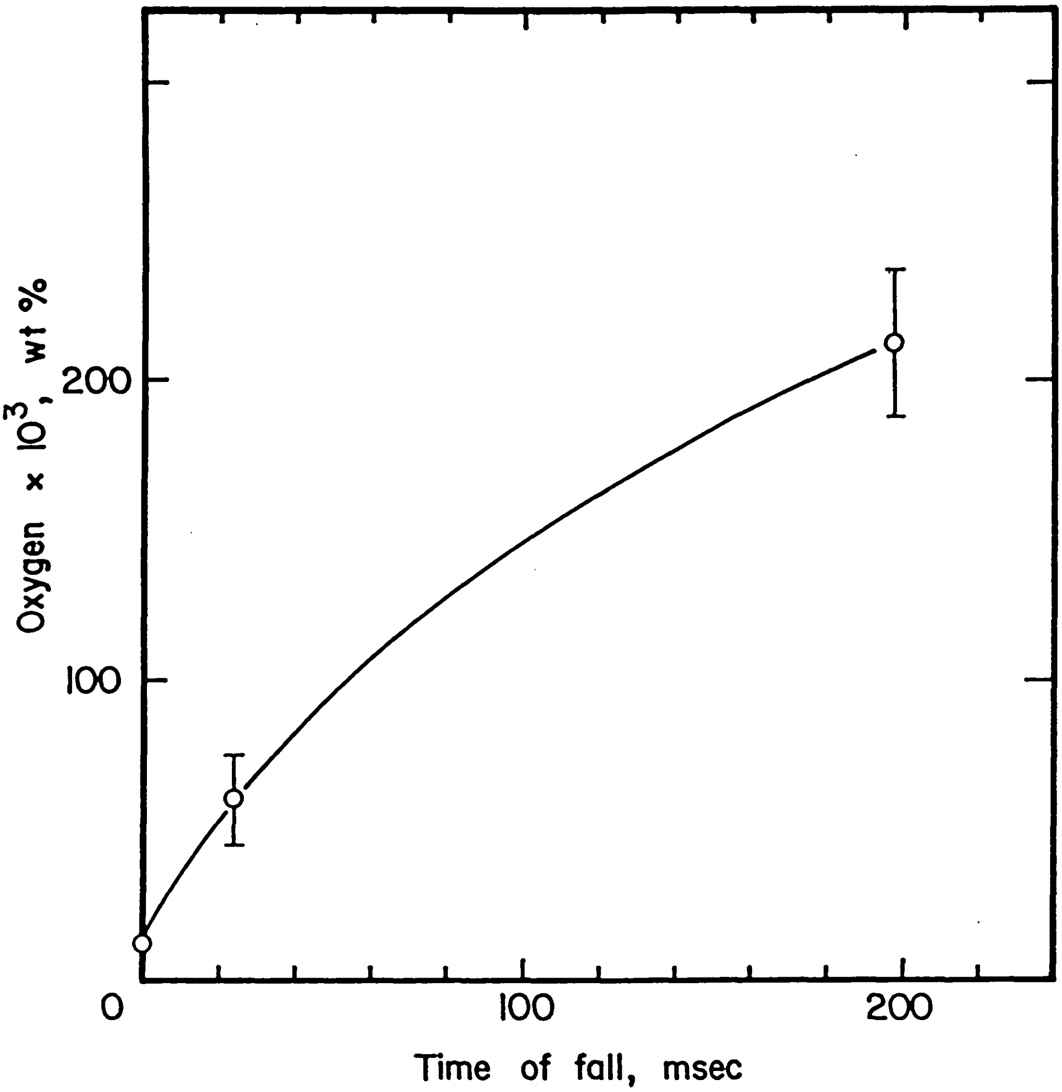

FIGURE 3.4. Oxygen concentration of oxidized drops as a function of time of fall in pure oxygen. Starting material: commercial Fe-18Cr-2C alloy. Initial temperature: 1650 °C (TCP).

(Plate 3.1). The thickness of the layer varied from a few microns to a maximum of about 40 μm.

Several methods of analysis of the layer of reaction product were tried including chemical extraction, X-ray diffraction analysis, electron probe micro analysis (EPMA) and laser induced ion mass analysis (LIMA)

The non-metallic constituents of the ribbon were chemically extracted by dissolving the metal in a bromine-methanol solution. Pieces of ribbons obtained from specimens oxidized for 24 msec and 267 msec were dissolved in different batches. The residues obtained were non-magnetic mixtures of black powder and lenses with metallic lustre. The microscopic analysis of the resides showed black particles with dendritic structure and about 1 to 2% of red-orange particles of irregular shape.

The residues were analyzed by X-ray diffraction. The measured patterns of the residues obtained in both extractions were the same. The pattern is given in Appendix 3. These analyses showed that the residue was $(Fe,Cr)_7C_3$ which was formed in the bulk of metal and it was not a product of the reaction as it will be shown later in this section and in section 3.5.

Samples of the ribbons containing the layer of reaction product were mounted edgeways in resin, ground and polished. EPMA of a sample obtained in run OCAT 1-1 (24 msec of reaction) showed iron in the outer zone of the layer and then chromium before reaching the bulk of metal. EPMA of a sample obtained in run OCAT 5 (197 msec of reaction) evidenced a thin layer containing only chromium. The results of these analyses are given in Figures 3.5 and 3.6 respectively.

The metallographic preparation of the specimens as described above proved to be very difficult as generally most of the thin

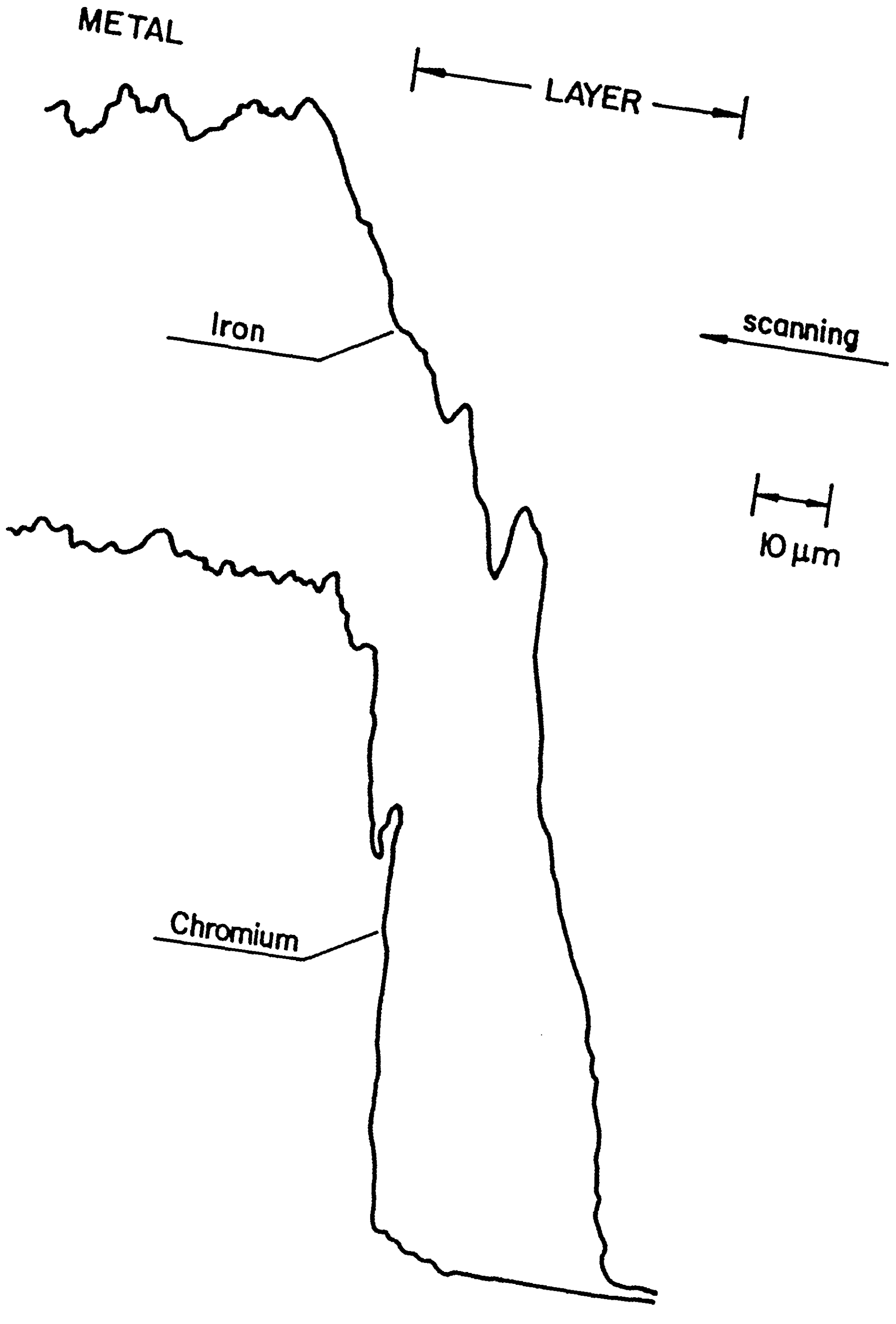

FIGURE 3.5. Electron probe micro analysis. Sample OCAT 1-1.

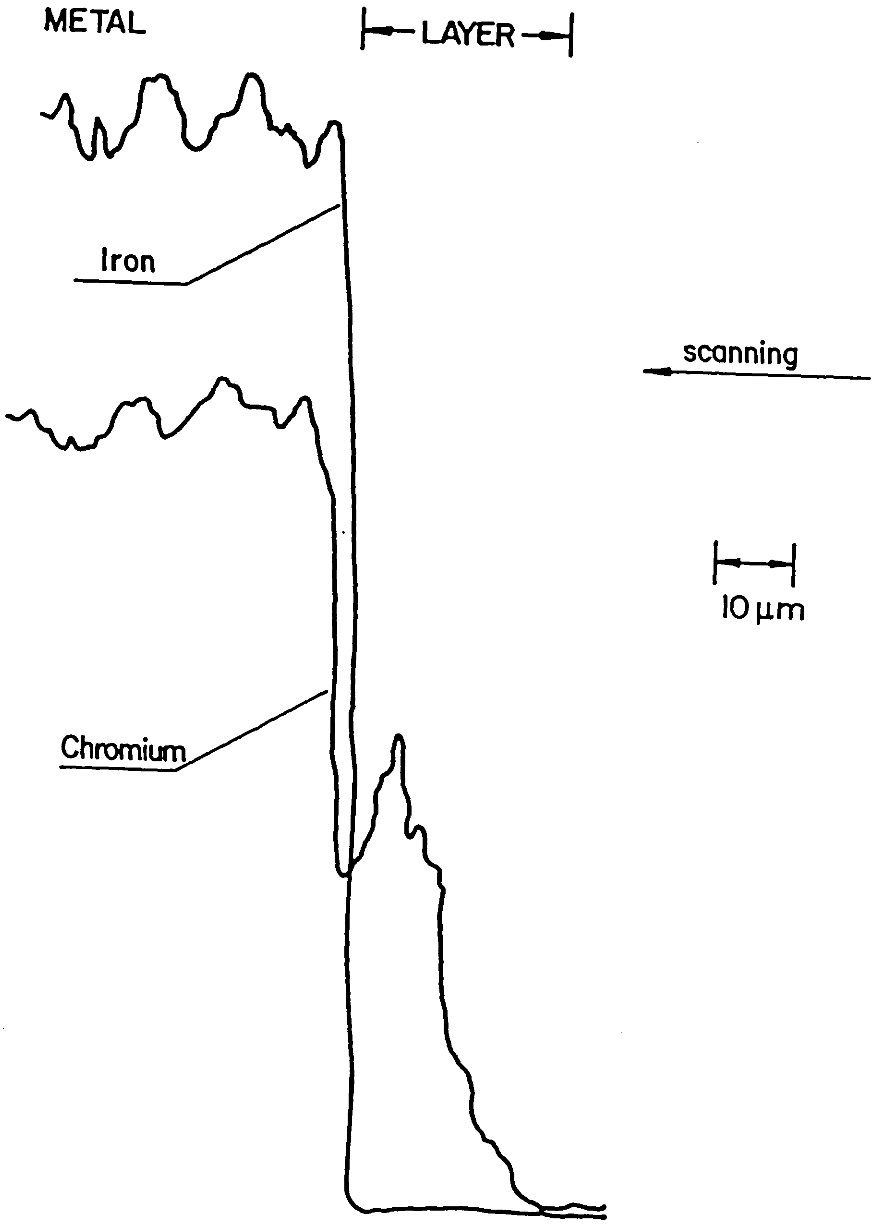

FIGURE 3.6. Electron probe micro analysis. Sample OCAT 5.

layer was ground off. A sample of a ribbon obtained in run OCAT 1-2 (24 msec of reaction) was silver painted and then electroplated with nickel by using a Watts solution. The sample was then mounted edgeways in resin and prepared in the usual way to obtain a polished surface. The sample was carbon-coated before EPMA. Scanning across two areas showed, in both cases, an outer layer containing iron and an inner layer with iron and chromium before reaching the metal. The concentration profiles obtained in one of these analyses are shown in Figure 3.7.

The layers of reaction product obtained in runs OCAT 1 and OCAT 6 were scraped from the ribbons. It was possible to obtain a small amount of material by this method. The flakes were analyzed by X-ray diffraction which indicated the possibility of their being Fe_3O_4. The measured pattern by X-ray diffraction is given in Appendix 3. The same particles were analysed by EPMA which showed the presence of chromium and iron. The particles were heterogeneous and lumpy so no quantitative analysis was possible. EPMA and X-ray analyses indicated that the flakes were an iron-chromium oxide of composition $(Cr,Fe)_3O_4$.

The layer of reaction product formed in run OCAT 1-14 (24 msec of reaction) was analysed by LIMA (see section 3.3.3). This technique did not require a special preparation of the sample. The analysis was carried out on a small area of the surface layer and by directing repeated pulses of laser energy on to this area it was possible to obtain analyses at different depths. The mass spectra obtained are shown in Figure 3.8. These spectra were obtained at low laser power. The first spectrum was produced by the first laser pulse so it gives the composition of the zone very close to the surface of the outer part of the layer. The analysis showed that the concentration of chromium is higher than iron and both are the

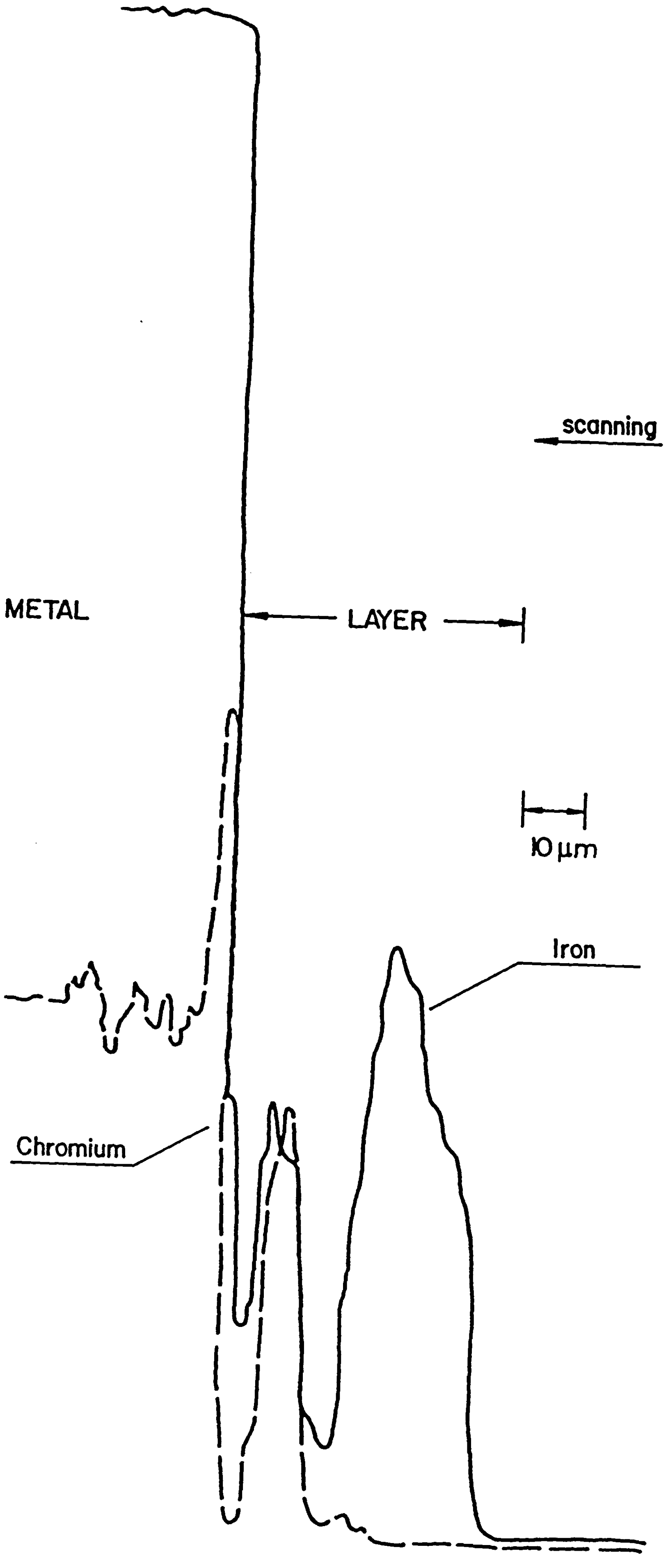

FIGURE 3.7. Electron probe micro analysis. Sample OCAT 1-2.

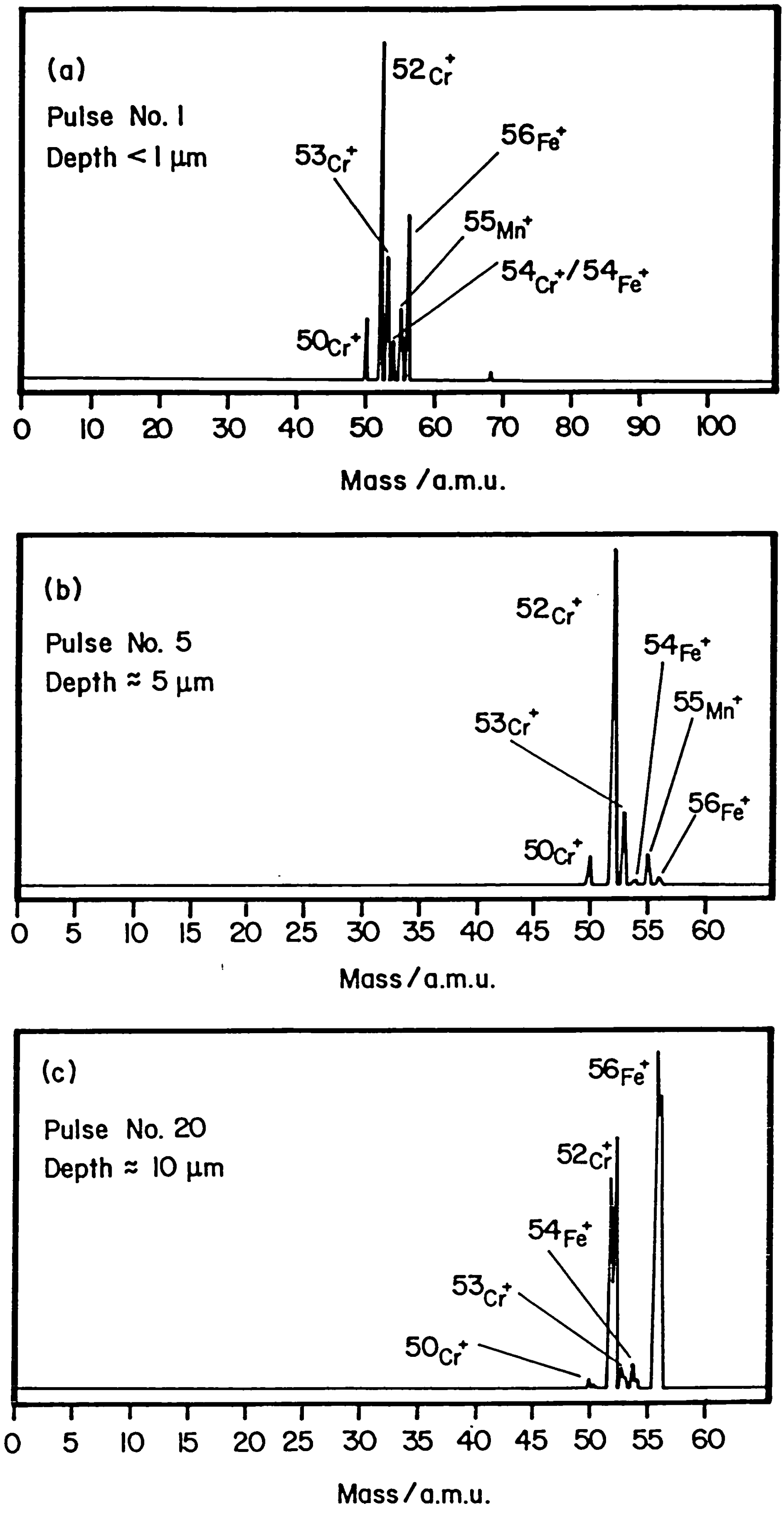

FIGURE 3.8. Oxide layer positive ion mass spectra by LIMA (low laser power). Run OCAT 1-14.

main constituents of the layer. The analysis also demonstrated that there is no carbon in the layer of reaction product. The spectrum showed that manganese, whose concentration in the alloy is 0.56 wt %, was also oxidized and segregated mainly to the outer part of the layer. The second spectrum was obtained after 10 pulses at a depth of about 5 μm. At this level chromium concentration is higher relative to iron concentration. The third spectrum was obtained after 20 pulses at a depth of about 10 μm. These results further supported the finding that the layer of reaction product is an iron-chromium oxide.

3.5 Evaluation of results

When the drop entered into the reaction column and was suddenly brought into contact with the atmosphere of pure oxygen the following modes of reaction could occur:

a) Immediate formation of an oxide phase with no carbon monoxide evolution.

b) Surface reaction between carbon and molecular oxygen to form carbon monoxide.

The occurrence of one or the other mode of reaction will depend on the relative rates of mass transport of reactants in the gas and liquid phases.

If the rate of transport of oxygen molecules to the liquid/gas interface is very fast a high oxygen concentration at the surface can be reached to allow the formation of an oxide phase. If the rate of transport of oxygen molecules to the surface is slow the oxidation of carbon will take place before an oxide layer is formed. In this case oxygen absorption will occur only when the rate of carbon transport to the surface becomes slower than the rate of oxygen arrival.

The experimental evidence obtained in this work indicated that the reaction proceeded according to the first mechanism mentioned above as a flame front was not observed and a layer of oxides was obtained at very short times of reaction.

The rapid increase of the oxygen concentration of the specimens shown in Figure 3.4 indicated the formation of an oxide phase. The oxygen concentration corresponded to the oxygen in the oxide phase and in the bulk of metal. Little or no oxygen absorption would have occurred if carbon oxidation at the surface had taken place.

The results of LIMA of the layer of reaction product together with the oxygen analyses of the ribbons demonstrated conclusively that an oxide of iron and chromium was formed during the first stages of reaction of molten Fe-18Cr-2C alloy with oxygen. The analyses of particles of the oxide layer by EPMA and X-ray diffraction indicated that the oxide is a distorted spinel of the type $(Fe,Cr)_3O_4$. This compound may be considered as Cr_3O_4 in which some of the chromium has been substituted by iron. The cations Cr^{3+} and Fe^{3+} have similar atomic radii, 0.69 and 0.64 Å respectively.

An explanation of the possible mechanism of reaction of the formation of oxides is given in the following paragraphs.

Oxygen molecules were rapidly transferred to the surface of the melt. Once oxygen was chemically adsorbed it will react with other elements at the interface. One would expect that Fe-O bonds would be formed first, because of the high concentration of iron relative to the other elements in the melt, to produce a liquid film of metastable 'FeO'. The formation of the liquid iron oxide could not occur if equilibrium conditions prevailed in the system because in this case oxidation of elements that form more stable oxides than iron would take place. The formation of a liquid oxide which wets the metal will be favoured as regards nucleation compared with a solid oxide, say Cr_3O_4, Cr_2O_3 or $FeO.Cr_2O_3$.

The immediate formation of a liquid oxide film on impure iron-carbon melts containing more than 4 wt % carbon during oxidation with pure oxygen[16,18] was mentioned in section 3.2. Baker and Ward[18] explained the formation of the liquid oxide assuming that the surface of the falling droplet became saturated with oxygen when it was put in contact with the gas stream. Robertson[16] proposed the formation of a liquid silicate, $FeO.SiO_2$, by a similar mechanism. The results of Rao[12] showed the formation of a liquid oxide film, assumed to be magnetite, at the start of the reaction of molten Fe-18Cr-2C with pure oxygen (section 3.4). Therefore, there is experimental evidence for the formation of liquid oxide films during the first stages of the reaction of high carbon iron-carbon melts with pure oxygen. The composition of this film may depend on the impurities or alloying elements present in the melt. However, the formation of metastable liquid FeO at the start of the oxidation rather than more complex molecules is reasonable.

If liquid FeO is formed it will cover the surface according to the following relationship that gives the condition for spreading:

$$\sigma_{Fe/g} > \sigma_{FeO/g} + \sigma_{Fe/FeO} \qquad (3.6)$$

where $\sigma_{Fe/g}$, $\sigma_{FeO/g}$ and $\sigma_{Fe/FeO}$ are the surface tensions of liquid iron, liquid iron oxide and between liquid iron and liquid iron oxide respectively. The values of these surface tensions at steel-making temperature are approximately 2000, 585 and 500 dynes/cm respectively.[37,9, 38]

The liquid oxide film may be further oxidized by reaction with oxygen at the gas-liquid oxide interface to form liquid magnetite. At the liquid oxide-liquid metal interface reduction of FeO would start to form more stable oxides. Due to the high concentration of chromium compared with the impurities in the melt (mainly Si and Mn) and with dissolved carbon, a chromium oxide nucleated first. It appears that solid Cr_3O_4 formed at this interface. This oxide has the lower oxygen potential at equilibrium compared with Cr_2O_3(s) and FeO.Cr_2O_3(s).[39]

Therefore, the main reactions considered by the author to occur at the start of the reaction of a drop of the Fe-18Cr-2C alloy with pure oxygen are as follows:

$$Fe(l) + \tfrac{1}{2}O_2(g) = FeO(l) \qquad (3.7)$$

$$4FeO(l) + 3\underline{Cr} = Cr_3O_4(s) + 4Fe(l) \qquad (3.8)$$

$$3FeO(l) + \tfrac{1}{2}O_2(g) = Fe_3O_4(l) \qquad (3.9)$$

The standard free energy changes of these reactions calculated from the thermodynamic data compiled by Turkdogan[40] are given in Table 3.4.

Table 3.4: Standard free energy changes of proposed reactions of oxidation of molten Fe-18Cr-2C alloy

REACTION	ΔG° cal/mole	RANGE °C
$Fe(l) + \tfrac{1}{2}O_2(g) = FeO(l)$	-61200 + 12.83T	1371 - 2000
$4FeO(l) + 3\underline{Cr} = Cr_3O_4(s) + 4Fe(l)$	-79100 + 11.93T	1650 - 1665
$3FeO(l) + \tfrac{1}{2}O_2(g) = Fe_3O_4(l)$	-56730 + 22.77T	1596 - 2000

In the AOD process the oxygen in the bubbles would be rapidly consumed in the tuyere zone so that the gas phase would consist mainly of argon. If a liquid film of FeO was formed it will not be oxidized at the gas-liquid interface to form liquid magnetite as in the case of a levitated or falling drop. The liquid oxide film would be very rapidly reduced by chromium. The chromium oxide would react with dissolved carbon as the bubble rises, in the same way as indicated by Fruehan[27] except that the oxide would probably be Cr_3O_4:

$$Cr_3O_4(s) + 4\underline{C} = 4CO(g) + 3\underline{Cr} \qquad (3.10)$$

The standard free energy change of this reaction relative to the weight-percent standard state is given by the equation:

$$\Delta G^\circ_{3-10} = 206740 - 138.45T \text{ (cal/mole)} \qquad (3.11)$$

3.6 Discussion

The reaction between the free-falling droplet and oxygen was observed only for 24 msec by high speed cinematography. After this time Rao[12] observed that a liquid oxide phase covered the levitated droplet and the appearance of small dark islands of oxide (Plate 3.3). These events were not observed on the cine film but the presence of an oxide layer on the metal showed that oxide formation occurred after this time of reaction. The process was not filmed at longer times of reaction. This prevented a definitive comparison between the behaviours of the free-falling and levitated drops.

In the proposed mechanism for the initial stages of the reaction the formation of metastable liquid 'FeO' was explained from a kinetic point of view considering the high concentration of iron atoms on the surface of the droplet. The liquid oxide could also wet the melt and a film covered the whole surface. As the nucleation of a gas phase within a homogeneous liquid requires high supersaturation[41] subsequent nucleation of another liquid or a solid phase on the metastable liquid oxide is more likely than CO bubble nucleation. A mechanism considering the nucleation of an oxide on a liquid substrate was also used by Robertson[16] to explain the formation of a liquid silicate layer on a Fe-4C-1Si alloy at 1600°C reacting with pure oxygen.

Therefore, the system under consideration was not in equilibrium. The assumption of equilibrium would lead to an order of oxidation in which the element in equilibrium with the lower value of the oxygen activity will be oxidized first. The following reactions and their standard free energy changes[40] may be considered to calculate the oxygen activity of the corresponding equilibria:

REACTION	ΔG° (cal/mole)	
$Fe(l) + \underline{O} = FeO(l)$	$-33200 + 13.52T$	(3.12)
$3\underline{Cr} + 4\underline{O} = Cr_3O_4(s)$	$-225700 + 99.61T$	(3.13)
$\underline{C} + \underline{O} = CO$	$-4740 + 9.71T$	(3.14)

The standard states were selected as pure liquid iron, pure liquid FeO, pure solid Cr_3O_4, one weight-per cent solution for dissolved elements (a ⟶ wt % at infinite dilution) and CO at one atmosphere. The interaction parameters e_{Cr}^{Cr}, e_{Cr}^{C} and e_{O}^{Cr} were taken as -0.022, -0.092 and -0.052 respectively.[41] The oxygen activities were 0.152, 0.034 and 0.0014 wt % for the equilibria given by equations 3.12, 3.13 and 3.14 respectively in a Fe-18Cr-2C melt at 1650°C. Hence, carbon should be oxidized first if the system were in equilibrium. The oxidation of chromium should only occur when the activity of oxygen increased, due to the decrease in the concentration of carbon in the melt, to the value corresponding to the equilibrium of chromium with its more stable oxide. Iron should be the last in being oxidized when the activity of oxygen reaches the value 0.152.

In high chromium iron melts, with chromium concentration in the range 9 to 25 wt %, at 1650°C and low oxygen potentials Hilty et al[39] found that Cr_3O_4 is the stable phase. The melting point of this oxide is higher than 1800°C.[39]

A different value of the standard free energy change of reaction 3.13 has been reported elsewhere[42] which gives lower values of the activity of oxygen at equilibrium. The standard free energy change (relative to the weight-per cent standard state) in this case is given by the equation:

$$\Delta G^\circ_{3-13} = -244800 + 109.6T \quad \text{(cal/mole)} \qquad (3.13a)$$

in the temperature range 1700-2000°K.

Hilty et al[39] identified a distorted spinel as a combination of Cr_3O_4 and $FeO.Cr_2O_3$ which forms at medium chromium concentration (3 to 9 wt % Cr). The diffraction pattern of this compound[39] shows that four interplanar spacings are coinciding with those found in the X-ray diffraction analysis of some particles of the oxide layer (Appendix 2). These interplanar distances (d) and relative intensities are:

d(Å)	2.52	2.10	1.62	1.48
I	100	40	50	40

LIMA of the oxide layer showed the presence of manganese segregated to the outer part of the layer indicating that despite its low concentration (0.56 wt %) manganese could be oxidized together with chromium. The oxygen concentration in equilibrium with 0.56 wt % Mn in liquid iron and pure liquid MnO is 0.136 wt % at 1650°C.[41] Normally the oxide is not pure MnO but is either a liquid or solid solution of MnO and FeO.[41] The activity of MnO is then less than unity and the equilibrium oxygen activity required to oxidize manganese is reduced.

The possibility of formation of carbides is discussed in the following paragraphs.

The Fe-Cr-C equilibrium diagram[43] shows that at 1650°C, 2 wt % C and 18 wt % Cr the stable phase is liquid containing carbon and chromium in solution. The only possibility of carbide formation is on cooling and solidification. Greaves[44] found that the solidification of high carbon steel containing high concentrations of chromium, comparable to the alloy used in the present work, produces carbides of the type $(Cr,Fe)_7C_3$ in which more than half of the chromium is substituted by iron. The carbides obtained in the residues when the metal was dissolved in bromine-methanol solution were formed in the bulk of metal during quenching. They were not part of the layer of reaction product.

Thermodynamically the formation of carbides may be predicted when an oxide of chromium is in contact with an iron melt with high carbon concentration. The formation of the carbide Cr_7C_3 through the reaction of Cr_3O_4 with dissolved carbon and the corresponding standard free energy change relative to the infinitely dilute weight-per cent solution are given by the following equations:[40]

$$7Cr_3O_4(s) + 37\underline{C}\ (\text{in iron}) = 3Cr_7C_3(s) + 28CO(g) \qquad (3.15)$$

$$\Delta G^\circ_{3-14} = 1191880 - 669.75T \quad (\text{cal/mole}) \qquad (3.16)$$

However, if Cr_7C_3 is formed in the presence of iron it should decompose after the reaction:

$$Cr_7C_3(s) = 7\underline{Cr}\ (\text{in iron}) + 3\underline{C}\ (\text{in iron}) \qquad (3.17)$$

$$\Delta G^\circ_{3-47} = 85100 - 99.8T \quad (\text{cal/mole}) \qquad (3.18)$$

which is highly spontaneous at 1650°C.

The works of Chu and Rahmel[45] and Vodop'yanov et al[46] demonstrated that chromic oxide can react with graphite in an atmosphere of CO. At relatively low temperatures, 1200-1400°C, a carbide was formed at the oxide surface in contact with graphite. The carbides were identified as Cr_3C_2 and Cr_7C_3. At temperatures higher than 1500°C Vodop'yanov et al[46] showed that the chromium carbides dissolved in chromium with the formation of a liquid metallic phase. Under this condition reduction of the chromic oxide by carbon dissolved in the liquid phase took place.

The kinetics of the reduction of dense Cr_2O_3 by dissolved carbon in iron-carbon melts have been studied by several investigators.[28,29,30]

The reduction occurred through the overall reaction:

$$Cr_2O_3(s) + 3\underline{C} = 2\underline{Cr} + 3CO(g)$$

without the formation of carbide on the surface of the chromic oxide at any stage of the reaction. In the work of Vostryakov and Lepinskikh[28] the carbon content was in the range 0.4-4.5 wt %.

The experimental evidence indicated that formation of a carbide as a stable phase from the reaction of chromium oxide with dissolved carbon at steelmaking temperature is not possible.

3.7 Conclusions

The results of the investigation described in this chapter are regarded as a contribution to the better understanding of the mechanism of reaction of Fe-Cr-C melts with oxygen-bearing gases.

The use of the free-fall technique allowed a step change in gas concentration to be obtained, thus the initial time of reaction was very well defined. Droplets of Fe-18Cr-2C alloy at 1650°C (TCP) were reacted for 24, 120, 197 and 267 msec with pure oxygen and for 24 msec with oxygen-argon gas mixtures. The reacted droplets were rapidly quenched in a spinning copper quencher in which a rate of cooling of 10^5 K/sec and a good separation between the metal and oxide phases were obtained.

When the droplets entered into the reaction column containing pure oxygen or oxygen-argon mixtures an oxide layer was formed immediately. Chemical analyses of the specimens oxidized in pure oxygen showed a steep increase in total oxygen concentration due to the formation of the oxide. Analyses of the layer of reaction product by LIMA, EPMA and X-ray diffraction demonstrated that the compound was an oxide and that the main constituents were chromium and iron.

The analyses also indicated that the oxide was a distorted spinel of the type $(Cr,Fe)_3O_4$.

A mechanism of reaction was proposed which considers the formation of a film of metastable liquid 'FeO' followed by reduction by chromium to form solid Cr_3O_4 at the liquid-liquid interface and further oxidation of the film at the liquid-gas interface to form liquid Fe_3O_4. Extension of this mechanism to the first stages of the reaction occurring at the tuyere zone in the AOD stainless steelmaking process considered the formation of solid Cr_3O_4 and subsequent reduction by carbon dissolved in the molten metal.

Further work is necessary in order to determine the effect of oxygen concentration in the gas phase on the mechanism of reaction. The few experiments done with oxygen-argon mixtures in this work did not allow any definitive conclusion to be drawn, except that a layer of oxide was obtained with oxygen to argon ratios in the range 3/1 to 1/3 as in the experiments with pure oxygen. The reaction in pure oxygen was observed by high speed cinematography for 24 msec and it is necessary to film the events during this time using different gas mixtures. This work would allow the oxygen concentration in the gas mixture at which a change in mechanism of reaction occurs to be determined.

Chapter Four

STUDY OF THE CARBON-OXYGEN REACTION IN MOLTEN IRON IN CO/CO_2 ATMOSPHERES

4.1 Introduction

This chapter describes the work carried out on the equilibria and kinetics of the reactions between molten iron and CO/CO_2 gas mixtures.

The equilibrium study was undertaken to investigate the effect of carbon on the activity coefficient of oxygen at constant oxygen activity. The study was carried out at 1550, 1650 and 1750°C at pressures up to 80 atmospheres.

The study of the kinetics of carburization and decarburization reactions at high pressure was aimed to interpret the experimental data obtained in this work. The effect of impurities, in the concentration range of parts per million, on the reaction rates was examined.

4.2 Equilibria between molten iron and CO/CO_2 gas mixtures

4.2.1 Previous work

The equilibria involving carbon and oxygen dissolved in liquid iron are of fundamental importance for the understanding of iron and steelmaking processes and have been studied by many investigators. Disagreements among their results were due to the difficulties and limitations inherent in the experimental techniques used in the past.

The earliest work[47,48] was aimed to obtain the carbon-oxygen product, wt % $\underline{C}$ x wt % $\underline{O}$ = m, under steelmaking conditions and under one atmosphere partial pressure of CO. It was assumed that the activities were directly proportional to the mole fractions. Later interest was centered on the study of the binary Fe-C and Fe-O systems in the molten state as a step to study the more complex Fe-C-O system.

Richardson and Dennis[49] provided the first work with the primary objective of determining the carbon activity in liquid iron. They covered most of the range of carbon compositions of interest in steelmaking by equilibrating molten iron with CO/CO_2 gas mixtures. Carbon contents in the melt from 0.1 to 1.1 wt % were obtained with CO/CO_2 mixtures of ratios up to 800/1 and temperatures 1560, 1660 and 1760°C. Later, Rist and Chipman[50] confirmed the results of Richardson and Dennis[49] and extended the data up to carbon contents of interest for ironmaking.

The Fe-C system has continued to be studied. The values found for the thermodynamic properties of carbon in iron melts coincide up to 1 wt % but there are discrepancies at higher carbon concentrations. Most investigations have been carried by equilibrating the melt contained in a crucible with a gas mixture at a total pressure of 1 atmosphere.

The carbon potential in the melt has been fixed by using CO/CO_2 and CH_4/H_2 gas mixtures. However the CH_4/H_2 gas mixture was found to be less convenient due to errors introduced by the reaction of methane with traces of moisture and with alumina crucibles.[51] The use of CO/CO_2 gas mixtures has been preferred because the equilibrium between β-graphite and CO/CO_2 mixtures is well known,[49] thus the activity of carbon can be defined taking β-graphite as standard state. Experimentally the use of CO/CO_2 gas mixtures at 1 atmosphere restricted the carbon concentration to low levels, those of interest in steelmaking. Higher equilibrium carbon concentrations in molten iron at steelmaking temperatures required very high CO/CO_2 ratios, greater than 10^4 for 4 wt % C at 1600°C and 1 atm,[52] which are very difficult to obtain and control. Furthermore, the CO/CO_2 ratio in gas mixtures which are very dilute in CO_2 will be greatly affected if carbon deposition occurs.

The most common sources of error in the determination of carbon activity have been crucible contamination, carbon deposition, thermal diffusion, measurement and control of temperature and flow rate of gases, and CO evolution during quenching.

The activity of dissolved oxygen in the liquid Fe-O system has been determined by studying the equilibrium between molten iron and CO/CO_2 or H_2/H_2O gas mixtures.[54,55,56] However more accurate results have been obtained by using the latter, as the carbon interference is avoided.[56] Tankins et al[56] found that Henry's Law is obeyed for dissolved oxygen in molten iron, that is the activity coefficient of oxygen in the Fe-O system is unity, in their investigation the experimental errors were minimized. The main sources of error which caused discrepancies among previous investigators were: crucible contamination, thermal diffusion and uncertainties in temperature measurement.

The liquid Fe-C-O system is more complex because of the interaction between carbon and oxygen. Dissolved carbon affects its own activity coefficient as well as that of oxygen. The study of this interaction has been carried out by fixing the activities of carbon and oxygen in molten iron with CO/CO_2 gas mixtures and by equilibrating carbon-saturated melts with carbon monoxide. The experimental errors were increased by segregation of carbon and oxygen in the solidified melt, inaccurate measurement of small concentrations of oxygen and the adsorption of oxygen or water-vapor in graphitic sample.[53,57]

In most of the previous work on the equilibria in the Fe-C-O system in the molten state it was concluded that carbon decreases the activity coefficient of oxygen but the studies of Matsumoto[57] and El-Kaddah and Robertson[15] found the opposite. The more detailed study was provided by El-Kaddah and Robertson[15] who equilibrated spec-pure iron and iron-carbon melts with CO/CO_2 gas mixtures at high pressure, up to 70 atmospheres, by using the levitation melting technique. Carbon and oxygen activities were measured in the temperature range 1550 to 1750°C over a wide range of carbon concentration. The use of the levitation melting technique avoided most of the sources of error found in previous work.

This new finding has been discussed by Matoba and Banya[58] in their extensive review of the thermodynamics of the liquid Fe-C-O system. Their criticism referred to carbon deposition, CO evolution during solidification and thermal diffusion, but it was centered in the last of these. However, El-Kaddah[14] quantified the effect of the thermal diffusion, finding only a small influence, as will be shown in section 4.2.3. Richardson[59] agreed with the results of El-Kaddah and Robertson[15] but pointed out that the work needed confirmation.

Therefore, the present work was undertaken with the objective of determining the effect of carbon on the interaction coefficient of oxygen in molten iron covering the range of high carbon content, greater than 1 wt %. The high pressure levitation melting technique was used to study the equilibria of CO/CO_2 gas mixtures with molten iron at 1550, 1650 and 1750°C.

4.2.2 Equilibria in the liquid Fe-C-O system

The equilibria of dissolved carbon and oxygen in molten iron with CO/CO_2 gas mixtures are given by the following equations:

$$CO_2 + \underline{C} = 2CO \tag{4.1}$$

$$CO + \underline{O} = CO_2 \tag{4.2}$$

$$\underline{C} + \underline{O} = CO \tag{4.3}$$

These equations represent only two independent relationships, since any one of them can be obtained by combining the other two.

Carbon activity

The carbon activity in molten iron in equilibrium with a CO/CO_2 gas mixture is defined by reaction 4.1. The equilibrium constant of the reaction is:

$$K_1 = P^2_{CO}/P_{CO_2}a_C \tag{4.4}$$

or

$$K_1 = P_T x^2_{CO}/x_{CO_2}a_C \tag{4.5}$$

where P_{CO} and P_{CO_2} are the partial pressures of CO and CO_2 respectively, P_T the total pressure, x_{CO} and x_{CO_2} the mole fractions of CO and CO_2 in the gas mixture and a_C the activity of carbon in solution in liquid iron. Equation 4.5 predicts that at a given temperature the activity of carbon is a function of the total pressure and of the gas composition.

Oxygen activity

The oxygen activity in liquid iron in equilibrium with a CO/CO_2 gas mixture is defined by equation 4.2.

The equilibrium data of reaction 4.2 can be obtained from the well known thermodynamic data of the reaction of H_2/H_2O gas mixtures with molten iron[56] and the water-gas reaction:[53]

$$H_2 + \underline{O} = H_2O \qquad (4.6)$$

$$H_2 + CO_2 = CO + H_2O \qquad (4.7)$$

The equilibrium constant of reaction 4.2 is given by:

$$K_2 = P_{CO_2}/P_{CO}a_O \qquad (4.8)$$

or

$$K_2 = x_{CO_2}/x_{CO}a_O \qquad (4.9)$$

Therefore, at constant temperature the activity of oxygen is independent of the total pressure and it is only a function of the ratio x_{CO_2}/x_{CO} defined by the composition of the gas mixture.

Carbon-oxygen reaction

The reaction between carbon and oxygen in solution in molten iron is given by equation 4.3, the equilibrium constant of this reaction is given by:

$$K_3 = P_{CO}/a_C a_O \qquad (4.10)$$

If the standard state is an infinitely dilute weight per cent solution for carbon and oxygen, equation 4.10 can be transformed to:

$$K_3 = P_{CO}/f_C(\text{wt \% C})\ f_O(\text{wt \% O}) \qquad (4.11)$$

where P_{CO} is the partial pressure of carbon monoxide, f_C and f_O are the activity coefficients of carbon and oxygen in molten iron, wt % C and wt % O are the concentrations of carbon and oxygen measured under equilibrium conditions.

The product wt % C x wt % O = m can be predicted by equation 4.11 in very dilute solutions and at a partial pressure of carbon monoxide equal to one atmosphere. The value of m has been found to be in the range 0.0020 to 0.0025 at 1600°C.[60]

4.2.3 Thermal diffusion

In a system with a temperature gradient a mass flux occurs due to the tendency of the species of a mixture to diffuse under the effect of this gradient. As a result the composition of the gas mixture is different in cold and hot regions. Levitated drops are characterized by a steep temperature gradient in the gas boundary layer so that thermal diffusion is inevitable.

The mass flux in a binary system of components 1 and 2 under the effect of concentration and thermal gradients is given by the equation:[61]

$$j_1 = -j_2 = -(C^2/\rho RT)M_1^2 M_2 D_{12} x_1 \; [(\partial(\bar{G}_1/M_1)/\partial x_1)_{T,P}(\partial x_1/\partial r)]$$

$$- D_1^T \; (\partial \ln T/\partial r) \qquad (4.12)$$

where C is the molar density of the mixture, ρ is the mass density of the mixture, M_1 and M_2 are the molecular weights of components 1 and 2, x_1 is the mole fraction of component 1, $\bar{G}_1$ is the partial molal free energy, D_{12} and D_1^T are the binary diffusion coefficient and the binary thermal diffusion coefficient respectively, and T is the absolute temperature. In a binary system, $x_1 + x_2 = 1$ and $D_{12} = D_{21}$. The thermal diffusivities of components 1 and 2 are numerically equal but of opposite sign, $D_1^T = -D_2^T$.

Equation 4.12 can be transformed by using $(d\bar{G}_1)_{T,P} = RTd\ln a_1$ and by defining a thermal diffusion ratio K_T:

$$K_T = (\rho/C^2 M_1 M_2).(D_1^T/D_{12}) \qquad (4.13)$$

to obtain:

$$j_1 = -j_2 = -(C^2/\rho)M_1M_2D_{12}[(\partial \ln a_1/\partial \ln x_1)_{T,P}(\partial x_1/\partial r) + K_T(\partial \ln T/\partial r)] \quad (4.14)$$

The mass flux due only to the temperature gradient is given by:

$$j_{1r}^{(T)} = -(C^2/\rho)M_1M_2D_{12}(K_T/T)(\partial T/\partial r) \quad (4.15)$$

The mass flux caused by the temperature gradient originates a concentration gradient. The mass flux due to the concentration gradient is given by:

$$j_{1r}^{(x)} = -(C^2/\rho)M_1M_2D_{12}(\partial x_1/\partial r) \quad (4.16)$$

When a steady state is reached there will be not net flux, therefore:

$$j_{1r}^{(T)} + j_{1r}^{(x)} = 0 \quad (4.17)$$

and

$$\partial x_1/\partial r = -K_T(\partial \ln T/\partial r) \quad (4.18)$$

When K_T is positive the component 1 moves to the cold region and vice versa. The thermal diffusion ratio is a function of temperature and composition. However the effect of composition is in general small and usually K_T is considered constant by using a mean temperature value. The integration of equation 4.18 gives:

$$\Delta x_1 = -K_{T_f} \ln(Ts/T_b) \quad (4.19)$$

where T_s and T_b are the temperatures of the melt and bulk gas.

The segregation of CO/CO_2 gas mixtures on iron droplets was measured by El-Kaddah and Robertson.[15] The technique consisted of determining the equilibrium carbon concentration between spec-pure iron and CO/CO_2 gas mixtures at constant P^2_{CO}/P_{CO_2} and different temperatures to obtain the graphite saturation temperature by extrapolation to the graphite solubility limit predicted by the Chipman equation:

$$\text{wt \% C} = 1.34 + 2.54 \times 10^{-3} t \ (°C) \tag{4.20}$$

The surface concentrations were calculated from the well known thermodynamic data of the β-graphite reaction with CO/CO_2:

$$C(\beta\text{-graphite}) + CO_2 = 2CO \tag{4.21}$$

and compared with the bulk concentration of the gas.

The thermal diffusion ratio was calculated by using equation 4.19. The values of K_T were used to define the thermal diffusion factor α which is nearly independent of concentration:

$$\alpha = K_T/x_1x_2 \tag{4.22}$$

where x_1 and x_2 are the mole fractions of CO and CO_2.

The thermal diffusion factor was found to be approximately the same under different conditions. The value obtained was 0.022 in the pressure range of 70 to 80 atm and CO/CO_2 gas mixtures with 0.076 to 2.15 vol. pct. CO_2. The accuracy of the thermal diffusion factor was ±50% due to temperature fluctuation and error of ±2°C in temperature reading from the TCP, which affected the equilibrium constant of the β-graphite reaction with CO/CO_2 gas mixtures.

There is no previous measurement of the thermal diffusion factor in CO/CO_2 gas mixtures dilute with respect to CO_2. Turkdogan[62] reported the value 0.0142 of the thermal diffusion ratio (k_T) at a mean temperature (T) of 323°K for a 1:1 CO/CO_2 gas mixture. The corresponding thermal diffusion factor is 0.057 which must be considered as a maximum because maximum separation of the components of a binary gas mixture is obtained at a mole fraction of 0.5 (equal concentrations).

The equation:

$$\Delta x_1 = -0.022x_1(1 - x_1)\ln(T_s/T_b) \qquad (4.23)$$

was used in the present work to calculate the change in concentration of CO_2 due to thermal diffusion.

The corrected x_{CO_2} at the surface of the droplet under the conditions of the present work is shown in Table 4.2. The effect of the thermal diffusion was that CO, the lighter gas, diffused towards the hot surface decreasing the concentration of CO_2. The effect was found to be small, about 4% relative, in the gas concentration and temperature ranges of the present work.

4.2.4 Experimental

The high pressure levitation apparatus (HPLA) described in section 2.5.5 was used in the present work. The levitation coil with the design 2 gave good stability of the droplet and temperatures in the range of interest, 1550 to 1750°C.

The general procedure given in section 2.6.5 was followed during the experimental runs. The compositions of spec-pure iron, iron-carbon alloys and gases used in this work were given in Tables 2.1 and 2.2 respectively.

The system was flushed out with argon at low pressure for 10 min. Specimens of 1 ± 0.1g were levitated and melted in argon which was changed immediately to a H_2/Ar mixture containing 25 vol. pct. H_2. The valve 15 (Figure 2.3) was shut, the pressure increased to 10 barg and the flow rate fixed at 3 slm. The droplet was maintained at 1750°C for 10 min. This time was considered enough to clean the surface of the specimen of any possible oxide film. The change to the CO/CO_2 gas mixture was followed by immediate pressurization and adjustment of the flow rate to 2 slm. A decrease in temperature of the droplet occurred during this operation. The temperature was then adjusted to the required level by manual operation of the H.F. generator. The flushing out of the H_2/Ar mixture occurred within 10 sec and the steady temperature of the droplet was reached in 40 to 60 sec. The specimen was reacted for a sufficient time to reach equilibrium, after which it was quenched at the operating pressure by the following procedure: the copper mould was raised and the power was switched off to quench the specimen. The CO/CO_2 gas mixture was then immediately changed to argon, the system was depressurized through valves 16 and 17 to atmospheric pressure and flushed out for 5 min before discharging the specimen. This technique avoided carbon deposition due to cracking of CO on the specimen during quenching. Carbon monoxide evolution while the specimen was solidifying was not observed at any temperature and pressure of this work. The total pressure of the CO/CO_2 gas mixtures was in the range 20 to 80 atm, however most of the work was carried out in the pressure range 40 to 70 atm.

The final specimens were weighed and kept in a dessicator before sending them for carbon and oxygen analysis to Wiggin Alloys Limited, Hereford. Some of the carbon analyses were carried out by the author (runs EFCO 3 to 27).

Carbon analysis

Carbon was determined at Wiggin Alloys Ltd by combustion analysis using a Leybold Hereaus CSA 2002 analyser. In this method the sample is burned in a stream of oxygen by HF heating. Carbon is converted to carbon dioxide and measured by infra-red absorption. The system is calibrated with iron and steel standard reference materials. Precision is about ±2% relative to homogeneous samples containing > 1 wt % carbon.

Carbon determination by the author was carried out using the standard combustion method.[63] The standard deviation of analyses of carbon steel samples (British Chemical Standards) was 0.03 wt % C and the standard error ± 2.5%.

The carbon content in carburized spec-pure iron specimens was estimated by mass balance. A comparison between estimated carbon and the values obtained by chemical analysis is shown in Figure 4.1. In general there was good agreement. The vaporization of liquid metal is reduced by the use of high pressure so that good mass balances would be expected. This fact was confirmed by measuring the vaporization rate of spec-pure iron at 1750°C in argon at 40.40 atm and 10 slm. The value found was 6.0×10^{-5} g/min.

Oxygen analysis

Oxygen was determined at Wiggin Alloys Ltd by vacuum fusion using a Balzer EAO 201 analyser. In this method the sample is melted under vacuum in a graphite crucible. Graphite is taken into solution and combines with the oxygen to form carbon monoxide which is then measured by infra-red absorption. Calibration is by direct injection of carbon monoxide gas into the system. Precision is 2 to 5% relative for homogenous samples, with a limit of detection of 0.001%.

Duplicate analyses of oxygen were carried out for specimens cut in half. The results are shown in Table 4.1. These specimens were obtained by reacting liquid spec-pure iron at 1750°C with CO-1.05 vol. pct. CO_2 at 40.48 atm. The precision was very good and within the precision of the analysis.

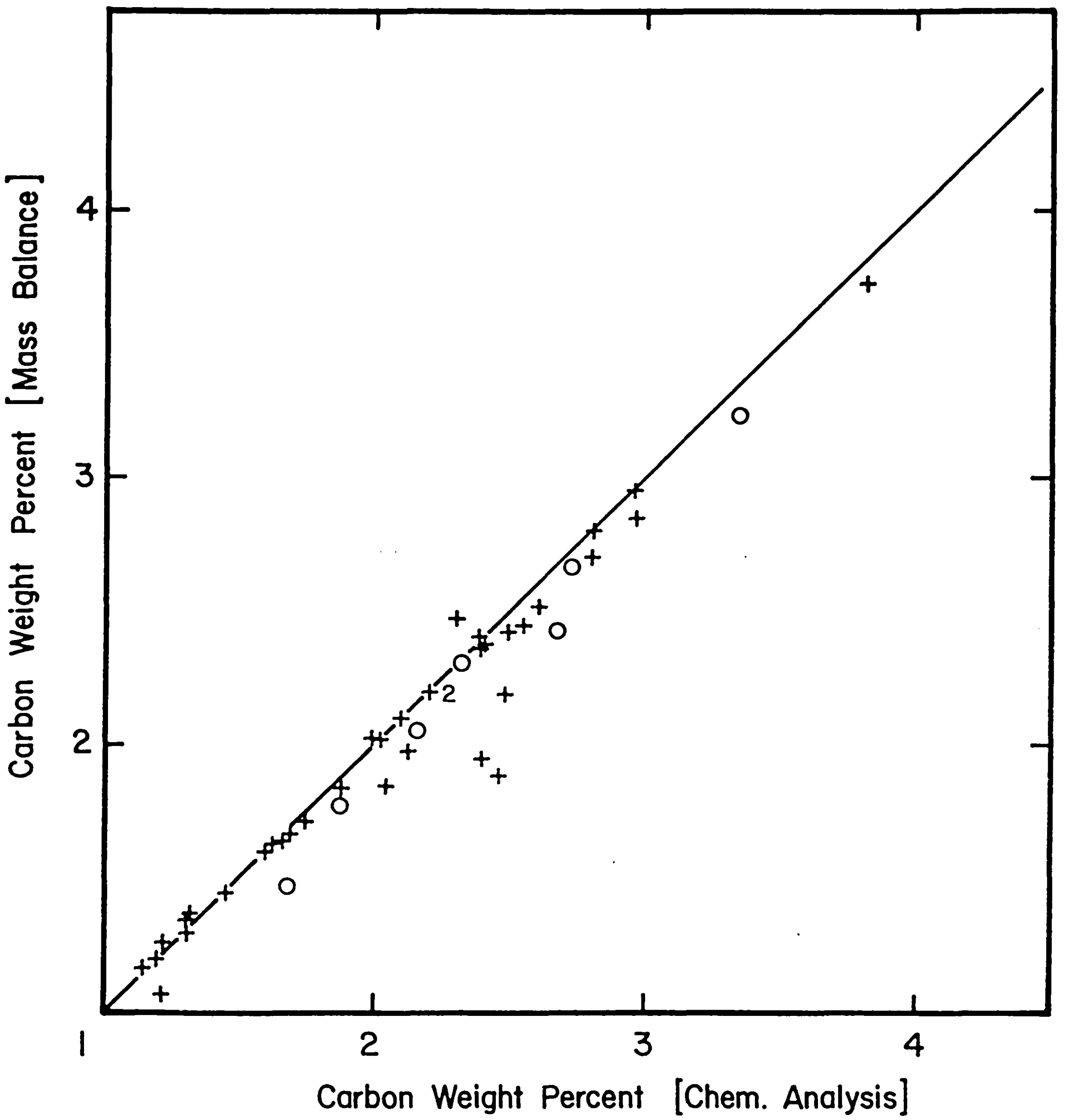

FIGURE 4.1. Comparison between carbon weight percent obtained by mass balance and by chemical analysis for carburized spec-pure iron. + Wiggin Alloys Ltd.; O Author.

During the present work most of the specimens were cut in half, one part was analyzed for oxygen and the other one for carbon. Only in the experimental runs with CO-1.05 vol. pct. CO_2 was the whole specimen used for analysis.

Table 4.1: Duplicate analyses of oxygen

Run number EFCO	Sample	Oxygen wt %
6	A	0.042
6	B	0.041
7	A	0.030
7	B	0.030
8	A	0.021
8	B	0.021
9	A	0.020
9	B	0.021
11	A	0.017
11	B	0.017

4.2.5 Results

The equilibria between carbon and oxygen in solution in liquid iron with CO/CO_2 gas mixtures were studied at temperatures of 1550, 1650 and 1750°C. The carbon and oxygen activities were determined by gas mixtures containing 0.995, 1.05, 2.00, 2.05 and 3.95 vol. pct. CO_2 in CO. The oxygen activity was kept constant at a given temperature and gas composition whereas the carbon activity was changed depending on the total pressure of the system. The pressure ranged from 20 to 80 atm covering the range of carbon concentration from 2.21 to 3.83 wt % at 1550°C.

1 Attainment of equilibrium

The approach to equilibrium was determined by chemical analysis of specimens quenched for different periods of time. Mass balances provided a very good check during carburization experiments because of the low rate of vaporization at high pressure, no CO evolution during solidification and an adequate system of quenching without splashing.

Oxygen analyses during carburization of spec-pure iron at 1750°C with 1.05 vol. pct. CO_2 gas mixture at 40.48 atm are shown in Figure 4.2. The equilibrium was reached after 20 min of reaction. Figure 4.3 shows the approach to equilibrium from both sides (carburization and decarburization) during the reaction of spec-pure iron and iron-carbon alloy with 3.95 vol. pct. CO_2 gas mixture at 65.15 atm and 1550°C. The equilibrium was reached after 25 min.

Even though the time to approach equilibrium was found to be longer than in the work of El-Kaddah and Robertson[15] still the equilibrium was approached in relatively short times compared to several hours required in similar studies carried out in crucibles.[49,50] The faster attainment of equilibrium in levitation melting is due to the small mass of melt, the large specific area of the drop and rapid mass transport processes in the liquid and gas phases.

The study of the kinetics of carburization and decarburization (section 4.3.4) indicated that the rates of reaction were slower than those observed by El-Kaddah[15] because of the effect of impurities on the surface of the drop despite high purity materials used in this work (section 2.10). The impurities were observed as bright islets formed at the start of the reaction. However analysis of the surface of the drop indicated that an apparently continuous film of oxide was present. A discussion of the behaviour of the

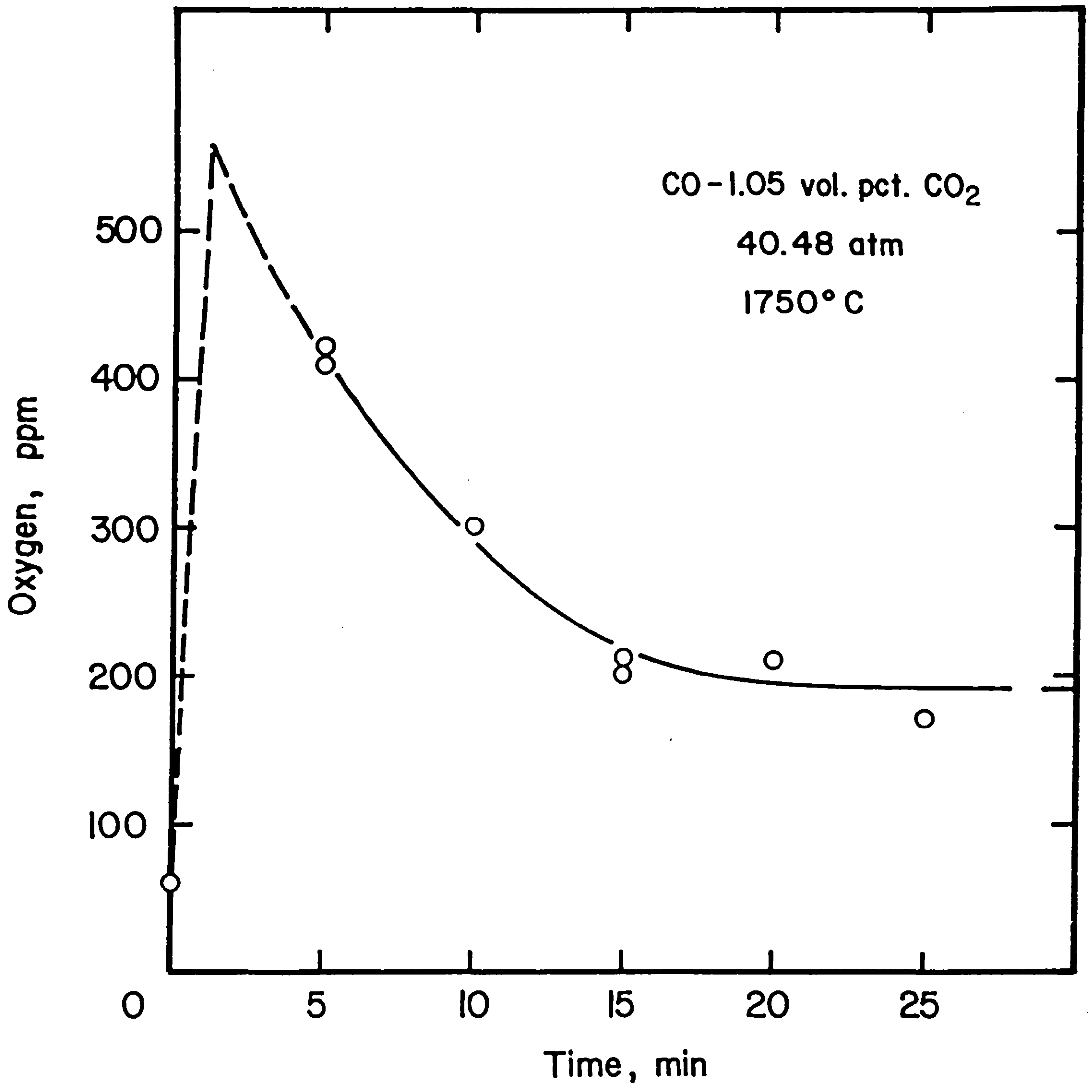

FIGURE 4.2. Oxygen concentration as a function of time during carburization of spec-pure iron (batch 1) with CO-1.05 vol. pct. CO_2 gas mixture at 40.48 atm and 1750 °C.

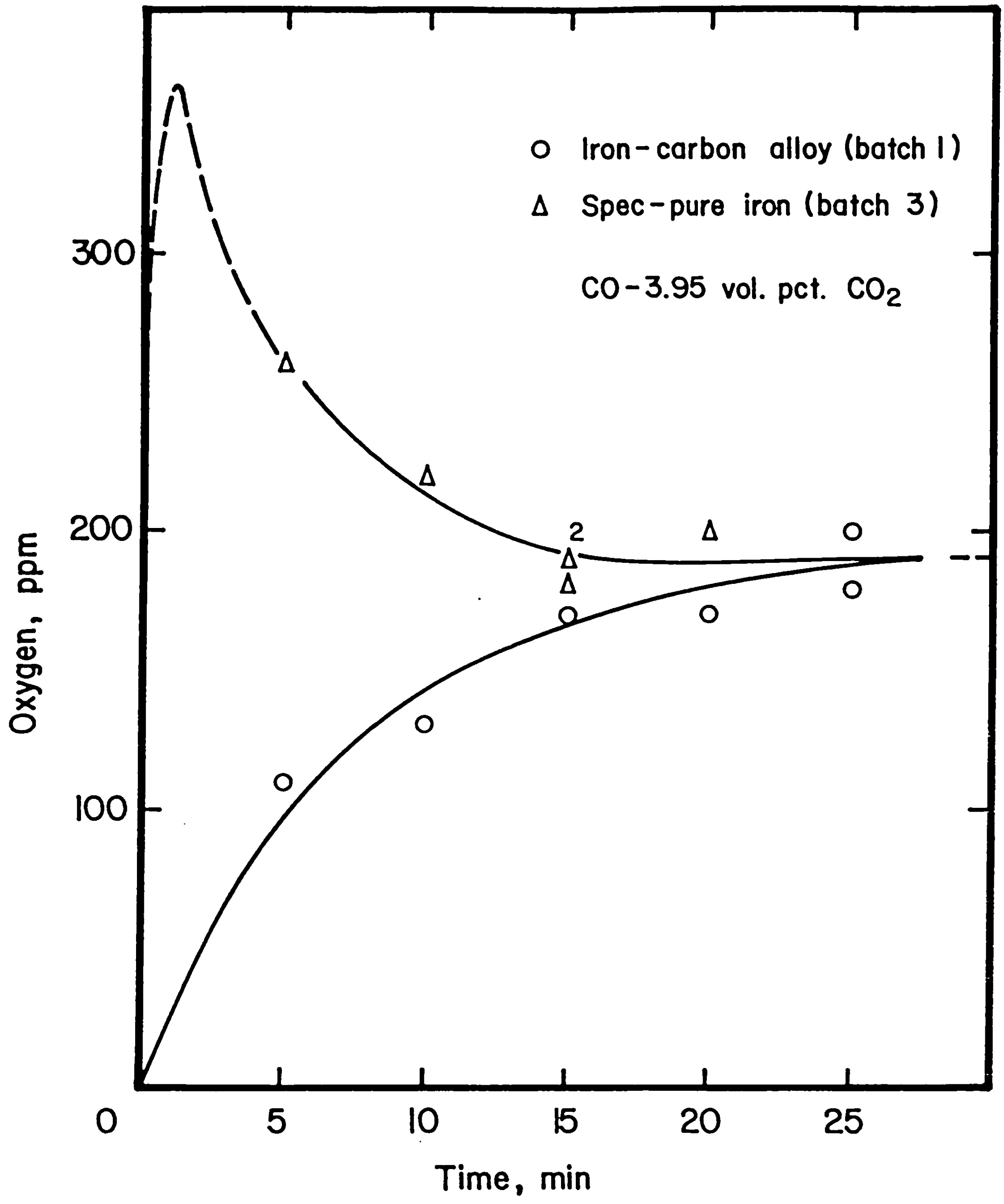

FIGURE 4.3. Oxygen concentration as a function of time during carburization of spec-pure iron and decarburization of an iron-carbon alloy at 65.15 atm and 1550 °C.

oxide islets, observed from the lateral window and through the bottom prism of the HPLA, and the analyses of the composition of these impurities is deferred to section 4.3.5.

The variation of carbon and oxygen concentrations with time were obtained by chemical analysis of oxygen and carbon in the same specimen (section 4.2.4) so that the approach to equilibrium either on carburization or decarburization could be determined from the study of both kinetic curves. The kinetic curves of carburization of spec-pure iron specimens (Figs 4.8, 4.9 and 4.10) and corresponding curves of oxygen absorption (Figs 4.11,4.12 and 4.3) showed that the specimens were very close to equilibrium after 30 min of reaction. The effect of impurities in carburization experiments was to retard the reaction but not to block it completely at any stage as occurred during decarburization (Figs 4.13 and 4.14). The oxide films on spec-pure iron were continuous or at least they covered most of the surface of the drop. These films may have meant that in certain runs the true equilibrium was not reached. The scatter of the results may be a consequence of these films which may slow down the reaction in different degrees depending on the temperature of the drop and gas composition.

The retarding effect of oxide films on specimens cut from the specially prepared iron-carbon alloys prevented the equilibrium from being attained with 0.995 and 2.00 vol. pct. CO_2 gas mixtures (Figs 4.8, 4.9, 4.11 and 4.12). During carburization with 0.995 vol. pct. CO_2 gas mixture the oxygen concentration remained constant for 10 to 20 min of reaction indicating that there was not decarburization during this period (Fig 4.11). During carburization with 2.00 vol. pct. CO_2 gas mixture the reaction was impeded for 5 to 10 min; the oxygen concentration in the specimen was still increasing after 40 min of reaction (Fig 4.12).

The concentrations of carbon and oxygen at equilibrium were nearly the same from both sides only in experiments with 3.95 vol. pct. CO_2 gas mixture (Figs 4.3 and 4.10). Hence the data obtained during decarburization with this gas mixture were included in the equilibrium data obtained with specimens cut from spec-pure iron.

The possibility of formation of different oxides under the experimental conditions of the present work is shown in section 4.3.5. The effect of impurities on the attainment of equilibrium is discussed in section 4.4.

2 Results of carbon and oxygen concentrations at equilibrium

The concentrations of carbon and oxygen in liquid iron in equilibrium with CO/CO_2 gas mixtures are given in Table 4.2. The starting material was spec-pure iron except in the experiments with 3.95 vol. pct. CO_2 gas mixture where the equilibrium was reached from both sides. The results of repeated experiments showed a precision of 0.06 wt % carbon and 10 ppm oxygen.

The values given in Table 4.2 allowed the calculation of the product of carbon and oxygen equilibrium concentrations relative to one atmosphere of partial pressure of CO. The results are given in Figure 4.4, which shows the product as a function of carbon concentration. In this calculation the mole fraction of CO was corrected by thermal diffusion. Figure 4.4 shows that the product decreases with carbon concentration. If the results are extrapolated to very low equilibrium carbon concentrations the product approaches the generally accepted value of 0.002 in the temperature range of this work.

The concentrations of carbon at 'equilibrium' during decarburization of iron-carbon specimens with 0.995 and 2.00 vol. pct. CO_2 gas mixtures are given in Table 4.3.

Table 4.2: Concentrations of carbon and oxygen in liquid iron in equilibrium with CO/CO_2 gas mixtures

Run Number	Corrected CO_2 vol. pct.	Pressure atm	Temp. °C	Carbon wt %	Oxygen wt %
Gas: CO-0.995 vol. pct. CO_2					
EFCO					
113	0.956	79.95	1550	3.83	0.006
Gas: CO-1.05 vol. pct. CO_2					
EFCO					
3	1.006	70.08	1750	2.67	0.016
8	1.006	40.48	1750	1.87	0.021
13	1.006	20.74	1750	1.29	0.017
18	1.007	60.21	1650	2.73	0.011
14	1.007	40.48	1650	2.32	0.010
25	1.007	20.74	1650	1.69	0.012
20	1.009	60.21	1550	3.34	0.007
22	1.009	40.48	1550	3.24	0.006
27	1.009	20.74	1550	2.16	0.007
Gas: CO-2.00 vol. pct. CO_2					
EFCO					
130	1.920	79.95	1650	2.49	0.020
131	1.920	79.95	1650	2.39	0.022
135	1.920	60.21	1650	1.88	0.022
136	1.920	50.35	1650	1.69	0.025
137	1.920	50.35	1650	1.67	0.025
142	1.920	40.48	1650	1.36	0.027
143	1.920	40.48	1650	1.46	0.030
128	1.922	79.95	1550	2.96	0.014
129	1.922	79.95	1550	2.80	0.014
133	1.922	60.21	1550	2.41	0.014
Gas: CO-2.05 vol. pct. CO_2					
EFCO					
29	1.965	70.08	1750	1.82	0.027
31	1.968	70.08	1650	2.14	0.018
64	1.968	50.35	1650	1.68	0.025
43	1.970	79.95	1550	3.17	0.008
35	1.970	70.08	1550	2.73	0.010
49	1.970	60.21	1550	2.14	0.016
Gas: CO-3.95 vol. pct. CO_2					
EFCO					
86	3.799	75.02	1550	2.38	0.018
88*	3.799	75.02	1550	2.71	0.017
82	3.799	65.15	1550	2.21	0.018
90*	3.799	65.15	1550	2.36	0.020

* Starting material: Fe-C alloy (batch 2)

Table 4.3 Concentration of carbon in liquid iron in equilibrium with CO/CO_2 gas mixtures in decarburization experiments

Run Number EFCO	Corrected CO_2 vol. pct.	Pressure atm	Temp. °C	Carbon wt %
Gas: CO-0.995 vol. pct. CO_2				
1-174	0.955	40.48	1650	2.23
Gas: CO-2.00 vol. pct. CO_2				
41	1.965	70.08	1750	2.86
39	1.968	70.08	1650	2.81
55	1.968	60.21	1650	2.60
62	1.968	40.48	1650	2.08
37	1.970	70.08	1550	3.27
50	1.970	60.21	1550	2.41

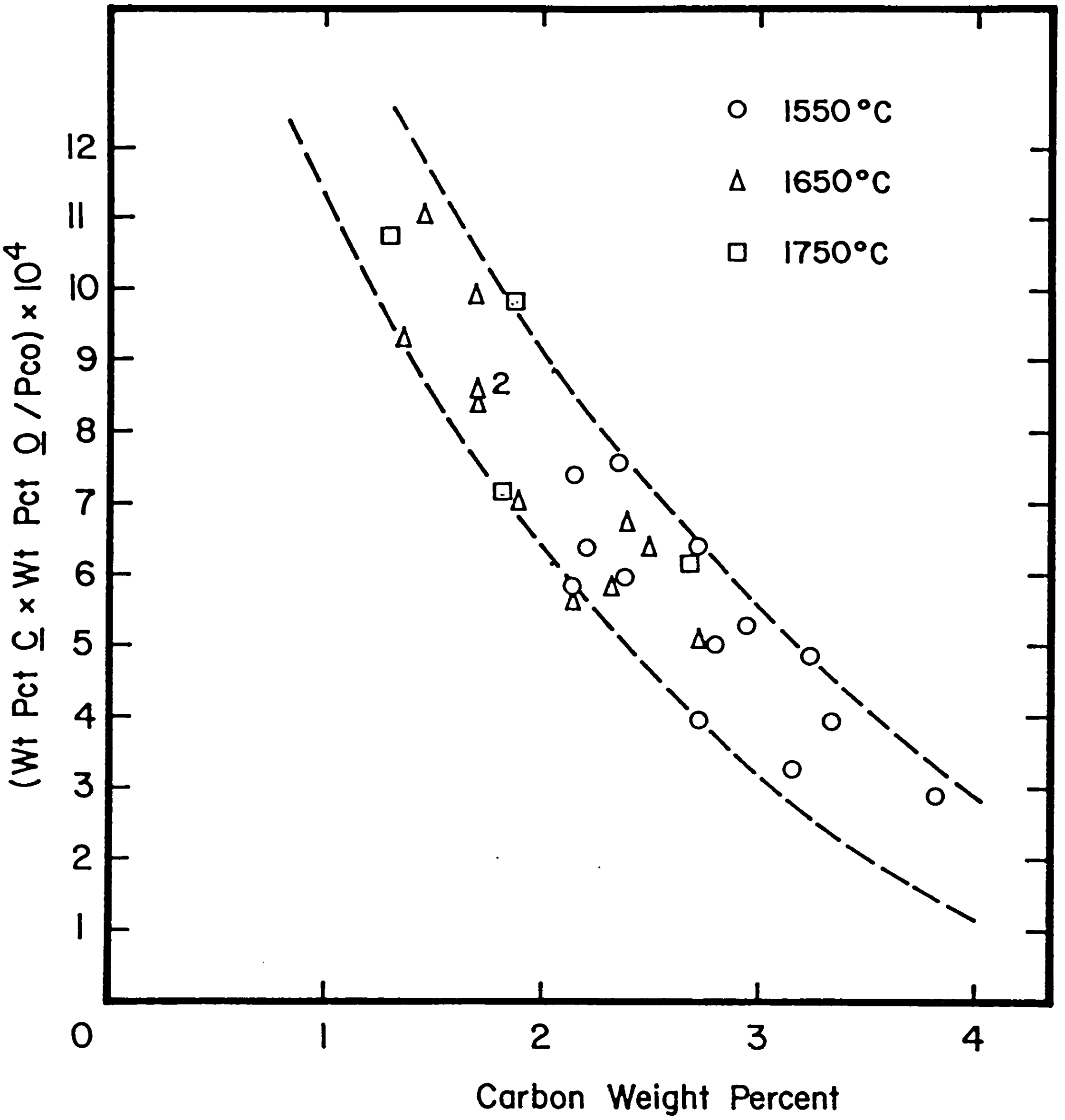

FIGURE 4.4. Carbon-oxygen product relative to 1 atm partial pressure of CO as a function of carbon concentration at different temperatures.

4.2.6 Evaluation of results

The measurements of carbon and oxygen concentrations in liquid iron in equilibrium with CO/CO_2 gas mixtures under different conditions of temperature, total pressure and gas composition allowed the study of the equilibria of reactions 4.1 and 4.2. Even though the primary objective of this work was to determine the effect of carbon concentration on the activity coefficient of oxygen in molten iron, the activity coefficients of carbon were evaluated too as a means of checking the accuracy of the present data as compared with the generally accepted values.

1 Carbon in liquid iron in equilibrium with CO/CO_2 gas mixtures

The apparent equilibrium constant of reaction 4.1 can be calculated from the available data (Table 4.2) by using the equation:

$$K_1' = (1 - x_{CO_2}')^2 P_T/x_{CO_2}' \text{ wt \% C} \qquad (4.24)$$

where x_{CO_2}' is the mole fraction of CO_2 on the surface of the droplet corrected for thermal diffusion and given in Table 4.2. The values of K_1' were analysed by the least squares method to obtain the linear variation of $\log K_1'$ with carbon concentration at each temperature. The following equations were obtained:

$$\log K_{1(1550)}' = 2.58 + 0.182 \text{ wt \% C} \qquad (4.25)$$

$$\log K_{1(1650)}' = 2.98 + 0.107 \text{ wt \% C} \qquad (4.26)$$

$$\log K_{1(1750)}' = 2.99 + 0.158 \text{ wt \% C} \qquad (4.27)$$

The correlation coefficients between $\log K_1'$ and wt % C in equations 4.25, 4.26 and 4.27 were calculated as 0.74, 0.79 and 0.97 respectively. The low values of the correlation coefficients of equations 4.25 and 4.26 show the scatter of the data at 1550 and

1650°C. Figure 4.5 shows the values of log K_1' as a function of carbon concentration, the best lines obtained by the least squares method were drawn at the limiting temperatures.

The logarithms of the true equilibrium constant (K_1) and the activity coefficient of carbon (f_C) are given by the first and second terms respectively on the right hand side of the equations 4.25, 4.26 and 4.27.

The relationship between the concentration of carbon and the ratio P^2_{CO}/P_{CO_2} (corrected by thermal diffusion) is shown graphically in Figure 4.6. The full lines were drawn taking into account the carburization data only. Extrapolation to lower carbon concentration is shown by dashed lines. The data of equilibrium carbon concentration in decarburization experiments are also shown in Figure 4.6.

2 Oxygen in liquid iron in equilibrium with CO/CO_2 gas mixtures

The activity coefficient of oxygen in the ternary system Fe-C-O is given by the equation:[64]

$$f_O = f_O^O \times f_O^C \qquad (4.28)$$

where f_O^O is the activity coefficient of oxygen in the binary solution Fe-O and f_O^C is the interaction coefficient of carbon on oxygen which is a measure of the change of f_O caused by the variation of carbon concentration in the ternary Fe-C-O at constant oxygen activity. Tankins[56] demonstrated that oxygen obeys Henry's Law in molten iron so that f_O^O is unity. It has been shown that the activity coefficients can be expressed in terms of interaction parameters.[64] Selecting the infinitely dilute weight-percent solution as standard state for dissolved oxygen, the oxygen activity coefficient is given by the equation:

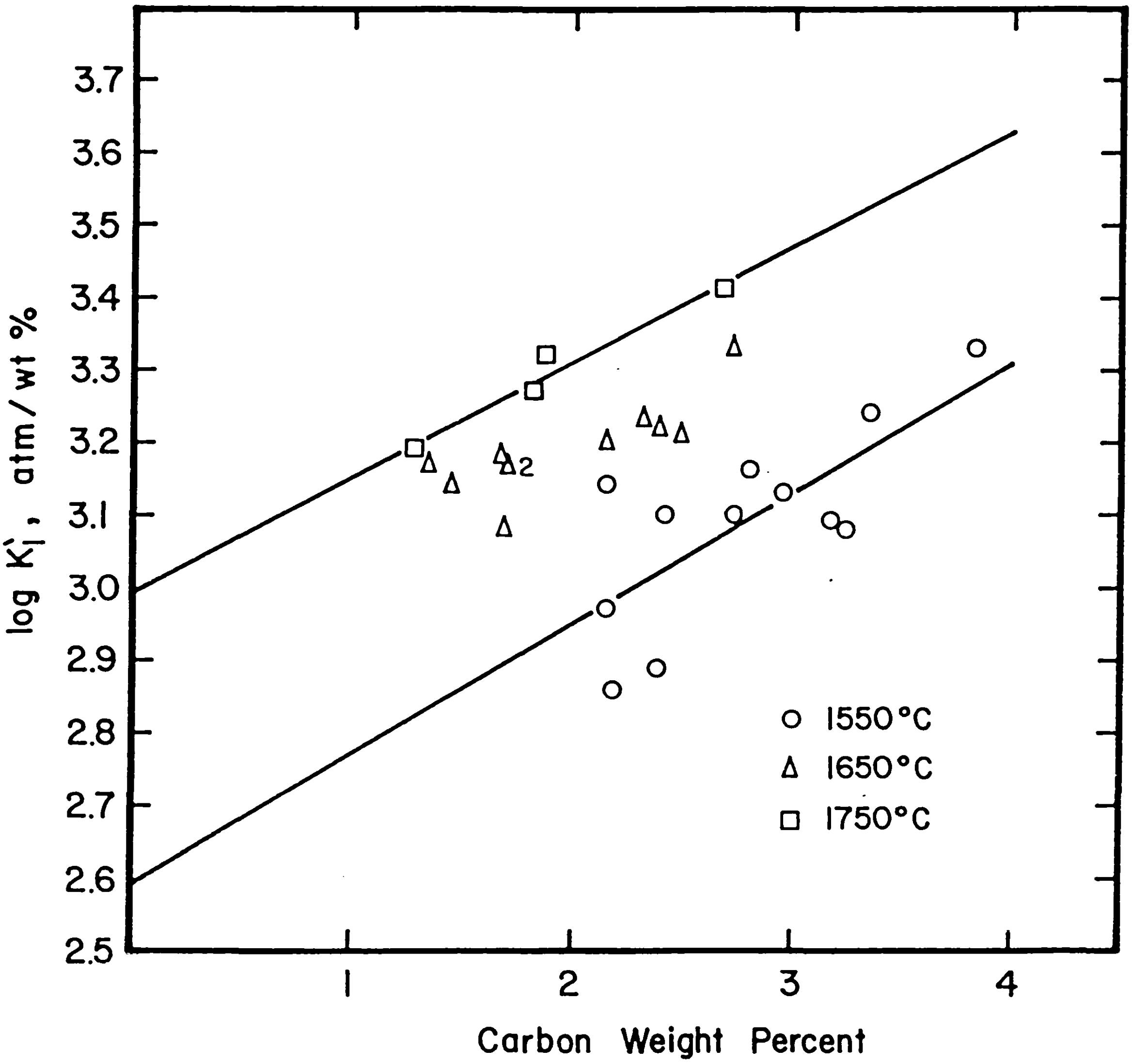

FIGURE 4.5. Apparent equilibrium constant of the reaction $CO_2(g) + \underline{C} = 2\ CO(g)$ as a function of carbon concentration in molten iron.

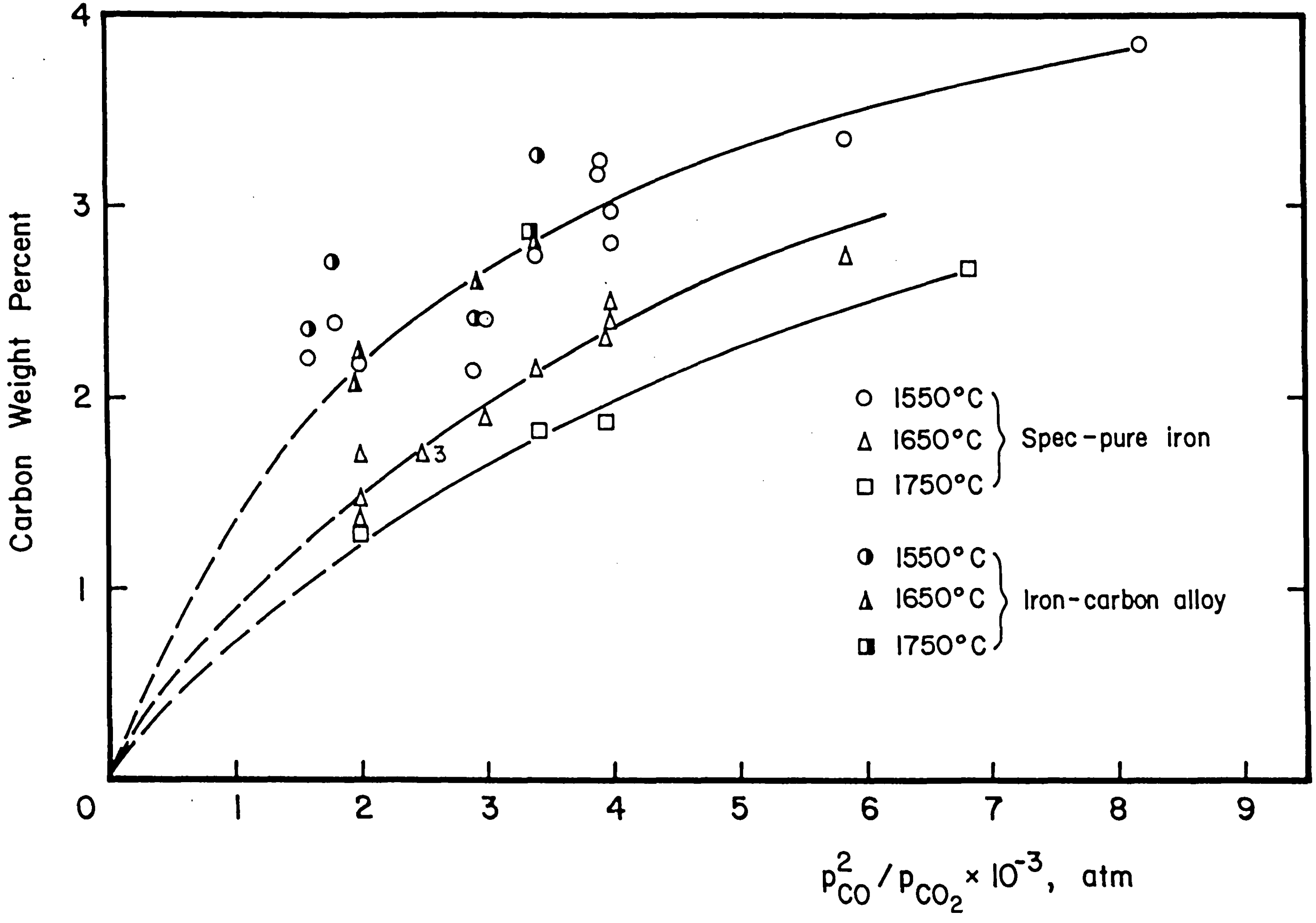

FIGURE 4.6. Equilibrium of carbon in liquid iron with CO/CO_2 gas mixtures.

$$\log f_O = \text{wt \% C} \, (\partial \log f_O / \partial \, \text{wt \% C})_{\text{wt \% C} \rightarrow 0} \tag{4.29}$$

or

$$\log f_O = \text{wt \% C} \, . \, e_O^C \tag{4.30}$$

The standard free energy change of reaction 4.6 is given by the following equation:[56]

$$\Delta G_6^0 = -31200 + 14.33 \, T \tag{4.31}$$

in which the standard state for oxygen is an infinitely dilute weight per cent solution. The ΔG° of the water-gas reaction (equation 4.7) is given by:[53]

$$\Delta G_7^\circ = 6400 - 6.30 \, T \tag{4.32}$$

Equations 4.31 and 4.32 can be combined to obtain the standard free energy change of the reaction of oxygen in molten iron with CO/CO_2 gas mixtures (equation 4.2):

$$\Delta G^\circ_{2(\text{wt \%})} = -37600 + 20.63T \tag{4.33}$$

and

$$\log K_{2(\text{wt \%})} = 8217/T - 4.51 \tag{4.34}$$

The activity coefficient of oxygen can be calculated by using the equation:

$$f_O = x'_{CO_2}/(1 - x'_{CO_2})K_2 \, \text{wt \% O} \tag{4.35}$$

where wt % O is the measured equilibrium oxygen concentration and x'_{CO_2} the mole fraction of CO_2 corrected by thermal diffusion (Table 4.2).

Figure 4.7 shows the variation of $\log f_O$ with equilibrium carbon concentration. It was found that the activity coefficient of oxygen increases with carbon concentration and is independent of temperature within the experimental error of this work.

Equation 4.30 predicts a linear variation of log f_O with wt % C. Analysis of the data by the least squares method gave the following regression line:

$$\log f_O = 0.06 \text{ wt \% C} + 0.06 \qquad (4.36)$$

with a regression coefficient of 0.5 as a result of the scatter, however the direct relationship is clear. The standard deviation about the regression line (s) was found to be 0.099. The confidence intervals (95% confidence) of the regression coefficient (slope) and the intercept with the ordinate were calculated as ± 0.02 and ± 0.06 respectively.

Figure 4.7 shows the linear regression defined by equation 4.36. As f_O should be unity at wt % C = 0, according to equation 4.30, the 'best line' can be defined by the equation:

$$\log f_O = 0.06 \ (\pm 0.02) \text{ wt \% C} \qquad (4.37)$$

so that

$$e_O^C = 0.06 \ (\pm 0.02) \qquad (4.38)$$

The interaction parameter of oxygen on carbon e_C^O is related to e_O^C by the equation:[64]

$$e_C^O = (M_C/M_O)e_O^C + 4.34 \times 10^{-3} \{(M_O - M_C)/M_O\} \qquad (4.39)$$

where M_C and M_O are the atomic weights of oxygen and carbon respectively. The following value was obtained:

$$e_C^O = 0.051 \ (\pm 0.015)$$

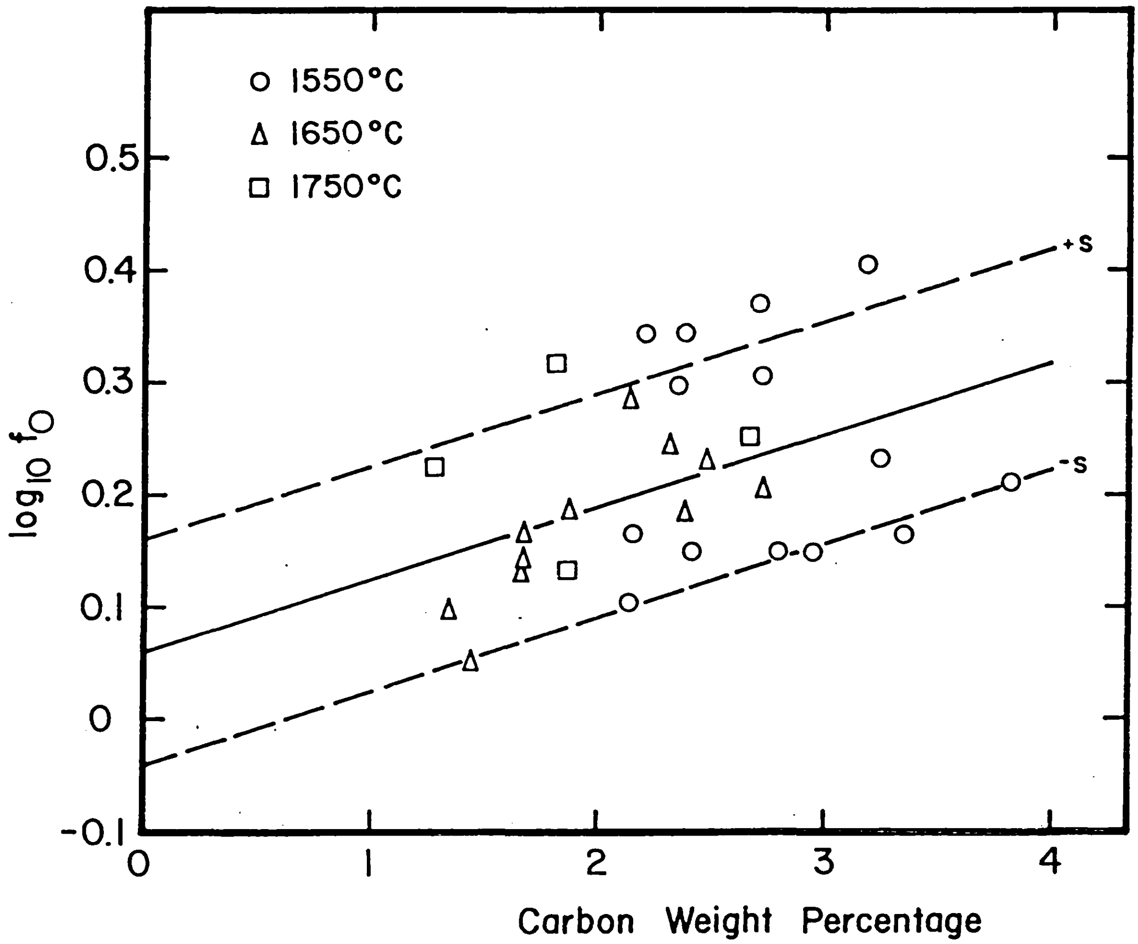

FIGURE 4.7. Activity coefficient of oxygen as a function of carbon concentration in molten iron at 1550, 1650 and 1750 °C. Solid line: least squares regression; dashed line: standard deviation about the fitted line(s).

The interaction parameter of carbon on oxygen in very dilute solution when the concentrations are expressed in atomic fraction is defined by the equation:

$$\varepsilon_O^C = (\partial \ln f_O/\partial N_C)_{N_C \longrightarrow 0} \qquad (4.40)$$

which has been shown to be equal to ε_C^O.[64]

The interaction parameter ε_O^C is related to e_O^C by the equation:[64]

$$\varepsilon_O^C = 230\ (M_C/M_{Fe})e_O^C + \{(M_{Fe} - M_O)/M_{Fe}\} \qquad (4.41)$$

where M_{Fe} is the atomic weight of iron. The calculated value was:

$$\varepsilon_O^C = \varepsilon_C^O = 3.68\ (\pm\ 0.99)$$

4.3 Kinetics of the reactions between molten iron and CO/CO$_2$ gas mixtures

4.3.1 Introduction

Decarburization is the most important heterogeneous reaction occurring in the steelmaking processes because it controls the rate of production. As a consequence the kinetics of decarburization of liquid iron-carbon alloys has been the subject of many investigations on laboratory and plant scales. Most of the laboratory studies of decarburization of slag-free iron carbon melts have involved the reaction of gaseous oxidants CO$_2$ and O$_2$ (or gas mixtures containing these reactants) with melts held in crucibles or with levitated drops.

The decarburization reaction, as any other gas/liquid metal gas reaction, occurs through a number of steps in series. The three elementary steps are:

a) Transport of reactants to the surface of the drop.
b) Chemical reaction at the surface.
c) Transport of reaction products from the surface.

If one of the elementary steps occurs at much slower rates than the others this step will determine the kinetics of the overall reaction.

The chemical reaction at the interface itself consists of a series of consecutive steps. A typical sequence might be:

b1) Adsorption of a reactant on an active site.
b2) Formation of an activated specie.
b3) Reaction between the activated specie and another reactant to give an adsorbed reaction product.
b4) Desorption of the reaction product.

The same concept of rate determining step is applied in this case.

The steps which are not rate determining are considered to be at equilibrium and the kinetics of the overall reaction simplifies to the kinetics of the rate determining step. It is usually possible by the choice of suitable experimental conditions to study the kinetics of each of the reaction steps, for example the study of the chemical kinetics will require the investigator to obtain rapid transport rates.

It is therefore clear that for any given reaction under various experimental conditions, different investigators will establish the rate constants for the various rate controlling steps. These rate constants should be different, when rate constants of the same magnitude are quoted for two different rate controlling steps then further work is required to determine which step is in fact controlling under the conditions of interest. A further complication is that of mixed control.

The relatively low rates of decarburization and carburization found in the present work while trying to achieve equilibrium between either iron-carbon specimens or spec-pure iron specimens with CO/CO_2 gas mixtures at high total pressures led to the study of the kinetics of these reactions under the present experimental conditions. The kinetics was followed by carbon and oxygen analyses of the reacted specimens for different periods of time.

The rates of decarburization and carburization appeared not to be depressed at the start of the reaction but after a certain time at which an oxide phase was formed covering part of all the surface of the drop this situation allowed us to compare the experimental initial rates with those predicted by theoretical models for slag-free melts. Attempts of analysing the composition of the oxide phases were made in the present work. The surface oxygen and carbon concentrations were calculated to show the magnitude of the increase of these concentrations when spec-pure iron drops are exposed to CO/CO_2 gas mixtures at high pressure.

4.3.2 Previous work

The overall reaction of decarburization is given by the equation:

$$CO_2(g) + \underline{C}\text{ (in iron)} = 2CO(g) \qquad (4.42)$$

If mass transfer in the gas phase is the rate controlling step the rate of decarburization will be given by the equation:[65]

$$N_C = (k_g^{\prime} P_T/RT_f)\ln[(P_T + p_{CO_2}^{b})/(P_T + p_{CO_2}^{i})] \qquad (4.43)$$

which simplifies to the following equation when the partial pressure of CO_2 at the interface ($p^i_{CO_2}$) is zero because of fast interfacial reaction:

$$N_C = k_g \ln (1 + x_{CO_2b}) \qquad (4.44)$$

where k'_g is the average gas phase mass transfer coefficient ($k'_g = D_{CO_2-CO}/\delta$), δ is the thickness of the gas film boundary layer, D_{CO_2-CO} the binary diffusivity of CO_2 and CO, $k_g = k'_g P_T/RT_f$, R the gas constant, T_f the film temperature and x_{CO_2b} is the mole fraction of CO_2 in the bulk of gas. From equation 4.44 one will expect that when mass transfer in the gas phase is controlling the rate of decarburization will be independent of the carbon concentration in the melt, it will be a linear function of $\ln (1 + x_{CO_2b})$, it will depend on the gas flow rate and on total pressure.

Baker et al[66] were the first in establishing clearly that gas phase mass transfer may be the rate controlling step of the decarburization reaction at high carbon levels in the metal, greater than 1 wt %. They studied the decarburization of 0.7g levitated drops from 5.5 to 0 wt % C with 1 to 100 vol. pct. CO_2 gas mixtures with CO or He as diluents. All the predictions from equation 4.44 were accomplished above about 1.0 wt % carbon. The gas phase mass transfer coefficient (k_g) found at 1660°C at a flow rate of CO/CO_2 gas mixture (89 vol. pct. CO_2) of 1000 cc/min was 10^{-4} mole/cm²sec. Further support that gas phase mass transfer is the rate controlling step at high carbon concentrations in levitated drops at atmospheric pressure was given by another investigation of Baker et al[67] using pure O_2 or O_2/He gas mixtures to decarburize specimens from 5.5 to 0 wt % C. The rates were found to be approximately 2.5 times those with CO_2 as oxidant. The rate of decarburization of graphite spheres was the same as that of Fe-C specimens under the same experimental conditions.

Distin et al[68] found that the decarburization reaction of levitated drops from 4.0 to 1.0 wt % C with O_2, CO_2, O_2/H_2O and Ar/H_2O gas mixtures at 1755°C was controlled by gas phase mass transport. The results of this investigation were comparable to those found by Baker et al.[66] The investigations of Kaplan and Philbrook[69] and Robertson[16] using the levitation melting technique at atmospheric pressure further supported that transport in the gas phase may control the decarburization reaction at high carbon concentrations. El-Kaddah and Robertson[70] found that the decarburization of one gram levitated drops of iron-carbon alloys from 5-5.5 wt % C to 1.7-2.7 wt % C with CO/CO_2 gas mixtures at 40 atm and 1650°C was controlled by mass transport in the gas phase. The effect of the high total pressure was to decrease the importance of the interfacial reaction in controlling the rate because of the high partial pressures of CO_2. The oxygen potentials of the gas mixtures were lower than required to form oxides. The gas phase mass transfer coefficient was 4.5×10^{-3} mole/cm^2 sec in 1.1 to 2.2 vol. pct. CO_2 gas mixtures, higher than the value given above because of the high total pressure.

In the investigations using the levitation melting technique the simple geometry of the system enabled the interpretation of results using well established mass transfer correlations for a gas flowing past a single sphere.

The investigation of Nomura and Mori[71] and Fruehan and Martonik[72] on the decarburization of liquid iron at high concentration of carbon with CO/CO_2 gas mixtures at 1600°C by using the crucible method have also shown that the rates were controlled primarily by gas phase mass transfer. Nomura and Mori[71] found that the rate of decarburization depended on the gas blowing conditions such as flow rate and size of the blowing tube. In the work of

Fruehan and Martonik[72] the CO/CO_2 gas mixture flowed parallel to the surface of the melt at 52 cm/sec, under their experimental conditions a gas phase mass transfer coefficient of 10^{-4} mole/cm²sec was found.

When transport in the liquid phase is the rate controlling step of the decarburization reaction the rate of the overall reaction is given by the equation:[68]

$$N_C = k_l(C^b - C^i) \tag{4.45}$$

where k_l is the average liquid mass transfer coefficient and C^b and C^i are the concentrations of carbon in the bulk and at the surface of the liquid. From equation 4.45 the rate of decarburization is expected to decrease with decreasing carbon concentration in the melt, the rate should be independent of the partial pressure of carbon dioxide and the gas flow rate. This was not the case in the investigations mentioned above in the high carbon concentration range. Distin et al[68] and Lee and Rao[65] found that at carbon concentrations below a certain critical level at which an oxide phase was formed the rate of decarburization was controlled by transport in the liquid phase. Under this condition the concentration of carbon at the surface becomes approximately zero and the rate of decarburization is transformed to:

$$N_C = k_l C^b \tag{4.46}$$

which allowed the experimental determination of k_l by taking the slope of the line defined by the rate of decarburization as a function of carbon concentration. Distin et al[68] found a k'_l (the mass transfer coefficient in the liquid phase when the concentration of carbon is expressed in weight - per cent) of 1.8×10^{-4} mole/cm²sec wt %

at 1800°C their results showed little scatter around the straight line defined by equation 4.46. Lee and Rao[65] found a value of k_l' of 3.2×10^{-4} mole/cm²sec wt % at 1700°C, in this work the carbon concentration at which the oxide appeared at a given rate of decarburization was widely scattered (spanning a range from about 0.05 to 0.14 wt % C) so that their value of k_l' was only approximate.

El-Kaddah and Robertson[70] demonstrated that the results of Distin et al[68] could be explained by an effective diffusivity model with a constant flux at the surface. They showed that the molar flux of carbon was given by the equation:

$$N_C = (5D/a)C^b \qquad (4.47)$$

where D is the effective diffusivity of carbon and a the radius of the sphere. An effective diffusivity of carbon of 1.8×10^{-3} cm²/sec was found to fit all the data of Distin et al.[68] Lee and Rao[65] found an effective diffusivity of carbon in liquid iron of 3.24×10^{-3} cm²/sec.

El-Kaddah and Robertson[70] observed rates of carburization of liquid iron with 1.1-2.15 vol. pct. CO_2 in CO/CO_2 gas mixtures at 40 atm and 1650°C which were predicted with an effective diffusivity of 4.0×10^{-4} cm²/sec. El-Kaddah and Szekely[8] have recently used calculations of the electromagnetically driven flow in a levitated drop to show that in fact levitated drops are not well stirred.

The results of the various investigations reviewed above should be compared with the molecular diffusivity of carbon in liquid iron of about 3×10^{-4} cm²/sec at 1700°C. The slow reaction studied by El-Kaddah and Robertson indicated a nearly stagnant drop. Higher D values were obtained for the much faster reactions (higher driving forces) observed by Distin et al[68] and Lee.[65] The higher liquid phase mass transfer rates were presumably due to interfacial turbulence.

When the chemical reaction at the surface of the melt is rate determining, the decarburization reaction may occur by the following consecutive steps:[73]

a) Adsorption of CO_2:

$$CO_{2(g)} = CO_{2(ad)}$$

b) Dissociation of CO_2:

$$CO_{2(ad)} = CO_{(ad)} + O_{(ad)}$$

c) Transport of carbon to the surface and its adsorption:

$$\underline{C} = C_{(ad)}$$

d) Chemical reaction between adsorbed carbon and oxygen:

$$C_{(ad)} + O_{(ad)} = CO_{(ad)}$$

e) Desorption of CO:

$$2CO_{(ad)} = 2CO_{(g)}$$

Sain and Belton[73] provided the first measurement of the kinetics of the chemical reaction step of the decarburization reaction of liquid iron with CO/CO_2 gas mixtures when the other elementary steps were clearly not rate determining. In their investigation the decarburization of carbon-saturated iron with varying carbon concentration (greater than 1 wt %) was studied by holding the melt in a crucible and using very high flow rates of CO/CO_2 gas mixtures to force the system into a regime of interfacial control. They found that under their experimental conditions the rate constants were independent of carbon concentration, proportional to the CO_2 partial pressure and independent of CO partial pressure. It was concluded that the rate of dissociative chemisorption of CO_2 at the surface was the rate determining step. They also found a marked sensitivity of the rate to small amounts of sulfur. The rate of decarburization, ignoring the back reaction in step (b), is given by the equation:[65]

$$N_C = k_R(p^i_{CO_2} - p^e_{CO_2}) \qquad (4.48)$$

where k_R is the rate constant and $p^e_{CO_2}$ is the partial pressure of CO_2 at equilibrium. As $p^e_{CO_2}$ is negligibly small equation 4.48 is transformed to:

$$N_C = k_R p^i_{CO_2} \qquad (4.49)$$

The rate constant, in mole/cm² sec atm, found by Sain and Belton[73] is given by the equation:

$$\log k_R = -(5080/T) - 0.208 \qquad (4.50)$$

in the temperature range of 1553 to 1873°K. When chemical reaction is rate determining the decarburization rates are much faster than in the case of transport control in the gas phase under the same conditions of temperature and gas composition.

If surface-active species (e.g. sulphur) are present in the melt they can slow down the rate of the chemical reaction either by displacing less surface-active reactants from the interface or by blocking the interface.[9,73] If a fraction of surface sites (θ_s) are occupied by an adsorbed specie the rate of reaction will be given by the equation:

$$N_C = k_R(1 - \theta_s)p^i_{CO_2} \qquad (4.51)$$

The rate of gas/liquid metal reactions, in general, may be also impeded by the presence of impurities which can form continuous films over the melt as found by Forster and Richardson[74] in their investigation of the kinetics of oxidation of levitated drops of copper with carbon dioxide. The presence of 2ppm of silicon caused the formation of a coherent layer of silica over the melt at the start of the reaction. These films evaporated at temperatures higher than 1500°C.

In contrast to decarburization the study of the kinetics of carburization of liquid iron has received little attention. Parlee et al[75] studied the kinetics of CO absorption in liquid iron in the carbon concentration range of 0.15 to 4.4 wt % C by using a modified Sieverts gas-solubility apparatus. Their results were greatly hampered by a secondary reaction between the alumina crucible and carbon dissolved in the melt. After correction for the dissolution of alumina it was found that the rate of the carbon-oxygen reaction was controlled by oxygen transport in the liquid phase. The investigation of El-Kaddah and Robertson[70] on carburization of spec-pure iron levitated drops with CO/CO_2 gas mixtures at high pressure showed conclusively that the rate was controlled by the transport steps (mixed transport control), as discussed in previous paragraphs.

4.3.3 Experimental

The experimental procedure was essentially the same as that described in section 4.2.4 on the equilibrium measurements. The specimens for decarburization were prepared from the three batches of iron-carbon alloy (section 2.9) containing 4.6, 5.7 and 4.3 wt % C. The specimens for carburization experiments were prepared from spec-pure iron batch 3 (section 2.10,Table 2.1). Each kinetic curve was obtained by using specimens from the same batch. The mass of the specimens was maintained in the range 1 ± 0.01g to ensure the same surface area in the experimental runs. Care was taken in cleaning the specimens with acetone before levitation.

The levitated drops were kept in the H_2/Ar gas mixture with the purpose of cleaning the surface of oxide contaminants before changing to the CO/CO_2 gas mixture. The temperature of the specimen was adjusted to the required level and maintained constant (± 5°C) during the experiment. The specimens were quenched under pressure and the reactive gas changed to argon. Quenching was carried out at different stages of the reaction, the shortest time was 75 sec. The reacted specimens were analyzed for carbon and oxygen (section 4.2.4).

The surface of the quenched specimen was examined by Secondary Ion Mass Spectrometer (SIMS) and by Laser Induced Ion Mass Analyser (LIMA). SIMS analyses were carried out using an ATOMIKA's Ionprobe A-DIDA 3000 at Imperial College. This technique allowed us to know the qualitative composition of the impurities and the depth distribution of the species in the film of a few microns thickness. The trace sensitivity of SIMS is very high (in the ppb range). Examination of the surface of the specimens by LIMA was carried out at AWRE, Aldermaston. The maximum sensitivity of LIMA is 1 ppm on most elements (section 3.3).

4.3.4 Results

The rates of decarburization and carburization were determined under the following conditions: 1) CO-0.995 vol. pct. CO_2 and 2.00

vol. pct. CO_2 gas mixtures at 40.48 atm and 1650°C, 2) CO-3.95 vol. pct. CO_2 gas mixture at 65.15 atm and 1550°C. The flow rate of the CO/CO_2 gas mixtures was fixed at 2 slm in all the experimental runs. Kinetic curves were obtained for carbon and oxygen.

The decarburization rate was found to be particularly slow when the gas mixture containing 2.00 vol. pct. CO_2 was used. Hence, a programme of runs was begun using this mixture and different starting materials.

In decarburization and carburization experiments islets of impurity oxides were observed to form shortly after the CO/CO_2 gas mixture entered into the levitation chamber. The oxides were distinguishable because of their higher emissivity than the metal.

1 Decarburization and carburization

The results of decarburization and carburization with 0.995 vol. pct. CO_2 and 2.00 vol. pct. CO_2 are presented in Figs 4.8 and 4.9 respectively.

The initial rate of decarburization increased with the increase of CO_2 in the gas mixture. The rate of decarburization was not constant and decreased with time. It is seen in Figure 4.9 that the rate of decarburization was practically nil after 30 min of reaction and the equilibrium carbon concentration was not reached.

The initial rate of carburization was the same with both gas mixtures. The carbon concentration reached 1 wt % in about 60 sec. The results suggested that the initial rate of carburization is independent of the CO_2 content in the gas mixture. After about 75 sec of reaction the rate of carburization decreased drastically. The rate of carburization in 0.995 vol. pct. CO_2 during this period was more than twice the rate of carburization in 2.00 vol. pct. CO_2.

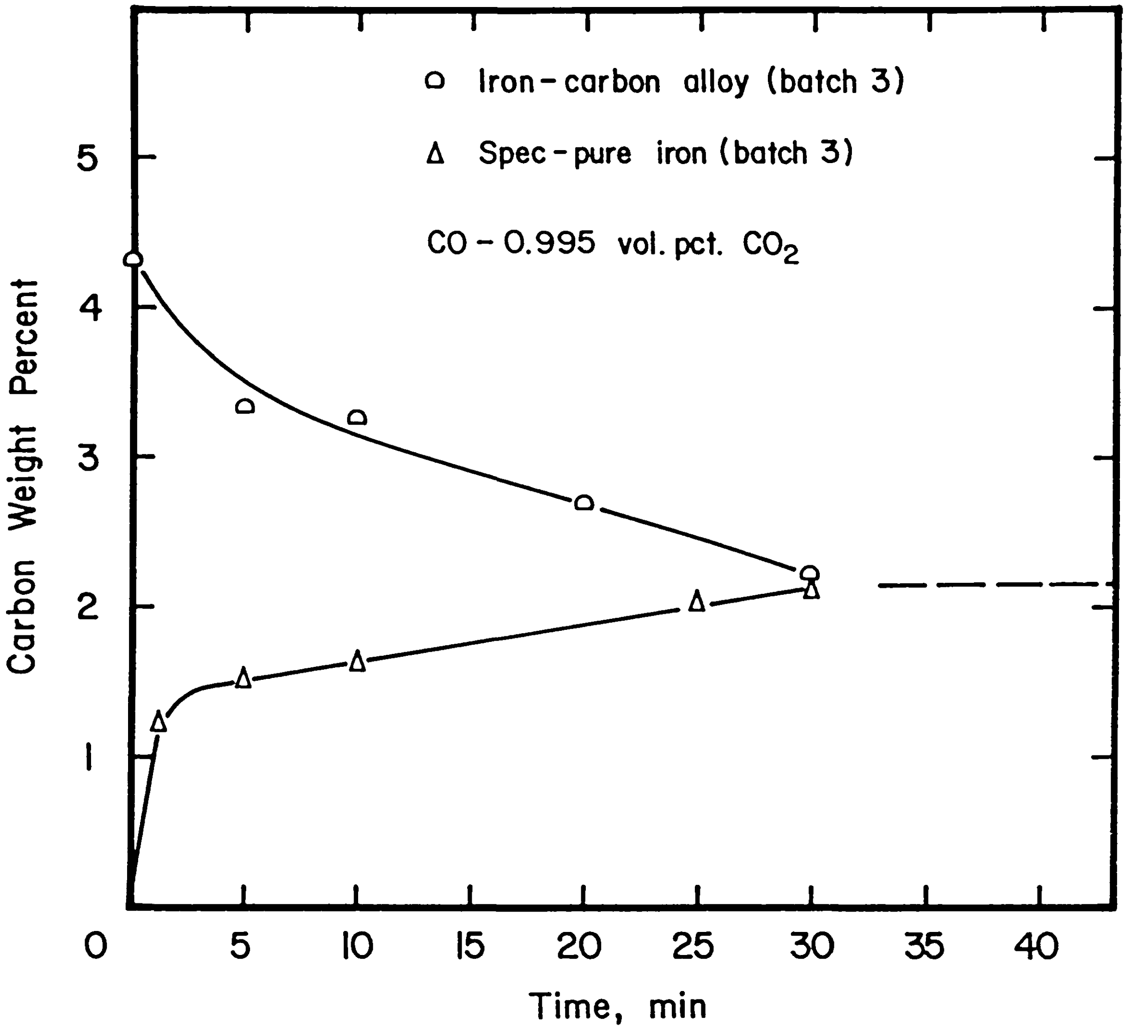

FIGURE 4.8. Carbon concentration as a function of time during carburization of spec-pure iron and decarburization of iron-carbon alloy with CO - 0.995 vol. pct. CO_2 gas mixture at 40.48 atm and 1650 °C.

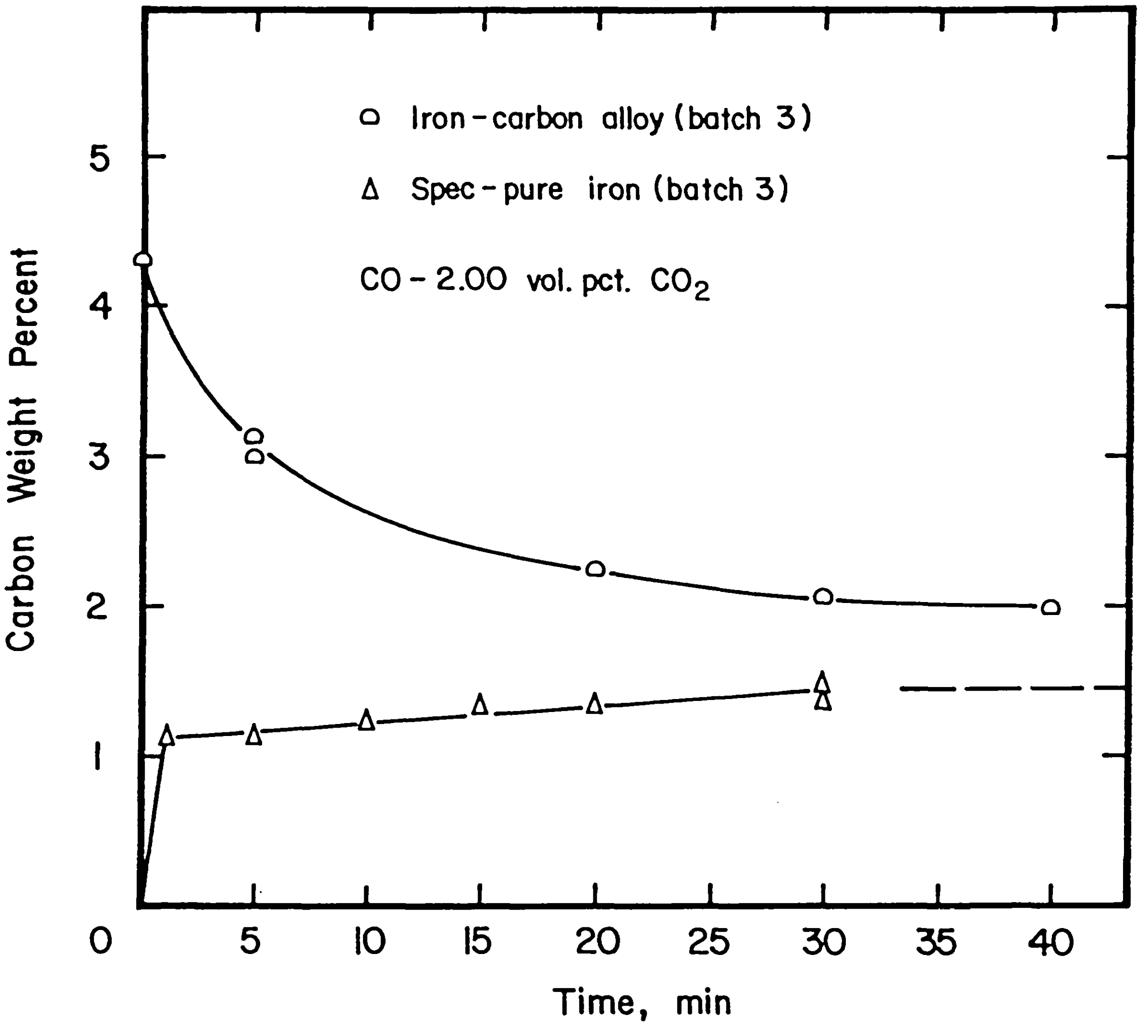

FIGURE 4.9. Carbon concentration as a function of time during carburization of spec-pure iron and decarburization of iron-carbon alloy with CO - 2.00 vol. pct. CO_2 gas mixture at 40.48 atm and 1650 °C.

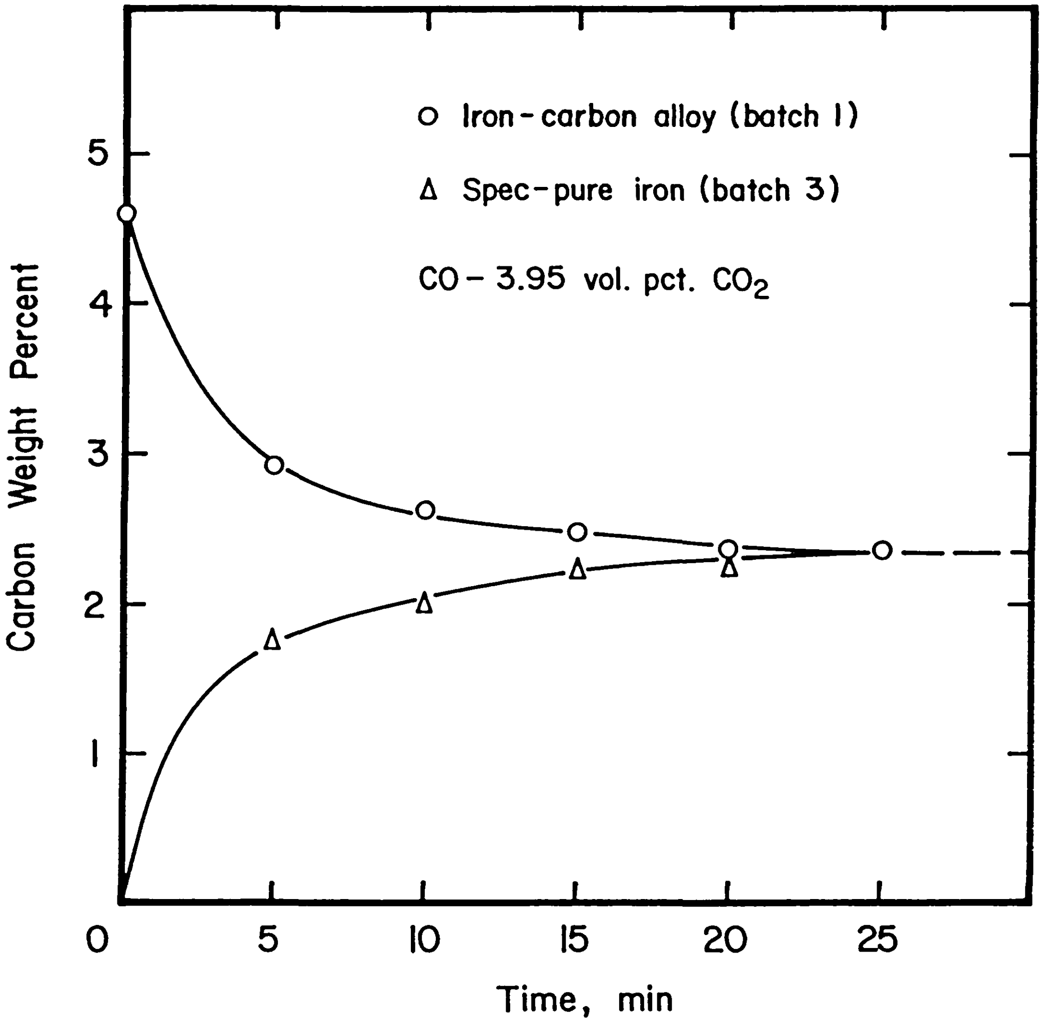

FIGURE 4.10. Carbon concentration as a function of time during carburization of spec-pure iron and decarburization of iron-carbon alloy with CO - 3.95 vol. pct. CO_2 at 65.15 atm and 1550 °C.

In Figure 4.10 are reported the results of decarburization and carburization in 3.95 vol. pct. gas mixture. The initial rates were high and then the rates slowed down as the reactions approached equilibrium.

2 Oxygen absorption during decarburization and carburization

The results of oxygen concentrations as a function of time obtained in decarburization and carburization with 0.995 vol. pct. CO_2 and 2.00 vol. pct. CO_2 at 40.48 atm and 1650°C are presented in Figs 4.11 and 4.12.

The initial rate of oxygen absorption in decarburization experiments was higher with 2.00 vol. pct. CO_2 than with 0.995 vol. pct. CO_2.

The oxygen concentration during carburization of spec-pure iron drops increased sharply at the start of the reaction to reach a peak value and then decreased non linearly as the reaction approached equilibrium. The oxygen absorption in 2.00 vol. pct. CO_2 during the first stage was more than twice the oxygen absorbed in 0.995 vol. pct. CO_2 in this stage. The rapid oxygen absorption extended for about 200 sec in 2.00 vol. pct. CO_2 and for a time shorter than 75 sec in 0.995 vol. pct. CO_2.

The results of oxygen absorption as a function of time during decarburization of iron-carbon specimens showed that in fact equilibrium was not reached in the experiments with CO-0.995 vol. pct. CO_2 and CO-2.00 vol. pct. CO_2.

The oxygen concentration measured during decarburization and carburization in 3.95 vol. pct. CO_2 at 65.15 atm and 1550°C was shown in Figure 4.3 (section 4.2.5).

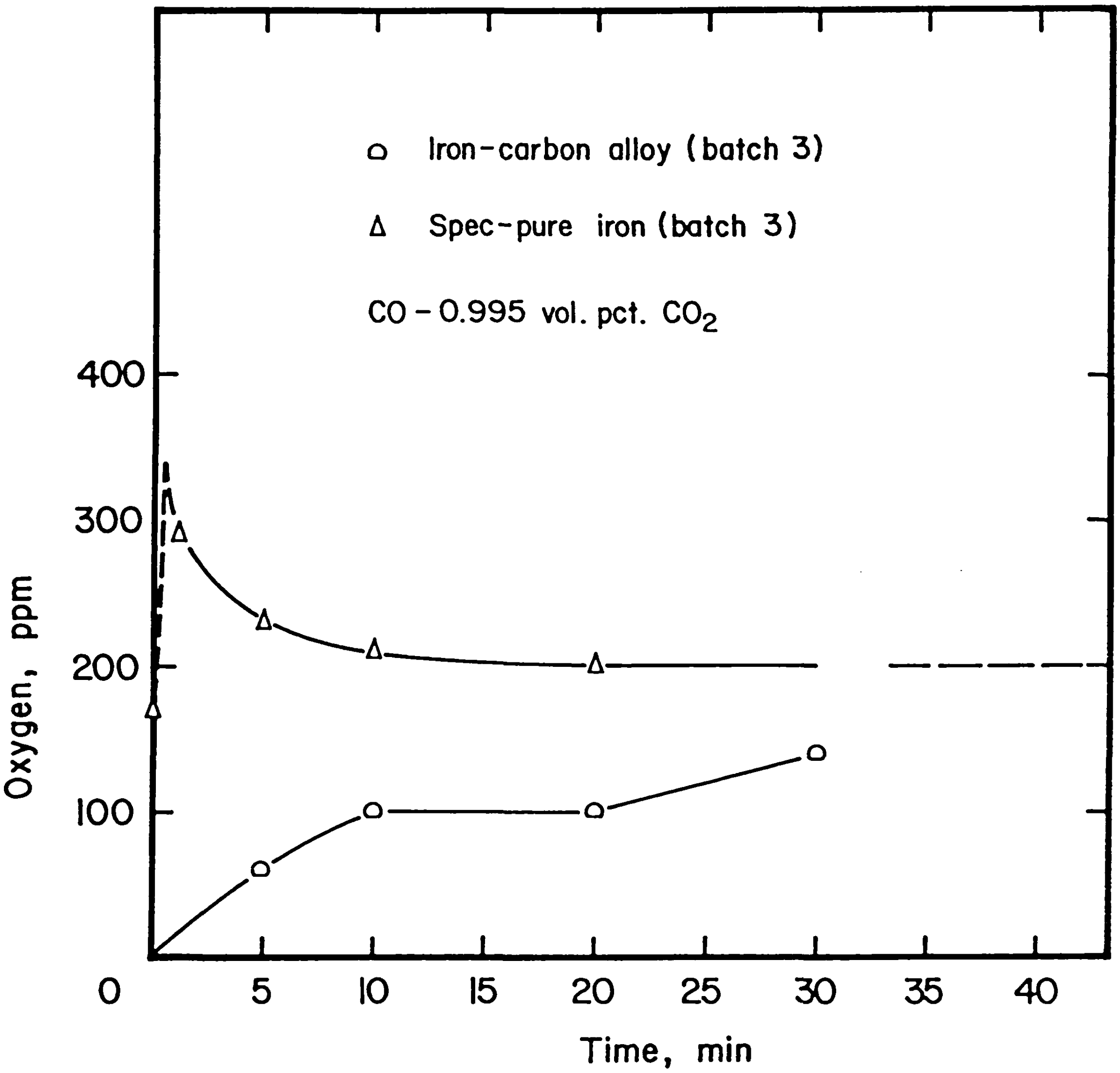

FIGURE 4.11. Oxygen concentration as a function of time during carburization of spec-pure iron and decarburization of iron-carbon alloy with CO - 0.995 vol. pct. CO_2 at 40.48 atm and 1650 °C.

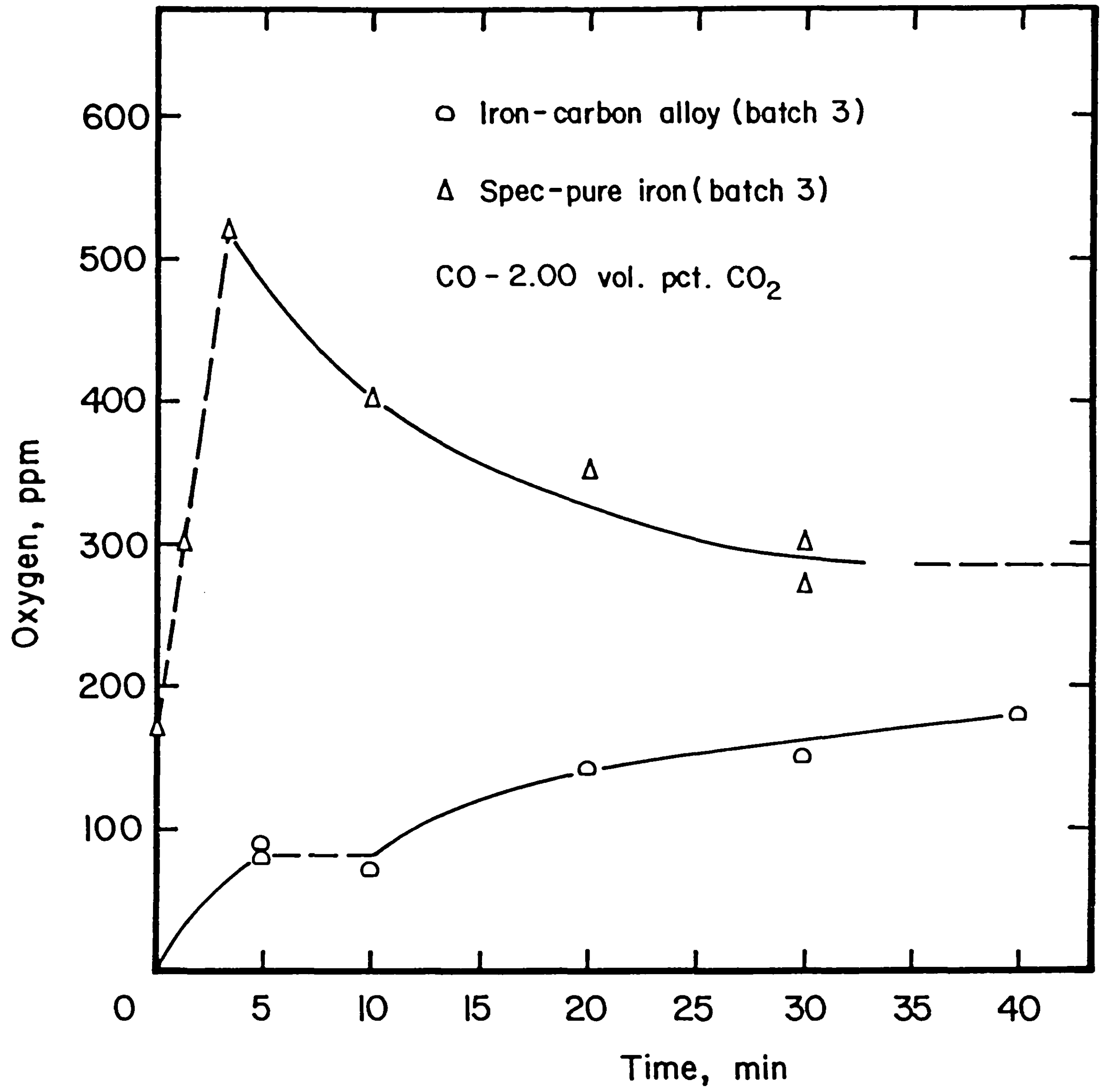

FIGURE 4.12. Oxygen concentration as a function of time during carburization of spec-pure iron and decarburization of iron-carbon alloy with CO - 2.00 vol. pct. CO_2 at 40.48 atm and 1650 °C.

3 Decarburization with CO-2.00 vol. pct. CO_2 gas mixture

The results of decarburization of different starting materials with 2.05 vol. pct. CO_2 at 40.48 atm and 1650°C are presented in Figure 4.13.

Specimens of iron-carbon alloy from batch 1 containing 4.6 wt % C (section 2.10)were decarburized. The kinetic curves showed a small effect of the surface cleaning with H_2/Ar gas mixture on the rate of decarburization. The rate of decarburization was practically nil after 5 minutes of reaction. Decarburization started again after 20 minutes and the rate decreased continuously.

An iron-carbon alloy was prepared by carburizing spec-pure iron specimens from batch 3 with 0.995 vol. pct. CO_2 at 80 atm and 1550°C. The kinetic curve obtained by using this alloy was very similar to that with iron-carbon alloy from batch 1, however the final carbon concentration was lower.

A mass of 15 mg of a pre-melted mixture of 10% Al_2O_3, 50% CaO and 40% SiO_2 (m.pt.1360°C) was added to specimens of iron-carbon alloy from batch 3 with the purpose of collecting the impurity oxides in the liquid slag. The kinetic curve showed that the initial rate of decarburization was approximately the same as that without slag addition. There was a period of no decarburization (between 10 and 30 min), this behaviour was similar to that found with specimens cut from the iron-carbon alloy (batch 1) and with spec-pure iron-carbon specimens. When the slag was used no oxide islets were observed on the surface of the drop and the metal surface looked apparently clean. It was observed that the area covered by the slag increased with time presumably because of changes in surface energies as oxygen was absorbed. The behaviour of the slag during a run is presented in Plate 4.1. The bottom prism was used

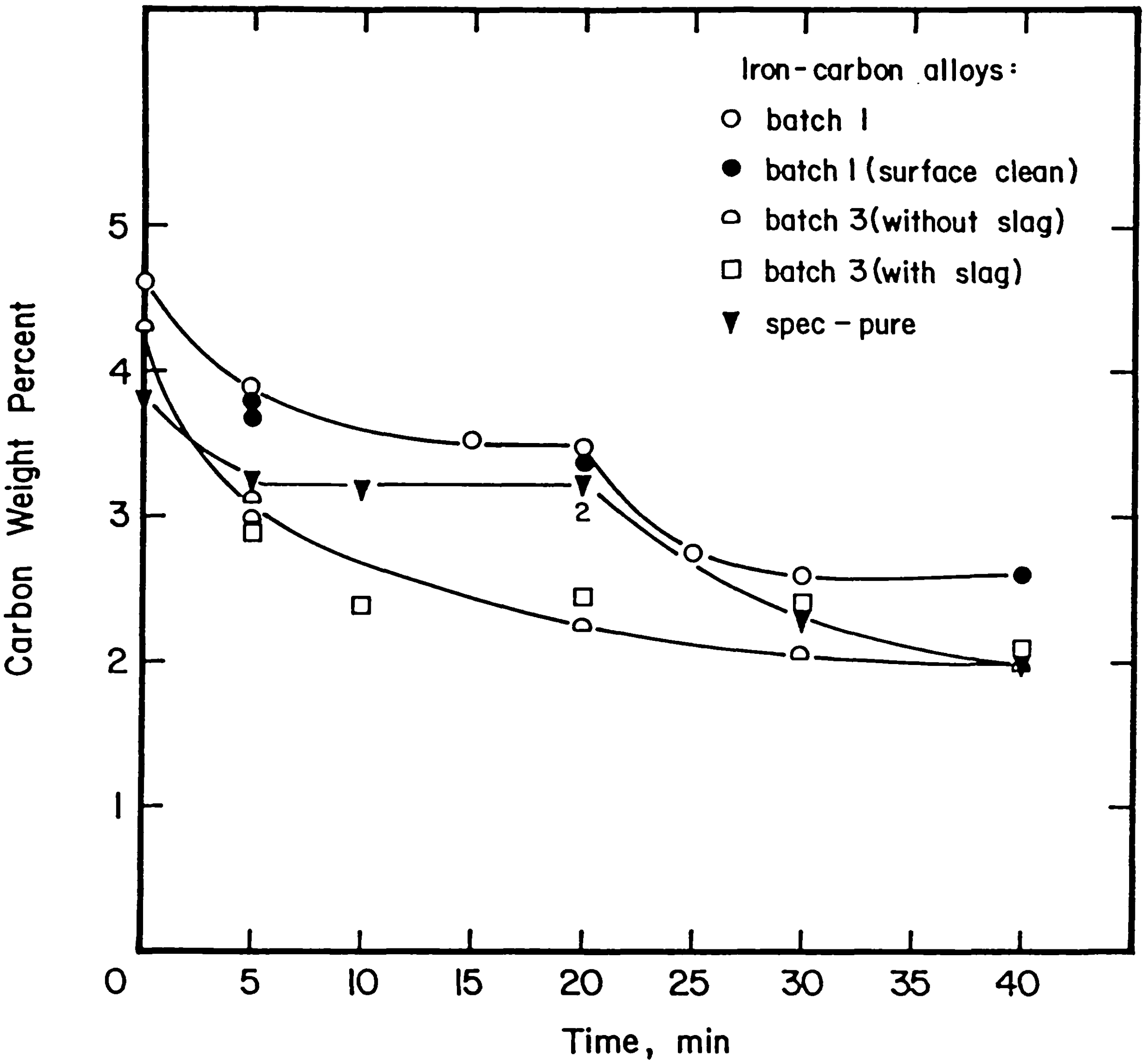

FIGURE 4.13. Decarburization of iron-carbon alloys with CO - 2.05 vol. pct. CO_2 at 40.48 atm and 1650 °C.

DESCRIPTION OF PLATE NO. 4.1

PICTURE NO.	TIME (Min)
1	9
2	10
3	17
4	18
5	19
6	20
7	21
8	22
9	24
10	28
11	29

TOTAL PRESSURE: 40.40 atm

MELT TEMPERATURE: 1650°C

SLAG COMPOSITION: 10 wt % Al_2O_3, 50% CaO, 40% SiO_2

SLAG MASS: 0.0151g

GAS COMPOSITION: 2.00 vol. pct. CO_2

RUN EFCO 154

PLATE No. 4.1

DECARBURIZATION OF IRON-CARBON ALLOY (BATCH 3) CONTAINING SLAG WITH A CO/CO_2 GAS MIXTURE

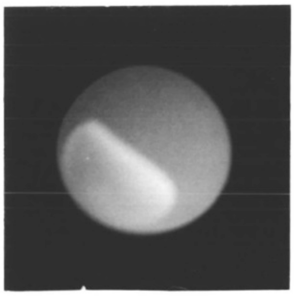

1

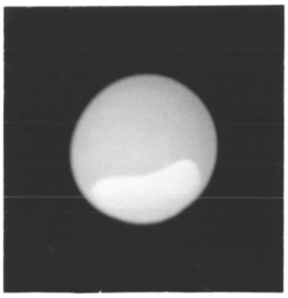

2

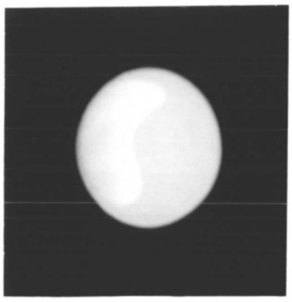

3

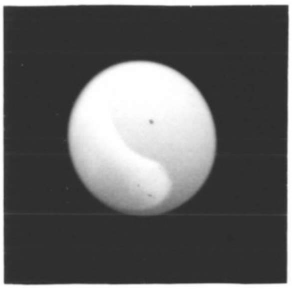

4

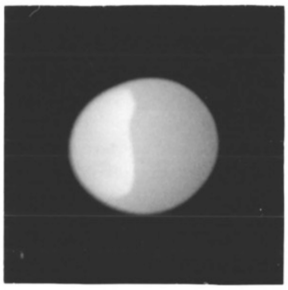

5

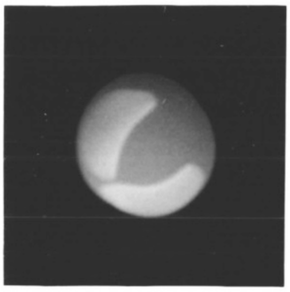

6

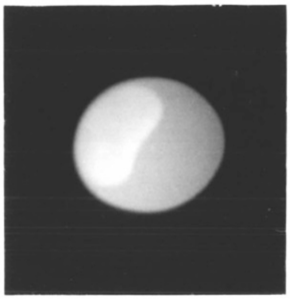

7

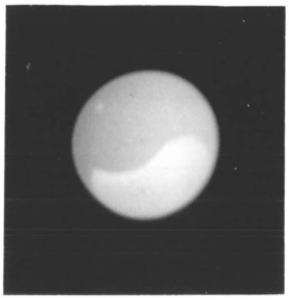

8

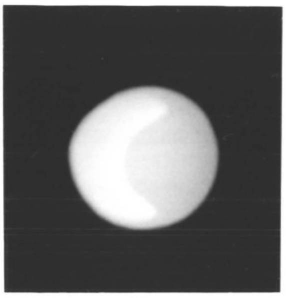

9

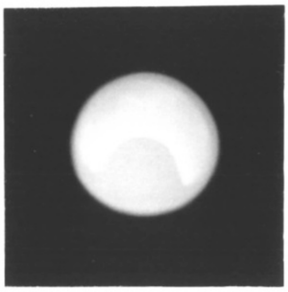

10

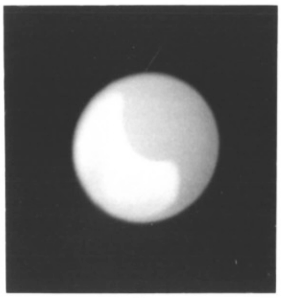

11

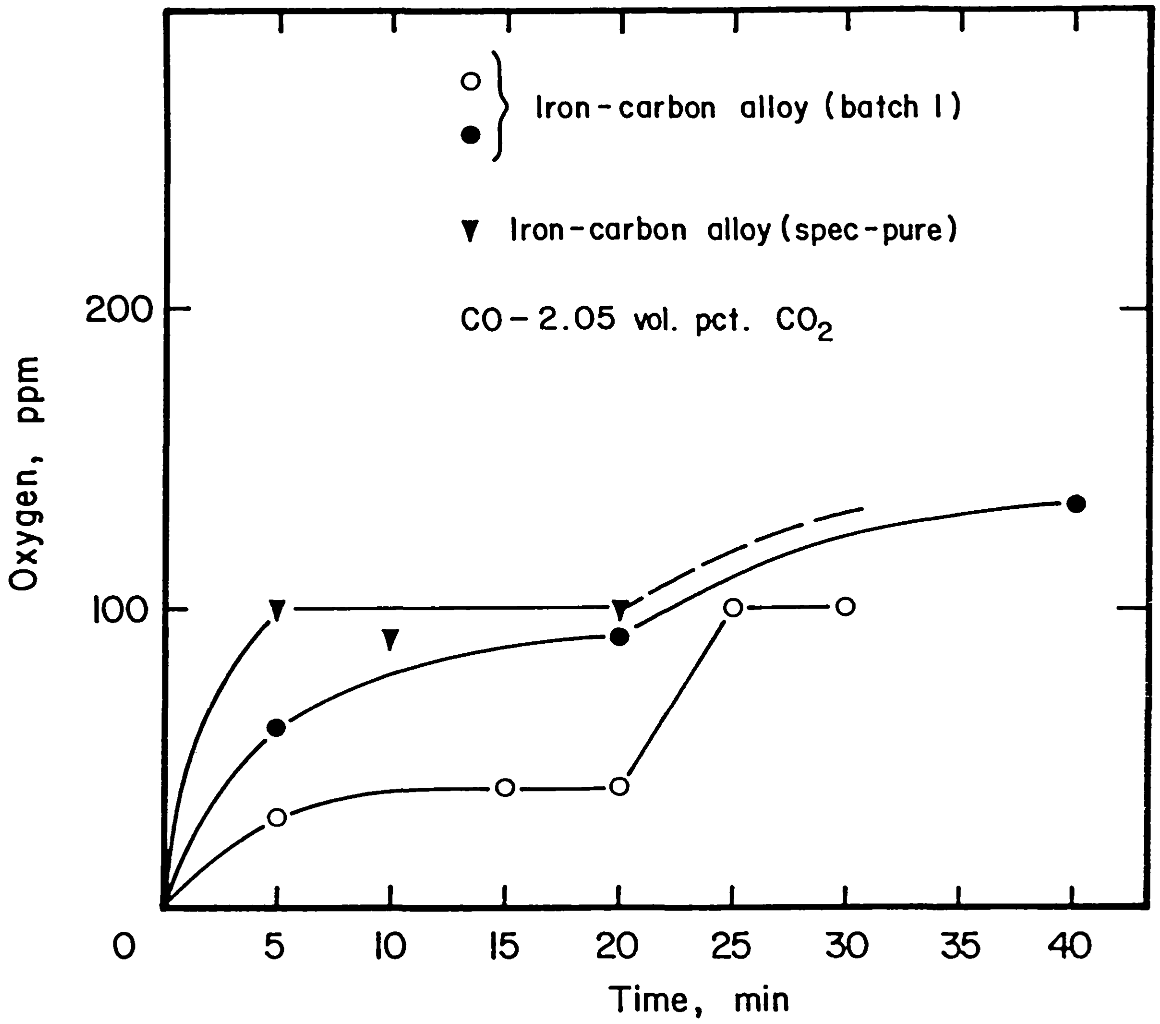

FIGURE 4.14. Oxygen concentration as a function of time during decarburization of iron-carbon alloys with CO - 2.05 vol. pct. CO_2 gas mixture at 40.48 atm and 1650 °C. Closed circles show the effect of surface cleaning with H_2/Ar gas mixture.

to photograph the events as more details of the slag movement could be observed since the slag hung on to the lower part of the drop.

Figure 4.14 shows the results of oxygen concentration as a function of time during decarburization of iron-carbon specimens. The oxygen concentration was higher when the drops were cleaned with a H_2/Ar gas mixture before the starting of the decarburization. The oxygen concentration in iron-carbon specimens prepared by carburizing spec-pure iron increased to 100 ppm and remained constant.

4 Behaviour and analysis of the impurities observed in decarburization and carburization experiments

The islets of impurity formed at about 20 sec after the change over from H_2/Ar to CO/CO_2 gas mixture in decarburization and carburization experiments. This time was almost the same regardless of the CO_2 content in the gas mixture. Later analysis of these impurities showed that they were oxides. The presence of an oxide film together with the oxide islets could not be detected by the naked eye.

The first oxide islets were small and very bright. A greater number were observed to form at higher CO_2 content in the gas mixture. The islets moved rapidly on the surface of the droplet and their number decreased with time. Finally a small number of them was observed on the bottom of the droplet as the reaction approached equilibrium. The islets formed during decarburization of iron-carbon specimens (batch 3) with 2.05 vol. pct. CO_2 at 40.48 atm and 1650°C are shown in Plate 4.2. The islets observed during carburization of spec-pure iron (batch 3) in 1.05 vol. pct. CO_2 at 80 atm and 1550°C are shown in Plate 4.3. The events were photographed from the lateral window of the HPLA.

PLATE No. 4.2

DECARBURIZATION OF IRON-CARBON ALLOY
(BATCH 3) WITH A CO/CO_2 GAS MIXTURE

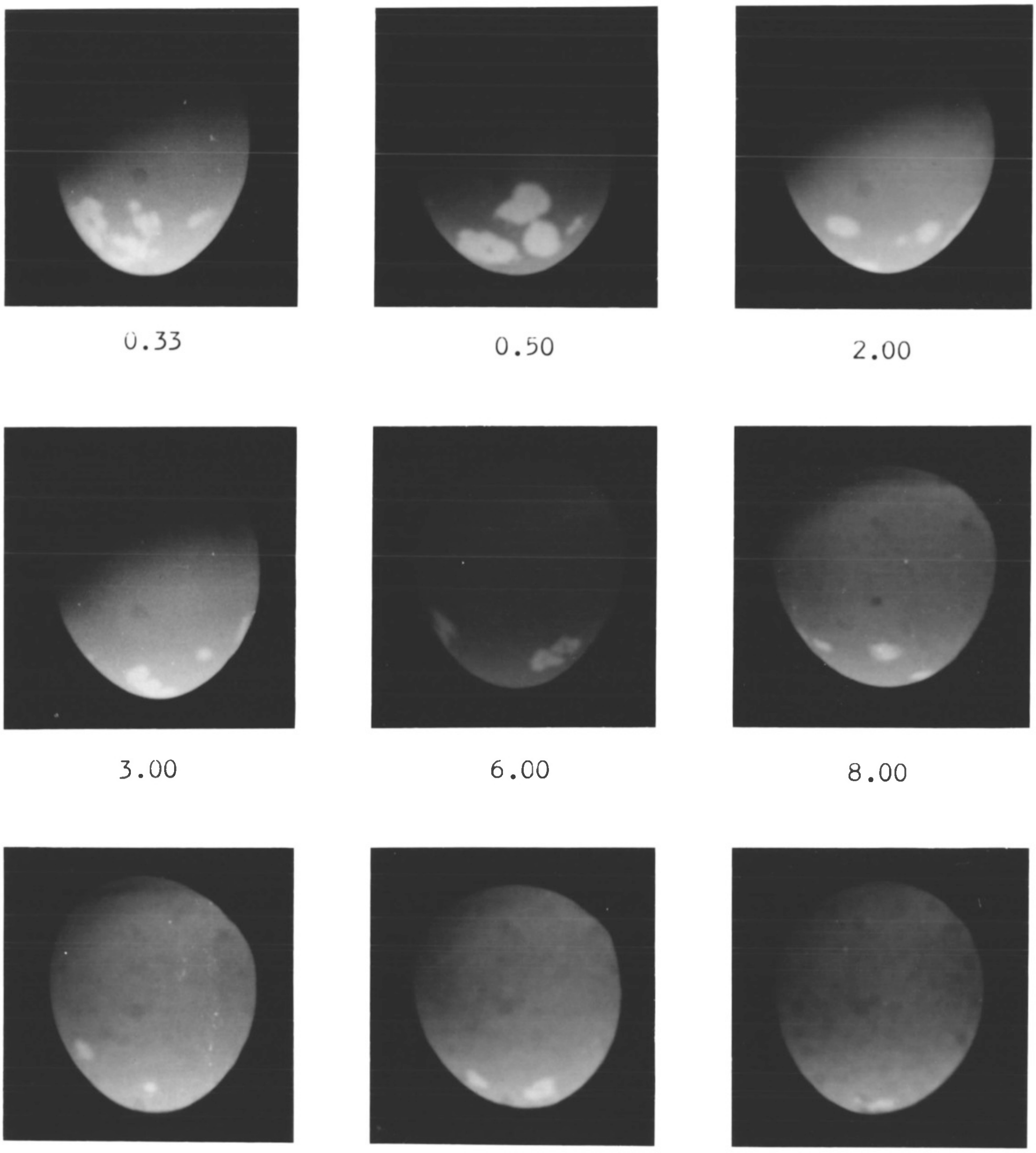

0.33 0.50 2.00

3.00 6.00 8.00

20.00 26.00 37.00

Gas composition: 2.05 vol. pct. CO_2
Pressure: 40.48 atm
Temperature: 1650°C

Time shown in min.

Run EFCO 108

PLATE NO. 4.3

CARBURIZATION OF SPEC-PURE IRON (BATCH 3) WITH A CO/CO_2 GAS MIXTURE

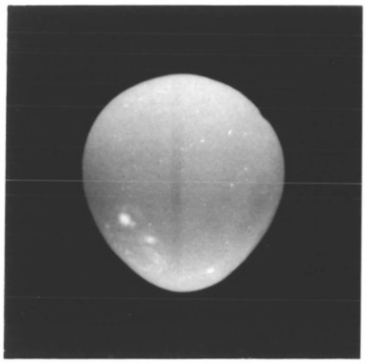

1

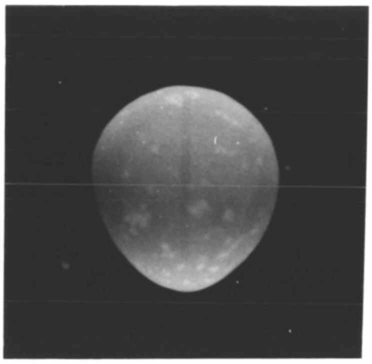

6

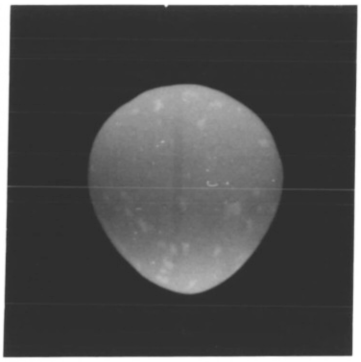

10

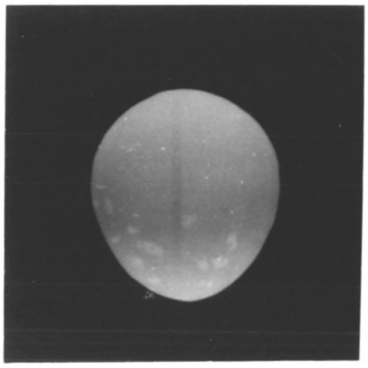

16

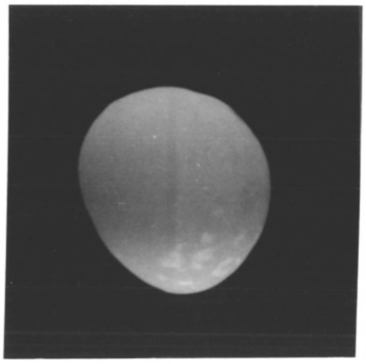

20

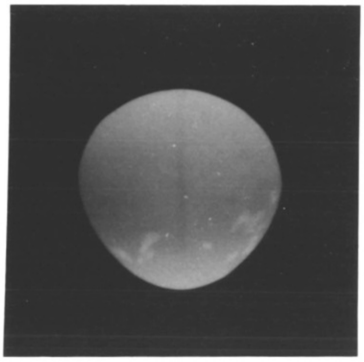

25

Gas composition: 1.05 vol. pct. CO_2
Pressure: 80 atm
Temperature: 1550°C

Time shown in min.

Run EFCO 117

In decarburization with 3.95 vol. pct. CO_2 a large number of islets were formed at the start of the reaction. In a later stage the islets coalesced and remained on the bottom of the drop. This transition occurred after 20 min of reaction, and it coincided with an increase of the rate of decarburization and an increase in temperature of 25°C (which was corrected by using the generator power control). The appearance of the oxide islets is presented in Plate 4.4. In run EFCO 97 the droplet was photographed through the lateral window whereas in run OXA 2 the photograph was taken by using the bottom prism.

The impurities formed a very thin black film on the bottom of the quenched specimens. These films were analysed by SIMS and LIMA.

SIMS analyses were carried out using a primary beam of ion oxygen (O_2^+), ion energy of 10.6 keV, ion density current of 0.2 $\mu A/cm^2$ and constant raster width. The secondary ions were analysed at constant energy filter, mass filter and secondary ion detection conditions. The analyses showed that the main impurities in the film were Al, Si and Ti. The elements Cr and Mg were also detected. Concentration profiles of all these elements in the oxide film were determined. In Figure 4.15 are presented typical results of the analyses of the film obtained in decarburization of the iron-carbon alloy (batch 2) specimens reacted for 30 min with CO-3.95 vol. pct. CO_2 at 1550°C. The concentrations are given as the ratio between the intensity of a positive ion and that of $^{56}Fe^+$. The depth into the specimen is given as the number of analysis cycles and was not measured. In Figure 4.16 are shown typical results of the analyses of spec-pure iron (batch 3) specimens carburized for 20 min in CO-3.95 vol. pct. CO_2 at 1550°C. The analyses of a spec-pure iron specimen reacted for only 2 min with CO-2.00 vol.

DESCRIPTION OF PLATE NO. 4.4

RUN EFCO 97

PICTURE NO.	TIME (Min)
1	2
2	6
3	28
4	30

TOTAL PRESSURE: 60.21 atm

MELT TEMPERATURE: 1550°C

IRON-CARBON ALLOY: BATCH 2

RUN OXA 2

TIME: 20 min

TOTAL PRESSURE: 35.54 atm

MELT TEMPERATURE: 1650°C

IRON-CARBON ALLOY: BATCH 1

PLATE No. 4.4

DECARBURIZATION OF IRON-CARBON ALLOYS WITH A CO/CO_2 GAS MIXTURE (3.95 vol. pct. CO_2)

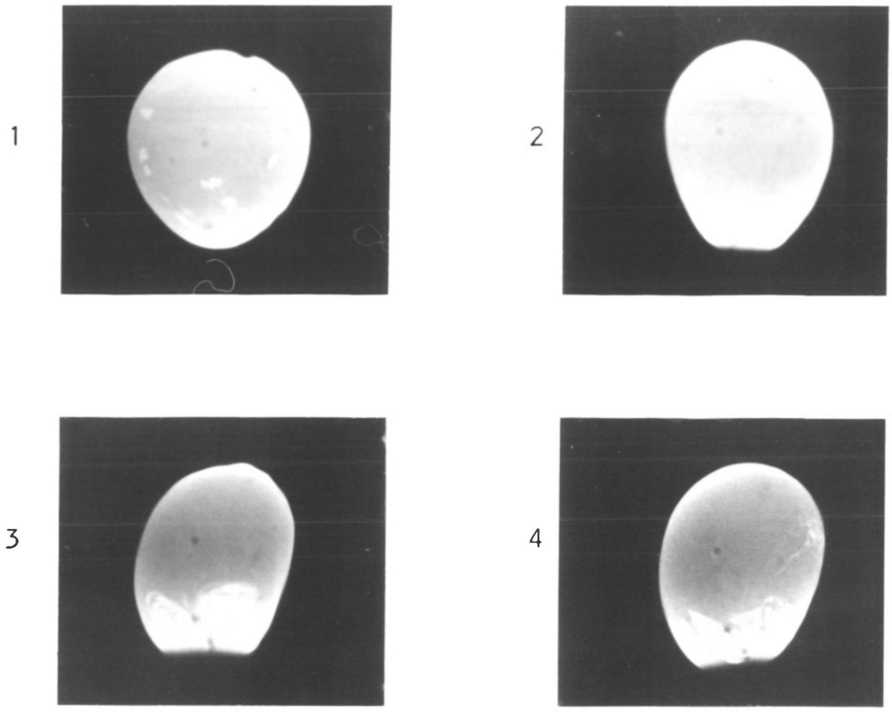

RUN EFCO 97

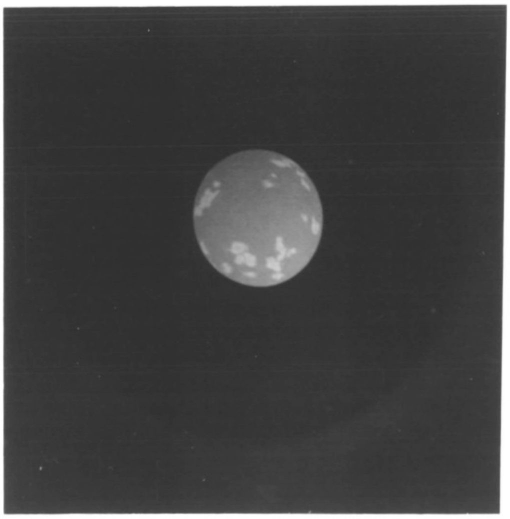

RUN OXA 2

pct. CO_2 gas mixture at 1650°C and quenched 'in situ' showed the presence of two phases. One of them was the slag observed by the naked eye due to its higher emissivity. The analysis of this phase showed profiles of concentration of Al, Mg, Ca, Si, Ti and Cr, the slag was very rich in Al, Mg, Ca and Si, all of them at concentrations (relative to $^{56}Fe^{+}$) in the outer part of the oxide film of the order of 10^{-1}. The other phase (identified in the clean area of the droplet) consisted of a Si and Ti rich oxide film. The apparent concentrations of Si and Ti in the outer part of the oxide film (relative to $^{56}Fe^{+}$) were 0.51 and 0.35 respectively. The analysis of a sample of the original spec-pure iron (batch 3) previously polished and cleaned showed a homogeneous material whose composition (relative to $^{56}Fe^{+}$) was as follows:

Mg	Al	Ca	Si	Ti	Cr	Fe
1.9×10^{-5}	7.3×10^{-4}	5.2×10^{-5}	3.3×10^{-5}	6.0×10^{-6}	1.3×10^{-5}	1

The analyses obtained by SIMS within a simple area were reproducible. The results, even though qualitative, showed the relative concentration of each impurity in the oxide film and in the bulk of metal. According to Figs 4.15 and 4.16 the bulk concentrations of silicon, chromium and magnesium were quite similar in the iron-carbon alloy and in the spec-pure iron. The bulk concentrations of aluminium and titanium were lower in the spec-pure iron.

LIMA analyses of specially prepared samples allowed the qualitative determination of the impurities in iron-carbon and spec-pure iron specimens. In Figure 4.17 are shown the results of the analyses of the surface of spec-pure iron specimens. Fig 4.17 (a) is the spectrum of positive ions obtained with the first pulse at low laser power on a small area of a specimen levitated in H_2/Ar

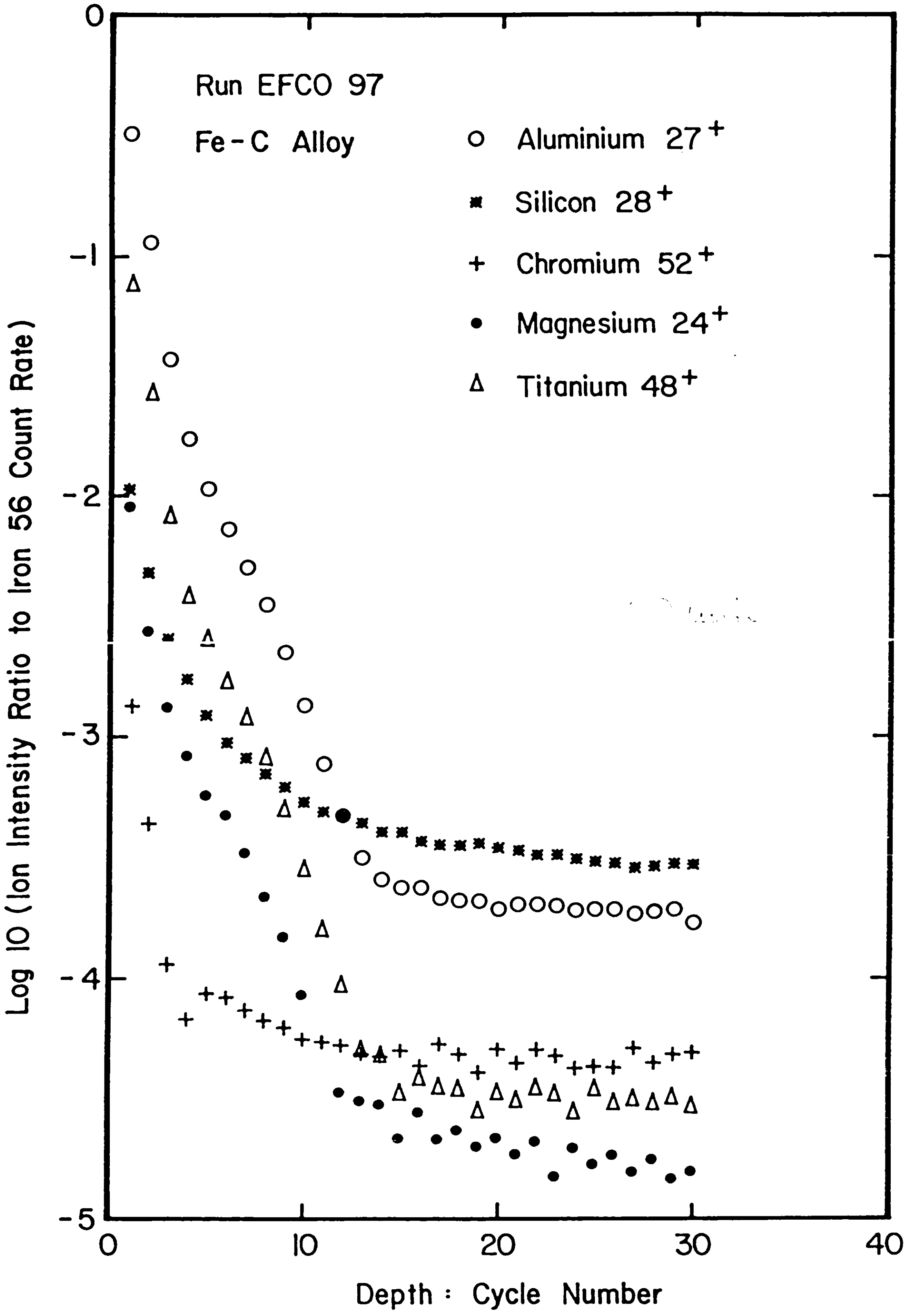

FIGURE 4.15. SIMS analysis of iron-carbon alloy (batch 2) equilibrated with CO - 3.95 vol. pct. CO_2 gas mixture at 60 atm and 1550 °C.

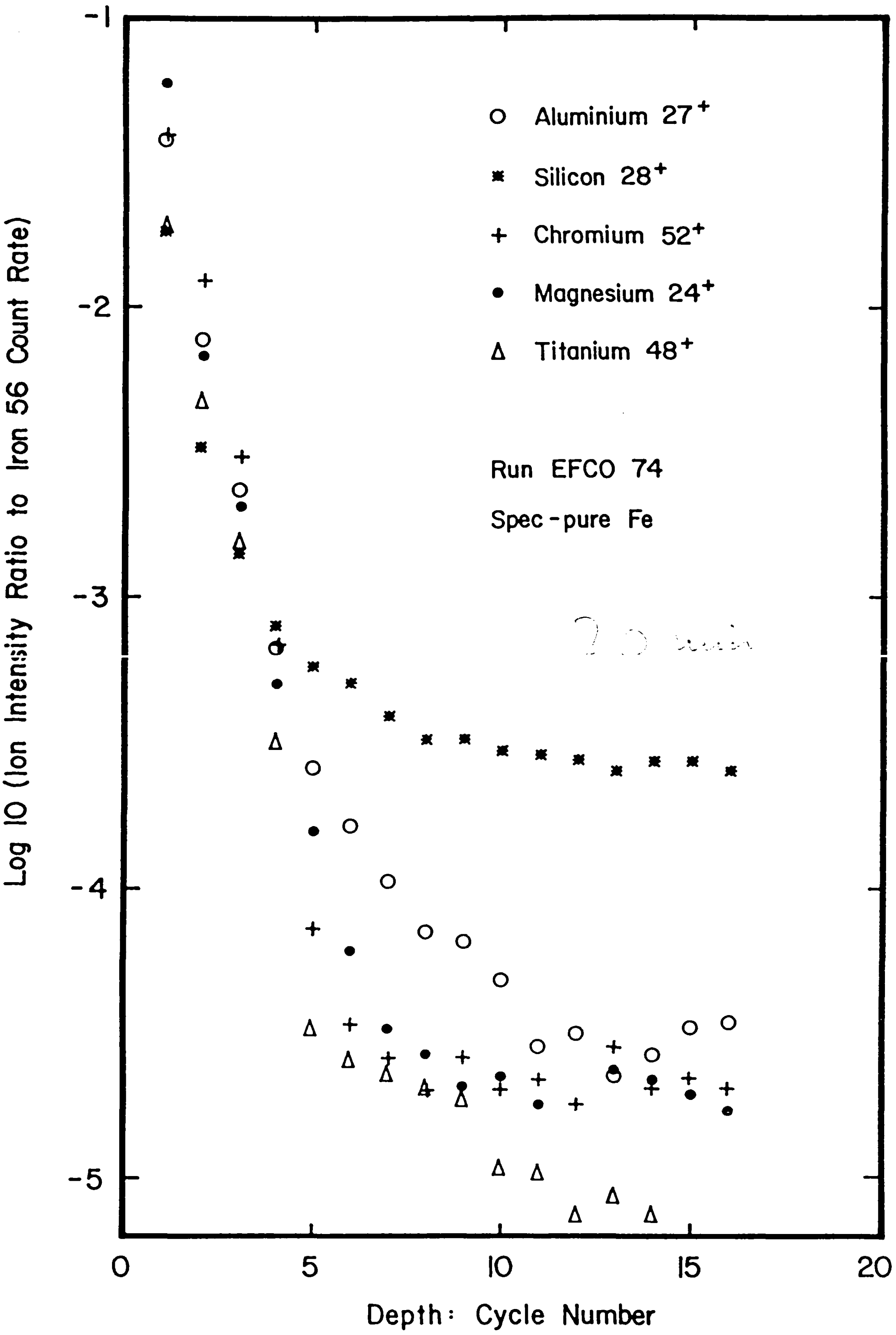

FIGURE 4.16. SIMS analysis of spec-pure iron (batch 3) equilibrated with CO - 3.95 vol. pct. CO_2 at 65 atm and 1550 °C.

at 1750°C for 10 min and quenched 'in situ' by changing the gas to helium and increasing the pressure. The area analysed was the one where an oxide phase (of blue colour) was observed, most of the surface drop was completely clean. Aluminium and calcium were the main constituents of the impurity oxides identified in this zone. Fig 4.17 (b) is the spectrum obtained with the first pulse at high laser power on the oxide islets (slag spots) formed on a spec-pure iron specimen reacted for 30 min with CO-2.00 vol. pct. CO_2 gas mixture at 1650°C. This specimen was quenched 'in situ'. The analyses revealed the presence of aluminium, calcium and titanium. Fig 4.17 (c) shows the spectrum obtained with the twelfth pulse at low laser power on the clean surface of the same carburized specimen. The analysis showed calcium and magnesium only. In Figure 4.18 are shown the analyses of an iron-carbon specimen (from batch 1) reacted for 28 min with CO-3.95 vol. pct. CO_2 gas mixture at 1650°C (sample OXA 2, see Plate 4.4). The spectra of positive ions were obtained at low laser power and with the first, third and twelfth laser pulses in the same area of analysis. Calcium decreased with the increase of depth, after twelve pulses the bulk of metal was reached. Analysis of another area of sample OXA 2 showed the presence of silicon, aluminium and magnesium, these elements were analysed after the first pulse at low laser power. In general the reproducibility of analysis with LIMA was not good.

The original slag added to iron-carbon specimens (10 wt % Al_2O_3, 50% CaO and 40% SiO_2) and the reacted slag after decarburization were mounted together in resin so EPMA could be done under exactly the same conditions. The results of these analyses are reported in Table 4.4. The analyses showed that Cr and Ti were present in the reacted slag but not in the original slag.

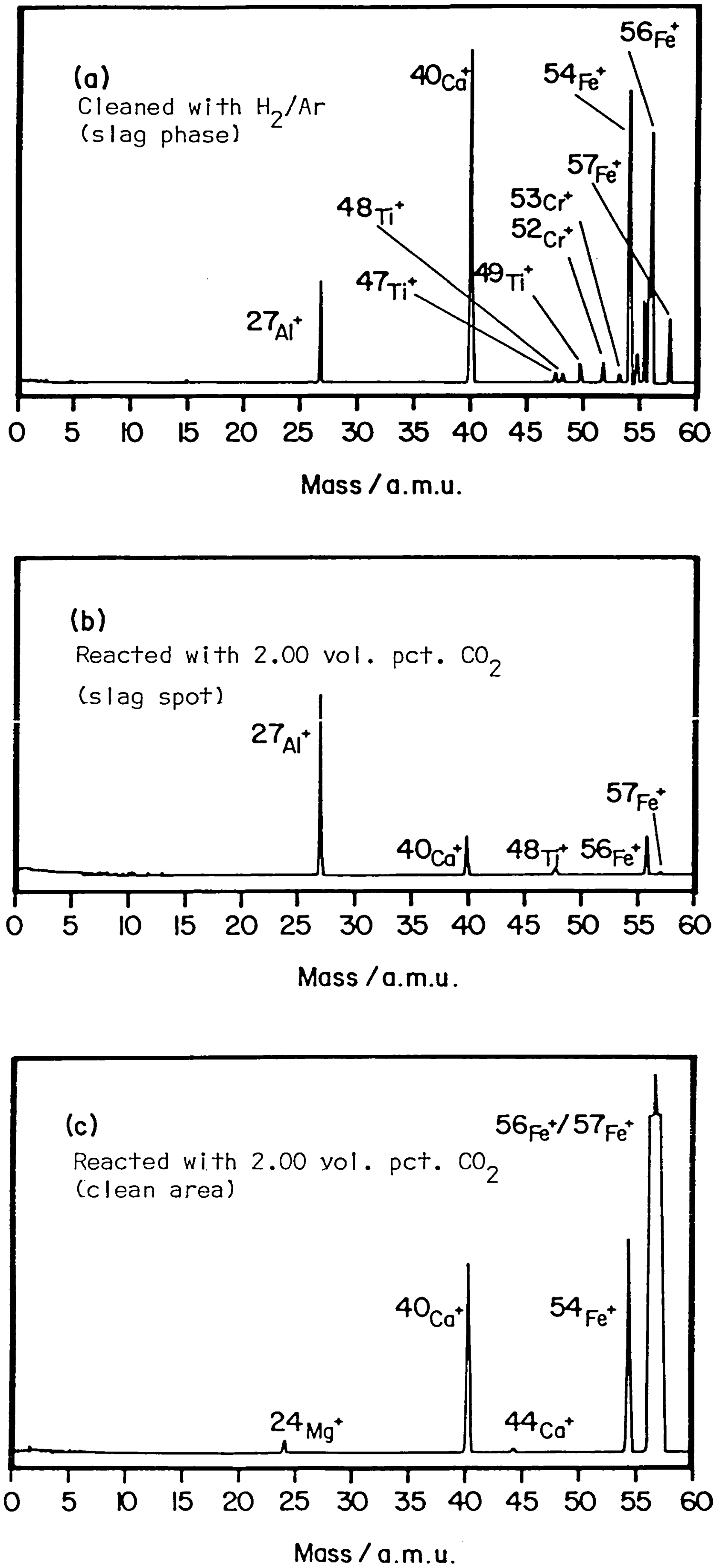

FIGURE 4.17. LIMA analyses of spec-pure iron samples.

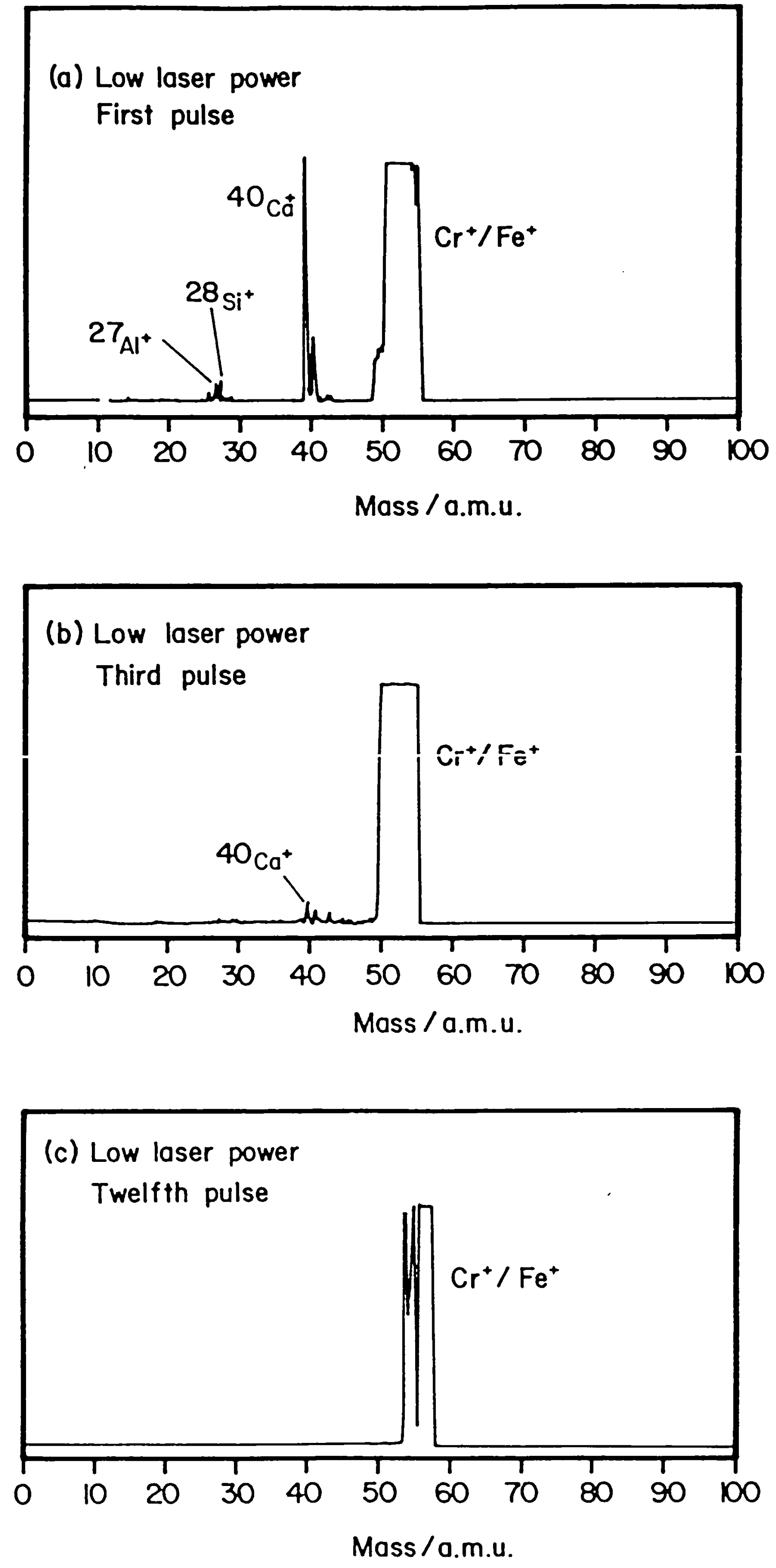

FIGURE 4.18. LIMA analyses of an iron-carbon alloy reacted with CO - 3.95 vol. pct. CO_2 at 1650 °C. Sample OXA 2.

Chemical analyses of carburized specimens were carried out to estimate the amount of oxygen present in the film of impurities. Spec-pure iron specimens, equilibrated with 3.95 vol. pct. CO_2 at 1550°C and high pressure, were cut in half. One of the parts was cleaned by filing off the film and both parts were analyzed for oxygen. The results of these analyses are shown in Table 4.5. The results indicated that the cleaned specimen contained about 10 ppm less of oxygen.

Table 4.4: Slag analysis

		ORIGINAL SLAG		REACTED SLAG	
ELM	OXIDE	ELM wt %	OXIDE wt %*	ELM wt %	OXIDE wt %*
Al	Al_2O_3	4.905	10.529	5.390	10.830
Si	SiO_2	17.291	42.019	18.731	42.607
Ca	CaO	29.804	47.373	28.916	43.022
Fe	FeO	.054	.078	2.342	3.204
Cr	Cr_2O_3	.000	.000	.035	.071
Ti	TiO_2	.000	.000	.150	.266
Co	CoO	.000	.000	.000	.000
Mn	MnO	.000	.000	.000	.000
O		35.975		38.479	

* Normalized

Table 4.5: Oxygen analysis of carburized spec-pure iron with and without cleaning of the surface

Run number	Oxygen wt % Cleaned	Oxygen wt % Uncleaned
78	0.018	0.019
81	0.018	0.019
87	0.019	0.021

4.3.5 Evaluation of results

1 Decarburization and carburization

The reactions between carbon dissolved in molten iron and CO/CO_2 gas mixtures can be represented by the equation:

$$CO_{2(g)} + \underline{C} \text{ (in iron)} \rightleftharpoons 2CO(g) \qquad (4.52)$$

In section 4.3.1 it was shown that there are various possibilities of rate determining steps of the overall reaction depending on the experimental conditions. El-Kaddah and Robertson[71] demonstrated that the decarburization of molten iron at high carbon concentrations (> 1 wt % C) with CO/CO_2 gas mixtures at high total pressures was controlled by gas phase mass transfer. These authors (using the same experimental technique) found that the carburization of molten iron was controlled by transport in the liquid and gas phases. The surface chemical reaction was not controlling because the high total pressures (39-40 atm) implied high partial pressures of CO_2 despite the dilute CO_2 in CO gas mixtures used (1.1-2.15 vol. pct. CO_2). Control of the reaction rate by mass transfer in the liquid was ruled out because the rates would be very much faster than those observed. Therefore, the model developed by El-Kaddah and Robertson[70] was used to calculate the rates of carburization and decarburization in the present work because the same arguments can be applied in this case.

In the following paragraphs the mixed transport model is briefly presented. The reaction 4.52 was considered at quasi-steady state condition and the following assumptions were used:

i) Instantaneous chemical reaction, that is, equilibrium between the gas and carbon at the interface.

ii) The liquid and gas mass transfer coefficients were the same at all points on the interface.

iii) The ratio k_g/k_l remains constant during the reaction.

The molar flux of CO_2 relative to stationary coordinates in the binary CO-CO_2 is given by the equation:[61]

$$N_{CO_2} = -C_T D[(\partial x_{CO_2}/\partial r) + K_T(\partial \ln T/\partial r)] + x_{CO_2}(N_{CO_2} + N_{CO}) \qquad (4.53)$$

where the first term on the right hand side represents the molar flux resulting from the concentration gradient which includes the contribution due to thermal diffusion. The second term represents the molar flux resulting from the bulk flow. In equation 4.53 C_T is the total molar concentration, D is the diffusivity for the binary CO-CO_2, x_{CO_2} is the mole fraction of CO_2, K_T is the thermal diffusion ratio (section 4.2.3), r is the position coordinate in the gas boundary layer, T is the absolute temperature, N_{CO_2} and N_{CO} are the molar fluxes of CO_2 and CO respectively.

Integration of equation 4.53 gives:

$$N_{CO_2} - x_{CO_2s}(N_{CO_2} + N_{CO}) = k_g(x'_{CO_2b} - x_{CO_2s}) \qquad (4.54)$$

where $k_g = C_T D/\delta$ is the average gas phase mass transfer coefficient, δ the thickness of the gas boundary layer and x'_{CO_2b} is the modified gas bulk composition defined by the equation:

$$x'_{CO_2b} = x_{CO_2b} + \Delta x_{CO_2} \qquad (4.55)$$

and

$$\Delta x_{CO_2} = K_{T_f} \ln(T_s/T_b)$$

where K_{T_f} is the thermal diffusion ratio at mean temperature (section 4.2.3).

From the stoichiometric relation of the reaction 4.52 it follows that: $N_C = -N_{CO_2}$ and $N_{CO} = -2N_{CO_2}$.

From equation 4.54 is obtained:

$$N_{CO_2} = k_g(x'_{CO_2b} - x_{CO_2s})/(1 + x_{CO_2s}) \qquad (4.56)$$

The term $(1 + x_{CO_2s})$ represents the contribution of bulk flow. This term is approximately unity above 0.4 wt % C.

After the quasi-steady state assumption:

$$N = k_g(x'_{CO_2b} - x_{CO_2s}) = k'_l(\text{wt \% } C_b - \text{wt \% } C_s) \qquad (4.57)$$

where k'_l is the average liquid phase mass transfer coefficient, wt % C_b and wt % C_s are the concentrations of carbon in the bulk of liquid and at the interface.

The overall mass transfer coefficient in the gas phase ($\overline{k}_g$) can be defined by the equation:

$$N = \overline{k}_g(x'_{CO_2b} - x_{CO_2e}) \qquad (4.58)$$

where x_{CO_2e} is the equilibrium mole fraction of CO_2 which is related to the bulk carbon concentration.

Figure 4.19 shows schematically the relationship between different concentrations in the gas and liquid phases in the case of decarburization. Each point of the curve in Figure 4.19 shows the gas and liquid concentratios at equilibrium at a given temperature and pressure. The bulk liquid and gas compositions are defined by the point A. A line of slope $-(k_g/k'_l)$ drawn from A intersects the curve in the point S which defines the surface compositions in the liquid and gas phases.

The ratio $\bar{k}_g/k_g$ is defined as η_g:

$$\eta_g = \text{actual rate/rate if no liquid phase resistance} \qquad (4.59)$$

$$\eta_g = (x'_{CO_2b} - x_{CO_2s})/(x'_{CO_2b} - x_{CO_2e}) \qquad (4.60)$$

It can be shown that:

$$\eta_g = 1/1 - (k_g/k'_l)S \qquad (4.61)$$

where

$$S = (x_{CO_2e} - x_{CO_2s})/(\text{wt \% } C_b - \text{wt \% } C_s) \qquad (4.62)$$

The parameter η_g quantifies the importance of the liquid transport resistance when there is mixed transport control.

Decarburization

The rate of decarburization is given by the equation:

$$(dC/dt) = -(1200A/w)\bar{k}_g(x'_{CO_2b} - x_{CO_2e}) \qquad (4.63)$$

where A is the surface area of the drop, w is the mass of the drop and C is the carbon concentration in weight-per cent. At high carbon concentration $\eta_g = 1$ or $\bar{k}_g = k_g$. Carbon concentration as a function of time is obtained by numerical integration of the equation 4.63:

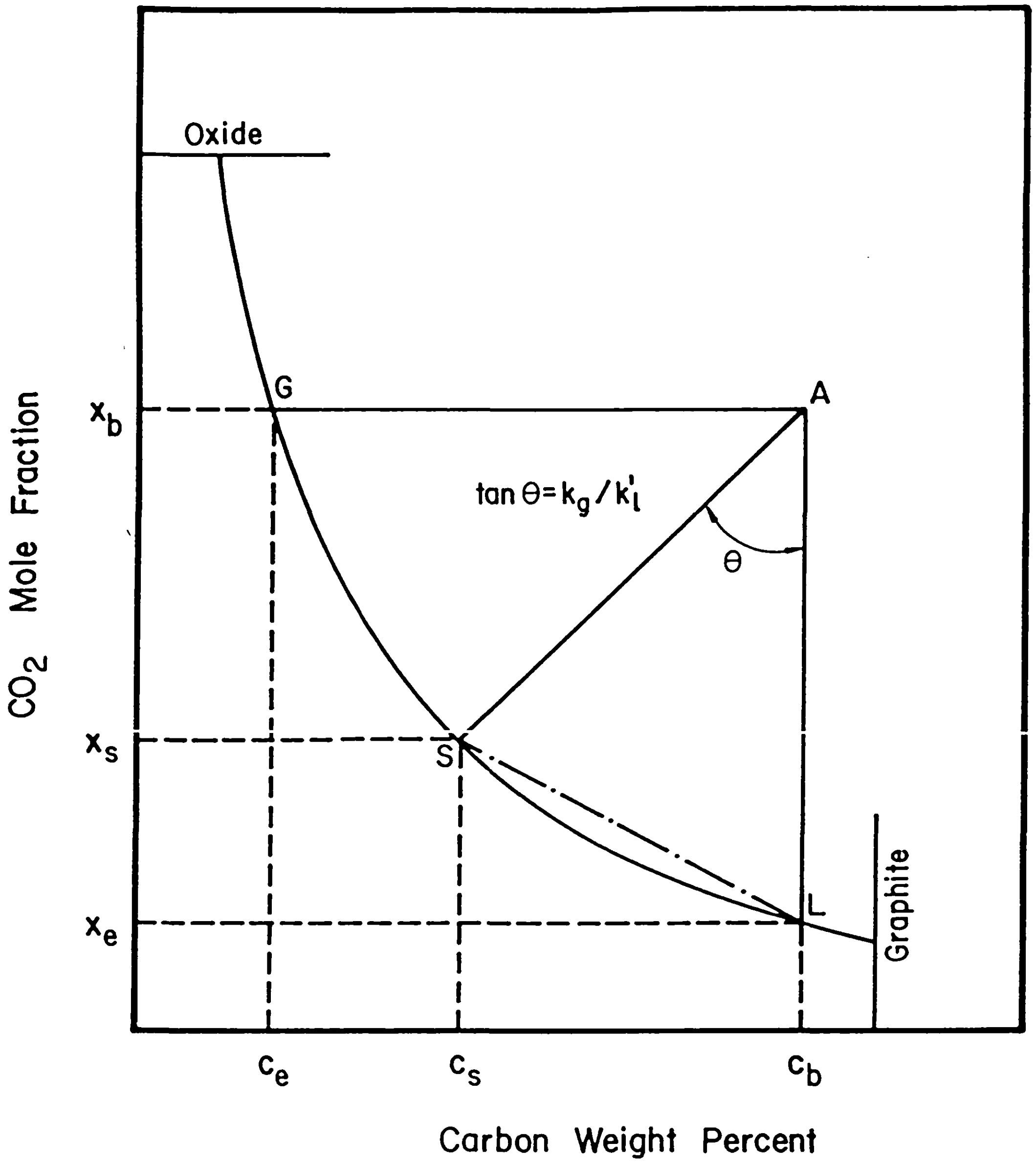

FIGURE 4.19. Relationships between gas and liquid concentrations during decarburization.

$$-\frac{w}{1200A}\int_{C=C_0}^{C=C}\frac{dC}{(x'_{CO_2b}-x_{CO_2e})} = k_g\int_0^t dt \qquad (4.64)$$

The equilibrium mole fraction of CO_2 is obtained from the equilibrium constant of reaction 4.1:

$$x_{CO_2e} = B - \sqrt{B^2 - 1} \qquad (4.65)$$

where

$$B = 1 + K_1 f_C C/2P_T \qquad (4.66)$$

The equilibrium constant K_1 was evaluated from the following equation obtained by El-Kaddah:[14]

$$\log K_{1(wt\ \%)} = -6836(\pm 187)/T + 6.37(\pm 0.097) \qquad (4.67)$$

The activity coefficient f_C was calculated from the results obtained in the present work.

The numerical integration was carried out using the routine DOIAHF (NAG FORTRAN Library). The results for decarburization with CO-3.95 vol. pct. CO_2 at 65.15 atm and 1550°C are shown in Figure 4.20. The experimental results were predicted at k_g of 1.4×10^{-4} (mole/cm² sec) at the start of decarburization and with a k_g of 5.7×10^{-5} (mole/cm² sec) when the reaction approached equilibrium. The value of k_g calculated using the correlation:[14]

$$Sh = 0.78\ (Gr\ Pr)^{0.25} \qquad (4.68)$$

was 6.7×10^{-4} (mole/cm² sec). The calculation is shown in Appendix 4.

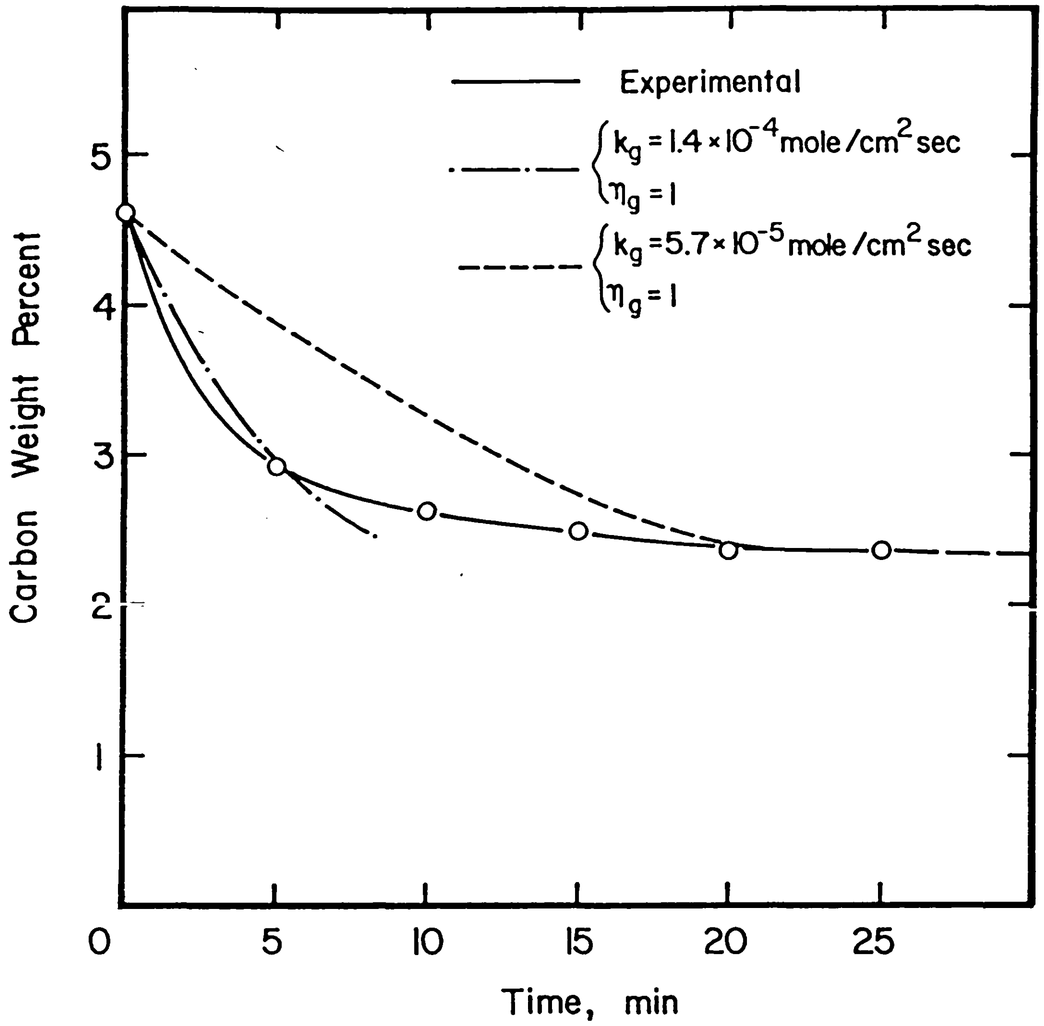

FIGURE 4.20. Superimposed experimental and predicted curves for the decarburization of iron-carbon alloy (batch I) with CO - 3.95 vol. pct. CO_2 at 65.15 atm and 1550°C.

Carburization

In carburization η_g is a continuous function of bulk carbon concentration as can be shown from equation 4.60. The mole fraction x_{CO_2e} can be calculated from equation 4.65. The values of x_{CO_2s} are obtained by solving equations 4.57 and 4.65 simultaneously.

The carbon concentration as a function of time can be obtained by solving the integral:

$$\int_0^C - \frac{W}{1200A} \times \frac{dC}{\eta_g (x'_{CO_2b} - x_{CO_2e})} = k_g \int_0^t dt \qquad (4.69)$$

The values of x_{CO_2e} and x_{CO_2s} were computed as a function of bulk carbon concentration to calculate η_g. Equations 4.57 and 4.65 were solved simultaneously by trial and error for each bulk carbon concentration. The term on the left hand side of equation 4.69 was integrated numerically using the Simpson's Rule.

The predicted results of carburization of molten iron with a CO-3.95 vol. pct. CO_2 gas mixture at 65.15 atm and 1550°C are given in Figure 4.21 assuming mixed transport control. The mass transfer coefficient in gas phase of 6.7×10^{-4} (mole/cm² sec) was used in the calculation along with different values of k'_l. The k'_l value of 1.8×10^{-4} (mole/cm² sec wt %) is the mass transfer coefficient for the transfer of carbon found by Distin et al[68] (k_l = 0.032 cm/sec). As the value of k'_l decreased the predicted rates were closer to the experimental rates. There were no measurements of carbon concentration at short times under the conditions of these calculations, however, from the results of carburization shown in Figs 4.24 and 4.25 the initial rate of carburization must be about 1 wt % C/min which is predicted with a k'_l of 1.8×10^{-5} (mole/cm² sec wt %).

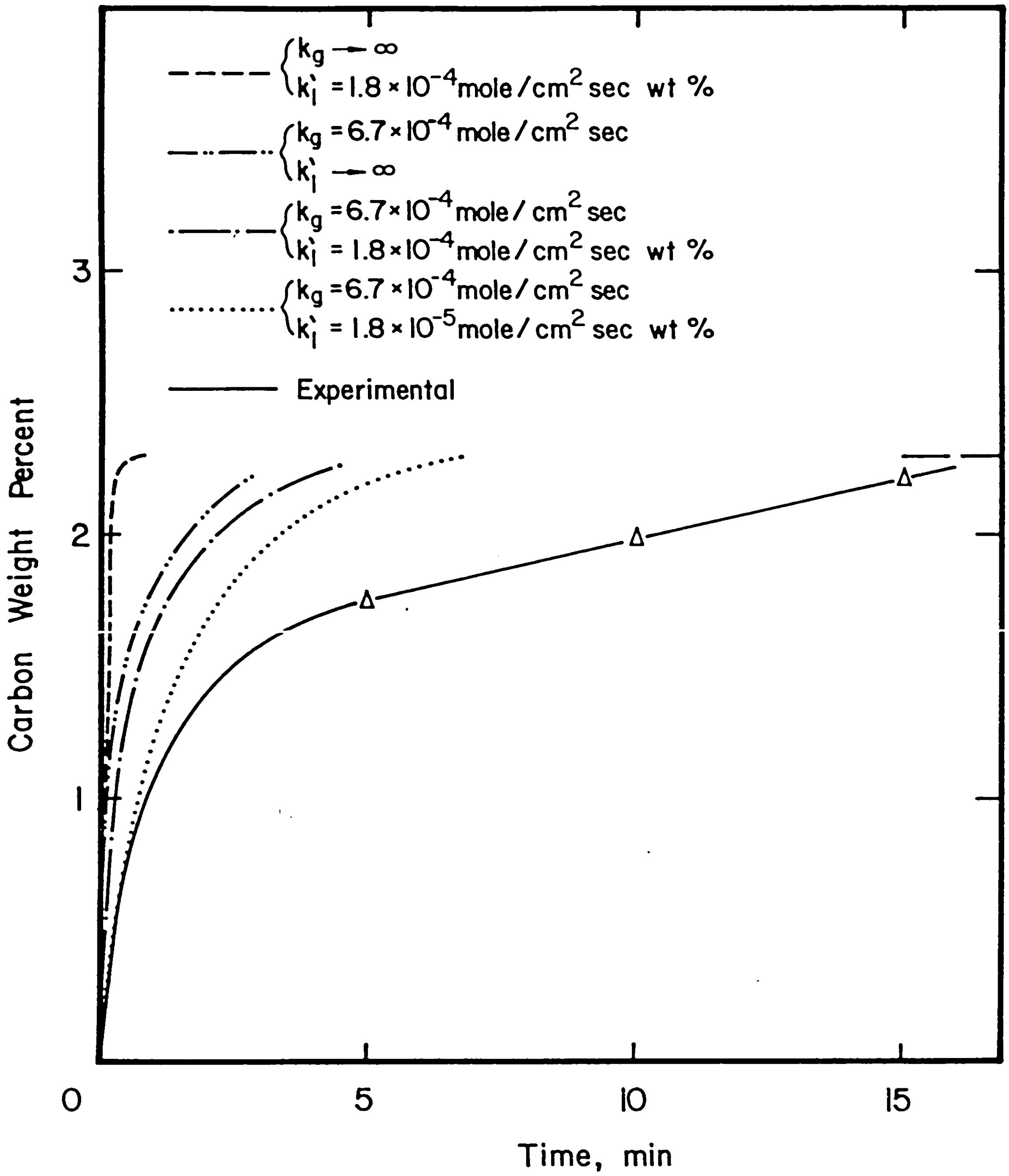

FIGURE 4.21. Superimposed experimental and predicted curves for the carburization of spec-pure iron (batch 3) with CO - 3.95 vol. pct. CO_2 at 65.15 atm and 1550 °C.

Figure 4.22 shows the variation of η_g with carbon concentration in molten iron at 1550°C in CO-3.95 vol. pct. CO_2 at different total pressures. At higher total pressures the importance of the liquid resistance as a step controlling the reaction rate increases. In this calculation the variation of k_g with total pressure was considered and a value of k'_l of 1.8×10^{-5} (mole/cm² sec wt %) was used. The equilibrium mole fraction of CO_2 as a function of carbon concentration at 65.15 atm and 1550°C is shown in Figure 4.23.

In Figs 4.24 and 4.25 are presented the theoretical results of carburization and decarburization at 40.48 atm and 1650°C with CO-0.995 vol. pct. CO_2 and CO-2.00 vol. pct. CO_2 respectively. The gas phase mass transfer coefficient calculated under these conditions using equation 4.68 was 5.3×10^{-4} (mole/cm² sec). The initial rates of decarburization with 0.995 vol. pct. CO_2 and 2.00 vol. pct. CO_2 were predicted with k_g values of 3.2×10^{-4} and 2.4×10^{-4} (mole/cm² sec) respectively. The initial rates of carburization in both cases were predicted with a k_g of 5.3×10^{-4} (mole/cm² sec) and a k'_l of 1.8×10^{-5} (mole/cm² sec wt %).

2 Oxygen and carbon concentration at the metal-liquid interface at the start of carburization

The results obtained during carburization of iron drops with CO/CO_2 gas mixtures showed a rapid oxygen absorption at the start of the reaction (Figs 4.11, 4.12 and 4.3). The mixed transport model applied to predict the results of carburization and decarburization in molten iron showed that x_{CO_2s} has values very much higher than x'_{CO_2b} at the start of carburization indicating that high oxygen concentration at the surface can be reached so the flux of oxygen into the drop can attain high values. However, this model

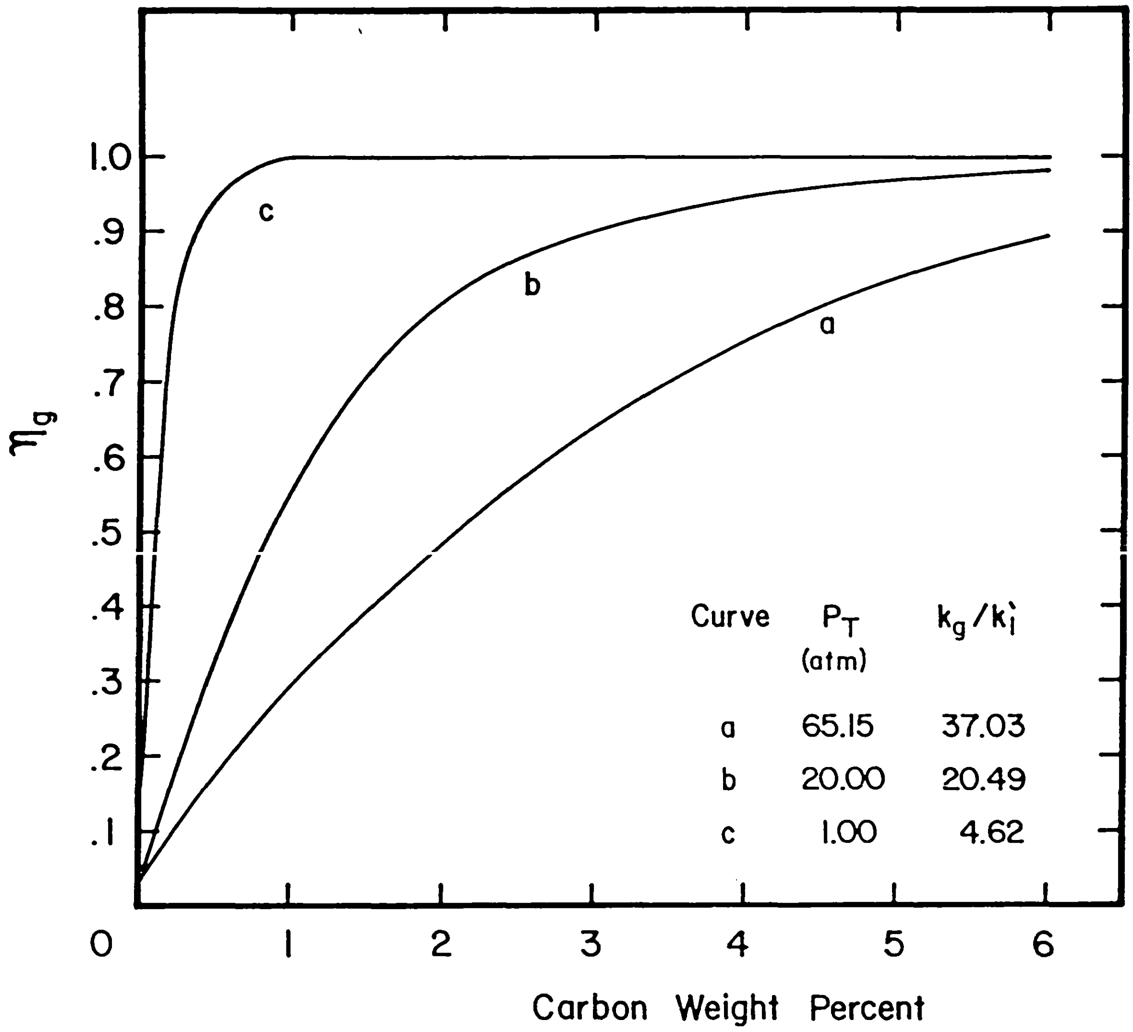

FIGURE 4.22. η_g as a function of carbon concentration during carburization and decarburization of molten iron with CO - 3.95 vol. pct. CO_2 at 65.15, 20.00 and 1.00 atm and at 1550 °C.
$k'_l = 1.82 \times 10^{-5}$ mole/cm^{2}sec wt%.

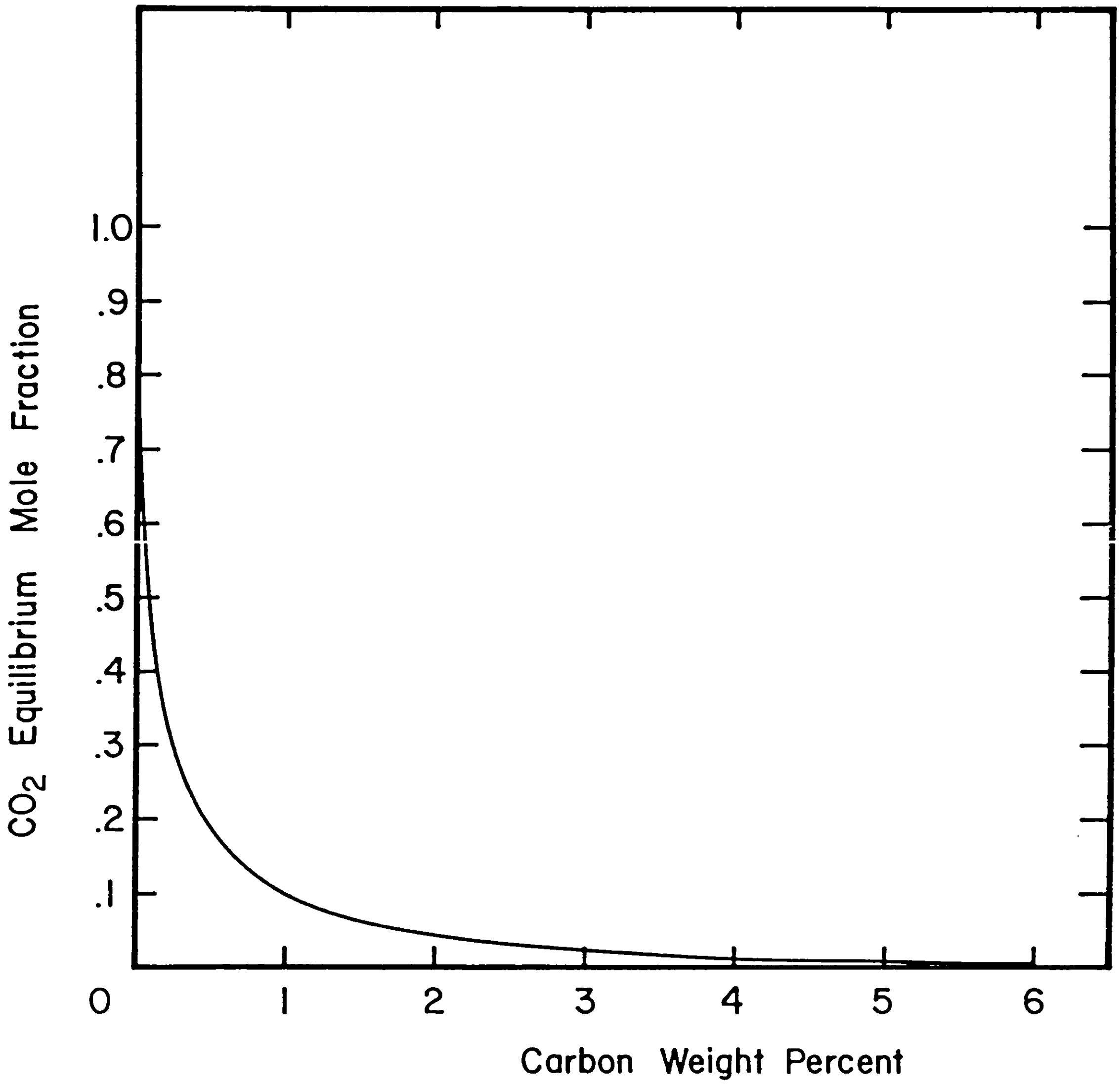

FIGURE 4.23. Equilibrium mole fraction of CO_2 as a function of carbon concentration. Temperature: 1550 °C. Total pressure: 65.15 atm.

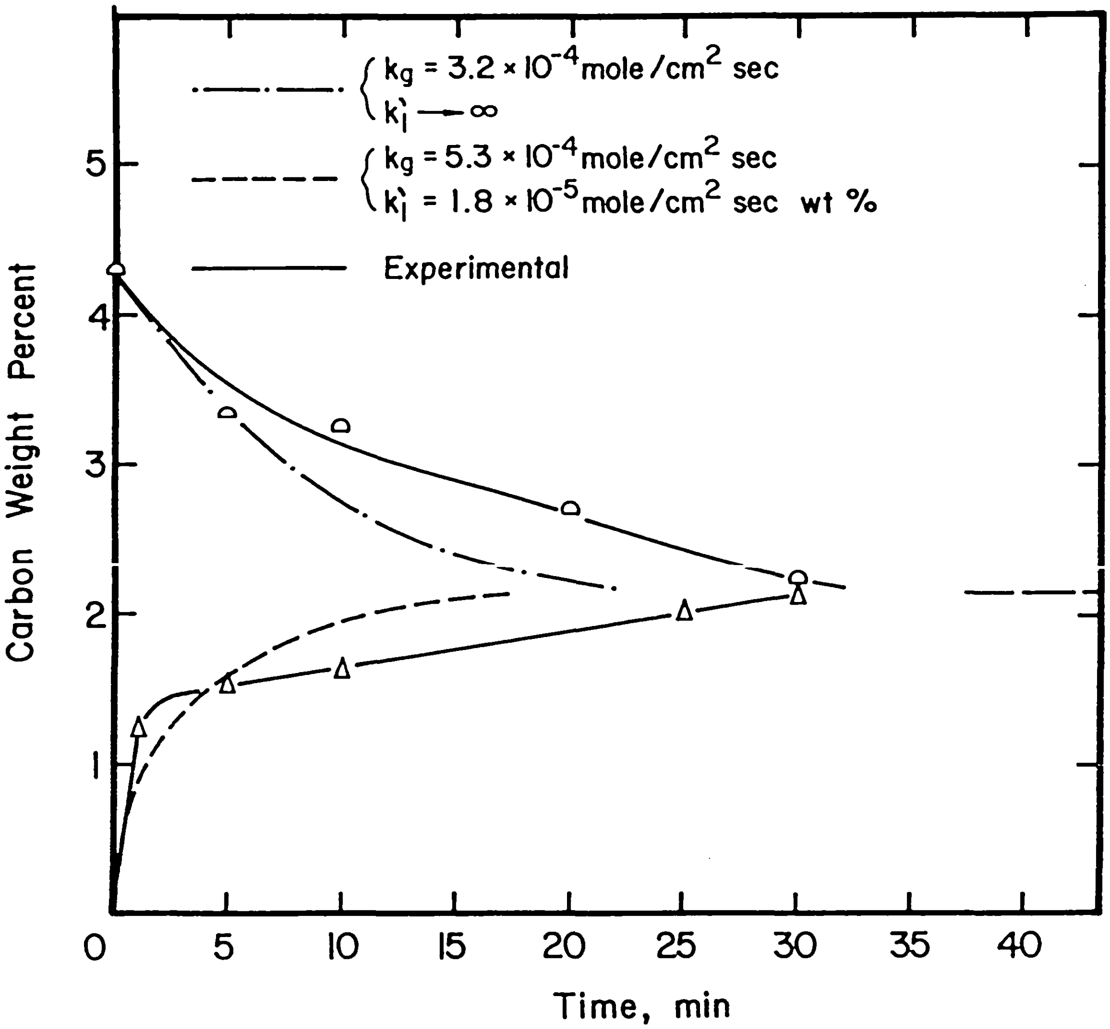

FIGURE 4.24. Superimposed experimental and predicted curves of decarburization of iron-carbon alloy (batch 3) and carburization of spec-pure iron (batch 3) with CO - 0.995 vol. pct. CO_2 at 40.48 atm and 1650 °C.

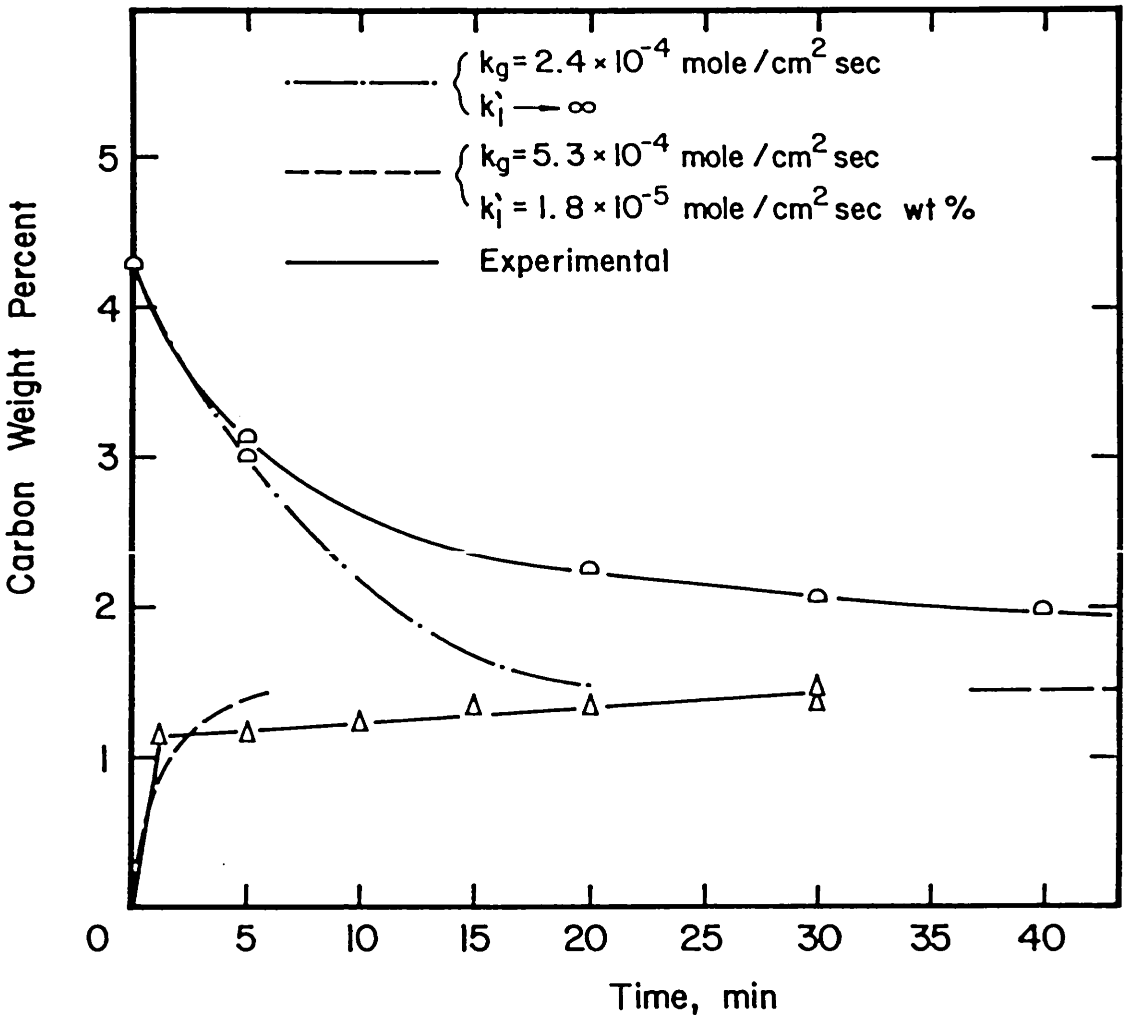

FIGURE 4.25. Superimposed experimental and predicted curves of decarburization of iron-carbon alloy (batch 3) and carburization of spec-pure iron (batch 3) with CO - 2.00 vol. pct. CO_2 at 40.48 atm and 1650 °C.

is not appropriate to calculate the oxygen absorption because the oxygen flux is not necessarily supplied by CO_2 diffusion away but by the bulk flow of CO. In fact the values of x_{CO_2s} calculated from equations 4.57 and 4.65 are overestimated and so is the oxygen surface concentration which depends on the CO/CO_2 ratio. In the mixed transport control model for decarburization of molten iron at low carbon content developed by El-Kaddah and Robertson[76] the reactions of carbon and oxygen dissolved in molten iron with CO/CO_2 gas mixtures defined by equations 4.1 and 4.2 are assumed to occur simultaneously and to be at equilibrium at all times at the gas-liquid interface assuming that the surface chemical reaction is fast. This model was applied to calculate the oxygen and carbon concentrations at the interface at the start of carburization under the experimental conditions used in the present work. The equilibrium and flux equations considered in the model are given in the following paragraphs.

Equilibria between molten iron and CO/CO_2 gas mixtures were defined by equations 4.1, 4.2 and 4.3 (section 4.2.2):

$$CO_2 + \underline{C} = 2CO \qquad (4.1)$$

$$CO_2 = \underline{O} + CO \qquad (4.2\ (a))$$

$$\underline{C} + \underline{O} = CO \qquad (4.3)$$

of which only two are independent equations.

A balance on carbon using equation 4.1 gives:

$$J_C = J_{CO} + J_{CO_2} \qquad (4.70)$$

and a balance on oxygen using equation (4.2(a)) gives:

$$J_O = J_{CO} + 2J_{CO_2} \qquad (4.71)$$

where J_C, J_O, J_{CO} and J_{CO_2} are the molar fluxes of C, O, CO and CO_2 respectively.

The fluxes from the gas and into the metal are considered positive.

After the assumption of fast chemical kinetics oxygen and carbon are in equilibrium at the interface and their concentrations are related by equation 4.3:

$$C_sO_s = (1/K_3)P_T(1 - x_{CO_2s}) \tag{4.72}$$

The flux equation for CO_2 transport in the gas phase is given by the equation:[77]

$$J_{CO_2} = -k^{\bullet}_x(x_{CO_2s} - x'_{CO_2b}) + x_{CO_2s}(J_{CO} + J_{CO_2}) \tag{4.73}$$

where $k^{\bullet}_x$ is the gas phase mass transfer coefficient, which in general depends on the mass transfer rate due to the distortion of the velocity and concentration profiles by the bulk flow of CO_2. However, El-Kaddah[14] demonstrated that at high pressure the correction is negligible, being much smaller than the error in estimating k_g (± 20%) using the correlation 4.68.

The fluxes of carbon and oxygen in the liquid phase are given by the equations:

$$J_C = k^C_l\ (C_s - C_b) \tag{4.74}$$

and

$$J_O = k^O_l\ (O_s - O_b) \tag{4.75}$$

Two equilibrium equations and the five flux equations allow the calculation of x_{CO_2s}, O_s, C_s, J_C, J_O, J_{CO} and J_{CO_2}. It can be shown that a combination of these equations gives:

$$k^{O}_{l}\,(O_b - K_{2a}x_{CO_2s}/(1 - x_{CO_2s})) - (1 + x_{CO_2s})k^{C}_{l}(C_b - (1 - x_{CO_2s})^2P_T/x_{CO_2s}K_1) = k^{\bullet}_{x}(x_{CO_2s} - x'_{CO_2b}) \qquad (4.76)$$

Equation 4.76 defines x_{CO_2s} as a function of bulk concentrations, equilibrium constants and mass transfer coefficients in the liquid and gas phases. The values of x_{CO_2s} can be used to calculate O_s and C_s using the equations:

$$O_s = K_{2a}x_{CO_2s}/(1 - x_{CO_2s}) \qquad (4.77)$$

and

$$C_s = (1 - x_{CO_2s})^2P_T/x_{CO_2s}K_1 \qquad (4.78)$$

At the start of carburization $O_b = 0$ and $C_b = 0$ and considering $k^{O}_{l} = k^{C}_{l}$ equation 4.76 becomes:

$$-K_{2a}x_{CO_2s}/(1 - x_{CO_2s}) + (1 + x_{CO_2s})(1 - x_{CO_2s})^2P_T/K_1x_{CO_2s} = (k^{\bullet}_{x}/k_l)(x_{CO_2s} - x'_{CO_2b}) \qquad (4.79)$$

Equation 4.79 was solved by trial and error. The values of the mass transfer coefficients $k^{\bullet}_{x}$ and k_l were taken as those of k_g and k'_l respectively used to predict the results of carburization. The values of oxygen and carbon surface concentrations were computed for carburization with 0.995 vol. pct. CO_2 and 2.00 vol. pct. CO_2 at 40.48 atm and 1650°C. Values of k_g of 5.3×10^{-4} (mole/cm² sec) and k'_l of 1.8×10^{-5} (mole/cm² sec wt %) were used in this calculation. Calculation for carburization at 65.15 atm and 1550°C in 3.95 vol. pct. CO_2 was carried out using a k_g of 6.7×10^{-7} (mole/cm² sec) and k'_l of 1.8×10^{-5} (mole/cm² sec wt %). The results are given in Table 4.6. The effect of increasing the mole fraction of CO_2 in the bulk at 40 atm and 1650°C is shown in Table 4.7. The oxygen concentration and carbon concentration at the gas-liquid interface increases and decreases respectively with the increase of CO_2 in the gas mixture, as is expected.

3 Composition of islets and oxide films caused by impurities

SIMS analyses of iron-carbon and spec-pure iron specimens reacted with CO/CO_2 gas mixtures demonstrated the presence of thin films of impurity oxides on the surface of these specimens. The analyses of oxide films observed on specimens quenched in the copper mould indicated that Al, Ti and Si, in the same order of importance, were the main components of the impurity oxides formed during decarburization of iron-carbon specimens (Figure 4.15). In the case of carburization of spec-pure iron specimens the impurity oxides contained mainly Si, Al, Ti and Cr (Figure 4.16). The analyses of a spec-pure iron specimen levitated in CO/CO_2 and quenched 'in situ' demonstrated that two oxide phases were formed when the reaction of carburization started. One phase covered most of the surface drop, the main constituents of this phase were Si and Ti. The other phase was formed as slag of high emissivity (which split forming oxide islets) rich in Al, Mg, Ca and Si.

LIMA analyses of specimens quenched 'in situ' also demonstrated the presence of impurity oxide films. However there were difficulties in analysing $^{28}Si^+$ so that the analyses cannot be directly compared with SIMS results. The analyses of an iron-carbon specimen reacted with a CO/CO_2 gas mixture showed the presence of Ca, Cr and traces of Al and Si (Figure 4.18), Mg was also analysed in another area of the same specimen. The analysis presented in Fig 4.7 (a) indicated that after cleaning the surface drop with H_2/Ar gas mixture for 10

Table 4.6: Oxygen and carbon concentrations at the gas-liquid interface at the start of carburization

P_T atm	T K	x_{CO_2b}	x_{CO_2s}	O_s wt %	C_s wt %
40.48	1923	0.00995	0.04992	0.0907	1.1203
40.48	1923	0.0200	0.05644	0.1032	0.9774
65.15	1823	0.0395	0.08652	0.0953	1.5068

Table 4.7: Oxygen and carbon surface concentrations. Start of carburization at 40.48 atm, 1923°K and different x_{CO_2b}.

x_{CO_2b}	x_{CO_2s}	O_s wt%	C_s wt%
0.00	0.0438	0.0790	1.2934
0.01	0.0499	0.0907	1.1203
0.02	0.0564	0.1032	0.9774
0.03	0.0599	0.1099	0.9150
0.04	0.0670	0.1239	0.8054
0.05	0.0745	0.1389	0.7125

min at 1750°C still some oxides remained on the surface of spec-pure iron specimens, the main constituents of the impurity oxide were Al and Ca. The analysis of the slag spots observed on the surface of a reacted spec-pure iron specimen showed the presence of Al, Ca and traces of Ti (Fig 4.17 (b)). The analysis of the apparently clean surface of a reacted spec-pure iron specimen showed the presence of Ca and traces of Mg only (Fig 4.17 (c)).

The slag added to an iron-carbon specimen picked up Ti and Cr (Table 4.4) whose concentrations were nil in the nonreacted slag. The concentrations of Ti and Cr in 0.0132g of slag were 0.150 and 0.035 wt % respectively. The concentrations in an iron-carbon specimen of one gram were calculated as 20 ppm of Ti and 5 ppm of Cr assuming that they were completely oxidised to the slag.

The chemical analyses of oxygen in carburized specimens reported in Table 4.5 indicated that the impurity elements formed oxides. The possibility of formation of different oxides is analysed in the following paragraphs considering that the concentration of each element is lower than 10 ppm, as indicated by the analyses of the iron-carbon alloys and spec-pure iron reported in section 2.10 (Table 2.1).

The oxygen activity in liquid iron in equilibrium with a CO/CO_2 gas mixture is defined by the reaction 4.2 (section 4.2.6):

$$CO + \underline{O} = CO_2$$

$$\Delta G^\circ_2 = -37600 + 20.63T \quad (cal/mole)$$

where ΔG°_2 is relative to the weight-per cent standard state. The oxygen activity is given by the equation:

$$a_{\underline{O}} = (P_{CO_2}/P_{CO})/K_2$$

The activity of oxygen in liquid iron in equilibrium with CO/CO_2 gas mixtures containing 1, 2 and 4 vol. pct. CO_2 at 1650°C are as follows:

CO_2 vol. pct.	P_{CO_2}/P_{CO}	$a_{\underline{O}}$ wt %
1.00	0.0101	0.0174
2.00	0.0204	0.0352
4.00	0.0417	0.0720

The formation of various oxides of Al, Si, Ti, Cr and Mg in liquid iron at 1650°C was considered. The activity of oxygen in equilibrium with the solute and the pure oxide was calculated and compared with the equilibrium oxygen activity fixed by the CO/CO_2 gas mixtures used in this work (1, 2, 4 vol. pct. CO_2).

The standard free energies of the reactions considered are given in Appendix 5. The infinitely dilute weight-per cent solution was taken as the standard state for the various solutes. Pure liquid iron, pure solid and liquid oxides were considered at unit activity.

The more relevant results of this calculation are given in Table 4.8. The values of oxygen activity given in Table 4.8 show that several oxides can be formed with the CO/CO_2 gas mixtures used in this work when the level of impurities is in the range of 1 to 10 ppm. It was found that under the same conditions silicon and chromium dissolved in liquid iron cannot form oxides at unit activity.

The iron-carbon alloys contained impurities in the parts per million range. The spectrographic analyses of the alloys gave the values (in ppm):

Ti 5-10; Al < 10; Si < 10; Cr < 5

where Al, Si and Cr were not detected. Magnesium was not analysed but its presence was shown in SIMS and LIMA analyses, presumably its concentration was around 1 ppm. At these concentration levels the oxides Al_2O_3, Ti_3O_5, $Al_2O_3.TiO_2$, $FeO.Al_2O_3$, $MgO.Al_2O_3$ and $MgO.TiO_2$ can be formed at unit activity with any of the CO/CO_2 gas mixtures. The oxide Ti_2O_3 can be formed with 2 and 4 vol. pct. CO_2 and $2FeO.TiO_2$ only with 4 vol. pct. CO_2.

The impurities in spec-pure iron were (in ppm):

Al, Cr, Ca	1
Si, Mg	2

Titanium was not reported, the limit of detection was 2 ppm.

At the level of impurity concentration in spec-pure iron the oxide $MgO.Al_2O_3$ can be formed at unit activity with any of the CO/CO_2 gas mixtures considered here. The oxides Al_2O_3, $Al_2O_3.TiO_2$, $FeO.Al_2O_3$ and $2MgO.TiO_2$ can be formed at unit activity with 2 and 4 vol. pct. CO_2 and the oxides TiO_2 and Ti_3O_5 with 4 vol. pct. CO_2.

The free energies of formation of MgO and CaO are very large,[40] consequently Mg and Ca require extremely low oxygen potential to form very stable oxides. Due to the relatively high oxygen concentration in spec-pure iron (Table 2.1) it can be assumed that magnesium and calcium are present as MgO and CaO inclusions respectively which remain solid at 1650°C. SIMS analysis of spec-pure iron indicated that the concentration of Al was the highest of all impurity concentrations. If its concentration were about 3 ppm it would be present as Al_2O_3 in the spec-pure iron. The oxides CaO, MgO and Al_2O_3 cannot be reduced by gaseous hydrogen at 1750°C so that they could remain on the surface of the drop (despite the H_2/Ar treatment before the start of the reaction) as solid particles.

Table 4.8: Oxygen activity as a function of the concentration of various elements in liquid iron at 1650°C in equilibrium with the oxide products at unit activity

CONCENTRATION, ppm REACTION	1	2	4	6	10
$\langle Al_2O_3\rangle = 2\underline{Al} + 3\,\underline{O}$	0.0338	0.0213	0.0134	0.0102	0.0073
$\langle TiO_2\rangle = \underline{Ti} + 2\underline{O}$	0.0613	0.0434	0.0307	0.0250	0.0194
$\langle Ti_2O_3\rangle = 2\underline{Ti} + 3\underline{O}$	0.1054	0.0664	0.0418	0.0319	0.0227
$\langle Ti_3O_5\rangle = 3Ti + 5\underline{O}$	0.0651	0.0430	0.0283	0.0222	0.0164
$\langle Al_2O_3.TiO_2\rangle = 2\underline{Al} + \underline{Ti} + 5\underline{O}$	0.0344*	0.0227	0.0137	0.0117	0.0086
$\langle FeO.Al_2O_3\rangle = \{Fe\} + 2\underline{Al} + 4\underline{O}$	0.0402	0.0284	0.0201	0.0164	0.0127
$\langle 2FeO.TiO_2\rangle = 2\{Fe\} + \underline{Ti} + 4\underline{O}$	0.0797	0.0670	0.0564	0.0509	0.0448
$\langle MgO.Al_2O_3\rangle = \langle MgO\rangle + 2\underline{Al} + 3\underline{O}$	0.0148	0.0093	0.0059	0.0045	0.0032
$\langle 2MgO.TiO_2\rangle = 2\langle MgO\rangle + \underline{Ti} + 2\underline{O}$	0.0298	0.0211	0.0149	0.0122	0.0094

* Equal concentrations of $\underline{Al}$ and $\underline{Ti}$

The standard free energy of the reactions (Appendix 5) at 1650°C indicated that the most stable oxide is $Al_2O_3.TiO_2$ (aluminium titanate) and then Ti_3O_5 (anosovite), $FeO.Al_2O_3$ (hercynite), $MgO.Al_2O_3$ (magnesium aluminum oxide) and Al_2O_3 (alumina). At the start of carburization the oxygen concentration at the surface reaches high values, around 100 ppm under the present conditions (Table 4.6), at which any of these oxides can be formed. As the initial rate of decarburization was high the oxygen surface concentration could have reached values high enough to form the most stable of these oxides at the start of the reaction.

SIMS and LIMA analyses indicated the presence of silicon in the oxide films. SiO_2 cannot form at unit activity under the present conditions. It is likely that silica was formed at low activity in solution with the stable oxides.

4.4 Discussion

4.4.1 Equilibria between molten iron and CO/CO_2 gas mixture

The results reported in section 4.2 allowed the effect of carbon on the activity coefficient of oxygen to be determined. This was the main objective of the present work. The equilibria between liquid iron and CO/CO_2 gas mixtures were studied in the high carbon range (> 1 wt % C) where there are few data from previous investigations. The oxygen activity was fixed by the CO/CO_2 ratio of the gas mixture at a given temperature whereas carbon activity could be changed by varying the total pressure of the gas mixture, hence the interaction between carbon and oxygen was well defined.

The approach to equilibrium in the present work was shown to be slow (Figs 4.2 and 4.3) due to the presence of thin films of oxide on the surface of the drop which retarded or impeded the reactions as will be discussed in section 4.4.2.

The results shown in Figure 4.4 indicated that the carbon-oxygen product relative to one atmosphere of CO decreased with increasing carbon concentration. At low carbon concentrations the results agreed with the value 0.002 reported by previous investigators[58] at steelmaking temperature. This agreement indicates that the partial pressure of CO at the surface of the drop corresponded to that of equilibrium between CO and carbon and oxygen dissolved in liquid iron. From equation 4.11 we obtain:

$$(\text{wt \% C. wt \% O}/p_{CO}) = (1/K_{3(\text{wt \%})})(1/f_C f_O) \qquad (4.80)$$

where K_3 is the equilibrium constant of the reaction 4.3:

$$\underline{C} + \underline{O} = CO$$

the standard free energy of reaction 4.3 relative to the weight-per cent standard state is obtained from equations 4.33 and 4.67:

$$\Delta G°_{3(\text{wt \%})} = -6325 - 8.51T \quad (\text{cal/mole}) \qquad (4.81)$$

Equation 4.80 shows that the carbon-oxygen product relative to 1-atm pressure of CO decreases with the increase of carbon concentration if f_O is considered constant as log f_C is directly proportional to the carbon concentration according to the equations 4.25-4.27. However, it can be readily shown that the magnitude of the decrease by considering only the effect of f_C is less than the observed in this work if $f_O \leqslant 1$. In order to have agreement between experimental and predicted results it is necessary that $f_O > 1$ which implies that $e_O^C > 0$ according to equation 4.30.

Matoba and Banya[58] found that the carbon-oxygen product in equilibrium with CO at 1 atm pressure increased with carbon concentration. However, they recognized the difficulties in crucible experiments of determining whether the product increases or decreases with the increase of carbon concentration due to errors introduced by melt contamination by the crucible, segregation of carbon and oxygen in the product, carbon monoxide evolution during solidification and accuracy of oxygen analysis. In fact Fuwa and Chipman[53] demonstrated that the results of Matoba and Banya were affected by errors commonly found in oxygen analysis of coarsely graphitic samples which adsorb oxygen or water vapor from the atmosphere. Fuwa and Chipman[53] found that the carbon-oxygen product relative to 1 atm pressure of CO decreased slightly with the increase of carbon concentration so that for practical purposes it could be considered constant. Their results must be also in error because of contamination with Al resulting from the use of alumina crucibles to hold the melt. Aluminium reduces the activity coefficient of oxygen, therefore it increases the oxygen concentration in the melt.

Carbon concentrations in the present work covered the range of 1.29 to 3.83 wt % C. At low carbon concentrations a significant fraction of carbon and oxygen may be lost due to carbon monoxide evolution during solidification. It was not the aim of this work to study the equilibrium of carbon in molten iron so no attempt was made to cover the low carbon range. There are excellent investigations on this subject,[58] such as those of Richardson and Dennis[49] in the low carbon range (< 1 wt % C) and El-Kaddah and Robertson[15] who covered nearly the whole carbon range up to carbon saturation at 1550°C and up to 3.5 wt % carbon at 1650°C and 1750°C.

The results of the present work should be compared directly with the results of El-Kaddah and Robertson[15] as the same experimental technique was used in both cases. Figures 4.26 and 4.27 show the data of carbon equilibrium concentrations obtained in both investigations. In these figures are plotted the carbon concentrations as a function of the ratio p^2_{CO}/p_{CO_2}. In Figure 4.26 the data of El-Kaddah and Robertson[15] at low carbon concentration are not shown. The data obtained in the present work with specimens cut from the iron-carbon alloys are also presented in these figures (half-closed symbols). The equilibrium carbon concentration obtained in carburization experiments were approximately the same in both works at a p^2_{CO}/p_{CO_2} or 2×10^3 atm (low total pressure) but lower carbon concentrations were obtained at higher ratios. In Figure 4.26 the carbon concentrations obtained in decarburization experiments increase the scatter of the results. In Figure 4.27 the results from both sides indicate that the true equilibrium carbon concentration is close to the values obtained by El-Kaddah and Robertson.

The difference of results obtained in both investigations may be due to the following sources of error:

a) Impurities in the starting materials (in the ppm range). Specpure iron, electrographite carbon and CO/CO_2 gas mixtures were of high purity quality and they were obtained from the same sources in both works. Iron carbonyl powder did not contain impurities that could affect the reactions. However, very different behaviour was found in the present work presumably because the materials were less pure. The presence of a minor amount of impurities (which were readily oxidized to form films on the surface of the specimens at the start of carburization and decarburization) must have been the main reason for the scatter of results found in the present work. These oxide films certainly slowed down the reaction of carburization and impeded the reaction of decarburization for short periods of time. These films may have also caused lack of attainment of true equilibrium in some cases.

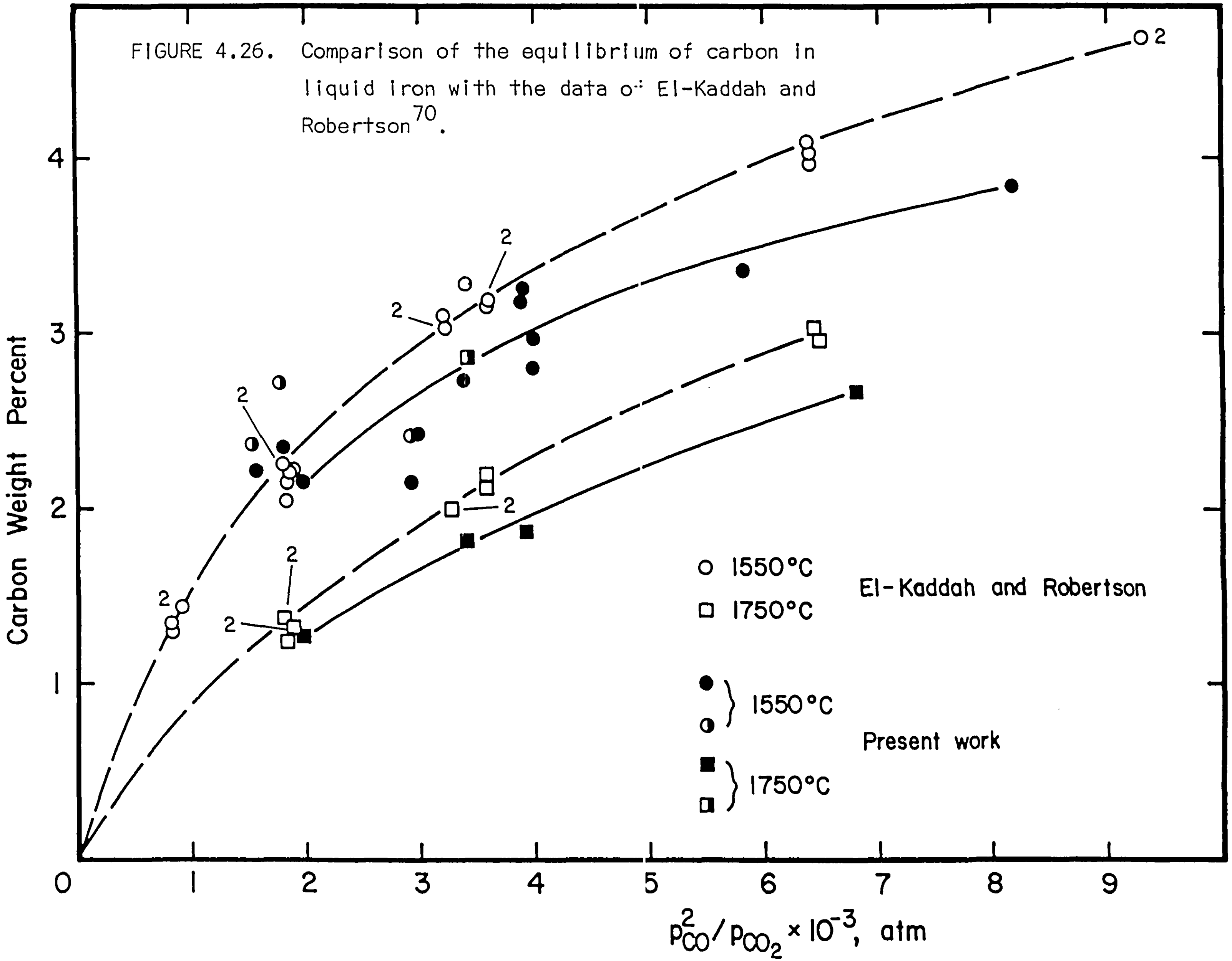

FIGURE 4.26. Comparison of the equilibrium of carbon in liquid iron with the data of El-Kaddah and Robertson[70].

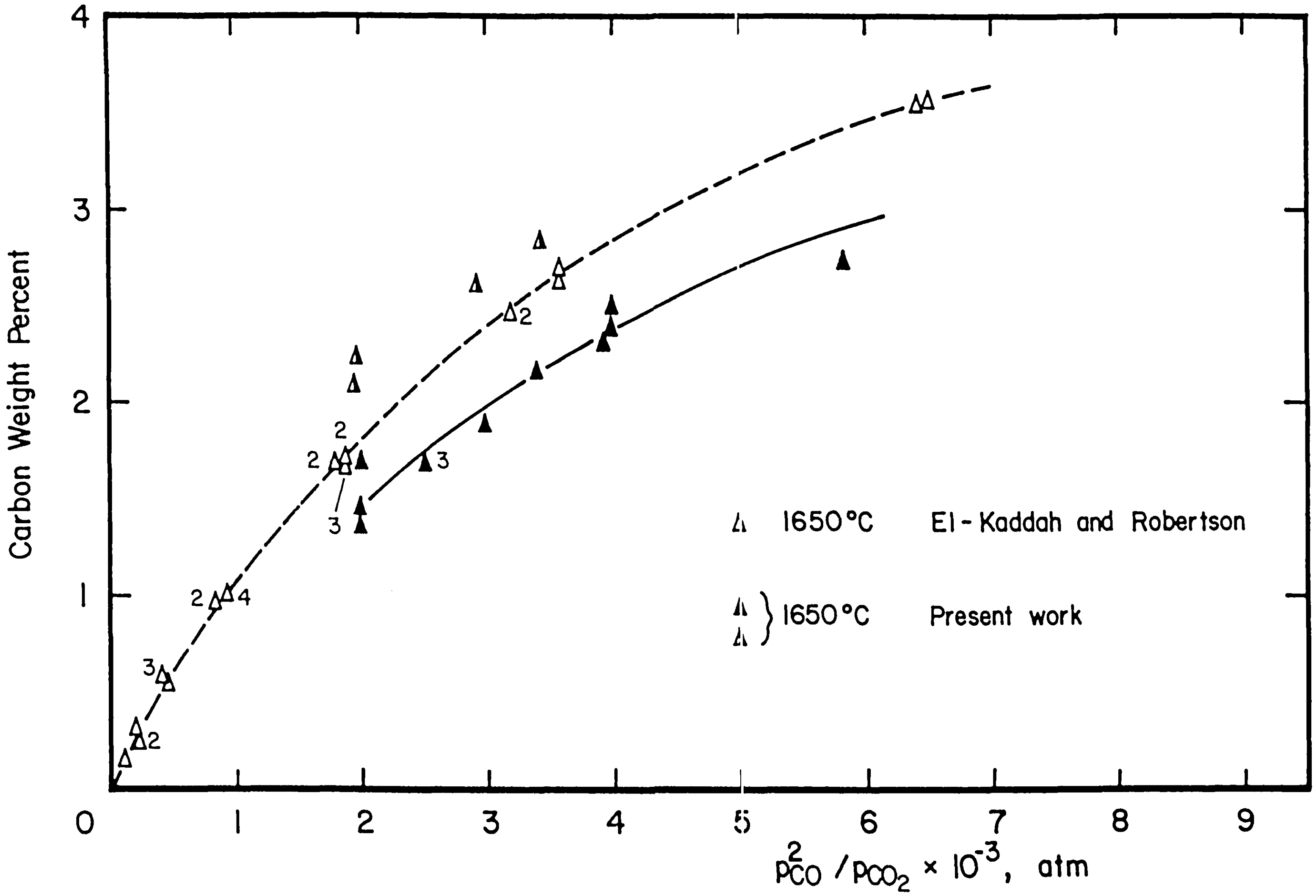

FIGURE 4.27. Comparison of the equilibrium of carbon in liquid iron with the data of El-Kaddah and Robertson[70].

b) Temperature measurement: Errors in calibration of the TCP cause consistent errors in temperature measurement. If the correction is constant the error will not originate scatter in the experimental results. If the temperature fixed is lower than the actual temperature it will result in a higher carbon concentration because the equilibrium constant of the carbon reaction decreases with the increase of temperature (equation 4.67). An experimental temperature 20°C lower than the actual temperature will increase the activity of carbon by 10% (relative).

The equilibrium constant of the β-graphite reaction (equation 4.21) is given by the equation:[50]

$$\log K_{4-21} = -8460/T + 8.85 \qquad (4.82)$$

which gives $p^2_{CO}/p_{CO_2} = 16.2 \times 10^3$ at 1550°C. Extrapolation of the present results up to this ratio gives 4.8 wt % C at 1550°C, extrapolation of the results of El-Kaddah and Robertson[15] at the same temperature gives 5.9 wt % C. The graphite solubility limit at 1550°C is 5.3 wt % C (equation 4.20). This calculation indicates that even though good temperature reproducibility was achieved in both investigations the temperature could be different (± 20°C approximately) from the actual temperature.

Other sources of error, such as thermal diffusion and carbon deposition, must have affected the results of both investigations in the same way. The effect of thermal diffusion is to increase the partial pressure of CO on the surface of the drop which would increase the carbon activity. This effect was found to be small by El-Kaddah.[14] Lacking other data of thermal diffusion ratio for dilute CO/CO_2 gas mixtures (with respect to CO_2) the same correction was applied in the present work. Carbon deposition due to thermal cracking of CO occurs through the reaction:

$$2CO = CO_2 + C \text{ (graphite)} \qquad (4.83)$$

the effect is to increase the partial pressure of CO_2 in the gas mixture. If the reaction occurs it would decrease the carbon activity in the melt.

Figure 4.28 shows that extrapolation of the present results to low carbon concentration agrees with the results of Richardson and Dennis.[49] In their work the equilibrium between liquid iron and CO/CO_2 gas mixtures was approached from both sides and the molten metal was held in alumina, lime or magnesia boats. The data not included in the curves of Richardson and Dennis correspond to their results with magnesia boats, which were considered in error by the authors because the reduction of magnesia caused large changes in the gas composition.

Despite the scatter of the present results the values of the interaction parameters of carbon (e_C^C) 0.182 and 0.158 at 1550 and 1750°C respectively compare well with other results reported by Matoba and Banya.[58] Rist and Chipman[50] obtained a value of 0.195 in the temperature range of 1460 to 1760°C. Fuwa and Chipman[53] obtained a value of 0.20 at 1560°C. El-Kaddah and Robertson[15] obtained lower values of the interaction parameter e_C^C: 0.135, 0.116 and 0.110 at 1550, 1650 and 1750°C respectively.

The results presented in Figure 4.7 demonstrated that the activity coefficient of oxygen in molten iron <u>increases</u> with the increase of carbon concentration thus confirming the prediction obtained by the decrease of the carbon-oxygen product (relative to 1 atm pressure of CO) with carbon concentration shown in Figure 4.4. The results obtained in this work confirm the finding of El-Kaddah

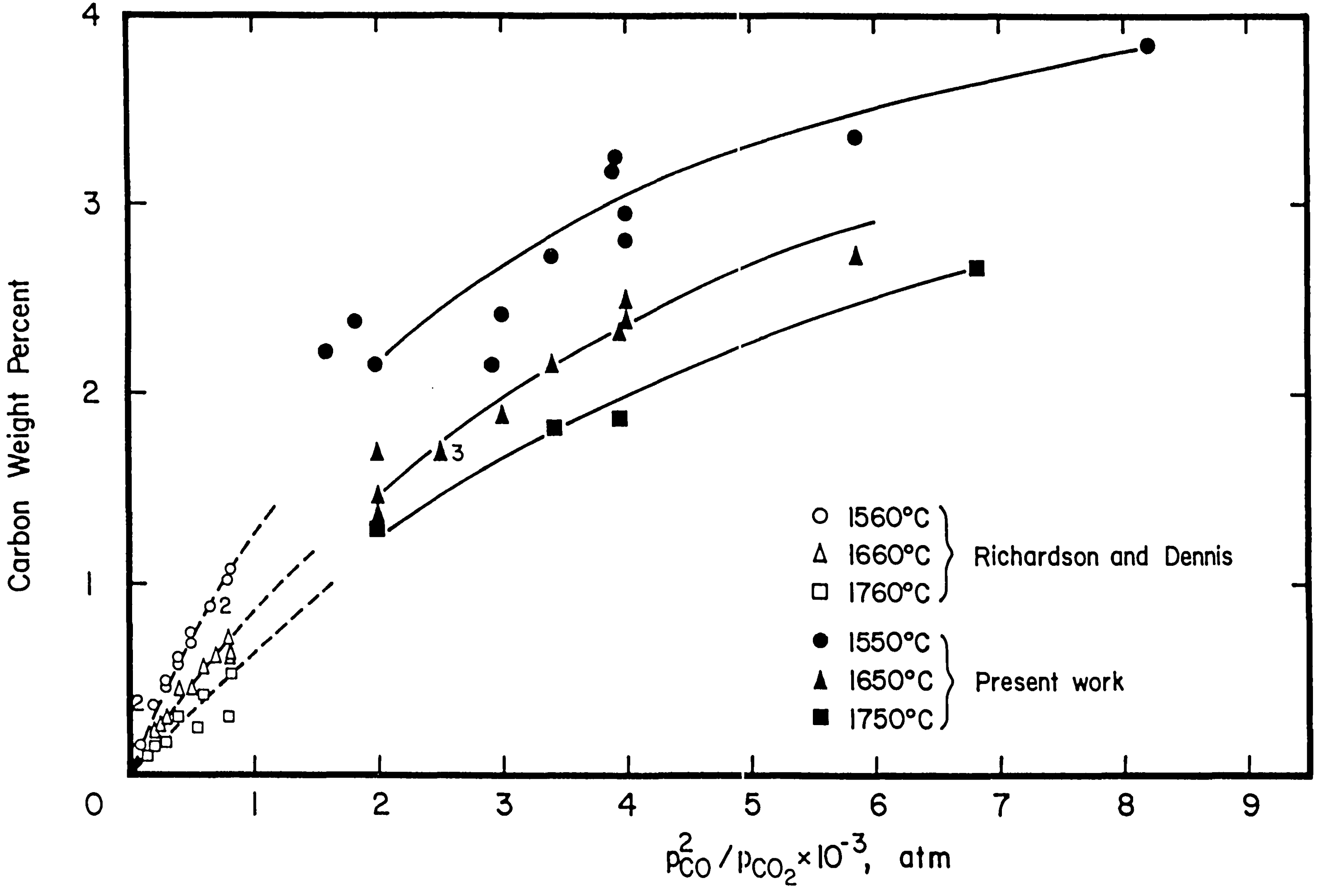

FIGURE 4.28. Comparison of the equilibrium of carbon in liquid iron with the data of Richardson and Dennis[49].

and Robertson[15] that the interaction parameter of carbon on oxygen (e_O^C) is positive. The value of e_O^C in the present work was +0.06 (±0.02) which compares with the value +0.1 (±0.02) obtained by El-Kaddah and Robertson.[15] As the investigation of these authors was highly precise as far as carbon concentration is concerned it must be concluded that their values of oxygen concentration were also correct and so the effect of carbon on the activity coefficient of oxygen. These results are contradictory to all previous investigations with the exception of that of Matsumoto[57] who found $e_O^C = +0.05$. The interaction parameter of carbon on oxygen reported by other investigators vary in a wide range, from -0.3 to -0.67, as given in the review of Matoba and Banya.[58]

The effect of carbon on the activity coefficient of oxygen is similar to that observed on the activity coefficient of sulfur.[41] The interaction parameter e_S^C is in the range of +0.11 to +0.29. The same behaviour of these elements would be consistent with the idea of periodicity.[14] Richardson[59] pointed out that the decrease of the activity coefficient of oxygen with carbon concentration measured by other investigators was as large as with vanadium or chromium, however the heat of formation of CO is very must smaller than that of the oxides of these elements so that a much smaller affinity between carbon and oxygen would be expected. The increase of the activity coefficient of oxygen by carbon may be interpreted as the tendency of oxygen to interact more strongly with iron than with carbon. Therefore the iron and oxygen atoms tend to associate preferentially and to reject atoms of carbon.

4.4.2 Kinetics of the reactions between molten iron and CO/CO_2 gas mixtures

The results given in Section 4.3.4 showed that the kinetics of carburization and decarburization were slow compared with the results obtained by El-Kaddah and Robertson[70] under the same experimental conditions. Figures 4.8 and 4.9 indicated that the equilibrium carbon concentration was obtained after 30 min of reaction during carburization with 0.995 and 2.00 vol. pct. CO_2 gas mixtures at 40.48 atm and 1650°C. In the experiments of El-Kaddah and Robertson with 1.1 and 2.15 vol. pct. CO_2 at 39 atm and 1650°C the equilibrium was reached after about 15 min and 10 min respectively. However, the initial rates of carburization were found to be 1 wt % C/min in both investigations and independent of the CO_2 content in the CO/CO_2 gas mixture in the range of composition used. The initial rates of decarburization obtained in the present work under the same conditions given above (Figures 4.8 and 4.9) were about one half of the corresponding initial rates reported by El-Kaddah and Robertson.[70]

The results of oxygen concentration as a function of time shown in Figure 4.3 obtained during carburization and decarburization with the 3.95 vol. pct. CO_2 gas mixture at 65.15 atm and 1550°C showed that equilibrium was reached after 25 min of reaction. In the investigation of El-Kaddah and Robertson[15] the equilibrium was attained after 12 min under the same conditions of pressure and temperature but with a 1.9 vol. pct. CO_2 gas mixture. The oxygen absorption after 5 min of reaction were 270 ppm and 110 ppm in carburization and decarburization respectively in this work, whereas the corresponding values reported by El-Kaddah and Robertson were 110 ppm and 50 ppm respectively, which agrees with the lower CO_2 concentration in their CO/CO_2 gas mixture.

The predicted kinetic curves for carburization given in Figures 4.24 and 4.25 are in good agreement with the results observed by El-Kaddah and Robertson.[70] The assumption of a low mass transfer coefficient in the liquid phase agrees with the previous finding of El-Kaddah[14] that the droplet may be considered nearly stagnant by assuming an effective diffusivity of carbon close to its atomic diffusivity. In the present work the initial rate of carburization was predicted with a k'_l of 1.8×10^{-5} mole/cm² sec wt % (0.003 cm/sec) which gives an effective diffusivity of carbon of 1.9×10^{-4} cm²/sec at 1650°C according with equations 4.46 and 4.47, this value is about 1.4 times the diffusivity of carbon in stagnant liquid iron which is 1.4×10^{-4} cm²/sec at 1650°C (extrapolated from the results of Goldberg and Belton).[78]

The predicted kinetic curves of decarburization (Figures 4.20, 4.24 and 4.25) showed longer times of attainment of equilibrium than in the investigation of El-Kaddah and Robertson[70] as expected because of the lower initial rates of decarburization found in the present work. The rates at the start of decarburization were predicted with gas phase mass transfer coefficients of the same order of magnitude but less than the values calculated using equation 4.68 for k_g around levitated drops. Presumably the drop was covered almost immediately by an oxide film when it was brought into contact with the reacting gas, thus retarding the reaction from the start. A critical test was the decarburization of an iron-carbon specimen prepared by carburizing spec-pure iron (Figures 4.13 and 4.14), its behaviour was similar to that of specimens cut from the specially made iron-carbon alloys. SIMS analyses have shown that carburized spec-pure iron specimens were covered by oxide films so that in this case the decarburization began with an oxide film on the surface of the droplet from the start of the reaction.

The results of carburization of spec-pure specimens indicated that the reaction proceeded for about one minute without any impediment. The direct observation of the droplets showed that oxide islets appeared after 20 sec in the reacting gas. This phase apparently did not affect the rate of reaction. The SIMS analysis of a spec-pure iron specimen reacted for 2 min in the 2.00 vol. pct. CO_2 gas mixture and quenched 'in situ' identified two phases over the surface drop. The oxide film covering most of the drop was a phase rich in Ti and Si whereas the slag (which formed the oxide islets) was a phase rich in Al, Mg, Ca and Si, however Al, Mg, Ca, Cr, Ti and Si were all present in both phases. It is interesting to note that analyses of the oxide film and oxide islets by LIMA allowed the identification of two phases but with compositions apparently different to those obtained by SIMS (Figure 4.17). As there were difficulties in LIMA analyses to identify the cation $^{28}Si^{+}$ and there was uncertainty about the depth of the analysis in the specimens it is considered that SIMS analyses are more reliable.

From the foregoing considerations it is now clear that the slow reaction rates observed in this work were due to the presence of an oxide film on the surface of the drop which acted as a physical barrier preventing the access of reacting gases to the surface of the metal. The structure of this film as well as that of the oxide islets must be very complex. The analyses carried out in this work were not comprehensive and were only of qualitative character so that limited information about the exact nature (structure and composition) of the two phases could be drawn from the present results.

Evidence of the presence of an oxide film covering the surface drop was obtained by adding a slag of composition 10 wt % Al_2O_3, 50% CaO and 40% SiO_2 to iron-carbon specimens. The slag collected the oxide islets but it did not absorb the film which remained over the surface so the rate of decarburization was not affected, being as slow as when the specimen reacted without slag addition.

The good agreement of the carbon-oxygen product at very low carbon concentration obtained in this work with previous investigations (Figure 4.4) indicated that the carbon and oxygen concentrations in the melt were at all times in equilibrium with CO. If oxygen is transferred through the liquid silicate the transfer of carbon should occur simultaneously so the carbon-oxygen product is maintained constant. Carbon exists in slags as carbide ions C_2^{2-} only under strongly reducing conditions and when barium or calcium are present at high activities.[79] It is considered that in general the concentrations of carbides in slag are very small. According to the available thermodynamic data[40] is not possible the formation of carbides of Al, Cr, Ti and Si at unit activity in liquid iron at 1650°C and when the concentrations of these elements are 10 ppm (maximum). It is suggested that the slow reactions occurred through breaks on the oxide film. It is also possible that the rapid movements and coalescence of the oxide islets allowed the gas mixture to become in contact with the metal surface so the reactions could proceed.

4.5 Conclusions

The results reported in this chapter on the equilibria of the reactions between CO/CO_2 gas mixtures and liquid iron in the range of high carbon concentrations (2.2-3.8 wt % C at 1550°C and 1.3-2.7 wt % C at 1650 and 1750°C) confirmed that the activity coefficient of oxygen increases with the increase of carbon concentration in liquid iron according with the equation:

$$\log f_O = 0.06\ (\pm 0.02)\ \text{wt \% C}$$

The carbon-oxygen product (wt % C x wt % O/p_{CO}) decreased with the increase of carbon concentration, which is in agreement with the finding that the activity coefficient of oxygen increases with carbon concentration. Extrapolation of the carbon-oxygen product at very low carbon concentration gave the value 0.002 (in the temperature range from 1550 to 1750°C) which is in agreement with previous measurements in plant and laboratory investigations.

The carbon equilibrium concentrations obtained in this work were scattered because the attainment of true equilibrium was impaired by the presence of thin oxide films on the surface of the drop. However, comparison of these results with the data of authoritative works on the subject showed reasonable agreement. The activity coefficients of carbon at 1550 and 1750°C were given by the equations:

$$\log f_C = 0.182\ \text{wt \% C}$$

and

$$\log f_C = 0.158\ \text{wt \% C}$$

Despite the high purity materials used in this work (impurities in the ppm range) oxide islets and a coherent oxide film were formed on the surface of the drop. These oxide phases formed after a short time of reaction (less than one minute) on spec-pure iron specimens and almost immediately on iron-carbon specimens. The oxide film was high in alumina and TiO_2 and the oxide islets were formed by a liquid silicate. The effect of the oxide film was to slow down the reactions of carburization and decarburization. The oxide film caused the reaction of decarburization to cease completely for short periods of time. The oxide film persisted throughout the reaction and was not absorbed by a liquid slag added to an iron-carbon specimen.

The calculation of the oxygen surface concentration at the start of carburization showed that high oxygen concentrations can be attained on the surface of the drop. These concentrations are greater than those corresponding to the oxygen potential in the CO/CO_2 gas mixtures. The prediction of this calculation is in accord with the experimental evidence obtained in this work.

A mixed transport control model allowed the prediction of the initial rates of carburization observed in this work. The low liquid phase mass transfer coefficient used was consistent with the previous finding that the levitated drops may be considered nearly stagnant by assuming an effective diffusivity of carbon close to its atomic diffusivity. The initial rates of decarburization were slower than those predicted by considering gas phase mass transfer control because of the formation of the impeding oxide film.

As the accuracy of the experimental results obtained in this work was affected by the formation of the oxide film it is considered necessary to study the carbon-oxygen reaction using the same technique (which has proved to be adequate) but with more pure materials. The graphite used to make the iron-carbon alloys is the main source of impurities, therefore it is recommended to use spec-pure graphite. As the use of spec-pure materials does not ensure impurity-free specimens methods to segregate the impurities to the surface of the drop followed by chemical or mechanical cleaning should be devised.

Chapter Five

STUDY OF THE OXIDATION OF NICKEL-SULFUR DROPS WITH OXYGEN-BEARING GASES AT LOW TEMPERATURES

5.1 Introduction

This chapter describes the work carried out on the oxidation of molten nickel-sulfur alloy drops containing 20 wt % sulfur with air and pure oxygen at temperatures as low as 1050°C.

The low initial temperatures required were obtained by levitation melting of the Ni-20S specimens in helium at high pressure. A theoretical model was used to predict the conditions for sulfur oxidation or formation of a nickel oxide layer. The growth of the oxide layer and the interaction between the layer and the liquid nickel-sulfur alloy were also studied.

This investigation is relevant to roasting of molten nickel-sulfur alloys in fluidized bed furnaces, however it should be stressed that it was not intended to simulate the industrial process in the experimental work.

5.2 Previous work

The study of the oxidation of molten nickel sulfide is essential for the understanding of the mechanism of reactions occurring in the direct reaction of nickel sulfide to produce pure nickel and in the roasting of nickel sulfide concentrations in fluidized beds to produce nickel oxide. Although these processes are operated on a commercial scale little is known about the kinetics of the reactions between molten nickel sulfide and oxygen-bearing gases.[81] The development of these processes has also been limited by an incomplete knowledge of the thermodynamics of the molten Ni-S-O system[82] as discussed in section 5.3.

In the direct reaction of molten nickel sulfide to nickel metal by the Inco Top Blown Rotary Converter (TBRC) process Ni_3S_2 (m.pt. 790°C) is oxidized with an oxygen lance directed onto the surface of a well-mixed bath.[83] During the process temperatures up to 1650°C are obtained. One of the main problems found in the conversion of nickel was the formation of solid nickel oxide (m.pt. 1984°C), the reaction is given by:

$$Ni(l) + \tfrac{1}{2}O_2(g) = NiO(s) \qquad (5.1)$$

The formation of NiO could be prevented if surface oxidation of sulfur (reaction 5.2) occurs preferentially to nickel oxidation.

$$\underline{S}\ (\text{in Ni}) + O_2(g) = SO_2(g) \qquad (5.2)$$

However, nickel oxide will eventually be formed when the surface concentration of sulfur decreases allowing the increase of oxygen concentration at the liquid surface up to the value corresponding to the equilibrium of reaction 5.1. Reaction 5.2 was found to occur at temperatures higher than 1600°C at atmospheric pressure and sulfur content of about 5 wt %. However, at high sulfur concentration (20 wt %) the process can be carried out at a temperature of about 1380°C.[83]

In fluidized-bed roaster the oxidation of molten nickel sulfide (about 20 wt % S) occurs at temperatures ranging from 900 to 1100°C to produce nickel oxide which emerges as a granular product. The nickel sulfide is fed to the reactor as pellets of nickel concentrate and nickel matte[84] or particles of nickel concentrate which melt and spread on nickel oxide particles contained in the fluidized bed.[85]

The levitation melting of nickel sulfides was first achieved by Roberts et al.[86] In this investigation 0.45g specimens of Ni-S alloys containing 27-31 wt % S were levitated in an inert gas at a total pressure of 1 atm. A steady temperature of 1800°C was reached in 40 sec after melting. The levitated drop of nickel sulfide was used to study the features of the oxidation with pure oxygen. With this purpose Ni-20S specimens levitated in helium at 1600°C were used. The reaction with pure oxygen for 7 sec increased the temperature up to about 2400°C. During reactions of 15 sec of duration ebullition was not observed. It was suggested that a large proportion of the oxygen which reacted with the specimen was absorbed to form a homogeneous Ni-S-O ternary liquid.

Fukunaka and Toguri[81,87] investigated the vaporization and the oxidation of molten nickel sulfide at high temperatures using the levitation melting technique. These investigations were carried out using 0.5g specimens of synthetic Ni_3S_2. In the oxidation experiments the specimens were reacted with oxygen-helium gas mixtures containing 5 to 40 vol. pct. of oxygen at temperatures above 1500°C. It was found that under these conditions the oxidation proceeded by two stages. In the first stage preferential sulfur oxidation occurred, so they assumed that the overall reaction could be represented by reaction 5.2. It was suggested that under their experimental conditions the overall rate of oxidation was controlled by oxygen mass transfer through the gas boundary layer. The second stage occurred at low sulfur concentration. It was characterised by oxidation of nickel vapor, oxygen absorption into the droplet and small desulfurization.

The oxidation of molten nickel-sulfur alloys at low temperatures has been studied in laboratory scale using a fluidized-bed roaster.[85,88]

There are no detailed studies about the mechanism of the reactions in this temperature range. Specifically, the mechanism of formation of a solid film of nickel oxide on the surface of the molten sulfide and the subsequent process of desulfurization through this oxide layer is not clear.

There is no previous work on the oxidation of molten nickel sulfide at low temperature (about 1000°C) using the levitation melting technique.

5.3 Thermodynamics

A knowledge of the thermodynamics of the reactions involving sulfur, oxygen and liquid nickel is a prerequisite to the study of the kinetics of the reactions between molten nickel sulfides and oxygen-bearing gas mixtures.

The molten Ni-O binary system has been studied by many researchers.[89,90,91,92] However, large discrepancies among their results are found.[91] Furthermore, most of these investigations show a large scatter in their data.[89,90] The thermodynamic properties of dilute solutions of oxygen in molten nickel have been studied using H_2/H_2O[91] and CO/CO_2[89] gas mixtures to fix the oxygen potential. In a recent investigation Kemori et al[92] used the e.m.f. method to measure the activity of oxygen in liquid Ni in the temperature range of 1460 to 1560°C. Their results almost agreed with those of Bowers[90] and Tankins et al.[91] The standard free energy for the reaction:

$$\tfrac{1}{2}O_2(g) = \underline{O}\ (\text{in liquid Ni}) \qquad (5.3)$$

according to Kemori et al[92] is given by:

$$\Delta G^\circ_{5-3} = -16948 + 7.02T \text{ (cal/mole)} \qquad (5.4)$$

where the standard state for dissolved oxygen is a mole fraction infinitely dilute solution.

The thermodynamic properties of sulfur in the molten Ni-S binary system have been determined by studying the equilibrium between Ni-S melts and H_2/H_2S gas mixtures.[82,93,94] Nagamori and Ingraham[93] determined the equilibrium sulfur partial pressures over Ni-S melts of various compositions (16 to 30 wt % S) for temperatures from 800 to 1100°C. Meyer et al[82] extended the data at temperatures ranging from 1100 to 1600°C for melt compositions ranging from nickel saturation up to about 27 wt % S. Venal and Geiger[94] investigated the equilibrium:

$$\tfrac{1}{2}S_2(g) = \underline{S} \text{ (in liquid Ni)} \qquad (5.5)$$

in dilute solutions of sulfur in pure liquid nickel over the temperature range from 1500 to 1575°C. The standard free energy of reaction 5.5 relative to the weight percent infinitely dilute solution was given by:

$$\Delta G^\circ_{5-5} = -28342 + 3.62T \text{ (cal/mole)} \qquad (5.6)$$

The molten Ni-S-O ternary system is not well known.[81,82] The only information available in this system is the interaction parameter of sulfur on oxygen[95] ($e_O^S = -0.089$) determined for solutions at 1600°C containing 5 wt % sulfur and up to 0.15 wt % oxygen. Using this value of e_O^S and those of the interaction parameters e_O^O and e_S^S determined in the studies of the Ni-O and Ni-S binary systems Solar and Bell[95] proposed the following equations for the activity coefficients of sulfur and oxygen in the Ni-S-O system:

$$\log f_O = -0.1 \text{ wt \% } \underline{O} - 0.089 \text{ wt \% } \underline{S} \tag{5.7}$$

$$\log f_S = -0.178 \text{ wt \% } \underline{O} - 0.053 \text{ wt \% } S \tag{5.8}$$

Lacking other data Solar and Bell[95] assumed that e_O^S was independent of temperature and oxygen concentration. Usually the behaviour of sulfur in molten nickel is considered similar to that in molten iron,[94] however in the Fe-S-O ternary system measured values for the interaction parameter e_O^S have been quoted over a wide range (from 0 to -0.44 at temperatures from 1550 to 1630°C).[41]

The oxygen potential at equilibrium between pure liquid nickel and nickel oxide is defined by the reaction:

$$Ni(l) + \tfrac{1}{2}O_2(g) = NiO(s) \tag{5.9}$$

the standard free energy of reaction 5.9 at temperatures in the range 1452 to 1900°C is given by:[96]

$$\Delta G^\circ_{5-9} = -62650 + 25.98T \text{ (cal/mole)} \tag{5.10}$$

The standard free energy of the reaction:

$$\tfrac{1}{2}S_2(g) + O_2(g) = SO_2(g) \tag{5.11}$$

is given by:[96]

$$\Delta G^\circ_{5-11} = -86620 + 17.31T \text{ (cal/mole)} \tag{5.12}$$

in the temperature range of 25 to 1700°C.

Reactions 5.3, 5.5, 5.9 and 5.11 define other equilibria in the Ni-S-O system. Combining equations 5.5, 5.9 and 5.11 the reaction between sulfur in solution and NiO can be obtained:

$$\underline{S} \text{ (in liquid Ni)} + 2NiO(s) = 2Ni(l) + SO_2(g) \tag{5.13}$$

$$\Delta G^{\circ}_{5-13} = 67022 - 38.27T \quad \text{(cal/mole)} \tag{5.14}$$

5.4 Experimental

One gram specimens of almost spherical shape were prepared by melting Ni-S alloy particles in small spec-pure graphite crucibles under an atmosphere of helium (section 2.9). Levitation melting of the specimens was carried out in the HPLA using the levitation coil of design (1).

Preliminary experiments were aimed to determine the conditions of levitation melting and to find out the effect of the total pressure, flow rate of gas and generator power (anode current) on the droplet temperature. Figure 5.1 shows the variation of droplet temperature with total pressure. Levitation was carried out at high anode current (1.7A). Helium was used because of its high thermal conductivity, flow rates in the range of 1 to 3 slm were used. Temperatures were measured using the TCP at temperatures higher than 1100°C which is the lower limit of this instrument (section 2.7). At temperatures lower than 1100°C L & N and LP optical pyrometers were used (Leeds and Northrup and Land Pyrometer). Temperatures are reported as °C measured on the particular instrument used. Because the pyrometers were not calibrated, they are considered to be in error by ±50°C. Figure 5.2 shows the droplet temperature as a function of the anode current at a total pressure of 30 barg and 1 slm of helium, a minimum temperature was attained at about 1.5A.

In the experiments on oxidation of the Ni-S alloy, the specimens were levitated in helium flowing at 3.0 slm. When the temperature reached the required steady value the oxidizing gas was introduced. Temperature changes above 1100°C were recorded. After oxidation the specimen was quenched at high pressure and the oxidizing gas was replaced by helium.

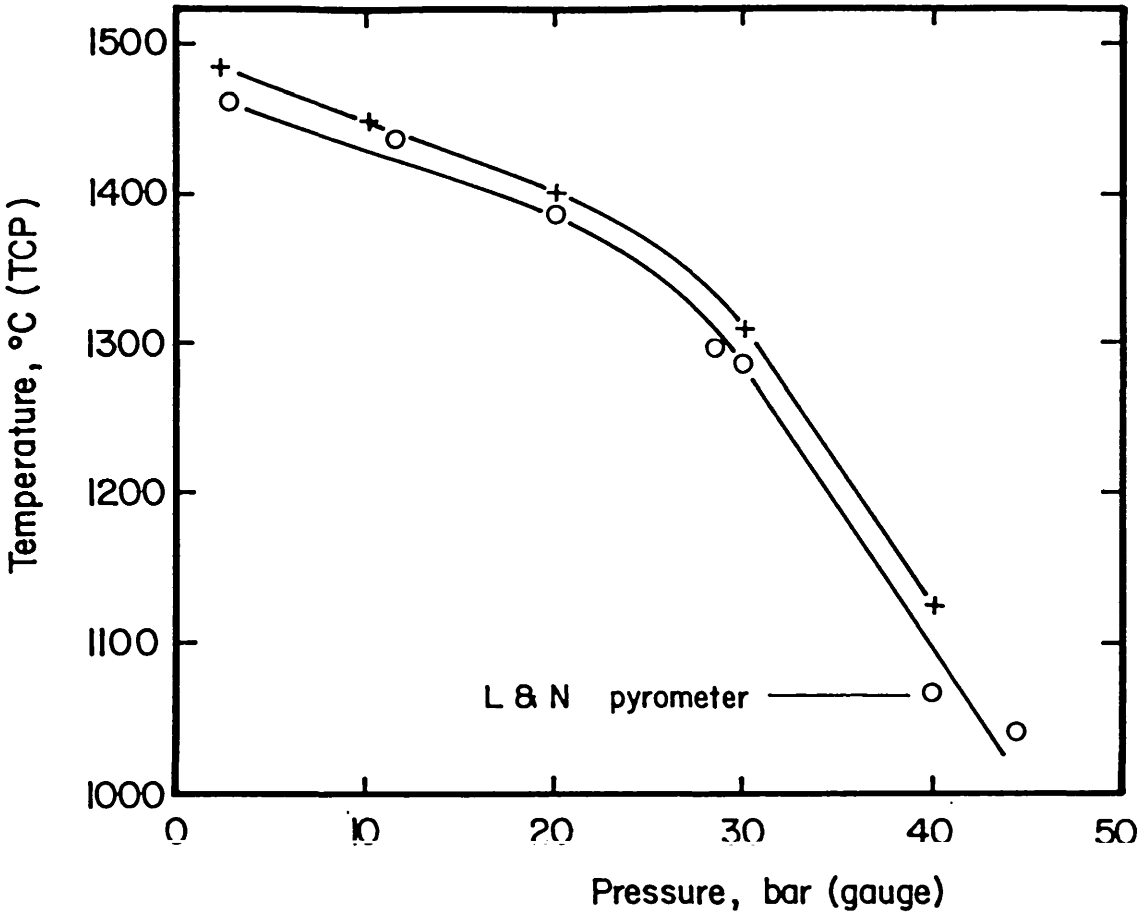

FIGURE 5.1. Droplet temperature as a function of the total pressure. (o) Run NIS 4; anode current: 1.7 A, flow rate: 3 slm. (+) Run NIS 5; anode current: 1.7 A, flow rate: 1 slm. Gas: He.

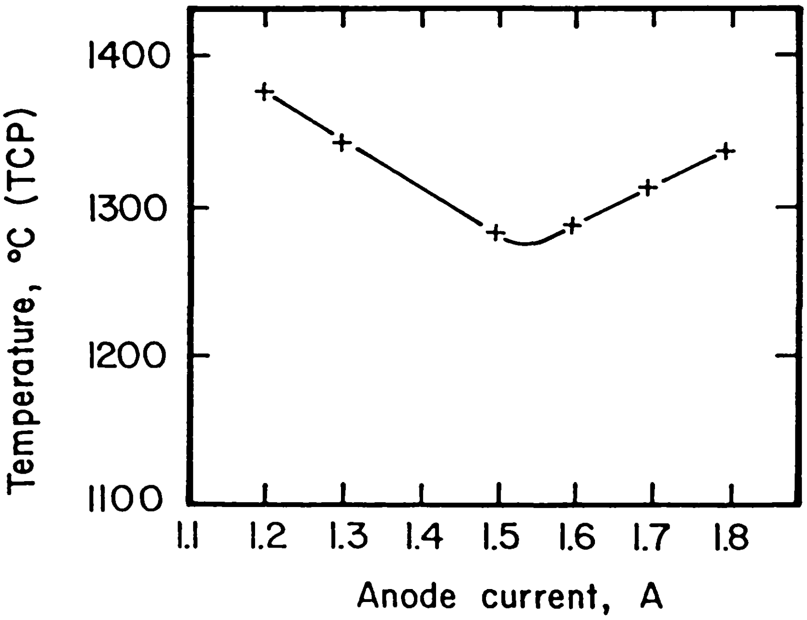

FIGURE 5.2. Droplet temperature as a function of the anode current. Run NIS 5. Total pressure: 30 barg.

In some experiments analysis of the outlet gas was carried out by iodometric titration.[97] Sulfur dioxide was absorbed in 100cc of distilled water containing 5cc of KI (1% w/v). A solution of potassium iodide and potassium iodate (0.022 Normal) as standard solution and starch as indicator were used.

The oxidized specimens were mounted in resin for microscopic analysis and thickness measurement of the oxide layer. Some specimens were analyzed using EPMA. The oxide layer of some specimens was removed and analyzed by X-ray diffraction. Sulfur analyses of some oxidized specimens were carried out. The oxide layer was removed and the remaining alloy was ground in an alumina mortar, 50 mg was taken as a sample for analysis by the combustion method.[98]

Filming during some runs was carried out using a Bolex cinecamera operated manually at a maximum speed of 72 pps (section 2.8). The events were filmed through the prism located at the bottom of the levitation chamber.

5.5 Results

The oxidation of molten Ni-20S alloy with air and oxygen at 1050°C (LP) and with air at 1150°C (TCP) was studied using high pressure levitation melting to obtain the low initial temperatures required.

5.5.1 Oxidation of molten Ni-20S alloy in air at 45 atm and 1050°C (LP)

The oxidation of the molten Ni-20S alloy at 1050°C (initial temperature) in air was characterized by an initial increase in temperature of the drop up to about 1400°C (TCP) due to SO_2 evolution followed by formation of a solid oxide which covered the droplet completely. Once the oxide layer was formed the temperature of the drop decreased as shown in Figure 5.3. The thickness of the oxide layer grew with time. Almost periodic instabilities in which SO_2 was evolved were observed at later stages of the process. After a long time of reaction (about 3 hours) the layer of oxide was dispersed by the liquid Ni-S alloy which became in contact with air and strong SO_2 evolution occurred.

First stage of the reaction

The reaction started after 20 sec due to the time required for the reaction gas to reach the levitation chamber. The sulfur dioxide evolved during the first stage of the reaction was measured by iodometric titration, passing the outlet gas through the absorbent solution (section 5.4). The actual time during which SO_2 was evolved was 40 sec because the oxidation of sulfur stopped when the oxide

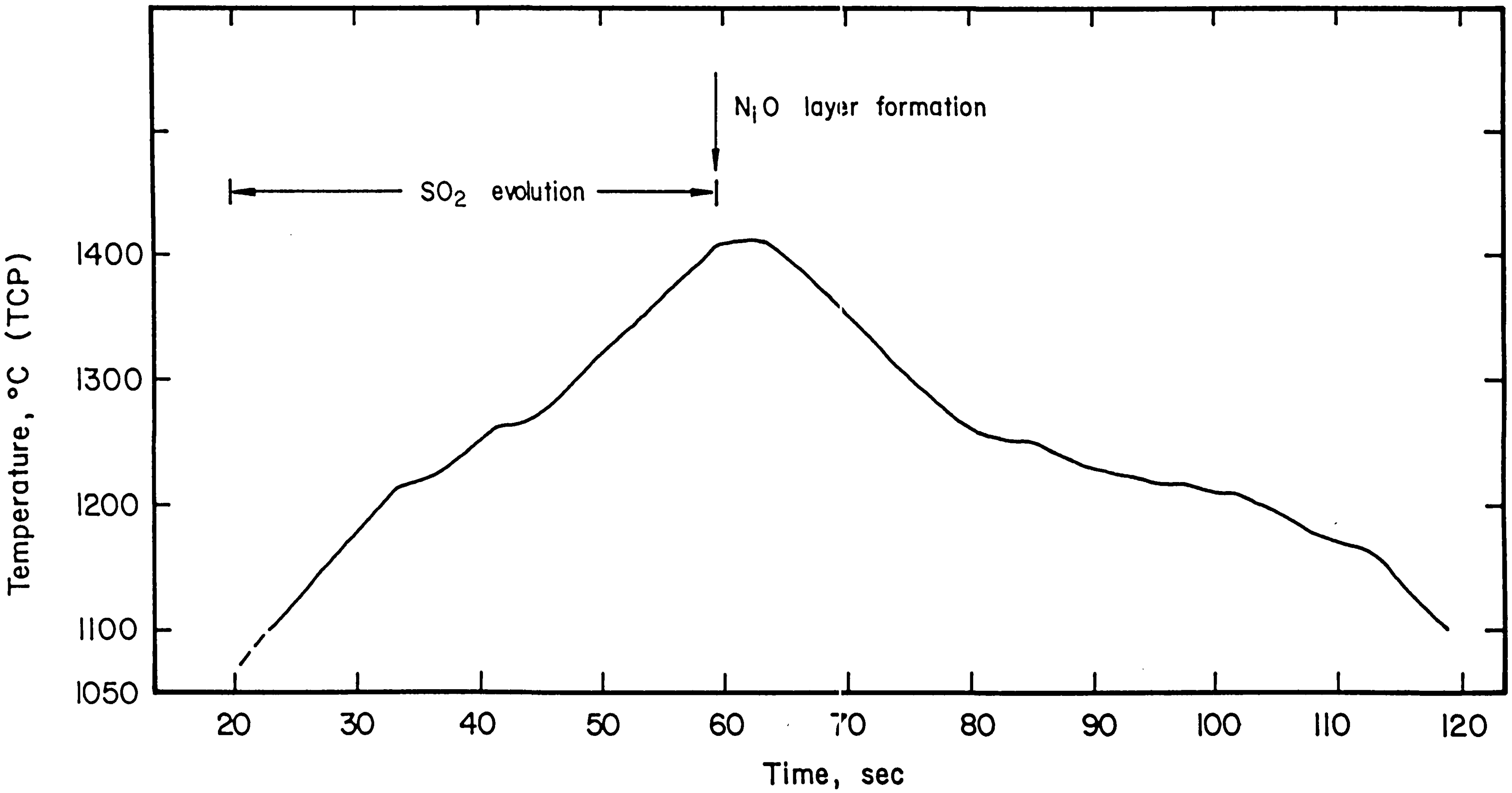

FIGURE 5.3. Temperature as a function of time during oxidation of molten Ni-20S alloy in air at 45 atm. Run NISO 47.

layer was formed. The sulfur lost during this stage and the corresponding rates are given in Table 5.1.

Table 5.1: Sulfur lost during the initial stage of oxidation of molten Ni-20S alloy

Run number NISO	Sulfur lost g	Rate g/min
37	0.0237	0.0356
38	0.0356	0.0354
39	0.0395	0.0593
41	0.0416	0.0624
42	0.0300	0.0450
43	0.0234	0.0351
44	0.0389	0.0584

Second stage of the reaction

After 40 sec of SO_2 evolution an oxide phase was observed to nucleate on the surface of the drop. The oxide film grew very rapidly to cover the whole surface in about 90 msec. The growth of the solid oxide layer is shown in Plate 5.1.

When the oxide layer was formed the temperature of the droplet remained constant for 3 to 5 sec (Figure 5.3) and then decreased to a steady value approximately the same as the initial temperature. The shape of the specimen was either ovoid or spherical.

The specimen consisting of liquid Ni-S alloy covered by the layer of oxide was kept levitated in air for different periods of time. The thickness of the layer and the mass of the specimen were measured, the results are given in Tables 5.2 and 5.3. The thickness of the layer and changes in mass as a function of time are shown in Figures 5.4 and 5.5 respectively.

DESCRIPTION OF PLATE NO. 5.1

PICTURE NO.	TIME (Sec)
1	30
2	45
3	60
4	60.032
5	60.034
6	60.037
7	60.044
8	60.052
9	60.059
10	60.065
11	60.118
12	60.119

INITIAL TEMPERATURE OF THE DROPLET: 1050°C (LP)

AIR PRESSURE: 45 atm

PLATE No. 5.1

OXIDE LAYER FORMATION DURING OXIDATION OF MOLTEN Ni-20S ALLOY WITH AIR. RUN NISO 52

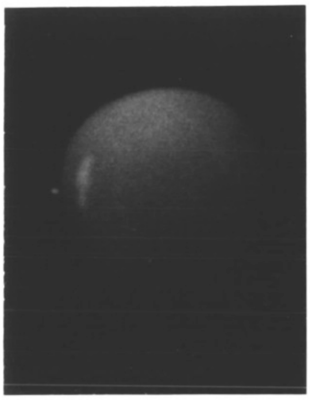
1

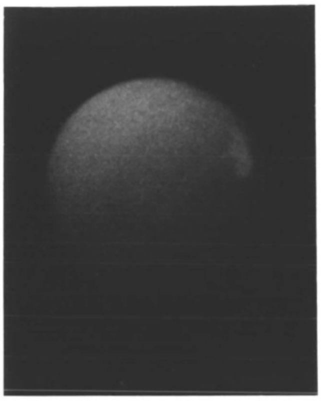
2

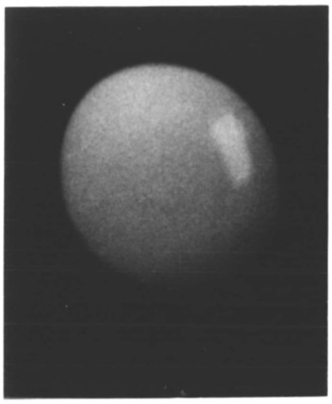
3

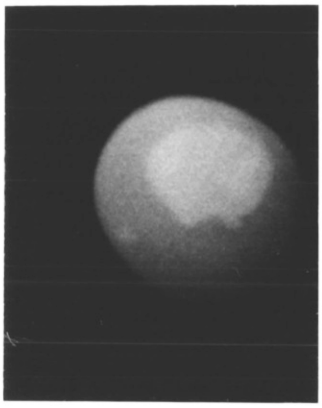
4

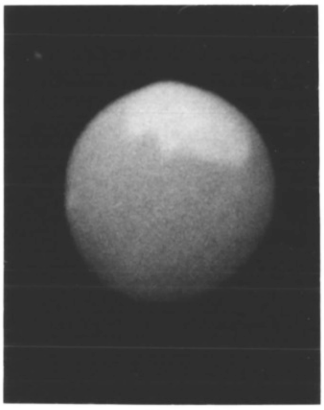
5

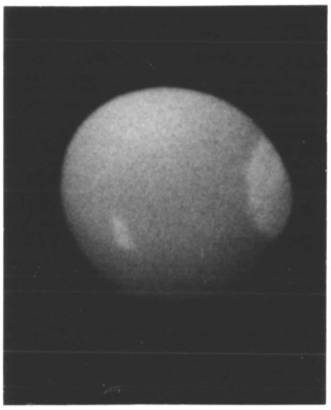
6

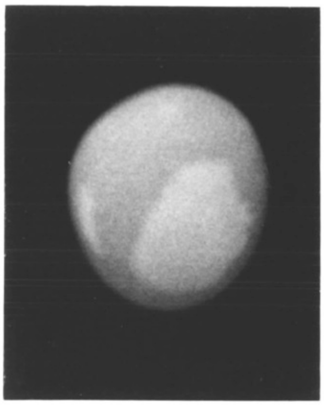
7

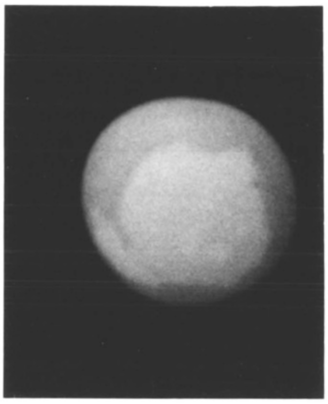
8

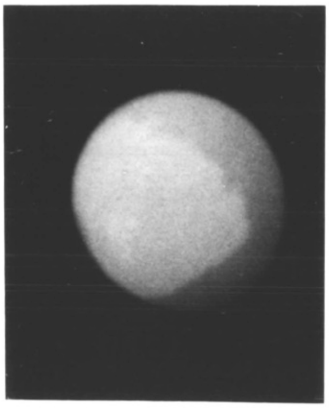
9

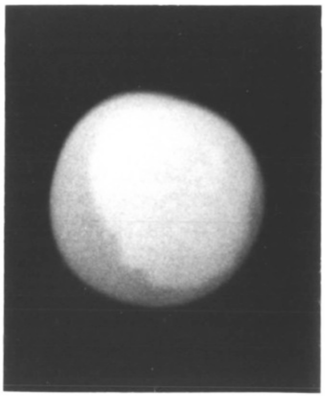
10

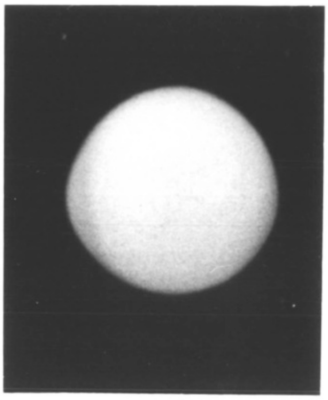
11

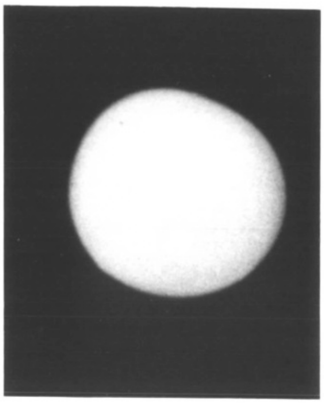
12

Table 5.2: Thickness of the oxide layer as a function of time during oxidation of molten Ni-20S alloy in air at 45 atm and at 1050°C (LP)

Run number	Reaction time min	Layer thickness µm
NISO		
45	1.75	14.84
46	2.50	14.84
1	3.50	25.81
38	20.00	51.00
5	23.00	42.40
48	30.00	65.72
6	40.00	63.60
39	40.00	76.50
40	61.00	93.50
42	99.00	113.33
16	120.00	245.00m
11	160.00	297.50m
22	189.87	317.75m
15	194.03	187.27m
24	254.92	0

m: maximum thickness

Table 5.3: Mass change with time of reaction during oxidation of molten Ni-20S alloy with air at 45 atm and at 1050°C (LP)

Run number	Reaction time min	Mass change g
NISO		
45	1.75	0.0004
46	2.50	0.0052
1	3.42	0.0119
49	6.00	0.0025
52	9.00	0.0092
38	20.00	0.0106
5	23.00	0.0094
48	30.00	0.0148
6	40.00	0.0067
39	40.00	0.0108
40	61.00	0.0237
50	80.00	0.0253
51	80.00	0.0165
42	99.00	0.0292
16	120.00	0.0266
41	120.00	0.0224
11	160.00	0.0120
43	160.00	0.0354
22	189.87	0.0098
15	194.03	-0.0362
24	254.92	-0.0477

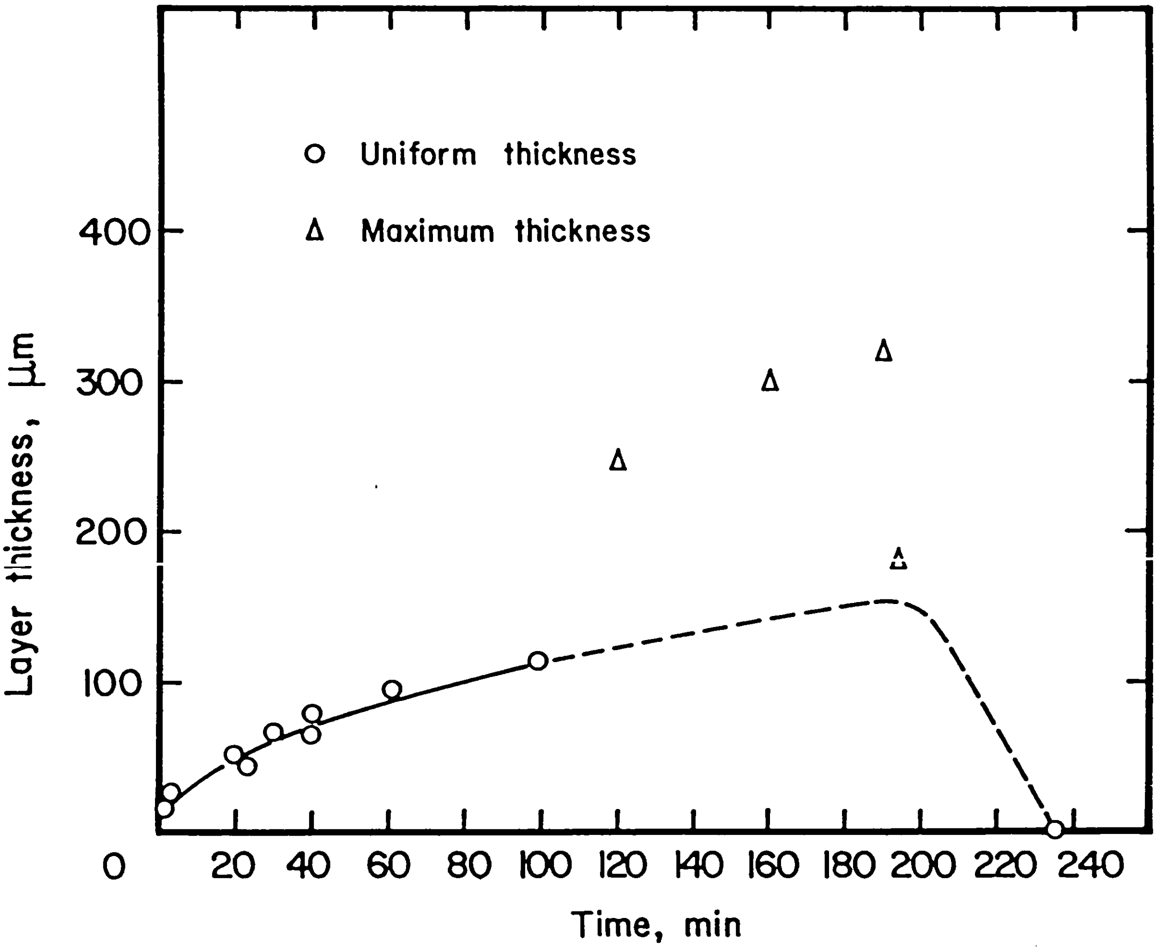

FIGURE 5.4. Thickness of the oxide layer as a function of time during oxidation of molten Ni-20S alloy in air at 45 atm and 1050 °C initial temperature.

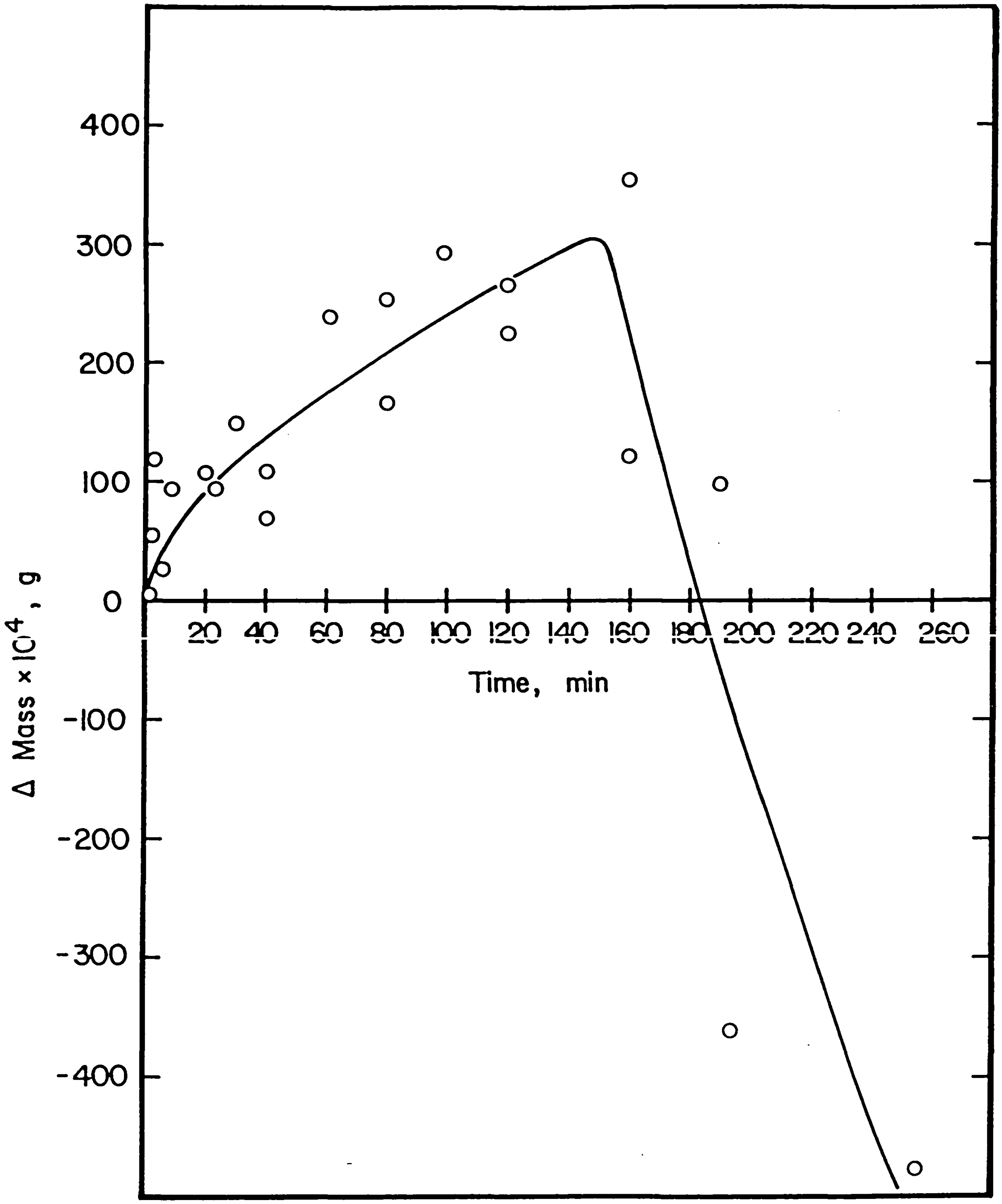

FIGURE 5.5. Mass change as a function of time during oxidation of molten Ni-20S alloy in air at 45 atm and 1050 °C initial temperature.

The thickness of the oxide layer increased uniformly up to 100 min of reaction. After this time localized dispersion of the oxide layer in the liquid Ni-S occurred. The maximum thicknesses of the layer after times of reaction longer than 100 min are shown in Table 5.2. The appearance of the oxide layer at different times of reaction is shown in Plate 5.2.

After 190 min of reaction the oxide layer was almost completely dispersed, the liquid sulfide that came in contact with air reacted producing strong SO_2 evolution. These events are depicted in Plate 5.3: the first frame shows the specimen after 120 min of reaction in air, the oxide is covering the drop. At time 204.3 min liquid alloy appeared on the surface of the drop and began to be oxidized. At 249.07 min the layer of oxide collapsed and strong SO_2 evolution occurred.

Two types of behaviour were observed during the last stages of the reaction: a) a thin oxide film was formed on the area where the liquid Ni-S was exposed to air and the specimen remained levitated; b) the vigorous sulfur oxidation continued so the temperature increased to higher values and the specimen became unstable hitting the silica tube.

The start of the instabilities observed during the reaction was erratic but in general occurred after 100 min. The instabilities continued during the process with a periodicity of about 13 to 15 min and they lasted for 5 to 8 min. A temperature increase of the drop up to 1275°C (TCP) was registered during this time. Black zones were observed on the surface of the specimens (Plate 5.3) attributed to sulfur dioxide evolution. The rate of sulfur lost in this period (measured in run NISO 43) was 0.0023g/min. The quenched specimens showed that the black zone on the surface corresponded to a place where the oxide layer was dispersed.

PLATE No. 5.2

OXIDE LAYER AT DIFFERENT TIMES OF OXIDATION
OF MOLTEN Ni-20S ALLOY WITH AIR

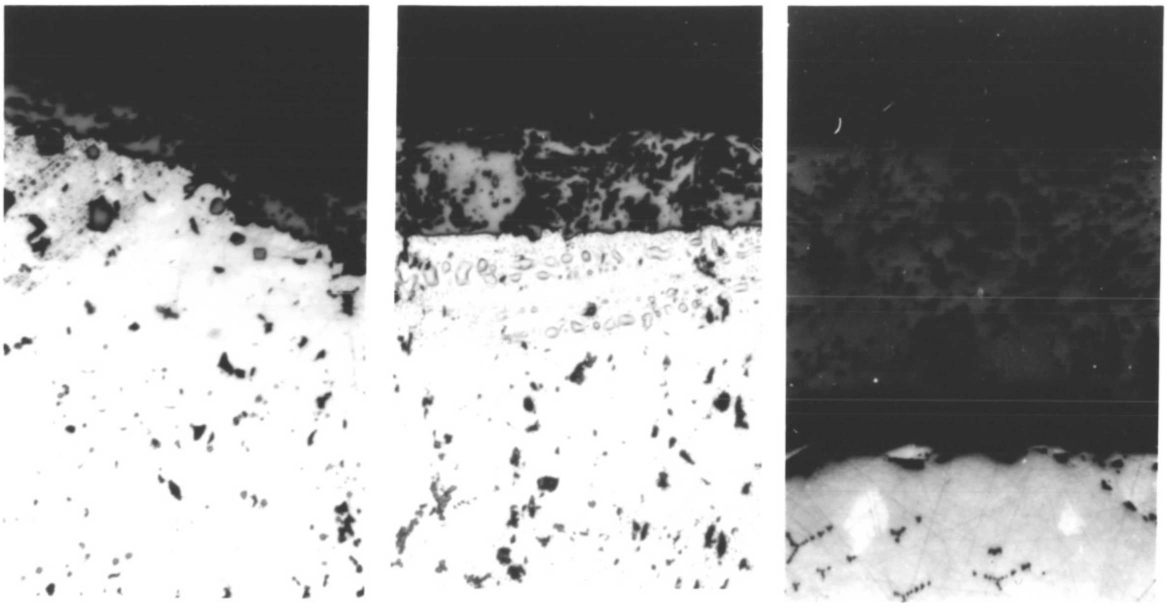

23 RUN NISO 5

40 RUN NISO 6

120 RUN NISO 16

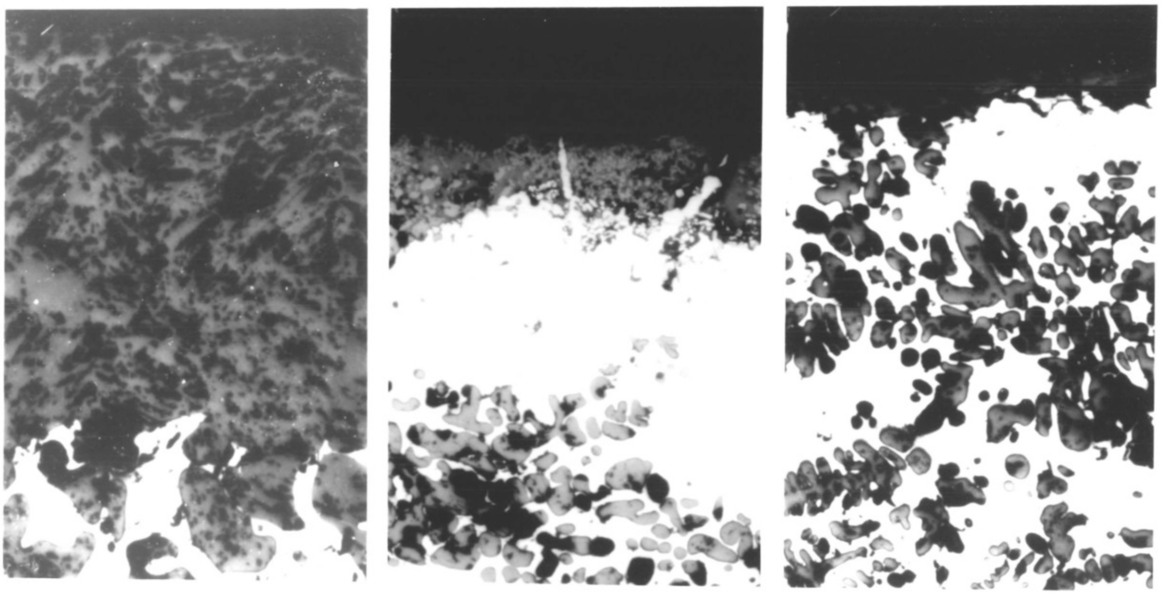

190 RUN NISO 22

194 RUN NISO 15

255 RUN NISO 24

Temperature: 1050°C (LP)
Time shown in min.

Pressure : 45 atm
Magnification : x200

PLATE No. 5.3

FINAL STAGES OF THE OXIDATION OF MOLTEN Ni-20S
ALLOY WITH AIR. RUN NISO 24

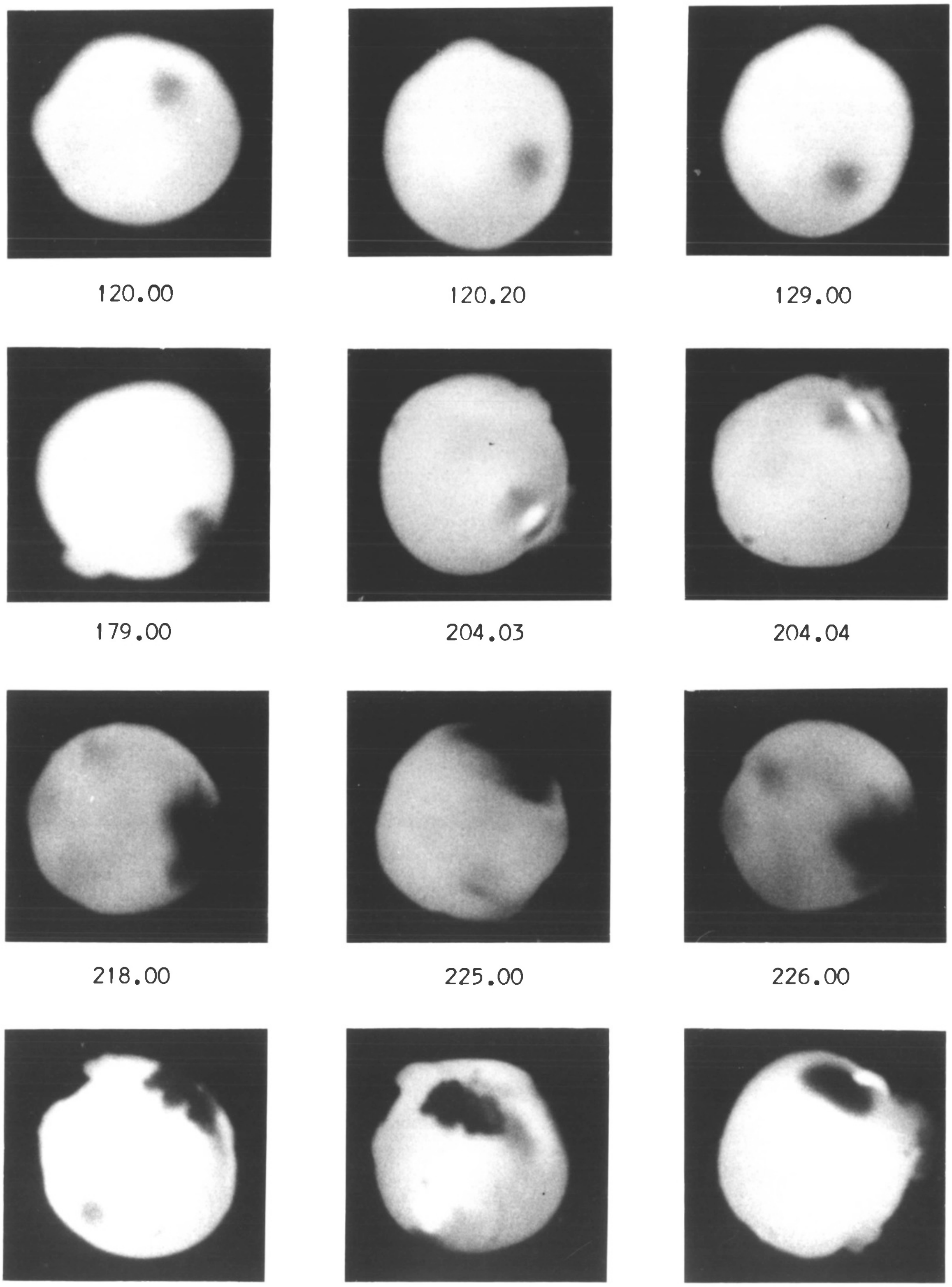

120.00 120.20 129.00

179.00 204.03 204.04

218.00 225.00 226.00

240.00 249.00 249.07

Initial temperature: 1050°C (LP) Pressure: 45 atm
Time shown in min.

Composition of the oxide layer and the bulk of metal

The observation of the oxide layer under a Vickers microscope showed the presence of pores (Plate 5.2). In the bulk of metal dendrites, a white phase and a brown matrix were observed.

The specimen obtained in run NISO 11 after 160 min of reaction was analyzed using EPMA. The concentrations profiles of sulfur, nickel, iron and cobalt were determined by scanning from the bulk of metal to the outer part of the oxide layer (of 300μm thickness). These profiles are shown in Figure 5.6. The concentration of sulfur was practically nil in the oxide layer. The concentration of nickel decreased in the outer part of the layer where the concentrations of iron and cobalt increased.

The elemental analyses of the oxide layer and different phases observed in the bulk of metal were determined using EPMA. The analyses were carried out on the specimen obtained in run NISO 15 (reacted for 194 min). The results are given in Table 5.4. The phases were identified as NiO (oxide layer and dendrites), Ni_3S_2 (brown matrix) and nickel (white phase). The same phases were observed in all the specimens.

X-ray diffraction analysis confirmed that the oxide layer is NiO (bunsenite). Scanning electron microscopy also confirmed the porosity of the oxide layer.

The sulfur concentration in the bulk of metal at different times of reaction was measured by chemical analysis. The results are shown in Figure 5.7. The concentration of sulfur varied erratically around the initial sulfur concentration which was 19.5 wt % (measured by the same analytical method).

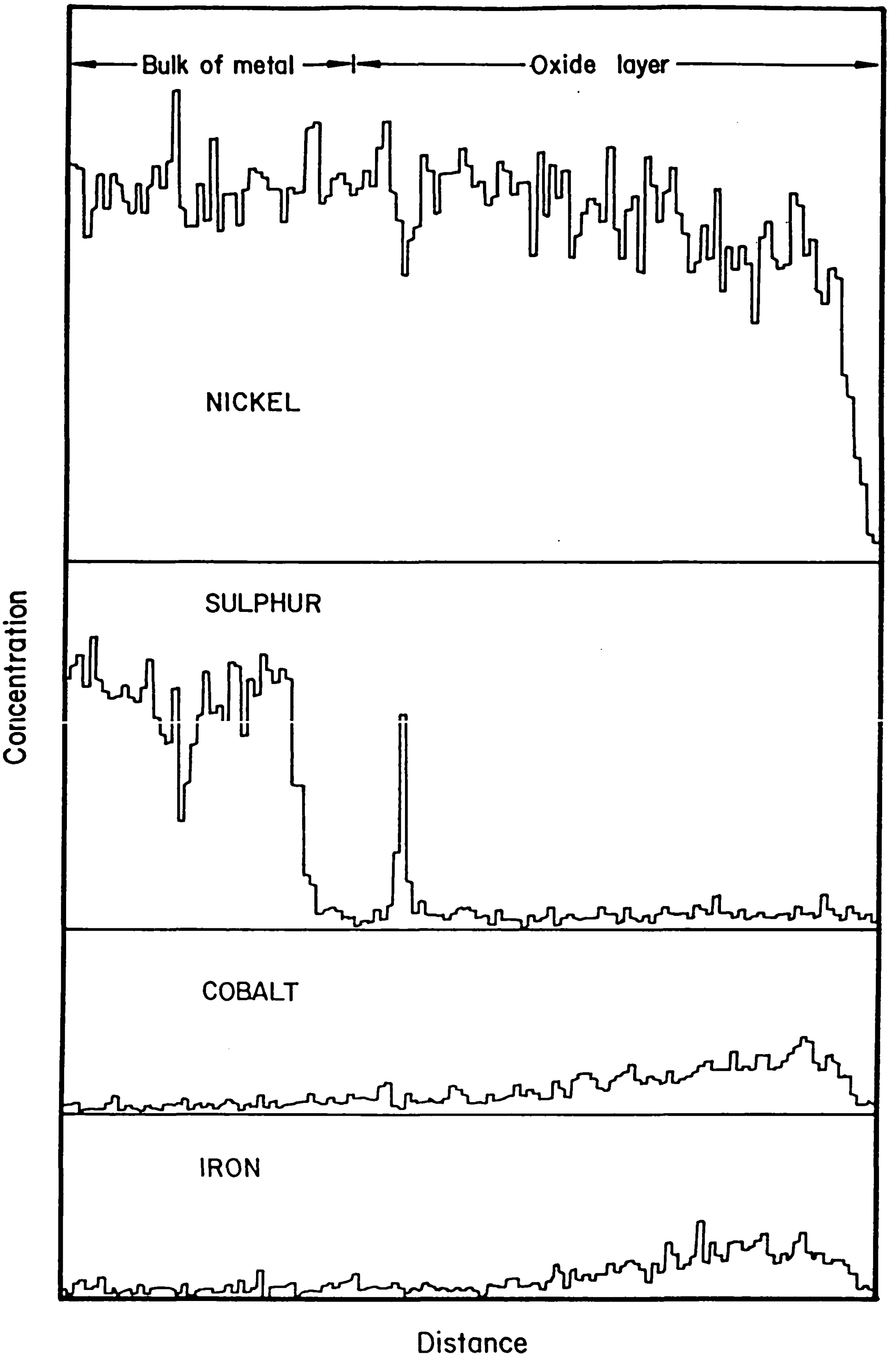

FIGURE 5.6. Concentration profiles of Ni, S, Co and Fe from the bulk of metal to the outer part of the oxide layer of a Ni-20S specimen oxidized in air. Run NISO 11.

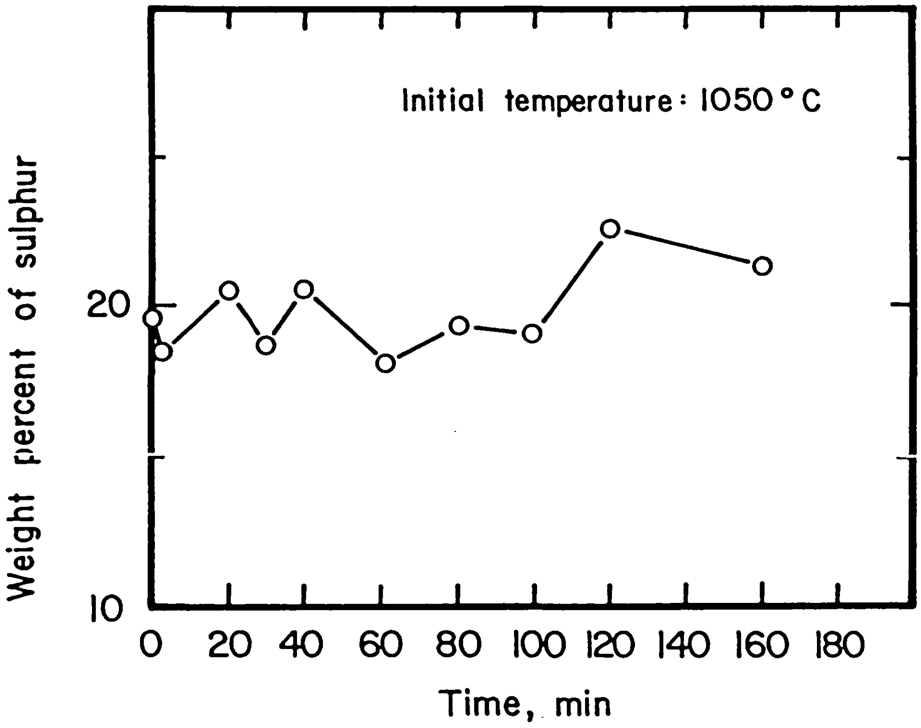

FIGURE 5.7. Weight percent of sulfur in the melt as a function of time during oxidation of Ni-20S specimens in air..

Table 5.4: Electron probe micro analysis of an oxidized Ni-20S specimen. Run NISO 15.

PHASE ELEMENT	OXIDE LAYER	DENDRITE	BROWN MATRIX	WHITE PHASE
	WEIGHT PER-CENT			
S	0.037	0.072	27.409	0.070
Fe	0.712	0.409	0.000	0.067
Ni	77.125	74.163	74.357	98.363
Total	77.874	74.644	101.766	98.500

5.5.2 Oxidation of molten Ni-20S alloy in pure oxygen at 45 atm and 1050°C (LP)

The oxidation of the molten Ni-20S alloy in pure oxygen at 1050°C (initial temperature) had similar characteristics to the oxidation in air at the start of the reaction. Evolution of SO_2 and a temperature increase began after 20 sec in oxygen and lasted for 40 sec. At this time an oxide layer started to form. The formation of the oxide layer is depicted in Plate 5.4. The layer of oxide covered the droplet in 36 msec. After the oxide layer was formed there were no instabilities nor other signs of reaction.

Observation of the specimen under the microscope showed a dense oxide layer and fine dendrites in the bulk of metal. A small increase of the thickness of the oxide layer was registered. The thicknesses were 60μm and 57μm after 180 min and 30 min of reaction respectively (runs NISO 34 and 35).

5.5.3 Oxidation of molten Ni-20S alloy in air at 1150°C (TCP)

The oxidation of the molten Ni-S alloy at an initial temperature of 1150°C (TCP) in air at 45 atm or 24 atm occurred with a continuous

DESCRIPTION OF PLATE NO. 5.4

PICTURE NO.	TIME (Sec)
1	30
2	45
3	55
4	60.000
5	60.002
6	60.014
7	60.017
8	60.025
9	60.032
10	60.034
11	60.035
12	60.036

INITIAL TEMPERATURE OF THE DROPLET: 1050°C (LP)

OXYGEN PRESSURE: 45 atm

PLATE No. 5.4

OXIDE LAYER FORMATION DURING OXIDATION OF MOLTEN Ni-20S ALLOY WITH PURE OXYGEN. RUN NISO 36

1
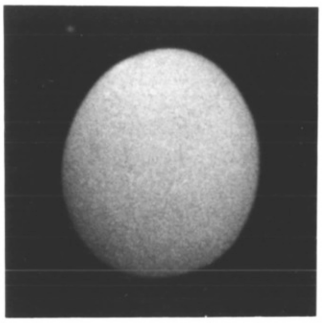

2
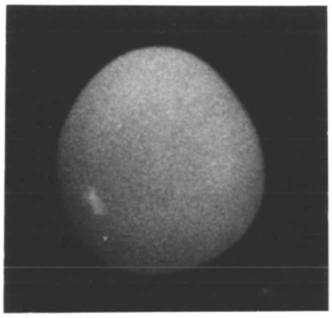

3
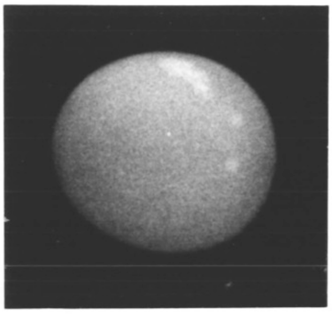

4
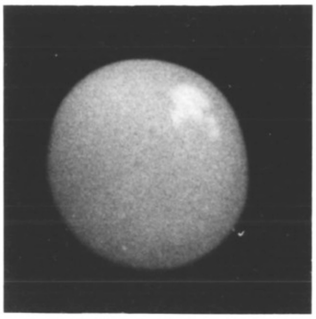

5
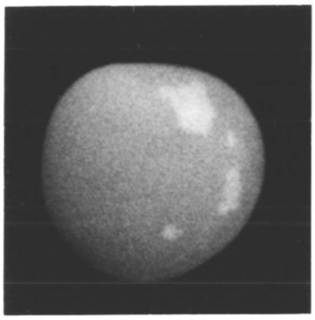

6
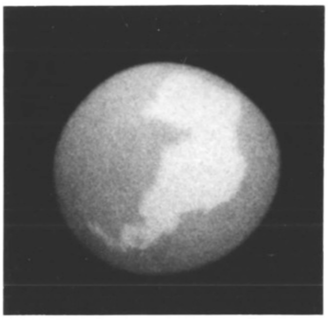

7
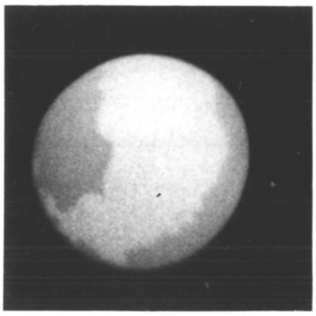

8
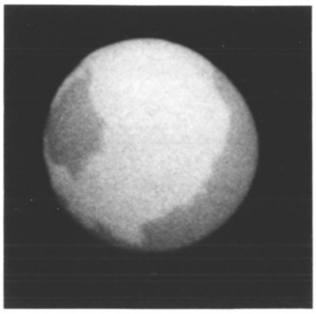

9
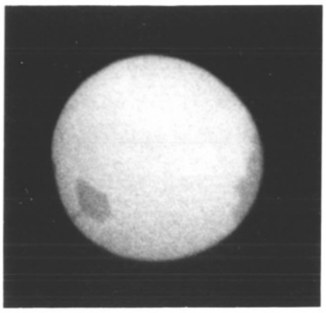

10
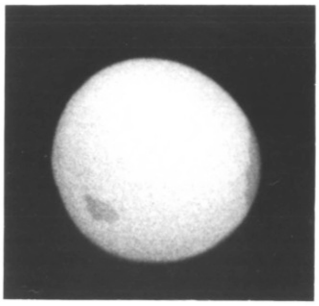

11
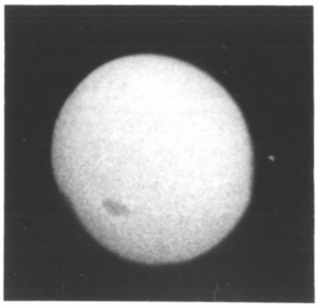

12
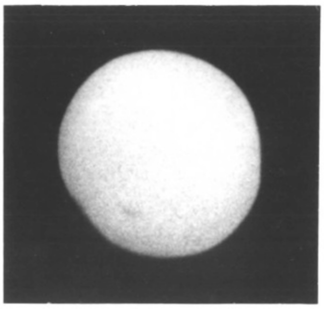

SO_2 evolution and a very rapid increase in temperature up to values higher than 2000°C (TCP). Under these conditions an oxide layer was not formed and a decrease of the mass of the specimen was registered.

Plate 5.5 shows typical pictures taken during the experiment at 45 atm. The droplet was deformed because of the vigorous surface reaction. After 120 sec of reaction the drop fell from the levitation coil.. In experiments at 24 atm the specimen invariably became unstable and hit the silica tube.

A picture of the typical microstructure of an oxidized specimen at 1150°C (TCP) is shown in Plate 5.5. Nickel and fine dendrites of NiO in a Ni_3S_2 matrix were observed.

PLATE No. 5.5

OXIDATION OF MOLTEN Ni-20S ALLOY WITH AIR
WITHOUT OXIDE LAYER FORMATION. RUN NISO 23

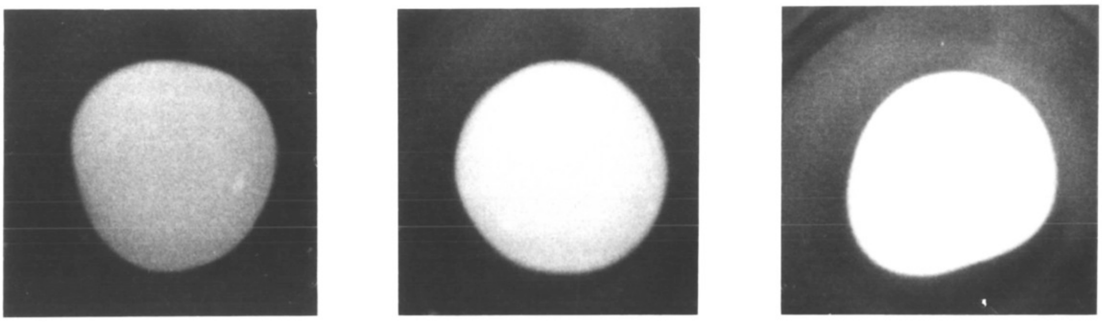

30 45 120

Initial temperature : 1150°C (TCP)
Air pressure : 45 atm
Time of oxidation shown in sec.

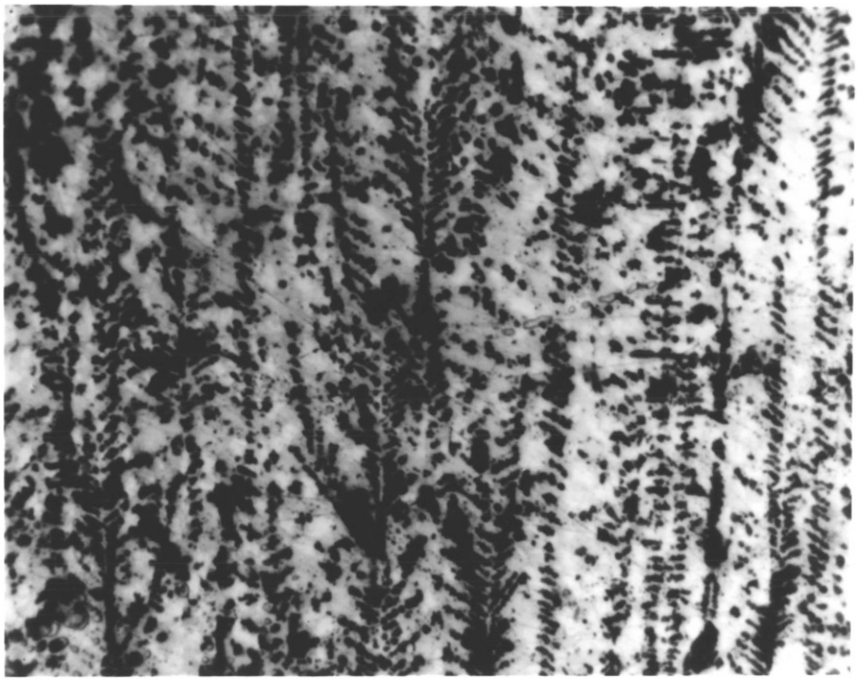

MICROSTRUCTURE OF THE METAL BULK AFTER OXIDATION IN AIR
AT 1150°C (TCP). x200 RUN NISO 10
Phases: Ni (white), NiO (dendrites), Ni_3S_2 (gray)

5.6 Evaluation of results

5.6.1 Model for the first stage of oxidation

According to equation 5.9 oxidation of liquid nickel occurs at very low oxygen potentials (the equilibrium partial pressure of oxygen is 4.5×10^{-10} atm at 1050°C and liquid nickel at unit activity) so that formation of NiO (solid) should occur almost immediately when the Ni-S melt is exposed to a gas containing high oxygen concentration. However, the experimental evidence in this work showed that SO_2 evolution occurred in the first stage of reaction of Ni-20S specimens at initial temperature of 1050°C (LP) with air and pure oxygen until an oxide layer covered the surface droplet. At temperatures higher than 1150°C (TCP) sulfur oxidation occurred without any hindrance. Hence, a theoretical model was developed to predict the conditions under which oxidation of sulfur or nickel takes place preferentially. This model is described in the following paragraphs.

A schematic representation of the concentration profiles in the gas and liquid phases is shown in Figure 5.8. The fluxes were considered positive from the gas to the liquid phase. The following assumptions were made:

a) The partial pressure of SO_2 in the bulk of gas is small and can be neglected.

b) The bulk concentration of sulfur in the liquid phase remains constant.

c) Fast chemical kinetics for the reactions:

$$\tfrac{1}{2}O_2(g) = \underline{O} \text{ (in liq. Ni-S-O)} \qquad (5.3)$$

$$\tfrac{1}{2}S_2(g) = \underline{S} \text{ (in liq. Ni-S-O)} \qquad (5.5)$$

$$\tfrac{1}{2}S_2(g) + O_2(g) = SO_2(g) \qquad (5.11)$$

d) The partial pressure of sulfur is small[82] and sulfur vapor may be neglected in the sulfur mass balance.

e) As the mole fraction of oxygen in the liquid phase is small compared with the sulfur mole fraction the activity coefficients f_S and f_O were considered to be given by the equations:

$$\ln f_S = \varepsilon_S^S\, S \qquad (5.15)$$

and

$$\ln f_O = \varepsilon_O^S\, S \qquad (5.16)$$

where ε_S^S and ε_O^S are the interaction parameters relative to the mole fraction infinitely dilute solution of sulfur on sulfur and sulfur on oxygen respectively.

f) Quasi-steady state conditions.

A balance on oxygen gives:

$$J_{O_2} = (J_O/2) + J_{SO_2} \qquad (5.17)$$

where J_{O_2}, J_O and J_{SO_2} are the molar fluxes of O_2, O and SO_2. This balance can be expressed as:

$$(k_g^{O_2}/RT)(p^b_{O_2} - p^s_{O_2}) = k_l^O(O^s - O^b)C_l/2 + (k_g^{SO_2}/RT)(p^s_{SO_2} - p^b_{SO_2}) \qquad (5.18)$$

A balance on sulfur gives

$$J_{SO_2} = J_S \qquad (5.19)$$

or

$$(k_g^{SO_2}/RT)(p^s_{SO_2} - p^b_{SO_2}) = k_l^S(S^b - S^s)C_l \qquad (5.20)$$

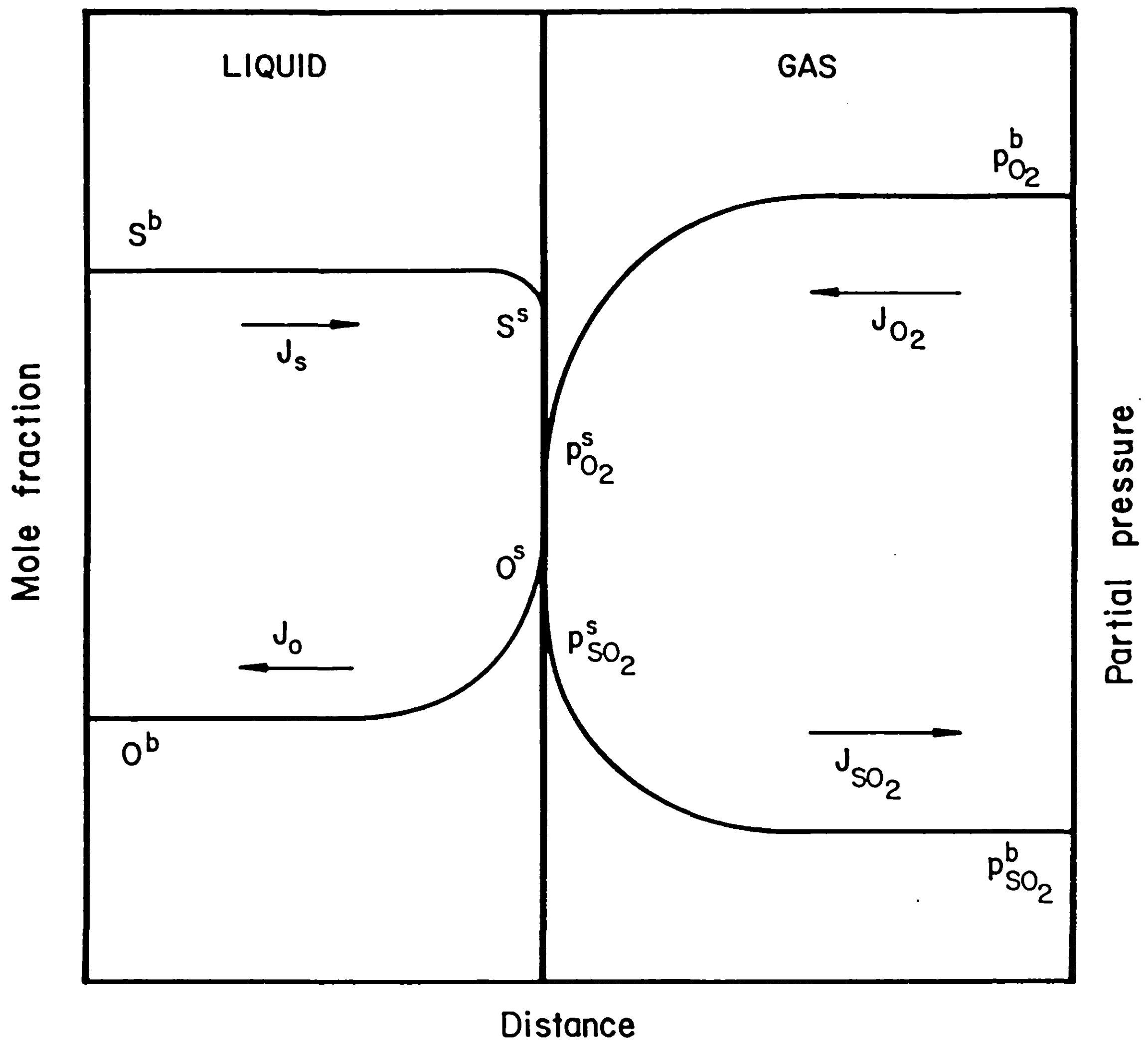

FIGURE 5.8. Schematic representation of the concentration profiles during the first stage of oxidation of liquid Ni-S alloy.

The corresponding true equilibrium constants of reactions 5.3, 5.5 (relative to the mole fraction infinitely dilute solution) and 5.11 are given by the equations:

$$TKO = a_O/p_{O_2}^{s\frac{1}{2}} = f_O O^s/p_{O_2}^{s\ \frac{1}{2}} \qquad (5.21)$$

$$TKS = a_S/p_{S_2}^{s\ \frac{1}{2}} = f_S S^s/p_{S_2}^{s\ \frac{1}{2}} \qquad (5.22)$$

$$TKSO2 = p_{SO_2}^{s}/p_{S_2}^{s\ \frac{1}{2}}\ p_{O_2}^{s\ \frac{1}{2}} \qquad (5.23)$$

In these equations $k_g^{O_2}$ and $k_g^{SO_2}$ are the average gas phase mass transfer coefficients of O_2 and SO_2; k_l^O and K_l^S are the average liquid phase mass transfer coefficients of oxygen and sulfur; C_l is the total molar concentration in the liquid phase; O and S are the mole fractions of oxygen and sulfur in the liquid phase respectively; p_{O_2}, p_{S_2} and p_{SO_2} are the partial pressures of oxygen, sulfur and sulfur dioxide respectively; R is the gas constant and T is the absolute temperature. Superscripts s and b refer to the property on the surface and in the bulk respectively.

The two flux equations and three equilibrium equations allow the calculation of O^s, S^s, $p_{S_2}^s$, $p_{O_2}^s$ and $p_{SO_2}^s$. Combining equations 5.21, 5.22 and 5.23 with equations 5.18 and 5.20 gives two equations for O^s and S^s in terms of bulk concentrations of oxygen and sulfur in the liquid phase (O^b and S^b respectively). The final equations are:

$$(O^s)^4 + B(O^s)^3 + C(O^s)^2 + D(O^s) + F = 0 \qquad (5.24)$$

$$S^s = S^b/\{E(O^s)^2 + 1\} \qquad (5.25)$$

where the coefficients B, C, D, E and F are dimensionless and defined by:

$$B = \alpha\beta \tag{5.26}$$

$$C = -\{\zeta - (1/\delta\varepsilon) + \alpha\beta O^b - \alpha\beta\eta S^b\} \tag{5.27}$$

$$D = \alpha\beta/\delta\varepsilon \tag{5.28}$$

$$E = \delta\varepsilon \tag{5.29}$$

$$F = -(\zeta/\delta\varepsilon) - (\alpha\beta/\delta\varepsilon)O^b \tag{5.30}$$

where α, β, δ, ε, ζ, and η are dimensionless defined by:

$$\alpha = k_l^O/2k_g^{O_2} \tag{5.31}$$

$$\beta = RTC_l(TKO/f_O)^2 \tag{5.32}$$

$$\delta = k_g^{SO_2}/k_l^s \tag{5.33}$$

$$\varepsilon = (1/RTC_l)(TKSO2)(f_O/TKO)^2(f_S/TKS) \tag{5.34}$$

$$\zeta = (TKO/f_O)^2(GO^b)P_T \tag{5.35}$$

$$\eta = 2k_l^S/k_l^O \tag{5.36}$$

In equation 5.35 GO^b is the mole fraction of oxygen in the gas phase and P_T the total pressure.

The coefficients of equations 5.24 and 5.25 are function of temperature, total pressure, composition of the oxidant gas, composition of the Ni-S alloy, ratios of mass transfer coefficients in liquid and gas phases, and thermodynamic properties of the ternary Ni-S-O system.

Equations 5.24 and 5.25 were solved by trial and error method (using a computer program) to calculate O^s and S^s for a particular set of conditions. At the start of the calculation the oxygen mole fractions in the liquid (O^b) was considered equal to zero, then it was increased in small intervals until the corresponding oxygen mole fraction at the surface of the liquid (O^s) was equal to the mole fraction of oxygen in equilibrium with liquid nickel and nickel oxide given by the reaction:

$$Ni(l) + \underline{O} \text{ (in liq. Ni)} = NiO(s) \qquad (5.37)$$

$$\Delta G^\circ_{5-37} = -45702 + 18.96T \text{ (cal/mole)} \qquad (5.38)$$

and

$$K_{5-37} = a_{NiO}/a_{Ni} f_O O^s \qquad (5.39)$$

where K_{5-37} is the equilibrium constant of reaction 5.37 relative to the mole fraction infinitely dilute solution as standard state. Considering NiO at unit activity the mole fraction of oxygen at equilibrium, defined as O^{sat}, is given by:

$$O^{sat} = 1/K_{5-37} a_{Ni} f_O \qquad (5.40)$$

The time to attain the oxygen mole fraction of saturation (O^{sat}) was obtained from the mass balance for oxygen in the liquid under unsteady state conditions given by the equation:

$$C_l V(dO^b/dt) = k_l^O C_l A\ (O^s - O^b) \qquad (5.41)$$

where A and V are the surface area and the volume of the droplet respectively. Considering a spherical droplet and an increment ΔO^b in the mole fraction of oxygen in the bulk of liquid we obtain:

$$\Delta t = (a/3k_l^O)\Delta O^b/(O^s - O^b) \qquad (5.42)$$

where a is the radius of the droplet. The accumulated time is given by:

$$t_{i+1} = t_i + \Delta t \quad (i = 0, 1, 2, \ldots\ldots) \tag{5.43}$$

with the condition $t = 0$ when $O^b = 0$.

Equations 5.24 and 5.25 were solved for different sets of conditions to find out the effect of the temperature of the liquid and of the gas composition on the value of the oxygen mole fraction at the surface (O^s). The conditions used in these calculations are given in Appendix 6. The absolute temperature in equations 5.18 and 5.20 was the film temperature defined as $T = (T_s + T_b)/2$, where T_s is the temperature of the liquid and T_b the bulk temperature of the gas. The true equilibrium constants were calculated at T_S and using the standard free energy values given by equations 5.3 and 5.5 (relative to the mole fraction infinitely dilute solution as standard state) and equation 5.11.

A dimensionless oxygen concentration was defined as O^s/O^{sat} so that when it was unity solid NiO will be formed, this condition will predict oxide layer formation. In Figure 5.9 is shown the effect of temperature on the oxidation of molten Ni-20S alloy with air at 45 atm. The calculation demonstrated that at temperatures lower than 1423°K an oxide layer is formed at $t = 0$. At 1473°K the reactions would proceed for 4 sec before solid NiO is formed. The time for nickel oxide formation increases with the increase of the temperature of the melt. Figure 5.10 shows the effect of decreasing the mole fraction of oxygen in the gas phase (GO^b) to 0.01; in this case oxidation of a molten Ni-20S alloy at 45 atm and at 1273°K would proceed for 18 sec before solid NiO is formed. Figure 5.11 shows the initial value of the ratio O^s/O^{sat} as a function of the mole fraction of oxygen in the gas phase for the oxidation of molten Ni-20S alloy at 45 atm; it is shown that oxidation in air will result in nickel oxide formation at $t = 0$ at any initial temperature less than 1423°K; at a temperature of 1273°K no nickel oxide will be formed in a gas with a mole fraction of oxygen less than 0.03.

Figure 5.12 shows the molar fluxes in the gas and liquid phases as a function of time for the oxidation of a molten Ni-20S alloy at 1823°K in air at 45 atm. At the start of the oxidation $J_0 \approx 2J_{O_2}$, as the mole fraction of oxygen at the surface (O^s) approaches the saturation value (O^{sat}) J_0 decreases to values less than J_{SO_2} so sulfur oxidation becomes more important than oxygen absorption. At low temperatures the increase of J_{SO_2} is small so $J_{SO_2} < J_0$ at any time up to nickel oxide formation, for example at 1623°K J_{SO_2} = 1.3×10^{-5} mole/cm²sec and $J_0 = 2.14 \times 10^{-4}$ mole/cm²sec after 33 sec when $O^s/O^{sat} = 1$.

It is important to note that when O^s is small equation 5.24 may be simplified to a linear equation:

$$D(O^s) + F = 0 \qquad (5.44)$$

Which combined with equations 5.28 and 5.30 gives:

$$O^s = O^b + 2k_g^{O_2} (GO^b)P_T/k_l^0 RTC_l \qquad (5.45)$$

which is equivalent to considering only oxygen absorption. Equation 5.45 contains all the practical variables. The mole fraction of oxygen at the surface of the liquid increases with the increase of the oxygen mole fraction in the gas phase or by increasing the total pressure. It also increases by decreasing the temperature of the melt (T_s) or be decreasing the total molar concentration (decreasing the sulfur concentration in the alloy).

The results predicted by the model have shown that when molten Ni-20S alloy at 1050°C is exposed to air at 45 atm nickel oxide formation should occur immediately without SO_2 evolution. At these

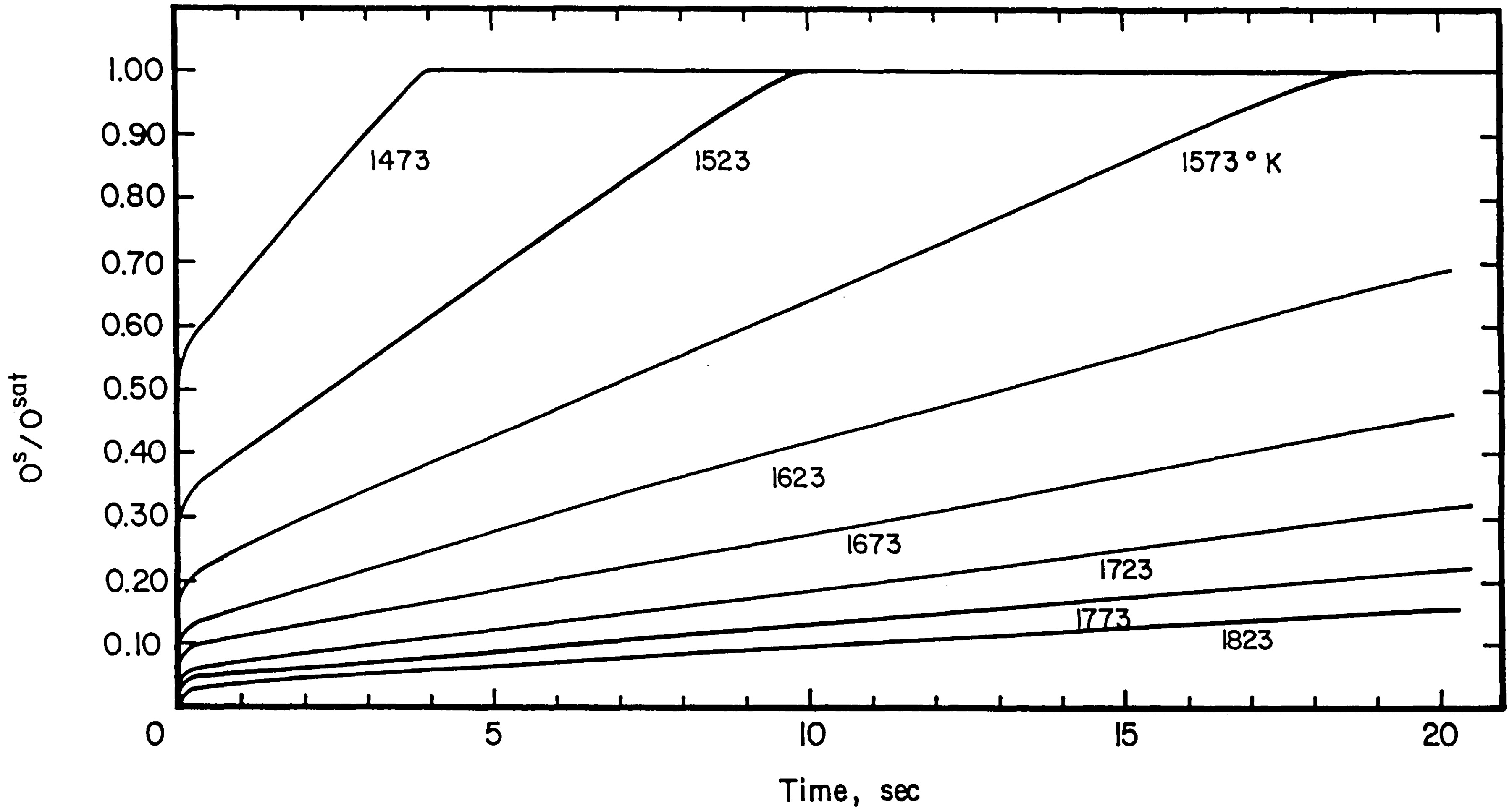

FIGURE 5.9. Change of the ratio O^s/O^{sat} with time during oxidation of molten Ni-20S alloy in air at 45 atm and at different temperatures.

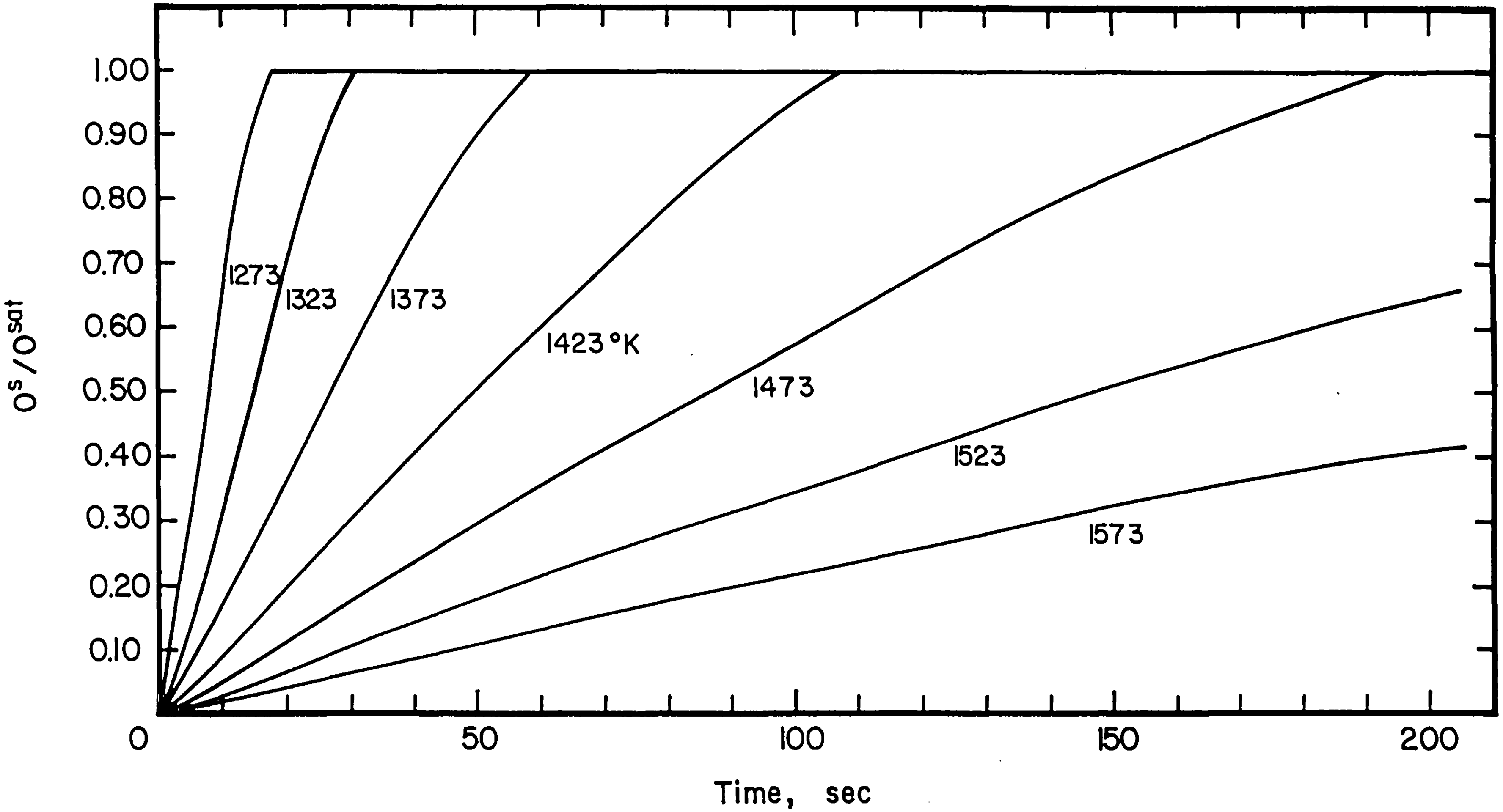

FIGURE 5.10. Change of the ratio O^s/O^{sat} with time during oxidation of molten Ni-20S alloy in a gas mixture containing 0.01 mole fraction of oxygen at 45 atm and at different temperatures.

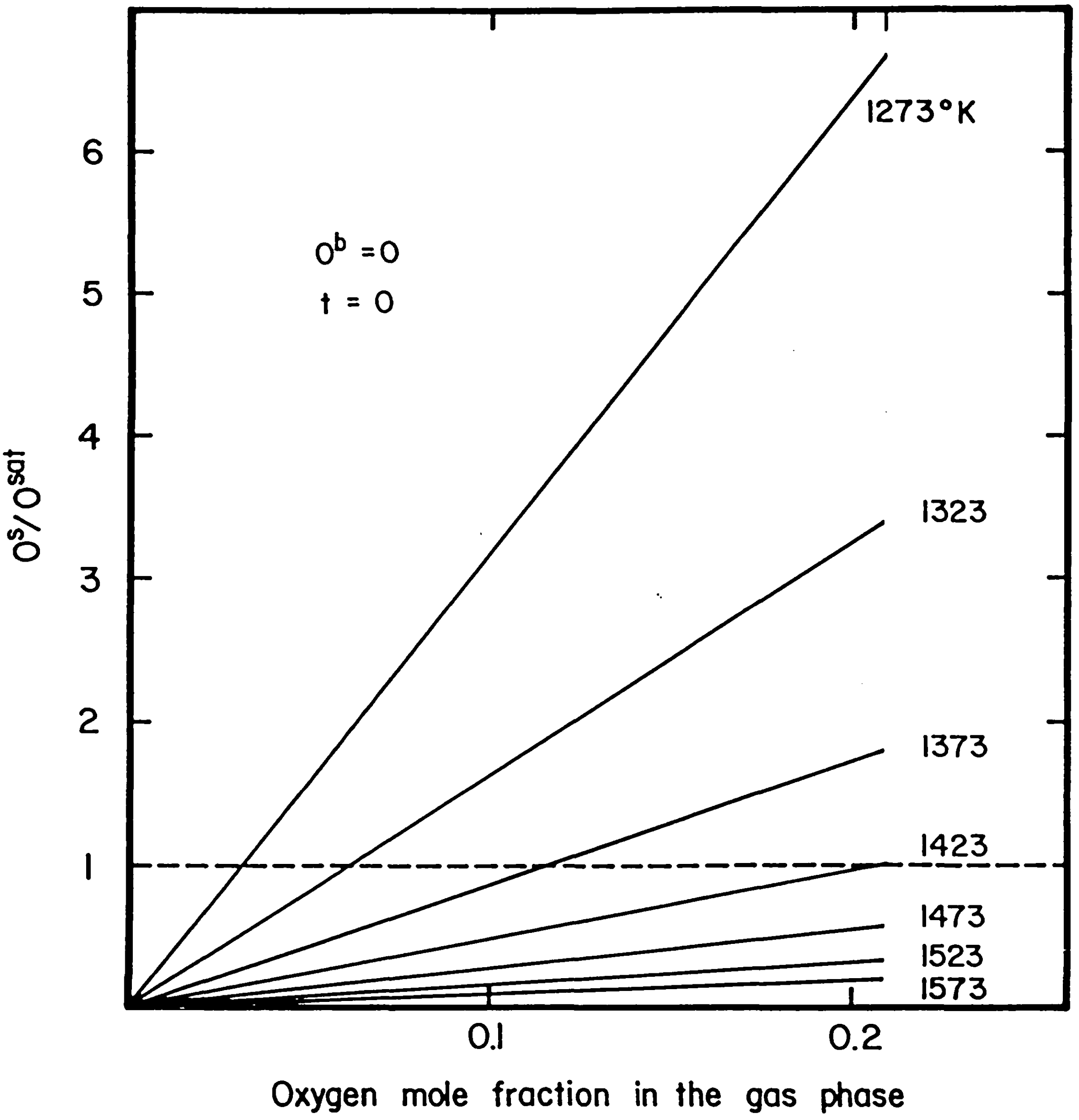

FIGURE 5.11. Initial ratio $0^s/0^{sat}$ as a function of the oxygen mole fraction in the reactant gas at different temperatures. Total pressure: 45 atm. Alloy: Ni-20S.

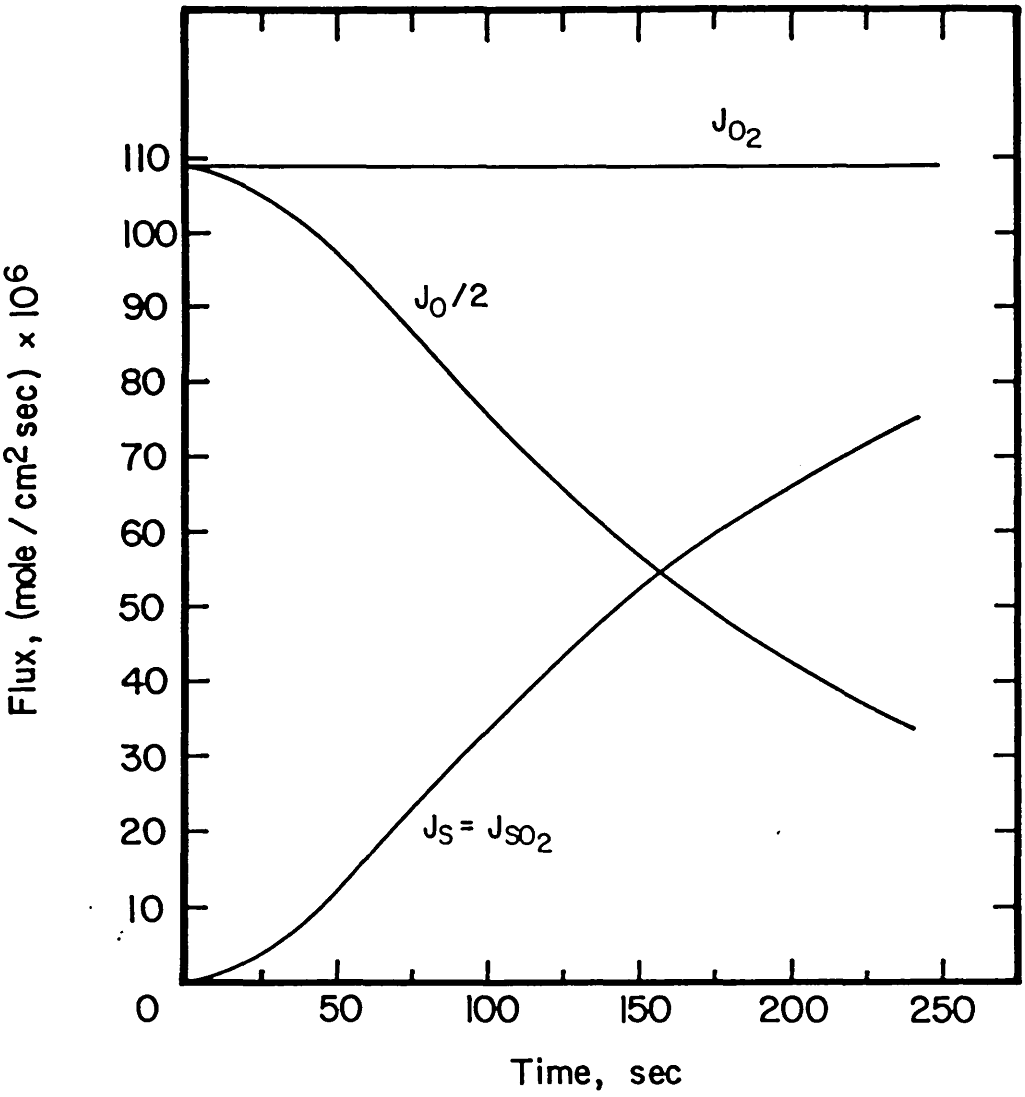

FIGURE 5.12. Molar fluxes as a function of oxidation time. Temperature: 1823 °K. Total pressure: 45 atm. Alloy: Ni-20S.

conditions of temperature and pressure oxidation of sulfur should take place if the oxygen mole fraction in the gas phase were less than 0.06 (Figure 5.11). If the initial temperature of the melt is 1150°C sulfur oxidation should occur if the oxygen mole fraction in the gas were just less than 0.21. Therefore, the results observed in this work during the first stage of oxidation of molten Ni-20S could be explained by an initial oxidation in a gas mixture dilute with respect to oxygen which occurred by the mixing of air and helium in the levitation chamber.

5.6.2 Second stage of the oxidation of molten Ni-20S alloy in air at 1050°C (LP)

A nickel oxide layer covered the droplet after the period of SO_2 evolution. This layer grew uniformly for 100 min (Figure 5.4). A possible mechanism of growth of the oxide layer is presented in the following paragraphs.

Growth of the nickel oxide layer

Nickel forms the oxides NiO, Ni_2O_3 and NiO_2 according to the data of Elliot.[99] Baur et al[100] found that NiO was the only nickel oxide formed during oxidation of nickel at temperatures between 1000 and 1200°C and at oxygen pressures up to 20 atm. Analysis of the oxide layer formed during oxidation of the Ni-20S under the conditions of the present work showed only NiO.

Nickel oxide is an ionic crystal which shows deviations from stoichiometry. Osborn and Vest[101] found that the deviation depends on temperature and oxygen partial pressure, in the formula $Ni_{1-y}O$, y is given by the relationship:

$$y = 0.107 p_{O_2}^{1/6} \exp(-9394/T) \qquad (5.46)$$

The deviation from stoichiometry in NiO is due to electronic and ionic defects in the lattice structure.[102] The defects are nickel ion vacancies with an equivalent number of trivalent nickel ions (Ni^{3+}) to satisfy the condition of electroneutrality:

$$\Sigma z_i M_i = 0 \qquad (5.47)$$

where z_i is the charge number for ions of type i, and $M_i = Ni^{2+}$, Ni^{3+} and O^{2-}. These types of defects characterize a p-type or electron-deficit semiconductor. The mole fraction of nickel ion vacancies is given by the value of y in equation 5.46. The positive excess charges of the nickel ion are called positive holes, they can migrate through the lattice by interchange of charge between divalent and trivalent nickel ions. The existence of vacancies allows the Ni^{2+} cations (which occupy normal positions in the lattice) to move through the lattice, in this process one nickel ion can diffuse to a neighbouring empty lattice position and thus advance by one lattice interval. As a result of this mechanism Ni^{2+} ions and vacancies diffuse in opposite directions.

The penetration of oxygen into the NiO lattice always takes place through chemisorption (which involves molecular dissociation and ionization) and surface reaction with nickel ions of the lattice. Every oxygen ion (O^{2-}) entering to the lattice produces one nickel ion vacancy and two positive excess charges. Using the notation suggested by Schottky[103] the equilibrium between oxygen and the oxide can be represented by the equation:

$$Ni^{2+}|Ni^{2+}| + \tfrac{1}{2}O_2 \rightleftharpoons |Ni^{2+}|'' + 2|e|^{\bullet} + NiO \qquad (5.48)$$

where $Ni^{2+}|Ni^{2+}|$ is a divalent nickel cation in the normal lattice position, $|Ni^{2+}|''$ is a nickel ion vacancy (an un-occupied nickel ion lattice position), $|e|^{\bullet}$ is an electron defect point (positive hole).

Corresponding to the NiO structure discussed above nickel migrates through the oxide lattice via vacancies in the form of Ni^{2+}. In order to maintain electroneutrality a stream of positive holes flows through the layer towards the oxide-liquid interface. The mobility of the positive holes is several orders of magnitude greater than that of ionic defects. Baur et al[100] found that at high oxygen partial pressures and at high temperatures (1000-1200°C) the oxidation rate of nickel was controlled by diffusion of Ni^{2+} through the oxide layer. Further, the rate of oxidation was insensitive to oxygen pressure at pressures above 1 atm. We can assume that the use of high oxygen pressure and high temperature in the present work reduced the importance of the chemical reaction at both interfaces as rate controlling steps. For these conditions it has been found[100,102,103] that the oxide layer grows at a rate which is inversely proportional to its thickness:

$$de/dt = k'/e \qquad (5.49)$$

yielding a parabolic growth relationship:

$$e^2 = 2k't \qquad (5.50)$$

where e is the thickness of the oxide NiO layer, k' is a constant (the parabolic scaling constant) and t the oxidation time. In general k' is a complex function of temperature, oxygen partial pressure and thermodynamic properties of the system.[102]

The thickness of the oxide layer on the liquid Ni-20S alloy under the conditions of the present work (Figure 5.4) grew according to the following relationship:

$$e^2 = 121.2t \qquad (5.51)$$

where e is the thickness of the layer in μm and t the time in min ($t < 100$ min).

If we assume that the mass gain during oxidation is equal to the oxygen mass in the NiO layer then:

$$\Delta m = Ae\rho_O \tag{5.52}$$

where Δm is the mass gain, A the surface area of the drop and ρ_O the density of oxygen in NiO. Combining equations 5.50 and 5.52 we obtain:

$$(\Delta m/A)^2 = (2k'/\rho_O^2)t \tag{5.53}$$

or

$$(\Delta m/A)^2 = k_p t \tag{5.54}$$

where k_p is a constant.

The mass gain measured in the present work (Figure 5.5) was given by the relationship:

$$(\Delta m/A)^{1.61} = 2.07 \times 10^{-5}t \tag{5.55}$$

where Δm is the mass gain in grams, A the surface area in cm² and t the time in sec ($t < 100$ min).

Instabilities

The occurrence of instabilities during the second stage of the reaction (section 5.5.1) was a complex phenomenon. An explanation of the possible mechanism through which the instabilities occurred is attempted in the following paragraphs.

The nickel oxide layer formed during oxidation of Ni-20S alloy specimens with air at 45 atm and 1050°C was porous (section 5.4.1). The porosity could be the result of the SO_2 evolution while the oxide layer was forming on the droplet surface. At the oxide-liquid interface the liquid nickel-sulfur alloy dispersed the oxide layer, this phenomenon could be more intense in zones of greater porosity because of liquid penetration into the pores, leading to a localized dispersion. Possibly the dispersion of the oxide layer was the effect of an incipient reaction between sulfur in solution and nickel oxide given by equation 5.13:

$$\underline{S}\text{ (in Ni)} + 2\text{NiO(s)} = \text{SO}_2\text{(g)} + 2\text{Ni(l)}$$

and the circulation of the liquid due to the electromagnetic field. Kharitidi et al[88] found that reaction 5.13 can develop perceptibly at temperatures as low as 900-1000°C and its rate increases sharply as the temperature increases.

If the liquid nickel-sulfur alloy comes into contact with the oxidizing gas an initial sulfur oxidation would take place by the reaction:

$$\underline{S}\text{ (in Ni)} + \text{O}_2\text{(g)} = \text{SO}_2\text{(g)} \qquad (5.56)$$

which free energy of reaction relative to the weight percent infinitely dilute solution is given by:

$$\Delta G^\circ_{5-56} = -58278 + 13.69T \quad \text{(cal/mole)}$$

No oxygen absorption would occur at the start of the instability because the melt is saturated, with oxygen corresponding to the oxygen concentration fixed by the equilibrium:

$$\text{Ni(l)} + \underline{O}\text{ (in Ni)} = \text{NiO(s)}$$

The temperature of the melt will increase if reaction 5.56 takes place. Corresponding to the decrease in surface sulfur concentration and the increase in temperature of the melt the surface oxygen concentration should increase to reach the new saturation value which would result in formation of a new NiO layer on the surface exposed to the oxidizing gas. Dispersion of this layer would eventually reopen the pore so the process would continue periodically as observed in the experiments.

According to equation 5.13 the interaction between sulfur in solution and nickel oxide is favoured by an increase in sulfur activity in the liquid which may be a result of the Ni^{2+} migration away from the oxide-liquid interface. The sulfur enrichment should increase as the oxide layer thickens. Experimentally the sulfur concentration in the bulk of liquid varied erratically (Figure 5.7), only small increases were obtained at long times of reaction before the oxide layer was dispersed.

5.7 Discussion

5.7.1 Data used and results predicted by the model for the first stage of oxidation

The model for the first stage of reaction predicted the conditions for sulfur oxidation and nickel oxide layer formation at the start of the oxidation of a nickel sulfur melt with an oxygen-bearing gas mixture. The time required to form an oxide layer assuming constant temperature and bulk sulfur concentration could also be estimated.

The data used to apply the model to the oxidation of the Ni-20S alloy under the conditions of the present work were given in Appendix 6. The gas phase mass transfer coefficient of oxygen at a film temperature of 783°K and at 45 atm was calculated as 1.1 cm/sec using the correlation obtained by El-Kaddah[14] for natural convection around levitated drops (Appendix 4). Based in this calculation the gas phase mass transfer coefficients of oxygen and sulfur dioxide, $k_g^{O_2}$ and $k_g^{SO_2}$, were taken as 1 cm/sec. Forster and Richardson[74] reported values of oxygen mass transfer coefficient in liquid nickel greater than 0.01 cm/sec. In the present calculation the mass transfer coefficients of oxygen and sulfur, k_l^O and k_l^S, were assumed to be equal to 0.02 cm/sec and 0.01 cm/sec respectively. Using the interaction parameter $e_O^S = -0.089$, reported by Solar and Bell[95] for Ni-S solutions at 1600°C the interaction parameter ε_S^O was calculated[41] as -10.58, the corresponding activity coefficient of oxygen was 0.037 at 1873°K. Extrapolation of f_O at an average temperature of 1500°K gave $f_O = 0.016$ assuming that the activity coefficient is inversely proportional to temperature.[104] The interaction parameter $e_S^S = -0.053$ was obtained by Solar and Bell[95] based on data for Ni-S melts at temperatures in the range of 800 to 1600°C. The interaction parameter ε_S^S was calculated as -6.20 which gave an activity coefficient of sulfur (f_S) of 0.146.

The linear approximation of equation 5.45 given by:

$$O^s = O^b + 2k_g^{O_2}(GO^b)P_T/k_l^0 \; RTC_l$$

is obviously valid for short times after the start of the oxidation (Figure 5.12). At longer times of reaction terms of higher order in equation 5.24 must be taken into account. However, equation 5.45 is useful to visualize the effect of practical variables on O^s. Particularly the use of high total pressure increases the possibility of oxide layer formation even though there is not direct proportionality between O^s and P_T because k_g is also pressure dependent. The predictions of the model are consistent with the observation of Queneau et al[83] of the preferential oxidation of sulfur at high sulfur concentration of the Ni-S melt (high C_l) in air at 1 atm of total pressure. The results predicted for the oxidation of molten Ni-20S alloy in air at 45 atm and at 1050°C showed that an initial surface sulfur oxidation by molecular oxygen may occur in gas mixtures dilute in oxygen (Figure 5.11). At 1150°C sulfur oxidation at the start of the reaction may occur at gas composition close to that of the air. Experimentally, oxidation of the molten Ni-20S alloy in air at 45 atm and at 1150°C initial temperature proceeded without nickel oxide layer formation. The microstructure of the oxidized specimen showed in Plate 5.5 indicated that even though the main reaction observed was:

$$\underline{S} + O_2 = SO_2$$

a large amount of oxygen was absorbed into the melt which separated as NiO dendrites on solidification. The flux of sulphur predicted by the model for the oxidation of molten Ni-20S alloy in air at 45 atm and at 1623°K (approximately the maximum temperature reached during the first stage) was 1.3×10^{-5} mole/cm²sec compared with an experimental value of 2.2×10^{-5} mole/cm²sec (average) according with the data presented in Table 5.1. The difference may be due to a GO^b in the experiments lower than the corresponding to the air and to the approximate values of melt temperature and of the time during which SO_2 was evolved.

5.7.2 The second stage of the oxidation

Analysis of the oxide layer by EPMA showed iron and cobalt in the outer part (Figure 5.6) indicating that these elements were oxidized together with nickel when the layer was formed.

The growth of the thickness of the oxide layer was very much faster than the oxidation of pure solid nickel at the same temperature. Menzies and Strafford[106] obtained NiO coupons of 150μm thickness by oxidizing nickel sheets in air at 1050°C for 160 hr. This thickness was obtained after 3 hr in the present work (Figure 5.4). The greater rate of growth of the NiO layer in the present work may be due to the following factors:

a) Porosity of the oxide layer. Diffusion of oxygen into open pores would decrease the effective thickness for Ni^{2+} diffusion therefore the oxidation rate would be increased according with equation 5.49.

b) Effect of impurities. The presence of impurities in the alloy with valencies greater than 2 would be expected to increase the concentration of cationic vacancies and hence the rate of oxidation.[102] Trivalent cations, like Fe^{3+} and Co^{3+}, lower the concentration of positive holes and increase the concentration of nickel ion vacancies by the substitution reactions:

$$2|e|^{\bullet} + M_2O_3 = 2M^{3+}|Ni^{2+}|^{\bullet} + 2NiO + \tfrac{1}{2}O_2(g) \qquad (5.57)$$

$$M_2O_3 = 2M^{3+}|Ni^{2+}|^{\bullet} + |Ni^{2+}|'' + 3NiO \qquad (5.58)$$

where $M^{3+}|Ni^{2+}|^{\bullet}$ is a trivalent M ion in the lattice position of a divalent nickel ion.

c) Growth of the oxide layer on a liquid sulfide. This situation has been found in sulfidation of nickel through a preformed NiO layer to produce a liquid nickel sulfide at the oxide-metal interface. Pope and Birks[107] investigated the sulfidation of nickel covered by a nickel oxide layer using gas mixtures of CO, CO_2 and SO_2, they found that a liquid sulfide phase (Ni_3S_2) was formed at the oxide-metal interface at 1000°C. Pope and Birks[107] found that the penetration of the nickel oxide layer by sulfur occurred predominantly by a physical mechanism involving SO_2 diffusion through defects like microcracks and grain boundaries. This finding was consistent with the fact that the sulfur solubility in nickel oxide is low (10^{-2} - 10^{-3} wt %).[108] Accordingly sulfur transfer by a chemical mechanism involving dissolution of sulfur in the oxide lattice and subsequent diffusion of sulfur ions through the nickel oxide layer must be small. Turkdogan[109] pointed out that even though the sulfur solubility in metal oxides is low the rate of oxidation is enhanced in the presence of sulphides. This increase of the rate is believed to occur by some sulfur dissolution in anion sites causing an increase in cation vacancy concentration. Analysis of the oxide layer in the present work showed that the concentration of sulfur was negligible (Figure 5.6) which is in accord with the low solubility of sulfides in nickel oxide at high temperatures mentioned above.

The instabilities observed in the second stage of the reaction were assumed to occur by a mechanism of localized oxide layer dispersion and sulfur oxidation of the fresh liquid sulfide which came in contact with air (section 5.6.2). The possibility of the instabilities being caused by a build-up of SO_2 partial pressure at the oxide-liquid sulfide interface is discussed in the following paragraphs.

The growth in the thickness of the oxide layer measured in this work may have caused a small increase of the bulk sulfur concentration. An oxide layer of 200 μm thickness would increase the sulfur concentration from 20 to about 23 wt %. This increase would have a small effect on the partial pressure of SO_2 if the temperature of the melt remained constant. Equations 5.5 and 5.13 (section 5.3) may be used to define the equilibrium partial pressure of SO_2 at the nickel oxide-liquid sulfide interface:

$$p_{SO_2} = K_{5-5}K_{5-13}(p_{S_2}^{\frac{1}{2}}/a_{Ni}^2) \qquad (5.59)$$

The partial pressure of sulfur over Ni-S melts increases with the increase of temperature or sulfur concentration.[82,93] The activity of nickel decreases sharply with the increase of sulfur concentration and increases slightly with the increase of temperature of the melt.[82] The values of $p_{S_2}^{\frac{1}{2}}$ and a_{Ni} in Ni-S melts at temperatures in the range of 1000 to 1800°C and sulfur concentrations up to 27 wt % may be obtained from the data reported by Meyer et al.[82] For a Ni-20S melt at 1000°C a $p_{S_2}^{\frac{1}{2}}$ of 6×10^{-4} $(\text{atm})^{\frac{1}{2}}$ and an activity of nickel of 0.6 relative to supercooled liquid nickel are obtained and the corresponding p_{SO_2} is 0.014 atm. If the sulfur concentration reached 23 wt % the values of $p_{S_2}^{\frac{1}{2}}$ and a_{Ni} would be 1.8×10^{-3} $(\text{atm})^{\frac{1}{2}}$ and 0.3 respectively leading to a p_{SO_2} of only 0.17 atm, which is very low compared with the total pressure of the system so that the possibility of SO_2 causing rupture of the oxide layer and hence instabilities cannot be considered as an alternative mechanism under the conditions of the present work.

5.8 Conclusions

The results presented in this chapter are regarded as a contribution to the understanding of the reactions between molten metal sulfides and oxygen-bearing gases.

The use of high pressure levitation melting allowed the levitation of a commercial Ni-20S alloy at the low temperatures relevant to roasting of nickel sulfur concentrates in fluidized bed furnaces. A steady temperature of about 1000°C was achieved by levitation in helium at 45 atm.

The oxidation of the levitated drop at 1050°C (LP) with air at 45 atm consisted of two stages. The first stage corresponded to a predominant oxidation of dissolved sulfur and oxygen absorption into the droplet. The temperature increased and later a porous nickel oxide layer was formed. In the second stage growth of the thickness of the oxide layer, almost periodic instabilities, complete dispersion of the oxide layer and SO_2 evolution occurred. The oxide layer consisted mainly of NiO with Fe and Co oxides in the outer part. Negligible sulfur content was found in the oxide layer. Oxidation of the droplet with pure oxygen at 45 atm and 1050°C produced a dense oxide layer which grew very slowly. Oxidation of the droplet in air at 45 atm and an initial temperature of 1150°C (TCP) occurred without nickel oxide layer formation. The oxidized specimen showed a large concentration of NiO dendrites in the bulk of the quenched specimen indicating that oxygen was absorbed into the droplet during reaction to form a homogeneous Ni-S-O liquid.

A simple theoretical model for the first stage of the reaction assuming sulfur surface oxidation and oxygen absorption into the droplet allowed the prediction of the conditions for either oxide layer formation or sulfur oxidation at the start of the reaction. It was shown that formation of nickel oxide is favoured by the use of high oxygen mole fractions in the gas phase, high total pressures, low temperatures of the melt and low sulfur concentration.

The growth of the thickness of the oxide layer was controlled by diffusion of Ni^{2+} ions through the nickel oxide layer. The following relationship was found to describe the growth rate under the conditions of the present work:

$$e^2 = 121.2t$$

where e is the thickness of the oxide layer in μm and t the time in min (< 100 min).

It was found in this work that the solubility of sulfur in the nickel oxide layer is negligible. This result may be relevant to the sulfidation of solid nickel through a preformed nickel oxide layer at high temperatures.

APPENDICES

APPENDIX 1

DESIGN OF VARIOUS PARTS OF THE HIGH PRESSURE LEVITATION APPARATUS

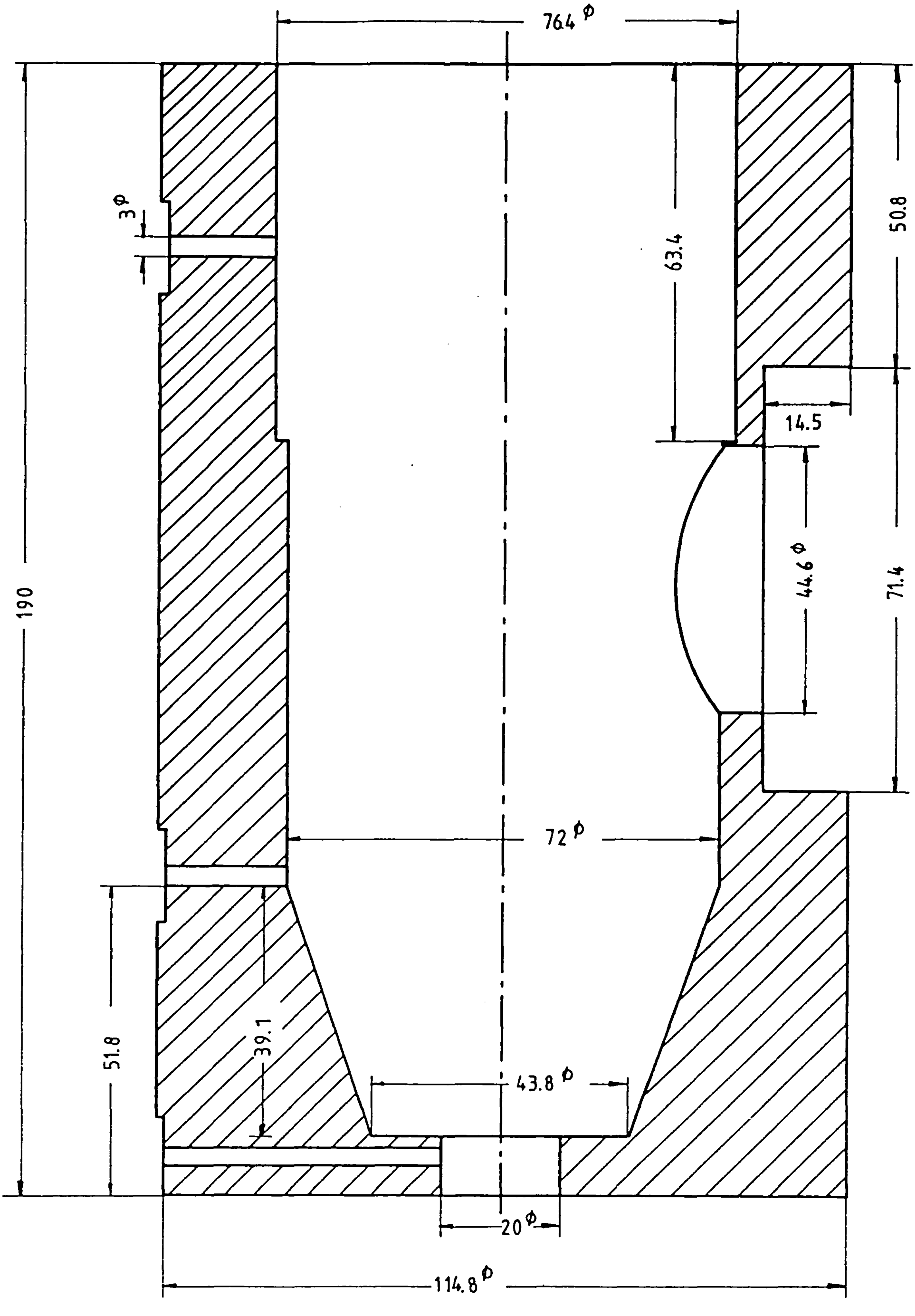

FIGURE A1.1. Cross section of the front view of the pressure chamber. Scale 1:1.

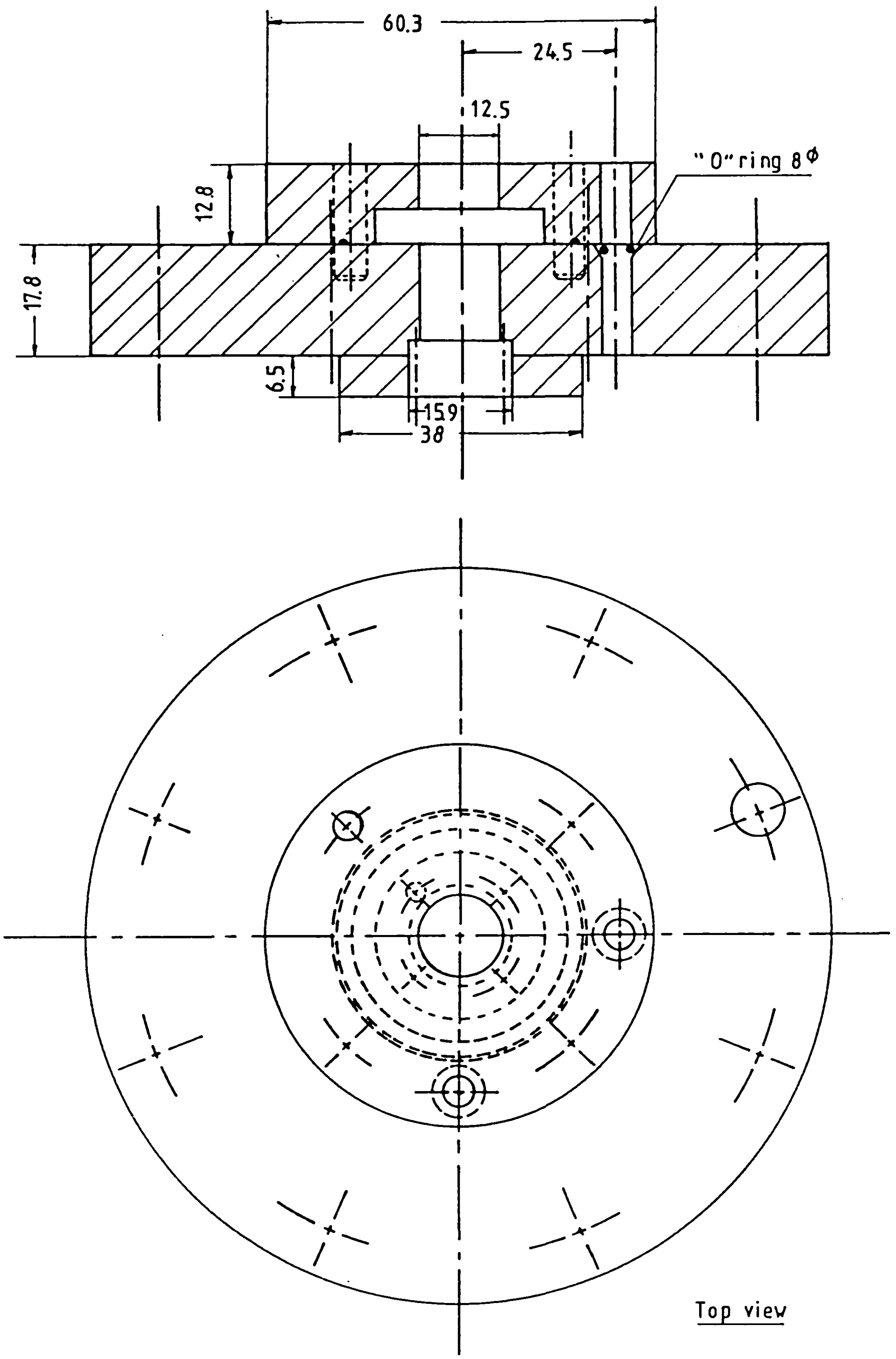

FIGURE A1. 2. Lid of the pressure chamber.
Scale 1 : 1 .

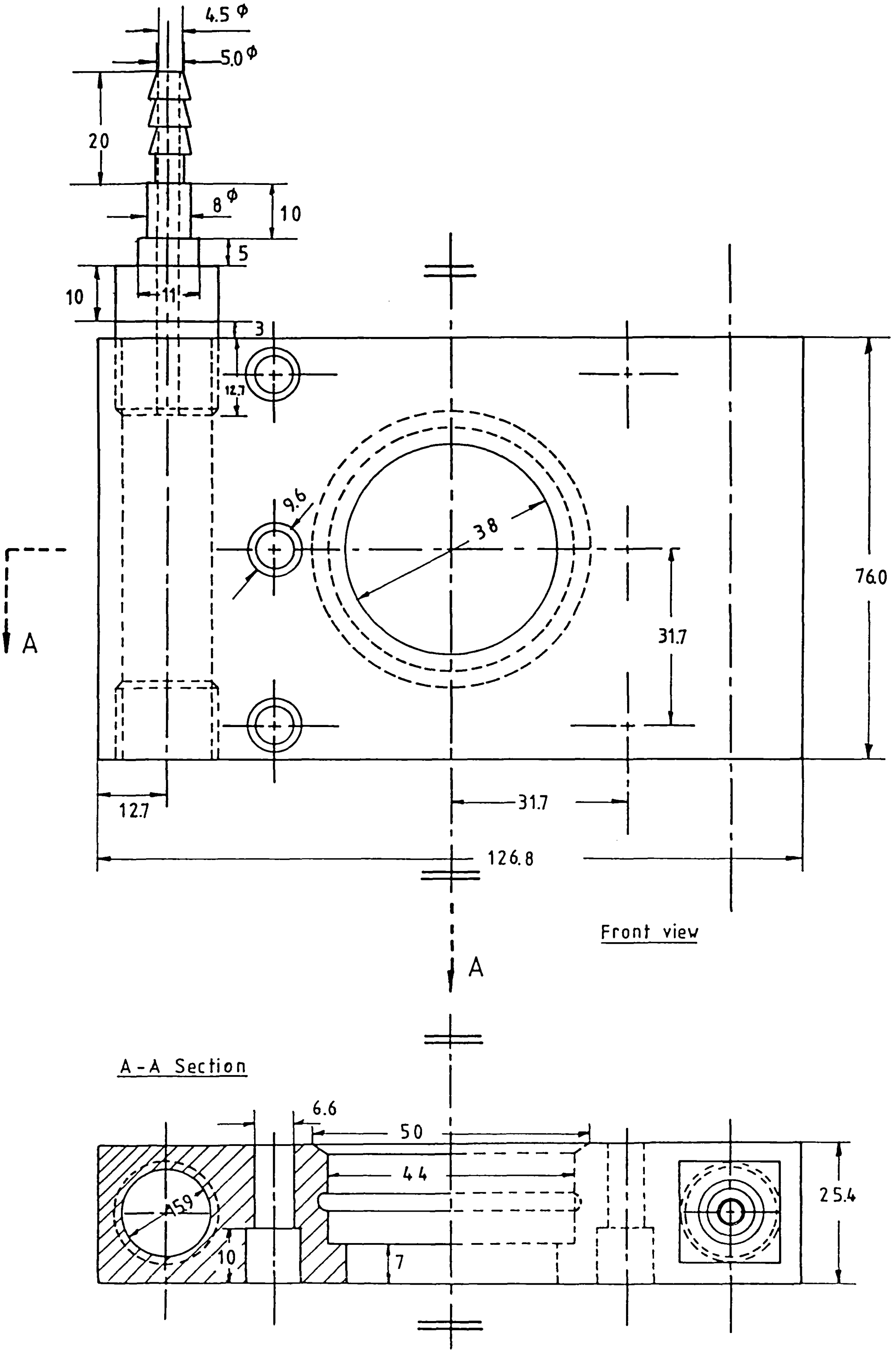

FIGURE A1. 3. Brass flange of the alumina block.
Scale 1:1 .

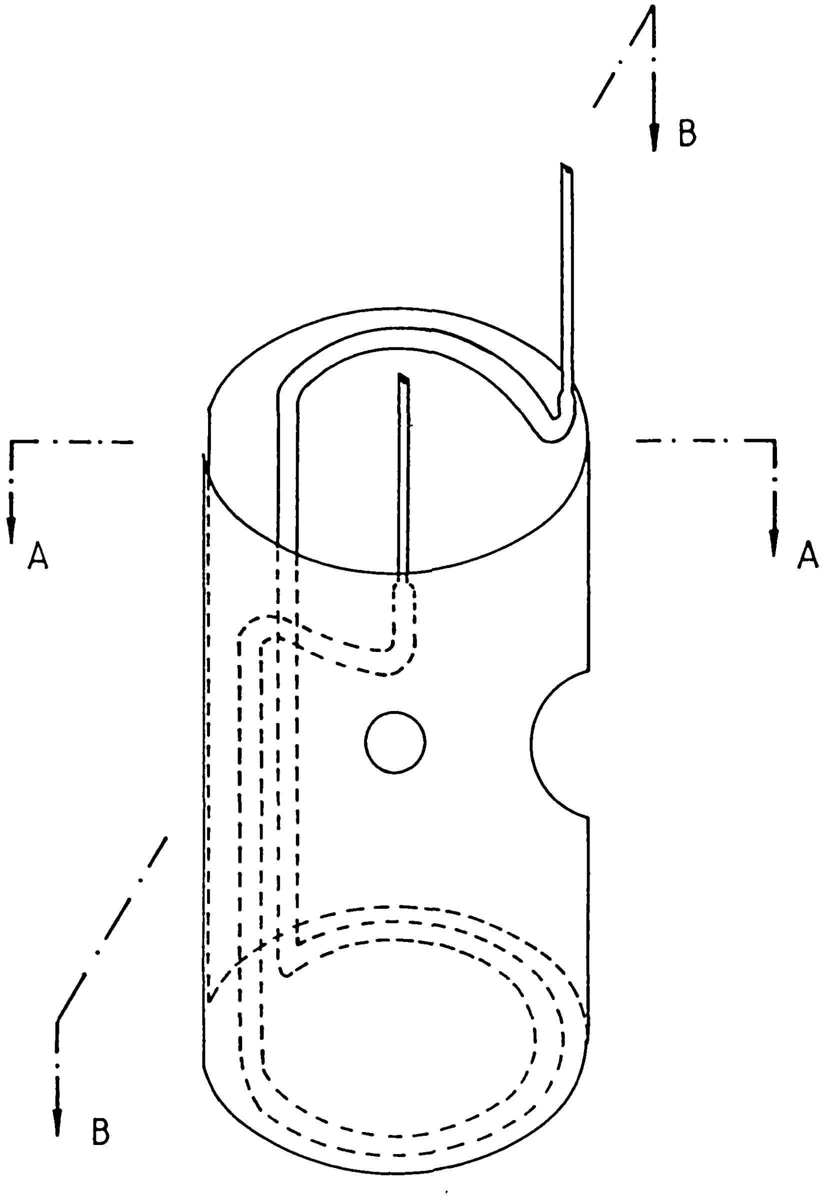

FIGURE A1.4. Cooling system of the HPLA.
Not to scale.

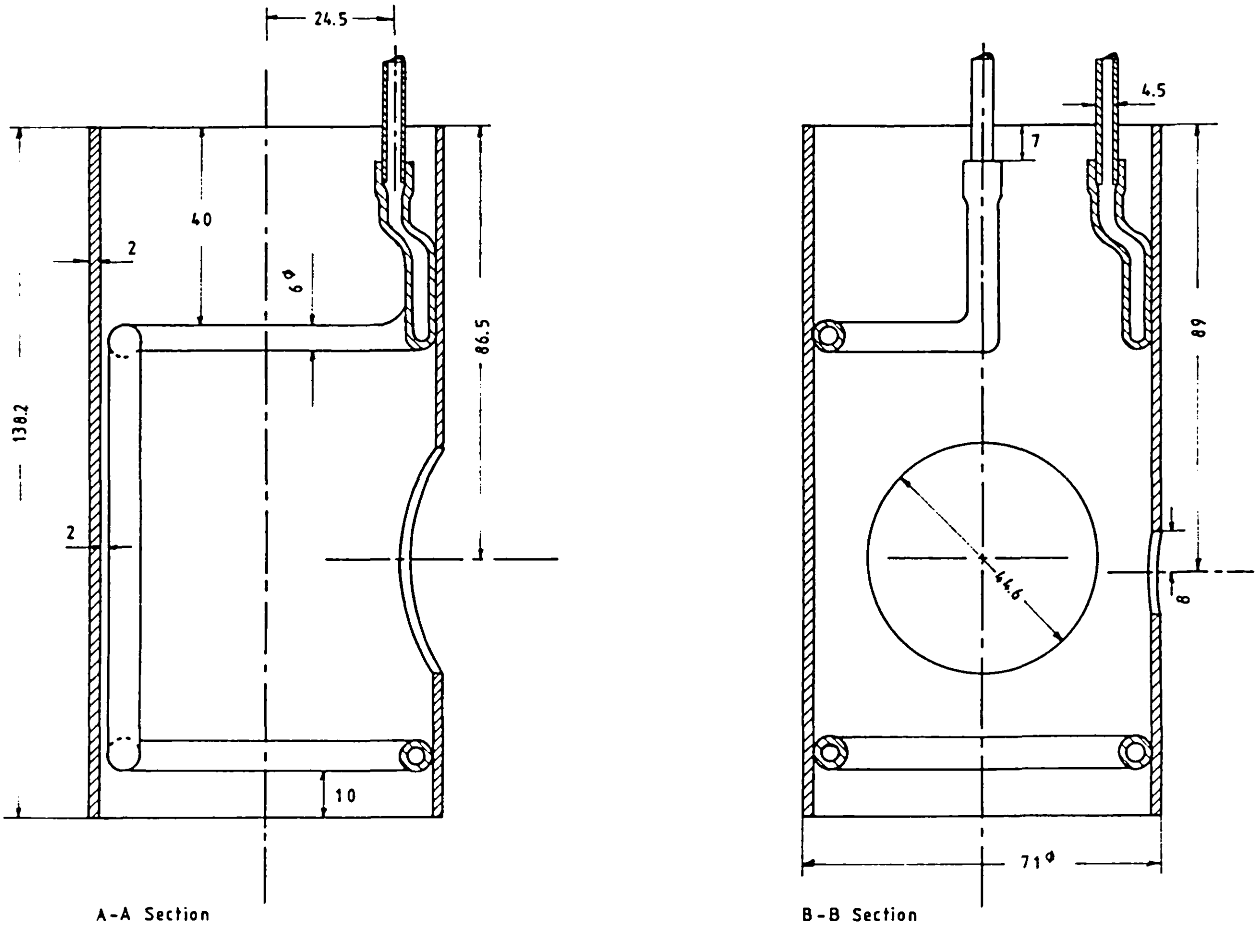

A-A Section

B-B Section

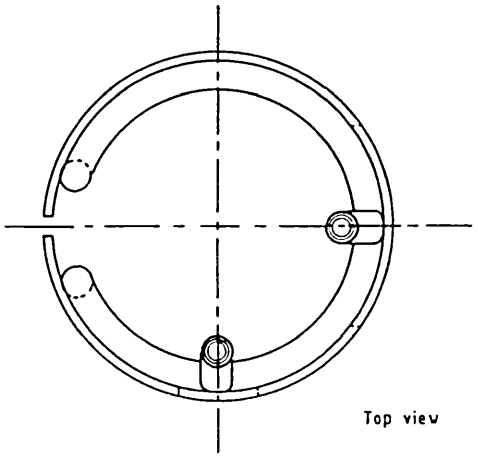

Top view

FIGURE A1.5. Cooling system of the HPLA.
Scale 1:1.5

APPENDIX TWO

Solidification time of liquid iron in the spinning copper quencher

When a liquid metal is suddenly brought into contact with a metal substrate at lower temperature the heat transfer coefficient, h, will depend on the nature of the contact between them. For poor thermal contact h will have low values whereas for ideal thermal contact between substrate and liquid h will tend to infinity. If the heat transfer coefficient is small the temperature gradients in the liquid and substrate are negligible and the cooling is interface-controlled. This situation corresponds to Newtonian cooling.[34]

The thickness of the ribbon is given by the following relationship for solidification:[35]

$$e \sim \tau^n \qquad (A2.1)$$

where τ is the solidification time and n a parameter which ranges from 0.5 for ideal cooling to 1 for Newtonian cooling.

The heat transfer coefficient in melt spinning processes is typically of the order 10^5 W/m²K. Davies et al[36] found that h is about $6 \pm 3 \times 10^4$ W/m²K for melt spinning of nickel-based superalloys. In splat cooling of liquid iron on copper substrate Ruhl[34] found that the heat transfer coefficient is about 42 kW/m²K when the heat transfer is controlled by the interface resistance (Newtonian cooling). This value was used in the present calculation for the liquid cooling and the isothermal solidification.

The heat transfer from the liquid to the substrate before reaching the melting point is given by the following equation:

$$hS(T - T_S) = -\rho VC_p(dT/dt) \qquad (A2.2)$$

where S is the surface area for heat transfer, h the heat transfer coefficient, T and Ts the temperatures of the liquid and substrate respectively, ρ the liquid density, V the liquid volume, C_p the specific heat of the liquid and t the time.

The instantaneous temperature can be calculated by integration of the equation A2.2 with the initial condition: $T = T_L$ at $t = 0$.

$$T = T_S + (T_L - T_S)\exp - (ht/\rho eC_p) \qquad (A2.3)$$

The time to remove the superheat, t_c, can be calculated as a function of the thickness of the liquid film from equation A2.3.

$$t_c = (e\rho C_p/h)\ln[(T_L - T_S)/(T_M - T_S)] \qquad (A2.4)$$

The heat flux during solidification is given by the following equations:

$$Q = h(T_M - T_S) \qquad (A2.5)$$

and

$$Q = \rho L(d\xi/dt) \qquad (A2.6)$$

where L is the heat of fusion and ξ the thickness of the solid. After the assumption of Newtonian cooling the thickness of the ribbon varies linearly with time so $d\xi/dt$ is constant.

$$d\xi/dt = e/t_s \qquad (A2.7)$$

where t_s is the solidification time which can be calculated as a function of the thickness of the ribbon from equations A2.5-A2.6:

$$t_S = L\rho e/h(T_M - T_S) \qquad (A2.8)$$

If the following physical properties are used:

T_L = 1923K, T_M = 1808K, T_S = 298K

h = 41.84kW/m²K, k = 71 W/mK

C_p = 0.790kJ/kg, ρ = 7200 kg/m³, L = 244kJ/kg

the total time for cooling and solidification, t, will be given by the following equation:

$$t = t_s + t_c = 38e \qquad \text{(A2.9)}$$

where t is given in sec and e in m. When the thickness of the ribbon is equal to 1.1 x 10^{-4}m, the average thickness obtained during quenching of iron specimens in this work, the total time is about 4 msec.

The criterion for determining the type of cooling was found by Ruhl[34] to be the quantity he/k where k is the thermal conductivity of the splat material. For high conductivity substrates, such as copper, ideal cooling prevails when he/k > 30 and Newtonian cooling when he/k < 0.015. The value of this quantity in this work is estimated to be 0.065. Accordingly the mechanism of cooling is close to Newtonian.

APPENDIX THREE

X-Ray Diffraction Analyses

A3.1: X-ray diffraction analyses of residues extracted by the bromine-methanol technique

Measured Pattern				Standard Pattern
Diffractometer (Cu-radiation)		Guinier Camera (Co-radiation)		$(Cr,Fe)_7C_3$ ASTM Index Number 5-0720
d(Å)	I	d(Å)	I	d(Å)
2.26	ms	2.27	m	2.30_{40}
2.10	ms	2.10	ms	2.12_{60}
2.03	vs	2.03	vs	2.04_{100}
2.00	ms	2.00	vw	
1.88	vw	1.88	vw	
1.83	ms	1.83	w	
1.80	ms	1.80	w	1.81_{60}
1.73	ms	1.73	vw	1.74_{60}
1.67	w			
1.60	w			
1.50	w			
1.42	m	1.40	vvw	1.46_{20}
1.34	w			1.35_{20}
1.32	w			
1.25	w			
1.20	m			1.20_{5}
1.18	m			1.18_{60}
1.16	ms			1.16_{60}
1.01	w			
0.97	w			
0.88	w			

A3.2: X-ray diffraction analysis of samples scraped from ribbons. Runs OCAT1 and OCAT6

Measured Pattern (Co-radiation)		Standard Pattern Fe_3O_4 ASTM Index Number 11-614
d(Å)	I	d(Å)
		4.85_{40}
2.96	vw	2.96_{70}
2.52	m	2.53_{100}
2.09	s	2.096_{70}
1.87	w	(1.71_{60})
1.81	w	
1.61	vw	1.614_{85}
1.48	vw	1.483_{85}
1.395	vw	1.327_{20}

APPENDIX FOUR

Calculation of the gas phase mass transfer coefficient

At high pressure the gas flow in the boundary layer is dominated by natural convection. El-Kaddah[14] found the following correlation for heat transfer around levitated drops:

$$Nu = 0.78(Gr_H Pr)^{0.25} \qquad (A4.1)$$

with an accuracy of ±10%. From the analogy between heat and mass transfer the following correlation is obtained for mass transfer:

$$Sh = 0.78(Gr_M Pr)^{0.25} \qquad (A4.2)$$

in which the Grashof number Gr_M defined as:

$$Gr_M = \rho_f g d^3(\rho_b - \rho_i)/\mu^2{}_f \qquad (A4.3)$$

contains the corrections due to changes in composition and temperature across the gas boundary layer and can be used as the overall Grashof number.

The terms of equations A4.2 and A4.3 are defined as: $Sh = k'_g d_s/D$ the Sherwood number; $Pr = (\mu c_p/k)_f$ the Prandtl number; d_s the diameter of the specimen; D the interdiffusivity; μ the gas viscosity; ρ the gas density; Cp the heat capacity of gas; k the thermal conductivity of gas; g the acceleration due to gravity; k'_g the average mass transfer coefficient in the gas phase. The subscript f refers to the property at film temperature.

Physical properties

Viscosity and thermal conductivity depend on the film temperature, total pressure and composition of the gas. They were calculated following the procedure given in Bird et al[80] which makes use of reduced properties. Gas densities were calculated as a function of temperature and pressure assuming ideal gas behaviour. Heat capacities were calculated at the film temperature.

The values of the physical properties used in this calculation were as follows:

$T_i = 1823K$
$T_b = 298K$
$T_f = 1060.5K$
$d_s = 0.6cm$
$x_{CO} = 0.9605$
$x_{CO_2} = 0.0395$
$P_T = 65.15$ atm
$g = 980.6\ cm.s^{-2}$
$\mu_{CO-CO_2} = 4.41 \times 10^{-4}\ g.cm^{-1}s^{-1}$

$\mu_{CO} = 4.18 \times 10^{-4} g.cm^{-1}s^{-1}$
$\mu_{CO_2} = 5.83 \times 10^{-4} g.cm^{-1}s^{-1}$
$C_{p_{CO}} = 0.287\ cal.g^{-1}.K^{-1}$
$C_{pCO_2} = 0.299\ cal.g^{-1}.K^{-1}$
$\rho_f = 0.0201\ g.cm^{-3}$
$\rho_b = 0.0716\ g.cm^{-3}$
$\rho_i = 0.0117\ g.cm^{-3}$
$k_{CO} = 136.67 \times 10^{-6}\ cal.cm^{-1}s^{-1}K^{-1}$
$k_{CO_2} = 119.56 \times 10^{-6}\ cal.cm^{-1}s^{-1}K^{-1}$

The interdiffusivity was calculated using the Chapman-Enskog equation for the gaseous state at low density and approximating by the ideal-gas law.[80] Carbon monoxide behaves as an ideal gas up to 100 atmospheres at 300°K,[14] as the gas mixture is dilute in CO_2 its behaviour can be approximated to the ideal. The value calculated of D was $0.0211\ cm^2.s^{-1}$.

Prandtl, Grashof and Sherwood numbers were 0.878, 1.31×10^6 and 25.72 respectively. The corresponding gas phase mass transfer coefficient was:

$$k'_g = 0.90\ cm.s^{-1}$$

from the equation $k_g = (P_T/RT_f)k'_g$ we obtain:

$$k_g = 6.74 \times 10^{-4}\ mole.cm^{-2}.s^{-1}$$

APPENDIX FIVE

Standard free energy of reaction of oxidation of various solutes in liquid iron

The standard free energy of various reactions between solute and dissolved oxygen in liquid iron to form pure oxide are given in this appendix. The standard free energy of formation of the oxides, standard free energy of fusion of elements and standard free energy of solution in liquid iron at 1600°C were taken from the compilation of Turkdogan.[40] The standard states were taken as follows: infinitely dilute weight-per cent solution for solutes, pure solid oxide, pure liquid iron, pure liquid FeO and pure liquid CrO.

REACTION	ΔG° (cal/mole)
$\langle \mathrm{Al_2O_3} \rangle = 2\underline{\mathrm{Al}} + 3\underline{\mathrm{O}}$	289060 - 93.52T
$\langle \mathrm{Cr_2O_3} \rangle = 2\underline{\mathrm{Cr}} + 3\underline{\mathrm{O}}$	190530 - 83.58T
$\langle \mathrm{Cr_3O_4} \rangle = 3\underline{\mathrm{Cr}} + 4\underline{\mathrm{O}}$	225700 - 99.61T
$\{\mathrm{CrO}\} = \underline{\mathrm{Cr}} + \underline{\mathrm{O}}$	56480 - 27.14T
$\{\mathrm{FeO}\} = \{\mathrm{Fe}\} + \underline{\mathrm{O}}$	33200 - 13.52T
$\langle \mathrm{SiO_2} \rangle = \underline{\mathrm{Si}} + 2\underline{\mathrm{O}}$	141150 - 54.62T
$\langle \mathrm{TiO} \rangle_{\beta} = \underline{\mathrm{Ti}} + \underline{\mathrm{O}}$	87560 - 29.14T
$\langle \mathrm{TiO_2} \rangle = \underline{\mathrm{Ti}} + 2\underline{\mathrm{O}}$	161460 - 54.57T
$\langle \mathrm{Ti_2O_3} \rangle = 2\underline{\mathrm{Ti}} + 3\underline{\mathrm{O}}$	260120 - 85.25T
$\langle \mathrm{Ti_3O_5} \rangle = 3\underline{\mathrm{Ti}} + 5\underline{\mathrm{O}}$	419680 - 136.20T
$\langle \mathrm{Al_2O_3.SiO_2} \rangle = \langle \mathrm{Al_2O_3} \rangle + \underline{\mathrm{Si}} + 2\underline{\mathrm{O}}$	143256 - 55.55T
$\langle \mathrm{Al_2O_3.TiO_2} \rangle = 2\underline{\mathrm{Al}} + \underline{\mathrm{Ti}} + 5\underline{\mathrm{O}}$	456560 - 149.03T
$\langle \mathrm{FeO.Al_2O_3} \rangle = \{\mathrm{Fe}\} + 2\underline{\mathrm{Al}} + 4\underline{\mathrm{O}}$	327645 - 108.23T
$\langle \mathrm{FeO.Cr_2O_3} \rangle = \{\mathrm{Fe}\} + 2\underline{\mathrm{Cr}} + 4\underline{\mathrm{O}}$	241530 - 103.47T
$\langle \mathrm{2FeO.TiO_2} \rangle = 2\{\mathrm{Fe}\} + \underline{\mathrm{Ti}} + 4\underline{\mathrm{O}}$	250941 - 92.09T
$\langle \mathrm{MgO.Al_2O_3} \rangle = \langle \mathrm{MgO} \rangle + 2\underline{\mathrm{Al}} + 3\underline{\mathrm{O}}$	297560 - 93.02T
$\langle \mathrm{2MgO.TiO_2} \rangle = 2 \langle \mathrm{MgO} \rangle + \underline{\mathrm{Ti}} + 2\underline{\mathrm{O}}$	167560 - 54.87T

APPENDIX SIX

Data used in the model for the first stage of oxidation of molten nickel-sulfur alloy

$k_g^{O_2} = k_g^{SO_2}$	1 cm/sec
k_l^{O}	0.02 cm/sec
k_l^{S}	0.01 cm/sec
f_O	0.016
f_S	0.146
a_{Ni}	0.6(1)
C_l	97×10^{-3} mole/cm³
S^b	0.314
wt %	20.00
ρ_{Ni-S}	4.88(2) g/cm³
P_T	45 atm
a	0.3 cm

(1) Constant in the range 1000 to 1800°C in a Ni-20 wt % S melt. Standard state is supercooled liquid nickel. (Ref: Meyer et al)[82]

(2) Average in the temperature range 1000-1550°C. (Ref: Byerley and Takebe)[110]

ACKNOWLEDGEMENTS

Sincere gratitude is expressed to my supervisor, Dr D G C Robertson, for his invaluable advice, assistance and encouragement received throughout the course of this work.

I am thankful to Messrs A Neve and M Andrews and their colleagues for technical help and for making several items of equipment. Thanks are also extended to Mr R Chater for SIMS analyses of iron specimens (Chapter Four). I am grateful to Mr J Rossdale and Miss P Martins for their excellent photographic work, and to Ms Heather Stanley for efficiently typing the manuscript.

I am greatly indebted to the Consejo de Desarrollo Cientifico y Humanistico de la Universidad Central de Venezuela for their financial support, which has made possible the period of study at Imperial College. Special thanks are due to the Department of Metallurgy and Materials Science of the UCV for kindly backing me during these years.

Finally, I am particularly grateful to my wife for her patience and constant encouragement, and also for helping in the preparation of the thesis.

LIST OF SYMBOLS

Roman

A	Surface area of the levitated drop
a	Radius of the sphere
a_i	Activity of specie i
C	Carbon concentration
C	Total molar concentration
C_p	Heat capacity
D	Effective diffusivity
D_{12}	Binary diffusion coefficient
D_1^T	Binary thermal diffusion coefficient
d	Interplanar spacing
d_s	Diameter of the levitated drop
e	Thickness
e	Interaction parameter (concentration in weight percent)
f	Activity coefficient
f_O^O	Activity coefficient of oxygen in the binary Fe-O
f_O^C	Interaction coefficient of carbon on oxygen
G	Gibbs free energy
$\overline{G}$	Partial molal free energy
GO^b	Oxygen mole fraction in the bulk of gas
g	Acceleration due to gravity
h	Heat transfer coefficient
I	Relative intensity
J	Molar flux
j	Mass flux
$j_{1r}^{(x)}$	Mass flux due to concentration gradient

$j_{1r}^{(T)}$	Mass flux due to temperature gradient
K	Equilibrium constant
K'	Apparent equilibrium constant
k	Thermal conductivity
k'	Parabolic scaling constant
k_g	Mass transfer coefficient in the gas phase
$\overline{k}_g$	Overall gas phase mass transfer coefficient
k_l	Mass transfer coefficient in the liquid phase
k'_l	Mass transfer coefficient in the liquid phase (concentration in weight percent)
k_R	Rate constant
L	Heat of fusion
M	Molecular weight
M_i	Ion of type i
m	Mass gain during oxidation
N	Angular speed of the spinning quencher
N	Molar flux
n	Parameter
O	Oxygen mole fraction
P_T	Total pressure
p	Partial pressure
Q	Heat flux
R	The gas constant
r	Position coordinate
S	Sulfur mole fraction
S	Surface area for heat transfer
s	Distance travelled by the freely falling drop
T	Absolute temperature (°K)
t	Temperature (°C)
t	Time

TK	True equilibrium constant
V	Volume of liquid
x	Mole fraction
x'	Mole fraction corrected for thermal diffusion
y	Mole fraction of nickel ion vacancies
w	Weight of the levitated drop
z_i	Charge number for ions of type i

Greek

α	Thermal diffusion factor
Δ	Change of the property value
δ	Thickness of the gas film boundary layer
ε	Interaction parameter (concentration in mole fraction)
η_g	Overall to actual mass transfer coefficient
θ	Angle of spinning quencher
θ_s	Fraction of surface sites occupied by an adsorbed specie
μ	Viscosity coefficient
ξ	Instantaneous thickness of the solid
ρ	Mass density
σ	Surface tension
τ	Solidification time

Subscripts

b	Bulk value
e	Equilibrium value
g	Gas phase
L	Liquid phase
l	Liquid phase
M	Value at the melting point

S	Substrate
s	Surface value
0	Initial value

Superscripts

b	Bulk value
e	Equilibrium value
i	Interfacial value
s	Surface value
sat	Saturation value
•	Transfer coefficient corrected for mass-transfer rate

Dimensionless groups

Gr	Grashof number
Nu	Nusselt number
Pr	Prandtl number
Sh	Sherwood number

Abbreviations

a.m.u.	Atomic mass unit
AOD	Argon-oxygen-decarburization
ELM	Chemical element
EPMA	Electron probe micro analysis
HPLA	High pressure levitation apparatus
LIMA	Laser induced ion mass analyser
LP	Land pyrometer
L & N	Leeds and Northrup pyrometer
ln	Natural logarithm ($\log_e$)

log	Common logarithm ($\log_{10}$)
SIMS	Secondary ion mass spectrometer
slm	Standard litre per minute
TCP	Two-colour pyrometer
vol. pct.	Volume percent
wt %	Weight percent
∞	Infinite value

REFERENCES

1. OKRESS, E.C. et al. Electromagnetic levitation of solid and molten metals. Journal of Applied Physics. May 1952: 23, 545-552.
2. LANGERON, J.P. and BIGOT, J. Preparation of perfectly controlled alloys by levitation melting. In: Proceedings of Sixth International Vacuum Metallurgy Conference on Special Melting, held in San Diego, California, 23-27 April 1979. 443-449.
3. SNEYD, A.D. and MOFFATT, H.K. Fluid dynamical aspects of the levitation melting process. Journal of Fluid Mechanics. 1982: 117, 45-70.
4. PEIFER, W.A. Levitation melting -a survey of the state of the art. Journal of Metals. May 1965: 17, 487-493.
5. ROSTRON, A.J. Levitation melting. Science Journal. July 1967: 3, 69-73.
6. JENKINS, A.E., HARRIS, B. and BAKER, L. Electromagnetic levitation and its use in physicochemical studies at high temperature. In: Symposium on Metallurgy at High Pressures and High Temperatures. Metallurgical Society of AIME, Gordon and Breach Science Publications, 1964. Vol. 22, 23-43.
7. JAHANSHAHI, S. and JEFFES, J.H.E. Design of coils for levitating droplets of metal with improved temperature control characteristics. Transactions of the Institute of Mining and Metallurgy C. December 1981: 90, 138-141.
8. EL-KADDAH, N.H. and SZEKELY, J. The electromagnetic force field, fluid flow field and temperature profiles in

levitated metal droplets. MIT, Department of Materials Science and Engineering, 1982. Unpublished work.

9. RICHARDSON, F.D. Physical chemistry of metals in metallurgy. London: Academic Press, 1974. Vol. 2, 462-474.

10. RODDIS, P.G. Mechanism of decarburization of iron-carbon alloys drops falling through an oxidizing gas. Journal of the Iron and Steel Institute. January 1973: 53-58.

11. SEE, J.B. and WARNER, N.A. Reactions of iron alloy drops in free fall through oxidizing gases. Journal of the Iron and Steel Institute. January 1973: 44-52.

12. RAO, G.S. Kinetics and mechanisms of gas-metal-slag reactions relevant to steelmaking. Ph. D. Thesis, University of London, August 1979.

13. HARRIS, J. Oxidation studies of molten steel drops. B. Sc. Project Report, Imperial College, Department of Metallurgy and Materials Science, 1979.

14. EL-KADDAH, N.H. Carbon-oxygen equilibrium and homogeneous nucleation of carbon monoxide bubbles in levitated molten iron. Ph. D. Thesis, University of London, November 1975.

15. EL-KADDAH, N.H. and ROBERTSON, D.G.C. Equilibria in reactions of CO and CO_2 with dissolved oxygen and carbon in liquid iron. Metallurgical Transactions B. December 1977: 8 B (4), 569-579.

16. ROBERTSON, D.G.C. Heterogeneous reactions and mass transfer from liquid metal drops in gases. Ph. D. Thesis, University of New South Wales, December 1968.

17. MORRIS, J.P., RIOTT, J.P. and ILLIG, E.G. A new look at the cause of fuming. Journal of Metals. July 1966: 803-810.

18. BAKER, L.A. and WARD, R.G. Reaction of an iron carbon droplet during free fall through oxygen. Journal of the Iron and Steel Institute. July 1967: 205 (7), 714-717.

19. BAKER, R. Oxidation studies of molten iron alloy drops. Journal of the Iron and Steel Institute. June 1967: 205 (6), 637-641.

20. HILTY, D.C. Relation between chromium and carbon in chromium steel refining. Transactions of the Metallurgical Society of AIME. February 1949: 185, 91-95.

21. DENNIS, W.E. and RICHARDSON, F.D. The equilibrium controlling the decarburization of iron-chromium-carbon melts. Journal of the Iron and Steel Institute. November 1953: 264-266.

22. NAKAMURA, Y., OHNO, T. and SEGAWA, K. Carbon and oxygen in molten high Cr-Fe alloys in equilibrium with Cr oxides. Proceedings of the International Conference on the Science and Technology of Iron and Steel, supplement. Transactions of the Iron and Steel Institute of Japan. 1971: 11, 456-459.

23. LEACH, J.C.C., RODGERS, A. and SHEEHAN, G. Operation of the AOD process in BSC. Ironmaking and Steelmaking. 1978: (3), 107-119.

24. BOCQUET, J.P. and THEVENIN, J.P. Accuracy and reliability of the AOD process at the Isbergues AOD converter. In:

Proceedings of the Third International Iron and Steel Congress, held in Chicago, Illinois, 16-20 , April 1978, Metals Park, Ohio: American Society for Metals, 1978. 168-173.

25. CHOULET,R.J., DEATH, F.S. and DOKKEN, R.N. Argon-oxygen refining of stainless steel. Canadian Metallurgical Quarterly. 1972: 10 (2), 129-136.

26. KUWANO, T., MARUHASHI, S. and AOYAMA, Y. Decarburization of molten high chromium steel under reduced pressure. Transactions of the Iron and Steel Institute of Japan. 1975: 15, 353-360.

27. FRUEHAN, R.J. Nitrogenation and decarburization of stainless steel. Metallurgical Transactions B. December 1975: 6 B, 573-578.

28. VOSTRYAKOV, A.A. and LEPINSKIKH, B.M. Kinetics of chrome-oxide reduction by carbon dissolved in iron. Russian Metallurgy (Metally). 1975: 5, 9-11.

29. FRUEHAN, R.J. Rate of reduction of Cr_2O_3 by carbon and carbon dissolved in liquid iron alloys. Metallurgical Transactions B. September 1977: 8 B, 429-433.

30. SUZUKI, K. and MORI, K. Rate of reduction of Cr_2O_3 by carbon dissolved in liquid Fe-Cr alloys. Transactions of the Iron and Steel Institute of Japan. 1980: 20, 607-613.

31. PATTERSON, R.J., COX, A.R. and VAN REUTH, E.C. Rapid solidification rate processing and application to turbine engine materials. Journal of Metals. September 1980: 34-39.

32. DINGLE, T., GRIFFITHS, B.W. and RUCKMAN, J.C. LIMA -a laser induced ion mass analyser. Vacuum. 1981: 31 (10-12), 571-577.

33. SMERKO, R.G. and FLINCHBAUGH, D.A. Recent progress in the chemical extraction of nonmetallic inclusions in steel- techniques and applications. Journal of Metals. July 1968: 43-51.

34. RUHL, R.C. Cooling rates in splat cooling. Materials Science Engineering. 1967: 1, 313-320.

35. HILLMAN, H. and HILZINGER, H.R. On the formation of amorphous ribbons by the melt spin technique. In: Third International Conference of Rapidly Quenched Metals, held in Brighton 1978. London: The Metals Society, 1978. Vol. 1, 22-29.

36. DAVIES, H.A., SHOHOJI, N. and WARRINGTON, D.H. The structures of rapidly quenched nickel based super alloy ribbons produced by melt spinning. In: Proceedings of the Second International Conference of Rapid Solidification Processing, held in Reston, Virginia, March 23-26, 1980. Baton Rouge: Claitor's Publishing Division, 1980. 153-164.

37. MURARKA, R.N., LU, W.K. and HAMIELEC, A.E. Effect of dissolved oxygen on the surface tension of liquid iron. Canadian Metallurgical Quarterly. 1975: 14 (2), 111-115.

38. TURPIN, M.L. and ELLIOT, J.F. Nucleation of oxide inclusions in iron melts. Journal of the Iron and Steel Institute. March 1966: 217-225.

39. HILTY, D.C. FORGENG, W.D. and FOLKMAN, R.L. Oxygen solubility and oxide phases in the Fe-Cr-O system. Journal of Metals. February 1955: 253-268.

40. TURKDOGAN, E.T. Physical chemistry of high temperature technology. New York: Academic Press, 1980. 5-24.

41. BODSWORTH, C. and BELL, H.B. Physical chemistry of iron and steel manufacture. 2nd. ed. London: Longman, 1972. 485-505.

42. DERGE, G. (ed). Basic open hearth steelmaking with supplement on oxygen in steelmaking. 3rd. ed. New York: AIME, 1964. 679.

43. WEST, D.R.F. Ternary equilibrium diagrams. 2nd. ed. London: Chapman and Hall, 1982. 99-104.

44. GREAVES, R.H. Cromium steels. London: HMSO, 1935. 93.

45. CHU, W.F. and RAHMEL, A. The conversion of chromium oxide to chromium carbide. Oxidation of Metals. April 1981: 15 (3/4), 331-337.

46. VODOP'YANOV, A.G., SEREBRYAKOVA, A.V. and KOZHEVNIKOV, G.N. Mechanism of the reaction of chromic oxide with carbide. Russian Metallurgy (Metally). 1979: 5, 11-14.

47. VACHER, H.C. and HAMILTON, E.H. The carbon-oxygen equilibrium in liquid iron. Transactions of the Metallurgical Society of AIME. 1931: 95, 124.

48. MARSHALL, S. and CHIPMAN, J. The carbon-oxygen equilibrium in liquid iron. Transactions of the American Society for Metals. September 1942: 30 (3), 695.

49. RICHARDSON, F.D. and DENNIS, W.E. Thermodynamic study of dilute solutions of carbon in molten iron. Transactions of the Faraday Society. 1953: 49, 171-180.

50. RIST, A. and CHIPMAN, J. Activity of carbon in liquid iron-carbon solutions. In: Proceedings of the Conference The Physical Chemistry of Iron and Steelmaking, held in Dedham, Massachusetts, 28 May to 3 June, 1956. New York: John Wiley, 1958. 3-12.

51. TURKDOGAN, E.T., LEAKE, L.E. and MASSON, G.R. Thermodynamics of iron-carbon melts. Acta Metallurgica. July 1956: 4 (6), 396-406.

52. ELLIOT, J.F. The carbon-oxygen equilibria in liquid iron. In: Proceedings of the Conference The Physical Chemistry of Iron and Steelmaking. Op. cit., 37-41.

53. FUWA, T. and CHIPMAN, J. The carbon-oxygen equilibria in liquid iron. Transactions of the Metallurgical Society of AIME. October 1960: 218, 887-891.

54. GOKCEN, N.A. Equilibria in reaction of hydrogen and carbon monoxide with dissolved oxygen in liquid iron, equilibrium in reduction of

ferrous oxide with hydrogen, and solubility of oxygen in liquid iron. *Transactions of the Metallurgical Society of AIME*. November 1956: 206, 1558-1567.

55. FLORIDIS, T.P. and CHIPMAN, J. Activity of oxygen in liquid iron alloys. *Transactions of the Metallurgical Society of AIME*. August 1958: 212, 549-553.

56. TANKINS, E.S., GOKCEN, N.A. and BELTON, G.R. The activity and solubility of oxygen in liquid iron, nickel and cobalt. *Transactions of the Metallurgical Society of AIME*. June 1964: 230, 820-827.

57. MATSUMOTO, N. Equilibrium between carbon and oxygen in liquid iron and carbon-monoxide under high pressure. *The Science Reports of the Research Institutes. Tôhoku University. Series A*. 1970: 22, 73-83.

58. MATOBA, S. and BAN-YA, S. Thermodynamics of liquid Fe-$\underline{C}$-$\underline{O}$ system. *Iron and Steel Institute of Japan*. 1980: 66 (9), 1406-1422. (in japanese)

59. RICHARDSON, F.D. The carbon oxygen reaction in liquid iron. In: *International Conference of Physical Chemistry and Steelmaking*, held in Versailles, France, 23-25 October, 1978. 194-197.

60. BODSWORTH, C. and BELL, H.B. Physical chemistry of iron and steel manufacture. Op. cit., 381.

61. BIRD, R.B., STEWART, W.E. and LIGHTFOOT, E.N. Transport phenomena. New York: John Wiley, 1960. 563-574.

62. TURKDOGAN, E.T. Physical chemistry of high temperature technology. Op. cit., 209.

63. Standard methods of analysis of iron, steel and associated materials. 5th. ed. Sheffield: The United Steel Companies, 1961. 23-27.

64. BODSWORTH, C. and BELL, H.B. Physical chemistry of iron and steel manufacture. Op. cit., 59-65.

65. LEE, H.G. and RAO, Y.K. Rate of decarburization of iron-carbon melts: Part II. A mixed-control model. Metallurgical Transactions B. September 1982: 13 B (3), 411-421.

66. BAKER, L.A., WARNER, N.A. and JENKINS, A.E. Kinetics of decarburization of liquid iron in an oxidizing atmosphere using the levitation technique. Transactions of the Metallurgical Society of AIME. October 1964: 230 (6), 1228-1235.

67. BAKER, L.A., WARNER, N.A. and JENKINS, A.E. Decarburization of a levitated iron droplet in oxygen. Transactions of the Metallurgical Society of AIME. June 1967: 239 (6), 857-864.

68. DISTIN, P.A., HALLET, G.D. and RICHARDSON, F.D. Some reactions between drops of iron and flowing gases. Journal of the Iron and Steel Institute. August 1968: 206 (8), 821-833.

69. KAPLAN, R.S. and PHILBROOK, W.O. The kinetics of gaseous oxidation of binary and ternary alloys of liquid iron. Transactions of the Metallurgical Society of AIME. October 1969: 245, 2195-2204.

70. EL-KADDAH, N.H. and ROBERTSON, D.G.C. The kinetics of gas-liquid metal reactions involving levitated drops. Carburization and decarburization of molten iron in CO-CO_2 gas mixtures at high pressures. Metallurgical Transactions B. June 1978: 9 B (2), 191-199.

71. NOMURA, H. and MORI, K. Kinetics of decarburization of liquid iron with high concentration of carbon. Transactions of the Iron and Steel Institute of Japan. 1973: 13, 265-273.

72. FRUEHAN, R.J. and MARTONIK, L.J. The rate of decarburization of liquid iron by CO_2 and H_2. Metallurgical Transactions. May 1974: 5 (5), 1027-1032.

73. SAIN, D.R. and BELTON, G.R. Interfacial reaction kinetics in the decarburization of liquid iron by carbon dioxide. Metallurgical Transactions B. June 1976: 7 B (2), 235-244.

74. FORSTER, A. and RICHARDSON, F.D. Oxidation of copper and nickel drops by carbon dioxide. Transactions of the Institution of Mining and Metallurgy. 1975: 84, C116-122.

75. PARLEE, N.A., SEAGLE, S.R. and SCHUHMANN, R. Rate of carbon oxygen reaction in liquid iron. Transactions of the Metallurgical Society of AIME. February 1958: 212, 132-138.

76. EL-KADDAH, N.H. and ROBERTSON, D.G.C. Kinetics of reaction of liquid iron at low concentrations of carbon in $CO-CO_2$. Imperial College, Department of Metallurgy and Materials Science. Unpublished work.

77. BIRD, R.B., STEWART, W.E. and LIGHTFOOT, E.N. Transport phenomena. Op. cit., 639.

78. GOLDBERG, D. and BELTON, G.R. The diffusion of carbon in iron-carbon alloys at 1560 °C. Metallurgical Transactions. July 1974: 5, 1643-1648.

79. RICHARDSON, F.D. Physical chemistry of melts in metallurgy. Op. cit., 307.

80. BIRD, R.B., STEWART, W.E. and LIGHTFOOT, E.N. Transport phenomena. Op. cit., 504-512.

81. FUKUNAKA, Y. and TOGURI, J.M. The oxidation of liquid Ni_3S_2. Metallurgical Transactions B. June 1979: 10 B, 191-201.

82. MEYER, G.L. et al. Thermodynamic properties of molten sulfides. Part I. The system Ni-S. Metallurgical Transactions B. June 1975: 6 B, 229-235.

83. QUENEAU, P. et al. Some novel aspects of the pyrometallurgy and vapometallurgy of nickel. Journal of Metals. July 1969: 35-45.

84. SADDINGTON, R., CURLOOK, W. and QUENEAU, P. Tonnage oxygen for nickel and copper smelting at copper cliff. Journal of Metals. April 1966: 440-452.

85. BUMAZHNOV, F.T. and ASTAF'EV, A.F. Mechanism of nickel oxide coarsening during fluidized roasting of nickel concentrate. The Soviet Journal of Non-Ferrous Metals. 1974: 15 (1), 23-25.

86. ROBERTS, O.C., ROBERTSON, D.G.C. and JENKINS, A.E. The electromagnetic levitation of liquid metal sulfides and their reaction in oxygen. Transactions of the Metallurgical Society of AIME. November 1969: 245, 2413-2420.

87. FUKUNAKA, Y. and TOGURI, J.M. The vaporization kinetics of Ni_3S_2. Metallurgical Transactions B. March 1978: 9 B, 33-43.

88. KHARITIDI, G.P., TIKHONOV, A.I. and SMIRNOV, V.I. Kinetics of deep roasting nickel calcine in a fluidized bed. The Soviet Journal of Non-Ferrous Metals. April 1968: 9 (4), 60-65.

89. WRIEDT, H.A. and CHIPMAN, J. Solubility of oxygen in liquid nickel and Fe-Ni alloys. Journal of Metals. March 1955: 477-479.

90. BOWERS, J.E. The equilibrium between oxygen and molten nickel-iron alloys. Journal of the Institute of Metals. 1961-62: 90, 321-328.

91. TANKINS, E.S., GOKCEN, N.A. and BELTON, G.R. The activity and solubility of oxygen in liquid iron, nickel and cobalt. Transactions of the Metallurgical Society of AIME. June 1964: 230, 820-827.

92. KEMORI, N., KATAYAMA, I. and KOZUKA, Z. Solubility limit and thermodynamic properties of oxygen in liquid nickel. Journal of Chemical Thermodynamics. 1981: 13, 313-325.

93. NAGAMORI, M. and INGRAHAM, T.R. Thermodynamics properties of Ni-S melts between 700 and 1100°C. Metallurgical Transactions. July 1970: 1, 1821-1825.

94. VENAL, W.V. and GEIGER, G.H. The thermodynamic behavior of sulfur in molten nickel and nickel-base alloys. Metallurgical Transactions. November 1973: 4, 2567-2573.

95. SOLAR, M.Y. AND BELL, M.C. Vacuum desulphurization of molten nickel. Canadian Metallurgical Quarterly. 1973: 12 (4), 475-486.

96. TURKDOGAN, E.T. Physical chemistry of oxygen steelmaking, thermochemistry and thermodynamics. Monroeville, Pennsylvania: United States Steel Corporation, 1970. 67-76. (Monograph Series on BOF Steelmaking. Vol. II: Theory and Fundamentals. Chapter A).

97. VOGEL, A.I. Oxidation and reduction processes involving iodine-iodimetry and iodometry. In: A text-book of quantitative inorganic analysis. 3rd. ed. London: Longmans, 1961. 343-349.

98. JONES, R.F. et al. A simple and rapid method for the determination of sulphur in iron and steel. Journal of the Iron and Steel Institute. May 1966: 505-508.

99. ELLIOT, P.R. Constitution of binary alloys. New York: Mc Graw Hill, 1965. 661.

100. BAUR, J.P. et al. High-pressure oxidation of metals, nickel in oxygen. Journal of the Electrochemical Society. March 1963: 110 (3), 185-189.

101. OSBURN, C.M. and VEST, R.W. Defect structure and electrical properties of NiO - I. High temperature. Journal of Physical Chemistry of Solids. 1971: 32, 1331-1342.

102. HAUFFE, K. Oxidation of metals. New York: Plenum Press, 1965. 171-193.

103. BOGDANDY, L. VON and ENGELL, H.J. The reduction of iron ores; scientific basis and technology. Düsseldorf: Verlag Stahleisen, 1971. 18-23.

104. TURKDOGAN, E.T. Physical chemistry of high temperature technology. Op. cit., 78.

105. TURKDOGAN, E.T. Ibid., 5-24

106. MENZIES, A. and STRAFFORD, K.N. Observations on the mechanical properties of nickel oxide scales. Journal of Materials Science. 1967: 2, 358-364.

107. POPE, M.C. and BIRKS, N. The penetration by sulfur of NiO scales growing on nickel. Oxidation of Metals. 1978: 12 (2), 173-181.

108. POPE, M.C. and BIRKS, N. Sulfur solubility in NiO and CoO at 1000 °C. Oxidation of Metals. 1978: 12 (3), 191-204.

109. TURKDOGAN, E.T. Physical chemistry of high temperature technology. Op. cit., 427-429.

110. BYERLEY, J.J. and TAKEBE, N. Densities of molten nickel mattes. Metallurgical Transactions. April 1971: 2, 1107-1111.